Microwave-to-Optical Transduction Using Rare-Earth Ions

Thesis by
Jake Herschel Lebi Rochman

In Partial Fulfillment of the Requirements for the
Degree of
Doctor of Philosophy

CALIFORNIA INSTITUTE OF TECHNOLOGY
Pasadena, California

2022
Defended January 20th, 2022

Jake Herschel Lebi Rochman
ORCID: [0000-0002-8475-3389]

ACKNOWLEDGEMENTS

I would first like to thank Andrei Faraon. Thank you Andrei for having the patience and giving me the freedom to learn and develop as a student under your watch. I first worked in Andrei's group as an undergraduate intern working on nanofabrication, and I have appreciated the ability to work on all aspects of the experiments over my time in your group. Thank you for your unwavering optimism over the years.

I would like to thank Tian Xie. I worked closely with Tian on the transduction project for around three years and would like to acknowledge his efforts in building experiments with me and leading our spectroscopy studies. Thank you for your tireless work and effort to help make the results of this thesis possible. I am happy to leave the project in your hands.

Thank you to our former post-doc John Bartholomew for your vast rare-earth ion spectroscopy knowledge and your mentorship within the group. I worked with John at the start of the transduction project and I appreciate his help with our initial superconducting device measurements and help working with the superconducting film deposition system. Thank you for always having the time to chat and explain things to me when needed.

Thank you to the former grad students in the quantum sub-group. Thank you to Ioana for being a great officemate and for your initial help with optical measurements. Thank you to Jon Kindem for your contributions building our lab infrastructure. I had a great time working with you on nanobeam devices. Thank you to Evan for building the confocal set-up that I used and for your initial work building telecom optical setups in the group.

Thank you to the current grad students in the quantum sub-group. Thank you Andrei Ruskuc, Mi, Chun-Ju, and Riku for helpful discussions and for your friendship. Thank you to all the current and former members of the metasurface subgroup.

I would like to thank the KNI cleanroom staff for your efforts to keep tools operational. I spent a lot of time in the cleanroom and appreciate all your work to make that possible. Thank you Guy for leading the way and for your help with electron beam lithography. I would also like to thank former staff members Matt and Nathan. Thank you Matt for training me on the FIB initially and your diligent troubleshooting documentation that made working on the tools as easy as possible. Thank you Nathan for our many discussions about etching and always being helpful when diagnosing the many problems I presented to you.

Thank you to Prof. Alireza Marandi, Prof. Mohammad Mirhosseini, Prof. Oskar Painter, and Prof. Keith Schwab for serving on my defense committee. I would also like to thank Prof. Ali Hajimiri and Dr. Sander Weinreb for serving on my candidacy committee.

Thanks Keith for our many discussions about science and life while working in your lab. Thank you for letting us use your superconducting film deposition system. It was a lot of fun to work with that.

Thank you to Rick LeDuc and Matt Shaw from JPL for advice to get our niobium sputtering process working. Thank you to Jevon Longdell and Yu-Hui Chen for discussions and help with rare-earth ion transduction theory when we were just getting started. Thank you to Hugo Wallner for help with transduction theory and simulations during your internship in our group.

Lastly, thank you to my family and friends for your support over the years and for helping me get through all the ups and downs.

ABSTRACT

Superconducting qubits that operate at microwave frequencies are one of the most promising platforms for quantum information processing. However, connecting distant processors with microwave photons is challenging since microwave photons suffer from thermal noise and large propagation losses in room temperature components. Conversely, optical photons within the telecommunications band are known to have extremely low loss in optical fiber and the thermal noise is minuscule at room temperature. In order to interface superconducting qubits with room temperature optical photons, a quantum transducer is required that can convert photons between microwave and optical frequencies.

This thesis describes the development of a microwave-to-optical transducer using an ensemble of erbium ions, doped within a yttrium orthovanadate (YVO_4) crystal, that are simultaneously coupled to a superconducting microwave resonator and a photonic crystal optical resonator. The erbium ions have spin transitions that couple to the microwave resonator and optical transitions at telecom wavelengths that couple to the optical resonator.

The electromagnetic design, atomic simulations, nanofabrication, and characterization of the transducer at cryogenic temperatures are presented. We measured the coupling of the ions to the cavities and determined the influence of optical light on the microwave resonator and atomic properties. The transducer efficiency is characterized in several different modes of operation including continuous-wave operation and pulsed operation with single photon detection. Lastly, the temperature of components within the transducer including the erbium ions and the microwave resonator are characterized during operation of the transducer. These results represent the first demonstration of a rare-earth ion transducer with integrated microwave and optical resonators.

PUBLISHED CONTENT AND CONTRIBUTIONS

1. Rochman, J., Xie, T., Bartholomew, J. G., Schwab, K. C. & Faraon, A. Microwave-to-optical transduction with erbium ions coupled to planar photonic and superconducting resonators. *In Preparation.*

   J.R. designed, fabricated, and measured the device, processed data, and wrote the manuscript.

2. Ruskuc, A., Wu, C.-J., Rochman, J., Choi, J. & Faraon, A. Nuclear spin-wave quantum register for a solid state qubit. *Nature* **602,** 408–413. `https://doi.org/10.1038/s41586-021-04293-6` (Feb. 2022).

   J.R. designed and fabricated the nanocavity device and participated in the writing of the manuscript.

3. Craiciu, I., Lei, M., Rochman, J., Bartholomew, J. G. & Faraon, A. Multifunctional on-chip storage at telecommunication wavelength for quantum networks. *Optica* **8,** 114. `https://doi.org/10.1364/optica.412211` (Jan. 2021).

   J.R. designed the nanocavity, assisted in the fabrication of the nanocavity and participated in the writing of the manuscript.

4. Xie, T. *et al.* Characterization of Er^{3+}:YVO_4 for microwave to optical transduction. *Physical Review B* **104.** `https://doi.org/10.1103/physrevb.104.054111` (Aug. 2021).

   J.R. contributed to the spectroscopy measurements and participated in the writing of the manuscript.

5. Bartholomew, J. G., Rochman, J., Xie, T., Kindem, J. M., Ruskuc, A., Craiciu, I., Lei, M. & Faraon, A. On-chip coherent microwave-to-optical transduction mediated by ytterbium in YVO_4. *Nature Communications* **11.** `https://doi.org/10.1038/s41467-020-16996-x` (June 2020).

   J.R. designed and fabricated the nanocavity device and participated in the writing of the manuscript.

6. Kindem, J. M., Ruskuc, A., Bartholomew, J. G., Rochman, J., Huan, Y. Q. & Faraon, A. Control and single-shot readout of an ion embedded in a nanophotonic cavity. *Nature* **580,** 201–204. `https://doi.org/10.1038/s41586-020-2160-9` (Mar. 2020).

   J.R. designed and fabricated the nanocavity device and participated in the writing of the manuscript.

7. Craiciu, I. *et al.* Nanophotonic quantum storage at telecommunication wavelength. *Physical Review Applied* **12.** `https://doi.org/10.1103/physrevapplied.12.024062` (Aug. 2019).

   J.R. designed and fabricated the nanocavity device and participated in the writing of the manuscript.

8. Bartholomew, J. G., Zhong, T., Kindem, J. M., Lopez-Rios, R., Rochman, J., Craiciu, I., Miyazono, E. & Faraon, A. Controlling rare-earth ions in a nanophotonic resonator using the ac Stark shift. *Physical Review A* **97.** `https://doi.org/10.1103/physreva.97.063854` (June 2018).

   J.R. designed and fabricated the nanocavity device and participated in the writing of the manuscript.

9. Zhong, T. *et al.* Optically Addressing Single Rare-Earth Ions in a Nanophotonic Cavity. *Physical Review Letters* **121.** `https://doi.org/10.1103/physrevlett.121.183603` (Oct. 2018).

   J.R. designed and fabricated the nanocavity device and participated in the writing of the manuscript.

10. Zhong, T. *et al.* Nanophotonic rare-earth quantum memory with optically controlled retrieval. *Science* **357,** 1392–1395. `https://doi.org/10.1126/science.aan5959` (Sept. 2017).

    J.R. designed and fabricated the nanocavity device and participated in the writing of the manuscript.

TABLE OF CONTENTS

LIST OF ILLUSTRATIONS

LIST OF TABLES

Chapter 1

INTRODUCTION

In this work, we demonstrate a microwave-to-optical transducer using an integrated superconducting microwave resonator and a photonic crystal optical resonator that are both simultaneously coupled to an ensemble of rare-earth ions. We start with a spectroscopic study of a promising rare-earth ion system, $Er^{3+}:YVO_4$, that we use for the transducer and design the integrated resonators within the transducer to maximize their mode overlap and quality factors. That is followed by the development of a new nanofabrication process to integrate superconducting microwave circuits and photonic circuits on a rare-earth ion doped crystal. We then present the microwave, optical, and cryogenic set-up that was built to measure the devices within a dilution fridge. The transducer is characterized in terms of its conversion efficiency and operation temperature in both continuous wave and pulsed operation. Lastly, we outline a path forward to improve the transduction efficiency.

This chapter covers the motivation for this thesis and then introduces quantum transducers, rare-earth ion properties, and rare-earth ion transducers.

1.1 Quantum Networks

Quantum technologies in the ‘second quantum revolution’ seek to solve problems where quantum mechanical effects such as superposition and entanglement can enable improved performance or novel functionality [1]. There has been specific interest in developing quantum technologies for quantum-secure communication [2, 3], quantum computing [4–6], and quantum metrology [7, 8] applications.

Quantum networks, consisting of quantum nodes that process quantum information and quantum channels that connect distant nodes, represent a useful platform to implement future quantum applications as they grow in size [9, 10]. They enable relatively small quantum processors to work together and form a larger, more powerful system in the case of distributed quantum computing [11] or offer new functionality beyond what a single node can accomplish in the case of quantum communication or blind quantum computing [12].

There are many physical systems that can be considered to be quantum nodes including trapped ions [13, 14], atomic-defects in solids [15], and superconducting qubits [16, 17]. Beyond just quantum information processing, quantum nodes require interfacing with quantum channels for connections between nodes. The most promising quantum channel is optical photons within the near-infrared spectrum where low loss propagation can be achieved in optical fiber or in free-space with satellites. Atomic systems are more naturally suited for this as they often have transitions at optical frequencies that can act as a direct interface with optical photons.

Superconducting qubits, on the other hand, have developed into a leading platform for quantum information processing, but they operate at microwave frequencies and would require an additional technology before they could be interfaced with a photonic quantum channel.

1.2 Superconducting Qubits

Over the past couple decades, superconducting qubits have emerged as one of the most promising platforms for quantum information processing. These macroscopic quantum electrical systems, based on the Josephson junction's quantum non-linearity at microwave frequencies, have emerged from pioneering single qubit experiments [18] to intermediate scale systems with tens of qubits in recent years. Demonstrations superconducting quantum systems, such as the quantum supremacy experiment from Google using their Sycamore processor [19] and follow-up work [20], have highlighted the significant advances in the field and show both the promise of superconducting qubit-based quantum computing, but also the challenges that lay ahead for more impactful devices.

Superconducting qubits are an appealing quantum technology platform for several reasons. Firstly, unlike atomic systems with constrained level structures and transitions given by nature, superconducting quantum circuits can be engineered through the nanofabrication of the different microwave components, which permits the development of many different types of superconducting qubits with unique level structure and transitions[16]. The nanofabrication process provides a natural way to scaling up the circuits to wafer-scale complexity.

Secondly, superconducting qubits interact strongly with photons, which allows for fast qubit operations including single qubit and two qubit gates (~10-100 ns) [19]. Lastly, although superconducting qubit coherence times are short compared to state-of-the-art atomic systems, the coherence times have continuously improved over the years and are currently around (~10-100 us), which allows several gates to be executed before the qubits decohere. Importantly, the coherence times have yet to reach a fundamental or practical limit, which gives hope that longer coherence times and higher gate fidelity may be achievable in future devices using new techniques [21, 22].

Like any quantum computing platform, superconducting qubits have several challenges to overcome in order for them to reach the full promise of a quantum computer. These include general challenges for quantum computing that are true for every platform, which are that devices do not have enough qubits and gate errors are too high for large-scale and practical implementation of error correction codes [23]. Some of the challenges more specific to superconducting qubits, that play into the more general challenges, are the cryogenic requirements and fabrication challenges.

Superconducting qubits typically have transition frequencies around ~ 5 GHz, which requires operation at temperatures T ~10 mK$\ll \hbar\omega/k_B$ to freeze out any thermal excitations. This can be achieved in the lab using dilution refrigerators, but maintaining low temperature operation of the entire circuit only becomes more challenging as the circuit size grows due to an increase in passive and active heat loads [24].

Although the nanofabrication techniques offer several advantages for superconducting qubits, 'lab-made' qubits also currently suffer from fabrication defects such as undesired oxides on metal surfaces or two-level-system defects that hinder the coherence of superconducting qubits. However, further developments in nanofabrication techniques and dedicated facilities towards superconducting qubit fabrication should only help mitigate these challenges in the future.

A limitation for superconducting circuits towards scaling up the system size is that quantum information encoded on a microwave photon cannot leave the dilution fridge without significant added noise from thermal excitations or losses from coaxial cables at room temperature. This has led researchers to focus on three-dimensional integration [25], die-to-die connections [26], fridge-to-fridge connections [27], and larger scale cryogenic systems as ways to increase the size of the circuits.

These solutions are viable for quantum computing or small/local quantum networks, but another solution is needed for using superconducting qubits within large scale quantum networks.

1.3 Quantum Transduction

In general, quantum transducers are devices that transfer quantum excitations between two different modes. The modes can differ in terms of their frequency and also can consist of different types of excitations such as photons, phonons, or spin-waves for example.

In terms of quantum transducers for integrating superconducting qubits with optical quantum networks, we are interested in the conversion between microwave (~5 GHz) and optical (~ 200 THz) photons. As shown in Figure 1.1, a microwave-to-optical (M2O) quantum transducer can be abstractly modelled as an effective linear coupling, S, between an optical mode, a, and a microwave mode, b. High efficiency can be reached when this device acts in an impedance-matched regime (i.e. no reflections from the device) and there are minimal internal losses.

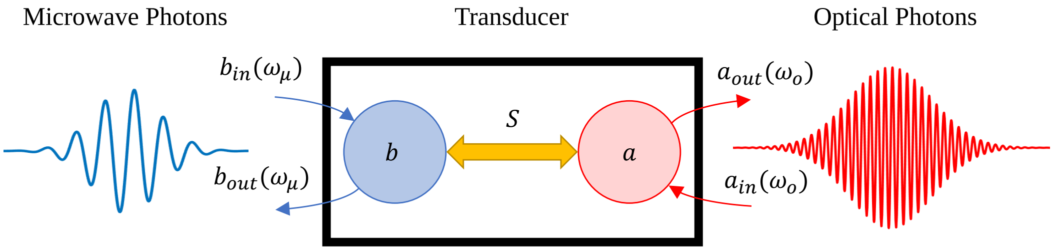

Figure 1.1: An abstract model of a transducer that utilizes an effective coupling, S, between an optical mode, a, and microwave mode, b, to convert photons from one frequency to the other.

A microwave-to-optical quantum transducer will allow quantum information encoded in microwave photons to be converted into optical photons where they can be readily propagated long distances at room temperature with minimal added noise or propagation losses. This would allow for remote entanglement between distant superconducting qubit processors within a quantum network.

Microwave-to-optical transducers may have additional applications if their performances can be proficient enough. For example, they could be used to replace microwave-based superconducting qubit readout chains that can offer a lower noise (i.e. no amplification would be required) solution that may reduce the heat load of the detection setup by replacing low temperature microwave amplifiers and coax lines with optical fiber. Further, non-classical states of light used in bosonic codes have been proven to be elusive at optical wavelengths. With a quantum microwave-to-optical transducer, these states of light could be generated in the microwave domain, where initial demonstrations have already been shown [28], and upconverted to optical frequencies.

General Requirements of Microwave-to-Optical Quantum Transducers

In order for a quantum transducer to live up to its potential, it should satisfy several requirements [29]. The primary requirements are high efficiency, low added-noise, and high bandwidth. The transducer should have high efficiency at the single photon level, such that if a single microwave photon is at the input, a single optical photon will exit from the output. It should also have low added-noise, which means that if a single microwave photon is at the input, *only* a single photon will exit from the output and the quantum information encoded on that photon remains intact. In order for low noise operation, low temperature operation is required ($T \ll \hbar\omega/k_B$) such that the device will not be contaminated by thermal photons. Thirdly, the bandwidth of the transducer needs to match or exceed the bandwidth of the photons that are used for transduction.

Beyond the three main requirements, we can consider additional features that are also important. The transducer should be bidirectional or, in other words, be able to convert microwave photons into optical photons and optical photons into microwave photons. It should operate with a high duty cycle, which means that the transducer should minimize the dead time where it cannot operate. It should consume as little power as possible. Likely the transducer will need to be thermally-connected to the lowest temperature stage of a sub-100 mK cryogenic refrigerator, where cooling power is limited, so low power consumption is required to keep the refrigerator cold. Lastly, the transducer should be easily integrated with superconducting qubits. Ideally, the transducer could be fabricated on the same chip as the superconducting qubits or at least within the same package.

Transduction Methods

There are many different physical systems one can use to make a quantum transducer. At the start of this project, there were only a small handful of experimental transduction demonstrations, but over the course of this project there has been significant progress in many different systems, which has been exciting to see. These two recent reviews go into the details of the different methods [30, 31]. The different systems range from optomechanical systems [32–34], piezo-optomechanical systems [35–43], electro-optical systems [44–52], atomic systems [53–59], and magnonic systems [60].

All processes use a parametric process where the input photon is mixed with an optical pump field to generate the output photon at the sum (or difference) of the input photon frequency and the optical pump field frequency. Typically the native interactions are not sufficiently strong to achieve high-efficiency, so resonators at both optical and microwave frequencies are used to enhance the interactions between photons and the transduction medium.

Optomechanical and piezo-optomechanical systems uses a mechanical resonator as the intermediate medium for the transducer and rely on electromechanical or piezoelectromechanical interactions to interface with microwave photons and optomechanical interactions to interact with optical photons. To date, groups have shown high efficiency optomechanical transducers (η ~50%)[34] and low added noise operation (N_{add} ~0.5)[42], but they have not been shown simultaneously or at high bandwidth. One challenge with these systems is keeping the mechanical resonator cold. Low frequency (~ MHz) mechanical resonators are able to achieve exceptional large quality factors, but require laser-cooling to reach low temperatures. High frequency mechanical resonators (~ GHz) are able to achieve low temperatures from passive cooling, but require low energy optical pulses in order to remain cold. High quality factors have been shown for high frequency mechanical resonators [61], but only in limited materials and not while integrated within a transducer to date.

Electro-optical systems rely on materials with electro-optical non-linearities to directly mix microwave and optical photons. For materials that have been used to date, this non-linearity is not particularly strong, so these transducers require exceptional large resonator quality factors (more typically optical quality factors) and/or large optical pump powers to enhance the interactions. To date, high efficiency (η ~50%) electro-optrical transducers have been achieved with low noise (N_{add} ~0.16), but at low duty cycles and not at the single photon level [52].

Atomic systems rely on ensembles of atoms with electronic transitions at optical and microwave frequencies. This can range from cold atoms in traps to atomic defects in solid-state systems. To date, efficiency of η ~5% has been achieved in cold atom systems [56], albeit at room temperature and at a microwave frequency of 84 GHz, while efficiencies of up to $\eta \sim 10^{-5}$ have been achieved in solid-state systems at 4 K[54].

Another distinguishing factor between different approaches is the use of bulk/large scale resonators or nanoscale/on-chip resonators. Bulk resonators tend to offer higher quality factors, but also tend to require larger optical pump power to overcome the larger mode volumes associated with the larger cavities. Bulk resonators also tend to have more efficient optical coupling schemes, as its not always easy to squeeze optical modes into nanophotonic devices. This is especially true with non-traditional material platforms that are being considered for microwave-to-optical transduction.

On-chip devices offer a more scalable solution that can potentially be integrated directly with superconducting circuits. Also, in principle, they can operate with less optical pump power due to the smaller mode volumes of their optical cavities. Less optical power is useful to minimize optical heating effects caused from optical losses from scattering or absorption. It is worth noting that in many of the first iterations of on-chip transducers, the optical losses are significant, so there may be more heating in these devices. However, these losses are not fundamental and should be improved in future devices that are more specifically designed to solve these problems.

1.4 Rare-earth Ion Properties

In this section, we will introduce some general rare-earth ion properties that are related to rare-earth ion transducers and will be used throughout this thesis.

The rare-earths are an ensemble of elements that include yttrium, scandium and the lanthanides. The lanthanides largely share similar chemical, physical and electromagnetic properties. Their most distinguished features are related to their magnetism and optical properties that lend them to many industrial applications from permanent magnets to lasing crystals.

When embedded in solids, they often reside in their trivalent state and have an electronic configuration of [Xe]$4f^N$, where N ranges from 1 to 14 for the different lanthanides. N is the main distinguishing factor between the different elements and strongly determines the differences in their properties.

All the lanthanides (except La and Lu, which have either an entirely full or empty $4f$ shell) have $4f$-$4f$ energy transitions when embedded in a crystal. Importantly, these $4f^N$ orbitals reside closer to the nucleus compared to the 5s and 5p orbitals, which act analagous to a Faraday cage and shield the transitions from external electronic perturbations [62]. This shielding is thought to be at least partly responsible for the long coherence times associated with these transitions [63].

This section will highlight a few properties of rare-earth ions that are relevant to this thesis, but more information can be found at these references [62, 64–66].

Energy Levels

The energy levels of the rare-earth ions embedded in crystals are defined by contributions from the free ion, the crystal field, and the magnetic field environment, which are listed in terms of their relative strength. There can also be contribution from hyperfine interactions, but those species are not the main subject of this thesis.

The free ion component consists of both Coulomb interactions and spin-orbit coupling that predominately define the energy levels for each ion, where the splitting between the lowest levels is a few hundred THz (or at optical frequencies). The levels can be labelled as ${}^{2S+1}L_J$, where S, J, and L are the spin, orbital angular momentum, and total angular momentum quantum numbers, respectively. Each level manifold has a $2J + 1$ degeneracy.

Erbium is an important rare-earth ion as its lowest energy level splitting (i.e. between ${}^4I_{15/2}$ and ${}^4I_{13/2}$) fortunately resides in the telecommunications C-band ($\lambda \sim 1530$ nm), which makes its optical transitions of significant value.

When the ions are placed in a crystal, the free ion states break their degeneracy due to the reduced site symmetry of the crystal field. The energy levels are also perturbed with a much smaller contribution compared to the spin-orbit coupling (i.e. ~THz). In order to relax the rare-earth ions into their crystal field ground state, cryogenic temperatures (T~1-10 K) are required. For Kramers ions, which are the subject of this thesis, each manifold can split into as many as $J + 1/2$ doublets. Kramers ions are defined by having an odd number of electrons.

Each doublet can be modelled as a spin-1/2 particle, where we observe Zeeman splitting of the doublet in the presence an external magnetic field. This energy splitting tends to be up to ~10-100 GHz for reasonable magnetic field strengths.

Optical and Microwave Transitions

For microwave-to-optical transduction using rare-earth ions, it is required to have a set of optical and microwave transitions to couple to the input/output fields.

The simplest way to generate microwave transitions with rare-earth ions is to apply a magnetic field and use their Zeeman transitions. There are some unique rare-earth ions and crystals that are subject to small crystal field splittings (i.e.~55 GHz in Er:YVO_4 [67] and ~35 GHz in Tm:YAG [68]) so potentially these types of transitions can also be considered if higher microwave frequencies are desired. Also, there are hyperfine transitions for rare-earth ions with a nuclear spin that can have transitions on the order of ~MHz - GHz at zero applied magnetic field.

Typically the optical transitions of note are between the lowest crystal field levels of the two lowest spin-orbit manifolds. The $4f$-$4f$ transitions are weakly allowed via electric dipole transitions (oscillator strength, $f \sim 10^{-7}$) due to mixing caused by the crystal field. They can also have magnetic dipole transitions that can be of comparable strength to the electric dipole transitions [69].

The optical transitions are subject to transition selection rules determined by the rare-earth ions quantum numbers and the crystal field site symmetry. This also determines the polarization of the dipole moment (i.e. σ or π polarized). More details can be found in these references [62, 65, 70].

Transition Inhomogeneity

Both the optical and microwave transitions of rare-earth ions experience inhomogeneous broadening of the transitions due to the ions having slightly different transition frequencies as a result of different local environments. Inhomogeneity for optical transitions typically ranges from ~0.1-100 GHz [71], while inhomogeneity for microwave Zeeman transitions is typically $\sim$1-100 MHz.

There are several factors that can cause inhomogeneous broadening of rare-earth ion transitions. Impurities and crystal defects from the crystal growth can be one cause of inhomogeneity. High purity materials and crystal growth facility are required to reduce these defects as much as possible. There can also be lattice strain introduced during the crystal growth (or after growth from poor handling) which can cause inhomogeneous broadening.

Due to the impact crystal growth can have on the properties, samples from different growers can vary quite dramatically and suffer from odd inclusions of unexpected impurities in some cases. Fortunately, many of the rare-earth host crystals have been extensively studied and used for the lasing/optics community (i.e. YAG or YVO_4), and it is possible to get very high quality crystals of these materials from commercial vendors (elemental impurities on the $\sim$100 ppb level).

Another factor that can cause inhomogeneity is the doping concentration of the rare-earth ion species itself. Due to lattice mismatch with the host site, the rare-earth ion dopants themselves can introduce inhomogeneity, which tends to increase as the concentration increases. In the extreme case of 100% rare-earth ion concentration, this problem can be alleviated and narrow inhomogeneous linewidths can be recovered in some crystals [72].

Lastly, there can be inhomogeneity introduced from an external magnetic field. This can either be a result of inhomogeneity of the magnetic field itself across the sample or from inhomogeneity in the g-factors of the different ions such that the transitions broaden at higher magnetic fields.

Coupling to Nano-scale Optical Structures and On-Chip Devices

As alluded to earlier, one drawback of rare-earth ions for quantum technology applications is their relatively weak optical transitions ($f \sim 10^{-7}$) that limit their interaction strength with photons. One way to overcome this is to place the ions within nano-scale optical structures. Due to the smaller mode volume associated with nano-scale devices, the coupling rate to optical fields can be enhanced significantly.

Further, the small mode volumes associated with nano-scale devices permit coupling to a few number of ions or even single rare-earth ions in some cases. Although this is not the direct focus of this thesis, single rare-earth ions are of significant interest to our group and the rare-earth ion community for their prospects in quantum communications and potentially in quantum computing [73].

There have been several different approaches to nano-scale photonic devices. These include: (i) fabrication nanophotonic resonators or waveguide directly in the rare-earth host material [74–76], (ii) patterning nanophotonic resonators or waveguide onto the rare-earth host surface for evanescent coupling [77–80], (iii) rare-earth ions in nanoparticles [81–84], (iv) thin rare-earth ion doped crystal slabs that are placed within a Fabry-Perot optical cavity [85], and (v) ion-implanted single rare-earth ions [86]. The Faraon group has focused primarily on methods (i) and (ii) to date.

Each of the different approaches has its own advantages and disadvantages. Generally speaking, the different approaches are relatively immature with significant progress only being made within the past 5-10 years by a handful of groups, so improved performance can be anticipated in the years to come.

There has also been considerable work interfacing rare-earth ions with on-chip microwave devices [87–95], where ensemble strong coupling has readily been achieved with several different species. These devices have ranged from superconducting devices patterned on the rare-earth ion host surface to resonators patterned on a conventional superconducting substrate and placing the rare-earth ion doped crystal on the resonator for coupling.

Ion-Cavity Coupling

Here I will introduce some useful expressions to describe coupling between ions and a cavity field.

The single photon coupling strength of a single ion with a magnetic dipole moment with a cavity field is given by:

$$\begin{aligned} g_m(\vec{r}) &= \sqrt{\frac{\mu_0\omega}{2\hbar}}\frac{1}{\sqrt{V_m}}\frac{\vec{\mu}\cdot\vec{B}(\vec{r})}{|\vec{B}_{max}|} \\ &= \sqrt{\frac{\mu_0\omega}{2\hbar}}\frac{1}{\sqrt{V_m}}\frac{\mu B_m(\vec{r})}{|\vec{B}_{max}|} \end{aligned} \tag{1.1}$$

where V_m is the magnetic mode volume, $\vec{\mu}$ is the magnetic dipole moment, μ is the magnitude of the magnetic dipole moment, ω is the angular frequency, $\vec{r}$ is the position of the ion, $B_m(\vec{r})$ is the magnetic field strength of the cavity mode along the direction of the magnetic dipole moment, and $\vec{B}_{max}$ is the maximum magnetic field strength of the cavity mode. The magnetic field mode volume is defined as:

$$V_m = \int \frac{|\vec{B}(\vec{r})|^2}{|\vec{B}_{max}|^2} dV. \tag{1.2}$$

Similarly, the single photon coupling strength of a single ion with an electric dipole moment with a cavity field is given by:

$$\begin{aligned} g_e(\vec{r}) &= \sqrt{\frac{\omega}{2\hbar\epsilon_0}}\frac{1}{\sqrt{V_e}}\frac{\vec{d}\cdot\vec{E}(\vec{r})}{\sqrt{(\epsilon_r(\vec{r})|\vec{E}|^2)_{max}}} \\ &= \sqrt{\frac{\omega}{2\hbar\epsilon_0}}\frac{1}{\sqrt{V_e}}\frac{dE_d(\vec{r})}{\sqrt{(\epsilon_r(\vec{r})|\vec{E}|^2)_{max}}} \end{aligned} \tag{1.3}$$

where V_e is the electric mode volume, $\vec{d}$ is the electric dipole moment, $\epsilon_r(\vec{r})$ is the relative permittivity at position $\vec{r}$, $\vec{E}(\vec{r})$ is the electric field strength of the cavity mode, $E_d(\vec{r})$ is the electric field strength along the electric dipole direction, and V_e is the electric field mode volume.

The electric field mode volume is defined as:

$$V_e = \int \frac{\epsilon_r(\vec{r})|\vec{E}(\vec{r})|^2}{(\epsilon_r(\vec{r})|\vec{E}|^2)_{max}} dV. \tag{1.4}$$

If we have many ions, we can express the collective coupling strength of all the ions as:

$$g_{tot}^2 = \sum_k^N g(\vec{r}_k)^2 \tag{1.5}$$

where N is the number of ions. When the ions have a uniform distribution within the crystal and the ions are sufficiently dense, we can approximate the sum as an integral. For electric dipole coupling this leads to:

$$g_{tot}^2 = \sum_k^N g_e(\vec{r}_k)^2 = \frac{\omega}{2\hbar\epsilon_0}\frac{d^2}{V_e}\sum_k \frac{E_d(\vec{r}_k)^2}{(\epsilon_r(\vec{r})|\vec{E}|^2)_{max}} = \frac{\omega}{2\hbar\epsilon_0\epsilon_{YVO}} d^2\rho\eta_e^2 \tag{1.6}$$

where η_e^2 is the electric energy filling factor that aligns with the electric dipole, ρ is the ion density and ϵ_{YVO} is the permittivity of YVO_4 (the rare-earth ion host crystal that we will use later). η_e^2 can be expressed explicitly as:

$$\eta_e^2 = \frac{\int_{YVO} \epsilon_r(\vec{r})E_d(\vec{r})^2 dV}{\int \epsilon_r(\vec{r})|\vec{E}(\vec{r})|^2 dV}. \tag{1.7}$$

If we assume the electric dipole and electric field are perfectly aligned, then η_e^2 reaches a maximum value of $\eta_{e,max}^2$, which is the conventional energy filling factor:

$$\eta_{e,max}^2 = \frac{\int_{YVO} \epsilon_r(\vec{r})|\vec{E}(\vec{r})|^2 dV}{\int \epsilon_r(\vec{r})|\vec{E}(\vec{r})|^2 dV}. \tag{1.8}$$

Similarly, the ensemble coupling for a magnetic dipole moment is given by:

$$g_{tot}^2 = \frac{\omega\mu_0}{2\hbar\epsilon_{YVO}}\mu^2\rho\eta_m^2 \tag{1.9}$$

where η_m^2 is the magnetic energy filling factor:

$$\eta_m^2 = \frac{\int_{YVO} B_m(\vec{r})^2 dV}{\int |\vec{B}(\vec{r})|^2 dV}. \tag{1.10}$$

The coupling rate can be enhanced by increasing the intensity of the optical field. The single ion Rabi frequency for a large classical optical field is:

$$\Omega = \sqrt{\langle n\rangle} g \tag{1.11}$$

where $\langle n\rangle$ is the mean photon number in the cavity, which can be determined from input-output theory of the cavity to be:

$$\langle n\rangle = \frac{P_{in}}{\hbar\omega}\frac{\kappa_{in}}{\kappa^2/4 + \delta_c^2} \tag{1.12}$$

where P_{in} is the input optical power, $\hbar\omega$ is the energy of the optical photon, κ_{in} is the coupling cavity decay rate, κ is the total cavity decay rate, and δ_c is the light-cavity detuning.

Another useful description is the cavity reflection spectrum when coupled to an ensemble of ions. In the low excitation limit, the reflection spectrum can be modelled as [96]:

$$R(\omega) = |r(\omega)|^2 = \left|1 - \frac{i\kappa_{in}}{\delta_c + i\kappa/2 - W(\omega)}\right|^2 \tag{1.13}$$

where $W(\omega)$ describes the coupling between the ions and the cavity. In general, $W = \sum_k g_k^2/(\omega_k - \omega - \gamma/2)$, where γ is the atomic decay rate and ω_k is the transition frequency of ion, k. For a large ensemble, we can approximate the sum with an integral. For a Gaussian distributed ion ensemble, $W(\omega) = -i\frac{\sqrt{\ln 2}g_{tot}^2}{\Delta}\sqrt{\pi}e^{-\left(\frac{\omega-\omega_i+i\gamma/2}{\Delta/\sqrt{\ln 2}}\right)^2} \operatorname{erfc}\left(-i\frac{\omega-\omega_i+i\gamma/2}{\Delta/\sqrt{\ln 2}}\right)$, where Δ is the linewidth of the ion ensemble and ω_i is the center frequency of the inhomogeneous linewidth. For a Lorentzian distributed ion ensemble, $W(\omega) = \frac{g_{tot}^2}{\omega-\omega_i+i\gamma/2+i\Delta/2}$.

The poles of the $r(\omega)$ spectrum for a Lorentzian line shape can be determined to be:

$$\omega_\pm = \frac{\omega_0 - \omega_i}{2} - \frac{i\gamma + i\kappa + 2i\Delta}{4} \pm \sqrt{g_{tot}^2 + \left(\frac{2(\omega_i - \omega_0) - i\gamma - 2i\Delta + i\kappa}{4}\right)^2} \tag{1.14}$$

where ω_0 is the cavity resonance frequency. The real part of the poles gives the frequency location of the modes and the imaginary part of the poles gives the linewidths.

A common parameter to characterize the coupling between an ensemble of ions and the cavity is given by the ensemble co-operativity:

$$C = \frac{4g_{tot}^2}{\kappa\Delta}. \tag{1.15}$$

The ensemble co-operativity is a ratio of the total ensemble coupling rate to the atomic and cavity decay rates. Generally speaking, a co-operativity of $C > 1$ is desired in most applications.

1.5 Rare-earth Ion Transducers

There have been a few different protocols proposed for using rare-earth ions for microwave-to-optical transduction [97, 98] and additional proposals for other atomic systems that can in principle be adapted for rare-earth ions [99, 100]. In general, they all involve at least three atomic levels, where one transition couples to the microwave input (or output) field, one transition couples to the optical output (or input) field and one transition is used to map coherence between the optical and microwave transitions as shown in Figure 1.2. In general, the transition that couples to the microwave field can have different origins, such as an electronic or nuclear spin transition and can exist within the ground or optically excited state of the atomic level structure.

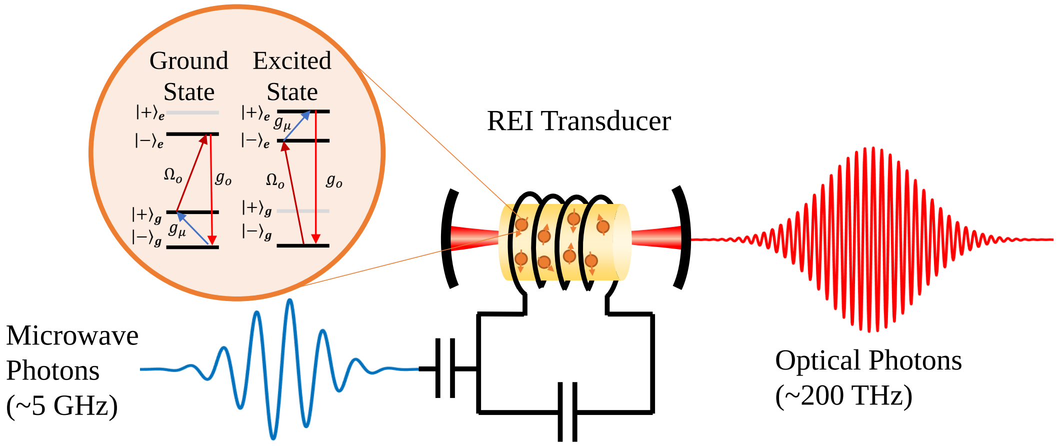

Figure 1.2: Schematic of a rare-earth ion based transducer that includes an optical cavity, depicted by two mirrors, and a microwave LC-resonator. The rare-earth ion doped crystal sits within the optical cavity and within inductor of the microwave cavity. Transduction can occur using the ground or excited state of the ions by coupling a microwave field to a spin transition (g_μ), a optical field to an optical transition (g_o) and optical pump field (Ω_o) to a second optical transition that conserves energy within the process.

We have been most interested in the proposal by Professor Jevon Longdell's group at the University of Otago [98], which seems to be the most straightforward proposal to experimentally implement in our opinion. Their proposal uses a cavity-enhance Raman heterodyne scheme, were the input and output fields have enhanced coupling to the rare-earth ion ensemble via coupling to a microwave and optical cavity. The energy difference between the optical and microwave photon is compensated by an optical pump at the difference (or sum) of the optical and microwave frequencies.

The Longdell group's first experimental implementation was done using Er^{3+}:YSO in a 3D loop-gap microwave resonator [101]. No optical resonator was used for the initial demonstration and the experiments were done at 4 K. The efficiency was quite small ($\eta \sim 10^{-12}$), but nonetheless showed that the method can work.

Their follow-up experiments added a macroscopic Fabry-Perot optical cavity and improved the efficiency seven orders of magnitude to $\eta \sim 10^{-5}$. They attributed most of the inefficiency to the warm temperature (T$\sim$ 4 K) which limited the microwave coupling to the spins and can be improved by loading the device in a colder cryogenic system. They required $\sim$ 6 mW of optical pump power to achieve this efficiency, which may make achieving much lower temperatures (i.e T<100 mK) challenging. Also, these measurements were done at high microwave power, while quantum transducers should operate at the single-photon level.

1.6 On-chip Quantum Transduction with Rare-Earth Ions

One potential way to improve the rare-earth ion based transducer is to move to an on-chip platform. As alluded to earlier, nanophotonic circuits offer much smaller mode volumes compared to bulk components which can enhance the optical coupling rates.

With on-chip resonators, less optical power is required to achieve similar optical Rabi frequency if we assume that the cavity parameters are otherwise identical in terms of the quality factors. In practice, achieving high-Q and well-coupled nanophotonic circuits is a challenge, especially in non-conventional photonic materials, but it is not a fundamental issue and should be improved over time with more dedicated efforts.

Further, on-chip transducers can be integrated with other on-chip components to create larger and more powerful systems. For example, rare-earth ions have shown to be a viable platform for quantum memories and optically-addressable qubits, so one could envision several of these functionalities on a single integrated chip.

The initial microwave-to-optical on-chip transducer from our group consisted of a co-planar microwave waveguide and a nanophotonic waveguide with a mirror on one end, such that light could double-pass the waveguide on a Yb^{3+}:YVO_4 substrate [102]. The waveguides resulted in quite low efficiency ($\sim$ 10^{-13}), but were a convenient way to explore several different configurations, such as a four-level transduction scheme, that would be more challenging to achieve with resonators.

In order to improve the on-chip microwave-to-optical transducer, optical and microwave cavities are needed. The design, fabrication, and measurement of a rare-earth ion transducer with integrated cavities is the subject of this thesis.

In brief, the rare-earth ion transduction device consists of a Er^{3+}:YVO_4 substrate, a superconducting niobium microwave resonator, and an amorphous-silicon photonic crystal resonator patterned on the substrate surface. An image of this device is shown in Figure 1.3, where the grey pattern is the microwave resonator and the black pattern is the optical resonator. This device will be described in more detail throughout this thesis.

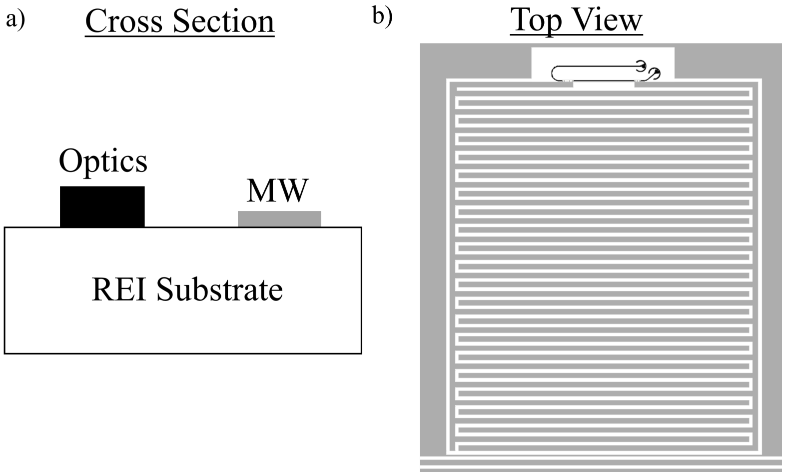

Figure 1.3: Schematic of an on-chip rare-earth ion transducer, where the microwave resonator (grey) and optical resonator (black) are patterned on a substrate that contains rare-earth ions.

1.7 Structure of this Thesis

Chapter 2 describes the theory of our rare-earth ion transducer and highlights a few different ways to calculate the transducer efficiency.

Chapter 3 highlights the spectroscopy of Er^{3+}:YVO_4 as a material for transduction and some experimental considerations to maximize the transducer efficiency.

Chapter 4 describes the transducer design choices that were considered in the design of the transducer and evaluates the performance of the transducer design that was chosen using both electromagnetic simulations and calculating the transducer efficiency.

Chapter 5 includes the fabrication process used to make the devices and some of the development to get the process to its current state.

Chapter 6 details the experimental setups used for conducting the measurements of the transducer.

Chapter 7 includes all the characterization of the transducer. This includes characterizing the device parameters, efficiency characterization, and noise/temperature characterization.

Chapter 8 concludes this thesis. The results from the previous chapters are summarized. An outlook to future devices and experiments are presented.

Chapter 2

REI TRANSDUCTION THEORY

This chapter will introduce some theoretical methods for calculating the transduction efficiency of a rare-earth ion based transducer using a Raman heterodyne protocol. These techniques were previously presented in several papers from Professor Jevon Longdell's group [54, 98, 102] and will be outlined here.

The system we have for the transducer is an ensemble of three level atoms coupled to three electromagnetic fields (see Figure 2.1). Two of these fields correspond to an optical and microwave cavity mode, which are the input and output modes of the transducer, while the third field corresponds to an optical laser field that compensates for the frequency difference between the input and output fields.

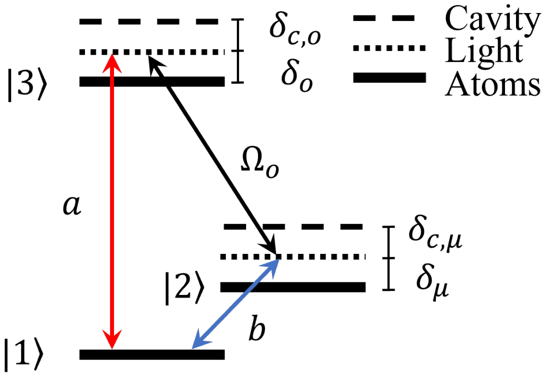

Figure 2.1: Three level atomic system for ground state transduction. The microwave field, b, is coupled to transition $|1\rangle \leftrightarrow |2\rangle$. The optical field, a, couples to transition $|1\rangle \leftrightarrow |3\rangle$. The optical pump field, Ω_o, makes up for the energy difference between the two fields and couples to transition $|2\rangle \leftrightarrow |3\rangle$. The detunings between the cavity resonance, the light field and the atomic transitions are all depicted.

In order to model this atom-cavity system, we can use the following Hamiltonian:

$$\begin{aligned} H/\hbar = {} & \delta_{c,o}\hat{a}^\dagger\hat{a} + \delta_{c,\mu}\hat{b}^\dagger\hat{b} + \\ & \sum_k^N \delta_{\mu,k}\sigma_{22,k} + \delta_{o,k}\sigma_{33,k} + (g_{\mu,k}\hat{b}\sigma_{21,k} + \Omega_{o,k}\sigma_{32,k} + g_{o,k}\hat{a}\sigma_{31,k} + HC) \end{aligned} \tag{2.1}$$

where $\delta_{c,o}$ is the optical light-cavity detuning, $\delta_{c,\mu}$ is the microwave light-cavity detuning, $\delta_{\mu,k}$ is the detuning between the k^{th} atom and the microwave field, $\delta_{o,k}$ is the detuning between the k^{th} atom and the optical field, $g_{\mu,k}$ is the coupling strength between the k^{th} atom and the microwave cavity, $\Omega_{o,k}$ is the optical pump Rabi frequency of the k^{th} atom, $g_{o,k}$ is the coupling strength between the k^{th} atom and the optical cavity, HC is the Hermitian conjugate, and N is the number of atoms. We denote the optical cavity by the annihilation operator, $\hat{a}$, the microwave cavity by the annihilation operator, $\hat{b}$, and $\sigma_{ij} \equiv |i\rangle\langle j|$ are the operators of the atoms. Symbols with a subscript o will be used for optical parameters, while symbols with subscript μ will be used for microwave parameters.

In the rotated frame of the Hamiltonian, we have assumed a three-photon resonance such that $\omega_a = \omega_b + \omega_o$, where ω_a is the angular frequency of the optical input (or output), ω_b is the angular frequency of the microwave output (or input) and ω_o is the angular frequency of the optical pump field. This Hamiltonian is suited for ground state transduction, but it can be reformulated in a similar fashion for excited state transduction (see Section 2.5).

We are interested in determining the transduction efficiency for this system. That is $\eta = |\frac{B_{out}}{A_{in}}|^2$ or $\eta = |\frac{A_{out}}{B_{in}}|^2$, where A_{in} & B_{in} are the cavity input fields and A_{out} & B_{out} are the cavity output fields for cavity mode $\hat{a}$ & $\hat{b}$, respectively. We can write down the equations of motion of the two cavity fields:

$$\dot{\hat{a}} = -i[\hat{a}, H] - \frac{\kappa_o}{2} - \sqrt{\kappa_{o,in}}A_{in} \tag{2.2}$$

$$\dot{\hat{b}} = -i[\hat{b}, H] - \frac{\kappa_\mu}{2} - \sqrt{\kappa_{\mu,in}}B_{in} \tag{2.3}$$

where κ_μ is the microwave cavity decay rate, $\kappa_{\mu,in}$ is the microwave cavity coupling decay rate, κ_o is the optical cavity decay rate and $\kappa_{o,in}$ is the optical cavity coupling decay rate.

In general, this system as described by the Hamiltonian in Equation 2.1 is not easy to solve directly as there are $9N + 2$ coupled equations to determine the state of all N three-level atoms and the two cavity modes. There are several ways to approach this problem and each offer different advantages and disadvantages. They will be briefly introduced below and detailed in the subsequent sections.

The first method, which we shall call the *adiabatic model*, is to make an adiabatic approximation in order to eliminate the excited states of the atomic system. This approach provides the simplest and most elegant form, but is limited to specific conditions to satisfy the adiabatic approximation and is thus not generally applicable.

The second method, which we shall call the *iterative numerical model*, involves numerically solving the Hamiltonian in a master equation formalism using an iterative method. This method makes the least amount of approximations of the three methods, but relies heavily on numerical root-solvers that need to iteratively solve the inverse of N $9x9$ matrices, which makes this method slow and cumbersome.

The third approach, which we shall call the *linear numerical model*, involves numerically solving the Hamiltonian after making a linear approximation (i.e. the cavity fields are sufficiently small). This method alleviates the need for the iterative solver, which makes this method much faster to solve. Importantly, for quantum transduction the cavity fields should be small (i.e. single photon level), so this linear approximation should be valid in this regime. All three methods have their merits and regimes that they are best suited for, so I will present results from all three methods.

2.1 Adiabatic Model

In the adiabatic model (originally presented in Reference [98]), we operate in the regime where $\left|\delta_{\mu,k}\right| \gg \left|g_{\mu,k}\right|, \left|\delta_{o,k}\right| \gg \left|g_{o,k}\right|, \left|\delta_{\mu,k}\delta_{o,k}\right| \gg \left|\Omega_{o,k}\right|^2$, such that we can adiabatically eliminate the excited states of the atomic system. For simplicity, we also neglect any atomic dephasing or energy dissipation and assume that T= 0 K (these assumptions will be dropped for subsequent models). Importantly, in this highly detuned regime used to satisfy the adiabatic condition, we expect to have reduced added noise from processes such as spontaneous emission and reduced absorption from parasitic ions (ions that are only coupled to one of the two cavities).

In the adiabatic limit, we have the following effective Hamiltonian:

$$H_{eff}/\hbar = \delta_{c,o}\hat{a}^\dagger\hat{a}+\delta_{c,\mu}\hat{b}^\dagger\hat{b}+\sum_k^N\left(-\frac{\delta_{\mu,k}|g_{o,k}|^2}{\delta_{o,k}\delta_{\mu,k}-|\Omega_{o,k}|^2}\hat{a}^\dagger\hat{a}-\frac{\delta_{o,k}|g_{\mu,k}|^2}{\delta_{o,k}\delta_{\mu,k}-|\Omega_{o,k}|^2}\hat{b}^\dagger\hat{b}\right.$$
$$\left.+\frac{\Omega_{o,k}g_{\mu,k}g_{o,k}^*}{\delta_{o,k}\delta_{\mu,k}-|\Omega_{o,k}|^2}\hat{a}^\dagger\hat{b}+\frac{\Omega_{o,k}^*g_{\mu,k}^*g_{o,k}}{\delta_{o,k}\delta_{\mu,k}-|\Omega_{o,k}|^2}\hat{b}^\dagger\hat{a}\right). \quad (2.4)$$

This effective Hamiltonian has four new terms, where the first two new terms correspond to the cavity mode-pulling from the atomic transitions and the last two terms correspond to an effective linear coupling between the two cavity modes $\hat{a}$ and $\hat{b}$, which we shall denote as S. We can further simplify the linear coupling coefficient due to the adiabatic elimination, such that:

$$S = \sum_k^N \frac{\Omega_{o,k}g_{\mu,k}g_{o,k}^*}{\delta_{o,k}\delta_{\mu,k}}. \quad (2.5)$$

Now we can write the effective Hamiltonian in a simplified beam splitter-like form:

$$H_{eff}/\hbar = (\delta_{c,o} - \omega'_a)\hat{a}^\dagger\hat{a} + (\delta_{c,\mu} - \omega'_b)\hat{b}^\dagger\hat{b} + S\hat{a}^\dagger\hat{b} + S^*\hat{b}^\dagger\hat{a} \tag{2.6}$$

where $\omega'_a = \sum_k^N \frac{\delta_{\mu,k}|g_{o,k}|^2}{\delta_{o,k}\delta_{\mu,k}-|\Omega_{o,k}|^2}, \omega'_b = \sum_k^N \frac{\delta_{o,k}|g_{\mu,k}|^2}{\delta_{o,k}\delta_{\mu,k}-|\Omega_{o,k}|^2}$ are the cavity mode pulling frequencies for the optical and microwave cavity, respectively.

We can use the input-output formalism to relate the cavity fields to their respective input/output modes:

$$\begin{aligned} \dot{\hat{a}} &= -i(\delta_{c,o} - \omega'_a)\hat{a} - iS\hat{b} - \frac{\kappa_o}{2}\hat{a} - \sqrt{\kappa_{o,in}}A_{in} \\ \dot{\hat{b}} &= -i(\delta_{c,\mu} - \omega'_b)\hat{b} - iS^*\hat{a} - \frac{\kappa_\mu}{2}\hat{b} - \sqrt{\kappa_{\mu,in}}B_{in}. \end{aligned} \tag{2.7}$$

We can solve these equations in steady state and assume that we are only inputting a field into one cavity (i.e. A_{in} or $B_{in} = 0$) and use $A_{out} = \sqrt{\kappa_{o,in}}a$ for microwave to optical transduction (or $A_{out} = \sqrt{\kappa_{\mu,in}}b$ for optical to microwave transduction), such that the photon number efficiency is:

$$\eta = \left|\frac{4iS\sqrt{\kappa_o\kappa_\mu}}{4S^2 + (2i(\delta_{c,o} - \omega'_a) + \kappa_o)(2i(\delta_{c,\mu} - \omega'_b) + \kappa_\mu)}\right|^2 \cdot \frac{\kappa_{o,in}}{\kappa_o} \cdot \frac{\kappa_{\mu,in}}{\kappa_\mu} \tag{2.8}$$

From Equation 2.8, we are able to obtain an impedance matching condition when $R \equiv \frac{4|S|^2}{\kappa_\mu\kappa_o} = 1$, the input field and pump laser frequency are chosen such that $\delta_{c,o} = \omega'_a$ and $\delta_{c,\mu} = \omega'_b$ and the two cavities are perfectly over-coupled, which provides a theoretical path for unit transduction efficiency.

More generally, the transduction efficiency when the light is resonant with mode-pulled cavity frequencies is $\eta = \left|\frac{2R}{R^2+1}\right|^2 \cdot \frac{\kappa_{o,in}}{\kappa_o} \cdot \frac{\kappa_{\mu,in}}{\kappa_\mu}$, which results in for small R (i.e. $R \ll 1$) the efficiency scales as $\eta \sim R^2$. We can also define the internal efficiency to be $\eta_{int} = \eta / \left(\frac{\kappa_{o,in}}{\kappa_o} \cdot \frac{\kappa_{\mu,in}}{\kappa_\mu}\right)$.

In Figure 2.2, the transducer internal efficiency and bandwidth are plotted using Equation 2.8 in the limit of $\kappa_\mu \ll \kappa_o$ and the light frequencies is at the optimal detuning. The bandwidth is the 3 dB bandwidth of the transducer efficiency. When R is small (i.e. $R \ll 1$), the bandwidth follows the bandwidth of the narrowest cavity, which in this case is the microwave cavity. When R is large (i.e. $R \gg 1$), the bandwidth can be increased, but at the cost of reduced efficiency. In practice, it would be more beneficial to work in a regime with larger cavity bandwidths (i.e. larger κ) to reduce R to unity and maximize the transducer bandwidth that way.

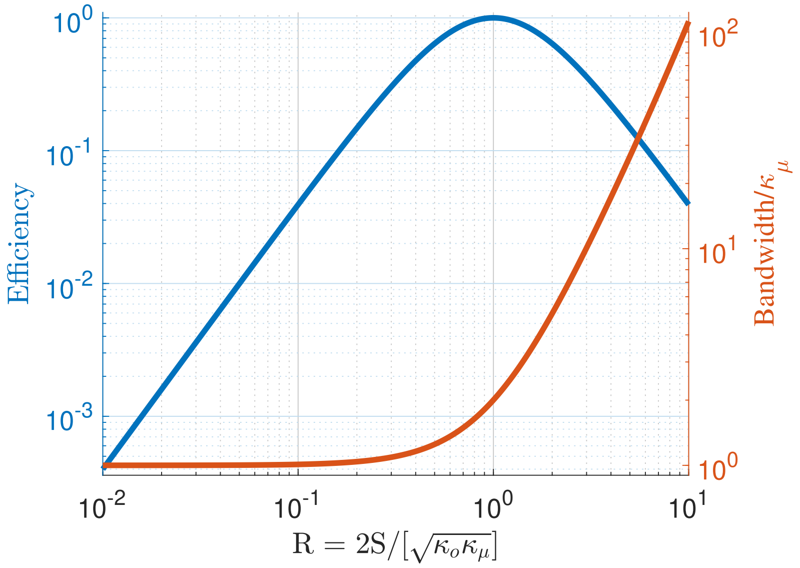

Figure 2.2: Adiabatic model efficiency and bandwidth as a function of the impedance matching parameter, R, in the limit of $\kappa_\mu \ll \kappa_o$.

Linear Transduction Coupling Coefficient –S

In order to maximize our efficiency it is important to maximize the linear transduction coupling coefficient, S, and have high quality factor optical and microwave cavities. S was defined in Equation 2.5, but we can take a closer look at different contributions of the transducer affect the parameter, S.

First, we can write down S more explicitly:

$$\Omega_{o,k} = \sqrt{\langle n_o \rangle}\sqrt{\frac{\omega}{2\hbar\epsilon_0}}\frac{d_{32}}{\sqrt{V_e}}\frac{E_{d,o,2}(r_k)}{\sqrt{(\epsilon_r(r_k)|E_{o,2}|^2)_{max}}} \tag{2.9}$$

$$g_{\mu,k} = \sqrt{\frac{\mu_0\omega}{2\hbar}}\frac{\mu_{21}}{\sqrt{V_m}}\frac{B_{m,\mu}(r_k)}{|B_{\mu,max}|} \tag{2.10}$$

$$g_{o,k} = \sqrt{\frac{\omega}{2\hbar\epsilon_0}}\frac{d_{31}}{\sqrt{V_e}}\frac{E_{d,o,1}(r_k)}{\sqrt{(\epsilon_r(r_k)|E_{o,1}|^2)_{max}}} \tag{2.11}$$

where d_{31} is the electric dipole moment of optical transition $|1\rangle \leftrightarrow |3\rangle$, d_{32} is the electric dipole moment of optical transition $|2\rangle \leftrightarrow |3\rangle$, and μ_{21} is the dipole moment of microwave transition $|1\rangle \leftrightarrow |2\rangle$. The subscripts m, d correspond to the field along the magnetic or electric dipole direction and the subscripts $1, 2$ are used to note the different electric fields between the pump field and the transduction signal field. We have assumed that an electric dipole moment for the optical transitions here, but similar expressions can be shown for a magnetic dipole transition (i.e. it is the same form as the microwave magnetic dipole transition).

If we assume no spectral and position correlations among the ion ensemble and assume the ion density is sufficiently large, then we can replace the sum with integrals and arrive at:

$$S = \sqrt{\omega_o \omega_\mu} \alpha F \Omega_{max} \tag{2.12}$$

where α contains the spectroscopic parameters of the atomic transitions, F is the mode overlap, and Ω_{max} is the maximum optical Rabi frequency of the pump field.

α can be expressed explicitly as:

$$\alpha = \sqrt{\frac{\mu_0}{\hbar^2 \epsilon_0}} d_{31} \mu_{21} \rho \int_{\epsilon_\mu}^{\infty} \frac{D_\mu(\delta_\mu)}{\delta_\mu} d\delta_\mu \int_{\epsilon_o}^{\infty} \frac{D_o(\delta_o)}{\delta_o} d\delta_o \tag{2.13}$$

where ρ is the number density of atoms and D_μ and D_o are the inhomogeneous broadening distribution functions of the microwave and optical transitions, respectively.

F can be defined as:

$$F = \frac{1}{\sqrt{V_o V_\mu}} \left| \int \frac{B_\mu(r) E_{o,1}(r) E_{o,2}(r)}{B_{\mu,max} \sqrt{(\epsilon_r(r_k) |E_{o,1}|^2)_{max}} E_{o,2,maxYVO}} dV \right|. \tag{2.14}$$

Ω_{max} can be defined as:

$$\Omega_{max} = \sqrt{\langle n_o \rangle} \sqrt{\frac{\omega_o}{2\hbar\epsilon_0}} \frac{d_{32}}{\sqrt{V_e}} \frac{E_{o,2,max}(r)}{\sqrt{(\epsilon_r(r) |E_{o,2}|^2)_{max}}}. \tag{2.15}$$

We can see from Equation 2.12 what the important spectroscopic properties of the rare-earth ion ensemble are and also what mode profiles for the microwave and optical cavity should be used in order to increase S.

In order to have high transduction efficiency, we want the rare-earth ion ensemble to have large optical and microwave dipole moments (i.e. d_{31}, d_{32} & μ_{21}), high density, and narrow inhomogeneity in the optical and spin transitions (as the light-atom detunings should be large compared to the transition inhomogeneities). That is, in the low efficiency limit, the efficiency scales with the spectroscopic parameters as:

$$\eta \propto \zeta = \left| \frac{d_{31} d_{32} \mu_{21} \rho}{\Delta_o \Delta_\mu} \right|^2 \tag{2.16}$$

where Δ_o and Δ_μ are the optical and microwave transition linewidths.

For the mode profiles of our three fields, we want to maximize the mode overlap between them. In a low quality factor optical cavity (i.e. $\kappa_o > \omega_\mu$), the two optical fields can couple to the same cavity mode, which simplifies this a bit. Due to the five orders of magnitude difference in wavelength between microwave and optical photons, increasing the overlap tends to require squeezing the microwave mode as much as possible and increasing the optical mode to match the size of the microwave mode.

It is also worth noting that $\Omega \sim \frac{1}{\sqrt{V_o}}$, which means we can obtain larger pump Rabi frequencies when we decrease the mode volume of the optical cavity (assuming all other parameters are constant). Although Ω can be increased by using more optical power, for quantum transduction it is desired to minimize the optical power in order to limit device heating or added noise, so there are practical advantages to using a smaller mode volume for the optical pump.

2.2 Numerical Model

In this section, we will look at a method to solve the system more directly using the Hamiltonian in Equation 2.1 (originally presented in Reference [54]). We can start with the equations of motion of the two cavity fields in terms of this Hamiltonian:

$$\begin{aligned} \dot{\hat{a}} &= -i[\hat{a}, H] - \frac{\kappa_o}{2} - \sqrt{\kappa_{c,o}} A_{in} \\ &= -\left(i\delta_{c,o} + \frac{\kappa_o}{2} \right) \hat{a} - i \sum_k g_{o,k} \sigma_{13,k} - \sqrt{\kappa_{o,in}} A_{in} \end{aligned} \tag{2.17}$$

$$\begin{aligned} \dot{\hat{b}} &= -i[\hat{b}, H] - \frac{\kappa_\mu}{2} - \sqrt{\kappa_{c,\mu}} B_{in} \\ &= -\left(i\delta_{c,\mu} + \frac{\kappa_\mu}{2} \right) \hat{b} - i \sum_k g_{\mu,k} \sigma_{12,k} - \sqrt{\kappa_{\mu,in}} B_{in}. \end{aligned} \tag{2.18}$$

We can make a semi-classical approximation by treating our cavity operators as complex numbers via $\hat{a} \rightarrow a$ & $\hat{b} \rightarrow b$. In order so solve these equations of motion, we need to know the state of the ion ensemble and we can solve for them using a master equation formalism:

$$\frac{d}{dt}\rho = -i[H, \rho] + L \tag{2.19}$$

where ρ is the density matrix of each atom and L describes energy and dephasing loss of the atoms. L can written as the sum of the different contributions by $L = L_{21} + L_{12} + L_{32} + L_{31} + L_{22} + L_{33}$.

$L_{21}\&L_{12}$ describe spin relaxation in the ground state:

$$L_{21} = \frac{\gamma_\mu}{2}(n_b + 1)(2\sigma_{12}\rho\sigma_{21} - \sigma_{21}\sigma_{12}\rho - \rho\sigma_{21}\sigma_{12}) \tag{2.20}$$

$$L_{12} = \frac{\gamma_\mu}{2}n_b(2\sigma_{21}\rho\sigma_{12} - \sigma_{12}\sigma_{21}\rho - \rho\sigma_{12}\sigma_{21}) \tag{2.21}$$

where γ_μ is the spin decay rate per phonon at the microwave frequency and n_b is the phonon bath population at the microwave frequency.

L_{31} & L_{32} describe energy loss via spontaneous emission from the optical excited state into the two ground states:

$$L_{31} = \frac{\gamma_{31}}{2}(2\sigma_{13}\rho\sigma_{31} - \sigma_{31}\sigma_{13}\rho - \rho\sigma_{31}\sigma_{13}) \tag{2.22}$$

$$L_{32} = \frac{\gamma_{32}}{2}(2\sigma_{32}\rho\sigma_{23} - \sigma_{23}\sigma_{32}\rho - \rho\sigma_{23}\sigma_{32}) \tag{2.23}$$

where γ_{31} and γ_{32} are the spontaneous emission rates.

L_{22} & L_{33} account for pure dephasing:

$$L_{22} = \frac{\gamma_{2d}}{2}(2\sigma_{22}\rho\sigma_{22} - \sigma_2\sigma 22\rho - \rho\sigma_{22}\sigma_{22}) \tag{2.24}$$

$$L_{33} = \frac{\gamma_{3d}}{2}(2\sigma_{33}\rho\sigma_{33} - \sigma_{33}\sigma 33\rho - \rho\sigma_{33}\sigma_{33}) \tag{2.25}$$

where γ_{2d} and γ_{3d} are the dephasing rates.

We can explicitly write down the equations from Equation 2.19 for each atom as:

$$
\begin{aligned}
\dot{\rho}_{11} &= -\gamma_\mu n_b \rho_{11} + i\Omega_\mu \rho_{12} + iA\rho_{13} - i\Omega_\mu^* \rho_{21} + \gamma_\mu (n_b + 1)\rho_{22} \\
&\quad - iA^* \rho_{31} + \gamma_{31}\rho_{33} \\
\dot{\rho}_{12} &= i\Omega_\mu^* \rho_{11} - \left[i\delta_\mu + \frac{\gamma_\mu (2n_b + 1) + \gamma_{2d}}{2} \right] \rho_{12} + i\Omega_o \rho_{13} - i\Omega_\mu^* \rho_{22} - iA^* \rho_{32} \\
\dot{\rho}_{13} &= iA^* \rho_{11} + i\Omega_o^* \rho_{12} - \left[i\delta_o + \frac{\gamma_\mu n_b + \gamma_{31} + \gamma_{32} + \gamma_{3d}}{2} \right] \rho_{13} - i\Omega_\mu^* \rho_{23} - iA^* \rho_{33} \\
\dot{\rho}_{21} &= -i\Omega_\mu \rho_{11} - \left[i\delta_\mu + \frac{\gamma_\mu (2n_b + 1) + \gamma_{2d}}{2} \right] \rho_{21} + i\Omega_\mu \rho_{22} + iA\rho_{23} - i\Omega_o^* \rho_{31} \\
\dot{\rho}_{22} &= \gamma_\mu n_b \rho_{11} - i\Omega_\mu \rho_{12} + i\Omega_\mu^* \rho_{21} - \gamma_\mu (n_b + 1)\rho_{22} \\
&\quad + i\Omega_o \rho_{23} - i\Omega_o^* \rho_{32} + \gamma_{32}\rho_{33} \\
\dot{\rho}_{23} &= -i\Omega_\mu \rho_{13} + iA^* \rho_{21} + i\Omega_o^* \rho_{22} \\
&\quad - \left[i\left(\delta_o - \delta_\mu\right) + \frac{\gamma_\mu (n_b + 1) + \gamma_{31} + \gamma_{32} + \gamma_{2d} + \gamma_{3d}}{2} \right] \rho_{23} - i\Omega_o^* \rho_{33} \\
\dot{\rho}_{31} &= -iA\rho_{11} - i\Omega_o \rho_{21} - \left[i\delta_o + \frac{\gamma_\mu n_b + \gamma_{31} + \gamma_{32} + \gamma_{3d}}{2} \right] \rho_{31} + i\Omega_\mu \rho_{32} + iA\rho_{33} \\
\dot{\rho}_{32} &= -iA\rho_{12} - i\Omega_o \rho_{22} + i\Omega_\mu^* \rho_{31} \\
&\quad - \left[i\left(\delta_o - \delta_\mu\right) + \frac{\gamma_\mu (n_b + 1) + \gamma_{31} + \gamma_{32} + \gamma_{3d}}{2} \right] \rho_{32} + i\Omega_o \rho_{33} \\
\dot{\rho}_{33} &= -iA\rho_{13} - i\Omega_o \rho_{23} + iA^* \rho_{31} + i\Omega_o^* \rho_{32} - \left(\gamma_{31} + \gamma_{32}\right)\rho_{33}
\end{aligned}
$$

where $A = g_o a$ and $\Omega_\mu = g_\mu b$ following the notation from [54].

We can now write the equations of motion for the atoms in matrix form:

$$\dot{\boldsymbol{\rho}} = \boldsymbol{L}\boldsymbol{\rho} \tag{2.26}$$

where $\boldsymbol{\rho} = [\rho_{11}, \rho_{12}, \rho_{13}, \rho_{21}, \rho_{22}, \rho_{23}, \rho_{31}, \rho_{32}, \rho_{33}]^\intercal$ and

$$
\boldsymbol{L} = \begin{bmatrix}
-\gamma_\mu n_b & i\Omega_\mu & iA & -i\Omega_\mu^* & \gamma_\mu (n_b + 1) & 0 & -A^* & 0 & \gamma_{31} \\
i\Omega_\mu^* & -i\delta_\mu - \Gamma_{21} & i\Omega_o & 0 & -\Omega_\mu^* & 0 & 0 & -iA^* & 0 \\
iA^* & i\Omega_o^* & -i\delta_o - \Gamma_{31} & 0 & 0 & -i\Omega_\mu^* & 0 & 0 & -iA^* \\
-i\Omega_\mu & 0 & 0 & -i\delta_\mu - \Gamma_{21} & i\Omega_\mu & iA & -i\Omega_o^* & 0 & 0 \\
\gamma_\mu n_b & i\Omega_\mu & 0 & i\Omega_\mu^* & -\gamma_\mu (n_b + 1) & i\Omega_o & 0 & -i\Omega_o^* & \gamma_{32} \\
0 & 0 & -i\Omega_\mu & iA^* & i\Omega_o^* & \begin{matrix} i(\delta_\mu - \delta_o) \\ - \Gamma_{32} \end{matrix} & 0 & 0 & i\Omega_o^* \\
-iA & 0 & 0 & -i\Omega_o & 0 & 0 & -\delta_o - \Gamma_{31} & 0 & 0 \\
0 & -iA & 0 & 0 & -i\Omega_o & 0 & i\Omega_\mu^* & \begin{matrix} i(\delta_\mu - \delta_o) \\ + \Gamma_{32} \end{matrix} & i\Omega_o \\
0 & 0 & -iA & 0 & 0 & -i\Omega_o & iA^* & i\Omega_o^* & -(\gamma_{31} + \gamma_{32})
\end{bmatrix}
$$

where $\Gamma_{21} = \frac{\gamma_\mu(2n_b+1)+\gamma_{2d}}{2}$, $\Gamma_{31} = \frac{\gamma_\mu n_b+\gamma_{31}+\gamma_{32}+\gamma_{3d}}{2}$ and $\Gamma_{32} = \frac{\gamma_\mu(n_b+1)+\gamma_{31}+\gamma_{32}+\gamma_{3d}}{2}$.

We can find the steady state solution by solving $\boldsymbol{L\rho} = 0$. We can also use $\mathrm{Tr}(\rho) = 1$ and rewrite the linear system of equations as $\boldsymbol{L'\rho} = \boldsymbol{v}$, where $\boldsymbol{v} = [1,0,0,0,0,0,0,0,0]$ and $\boldsymbol{L'}$ uses $\mathrm{Tr}(\rho) = 1$ for one of the equations of $\boldsymbol{L}$:

$$\boldsymbol{L'} = \begin{bmatrix} 1 & 0 & 0 & 0 & 1 & 0 & 0 & 0 & 1 \\ i\Omega_\mu^* & -i\delta_\mu - \Gamma_{21} & i\Omega_o & 0 & -\Omega_\mu^* & 0 & 0 & -iA^* & 0 \\ iA^* & i\Omega_o^* & -i\delta_o - \Gamma_{31} & 0 & 0 & -i\Omega_\mu^* & 0 & 0 & -iA^* \\ -i\Omega_\mu & 0 & 0 & -i\delta_\mu - \Gamma_{21} & i\Omega_\mu & iA & -i\Omega_o^* & 0 & 0 \\ \gamma_\mu n_b & i\Omega_\mu & 0 & i\Omega_\mu^* & -\gamma_\mu(n_b+1) & i\Omega_o & 0 & -i\Omega_o^* & \gamma_{32} \\ 0 & 0 & -i\Omega_\mu & iA^* & i\Omega_o^* & \begin{array}{c} i(\delta_\mu - \delta_o) \\ -\Gamma_{32} \end{array} & 0 & 0 & i\Omega_o^* \\ -iA & 0 & 0 & -i\Omega_o & 0 & 0 & -\delta_o - \Gamma_{31} & 0 & 0 \\ 0 & -iA & 0 & 0 & -i\Omega_o & 0 & i\Omega_\mu^* & \begin{array}{c} i(\delta_\mu - \delta_o) \\ +\Gamma_{32} \end{array} & i\Omega_o \\ 0 & 0 & -iA & 0 & 0 & -i\Omega_o & iA^* & i\Omega_o^* & -(\gamma_{31}+\gamma_{32}) \end{bmatrix}.$$

In order to find the state of each atom, we need to find the inverse of $\boldsymbol{L'}$ and do some matrix multiplication. We can combine this result with the equations of motion of the cavities (Equation 2.17 & 2.18) after tracing over all the atoms $\langle\sigma_{i,j}\rangle = \mathrm{Tr}(\rho\sigma_{i,j}) = \rho_{j,i}$ and solving in the steady state:

$$\dot{a} = -\left(i\delta_{c,o} + \frac{\kappa_o}{2}\right)a - i\sum_k g_{o,k}\rho_{31,k} - \sqrt{\kappa_{o,in}}A_{in} = 0 \tag{2.27}$$

$$\dot{b} = -\left(i\delta_{c,\mu} + \frac{\kappa_\mu}{2}\right)b - i\sum_k g_{\mu,k}\rho_{21,k} - \sqrt{\kappa_{\mu,in}}B_{in} = 0. \tag{2.28}$$

In order to solve our system of equations (i.e. two cavity equations, N 9x9 matrices for the atoms), we use an iterative root-solving method. First, we have some initial guess for the cavity fields. We can use those initial guesses to estimate the density matrix of all the atoms. The numerical root-solver then iteratively searches for complex values of a & b that can simultaneously satisfy the cavity field equations and the atomic density matrices.

Once satisfactory values of a & b have been found numerically, the transducer output field can be calculated (i.e. if microwave to optical transduction, then $A_{out} = \sqrt{\kappa_{o,in}}a$) and the transduction efficiency can also be calculated (i.e. if microwave to optical transduction, then $\eta = A_{out}/B_{in}$).

2.3 Linear Model

In this section, we will look at a linear approximation to make the numerical calculations easier and faster to solve (originally presented in Reference [102]).

Starting from Equation 2.26, we can rewrite $\boldsymbol{L}$ without approximation in terms of its linear dependence on the two cavity fields:

$$\mathbf{L} = \mathbf{L}_0 + a\mathbf{L}_{\mathbf{a}} + a^*\mathbf{L}_{\mathbf{a}^*} + b\mathbf{L}_{\mathbf{b}} + b^*\mathbf{L}_{\mathbf{b}^*}. \tag{2.29}$$

We can now make an approximation that our density matrix for each atom depends linearly on the cavity field amplitudes, which should be true for sufficiently small cavity field amplitudes:

$$\boldsymbol{\rho} = \boldsymbol{\rho}_0 + a\boldsymbol{\rho}_{\boldsymbol{a}} + a^*\boldsymbol{\rho}_{\boldsymbol{a}^*} + b\boldsymbol{\rho}_{\boldsymbol{b}} + b^*\boldsymbol{\rho}_{\boldsymbol{b}^*}. \tag{2.30}$$

We can combine these results in the steady state:

$$\mathbf{L}\boldsymbol{\rho} = (\mathbf{L}_0+a\mathbf{L}_{\mathbf{a}}+a^*\mathbf{L}_{\mathbf{a}^*}+b\mathbf{L}_{\mathbf{b}}+b^*\mathbf{L}_{\mathbf{b}^*})(\boldsymbol{\rho}_0+a\boldsymbol{\rho}_{\boldsymbol{a}}+a^*\boldsymbol{\rho}_{\boldsymbol{a}^*}+b\boldsymbol{\rho}_{\boldsymbol{b}}+b^*\boldsymbol{\rho}_{\boldsymbol{b}^*}) = 0. \tag{2.31}$$

We know that $\mathbf{L}_0\boldsymbol{\rho}_0 = 0$ as this is the steady state solution for empty cavities. Following the linear approximation above, we can neglect second order terms in terms of the cavity amplitudes:

$$a(\mathbf{L}_0\boldsymbol{\rho}_a + \mathbf{L}_a\boldsymbol{\rho}_0) + a^*(\mathbf{L}_0\boldsymbol{\rho}_{a^*} + \mathbf{L}_{a^*}\boldsymbol{\rho}_0) + b(\mathbf{L}_0\boldsymbol{\rho}_b + \mathbf{L}_b\boldsymbol{\rho}_0) + b^*(\mathbf{L}_0\boldsymbol{\rho}_{b^*} + \mathbf{L}_{b^*}\boldsymbol{\rho}_0) = 0. \tag{2.32}$$

From here, we can solve for ρ using $\mathbf{L}_0\boldsymbol{\rho}_0 = 0$, $\mathrm{Tr}(\boldsymbol{\rho}) = 1$ and $\boldsymbol{\rho}_x = -\mathbf{L}_0^{-1}\mathbf{L}_x\boldsymbol{\rho}_0$, for $x = a, b, a^*, b^*$. We can use this result toward solving the equations of motion of the cavity (equations 2.27 & 2.28), such that:

$$\dot{a} = -\left(i\delta_{c,o} + \frac{\kappa_o}{2}\right)a - i\sum_k g_{o,k}(a\rho_{a,31,k} + b\rho_{b,31,k}) - \sqrt{\kappa_{o,in}}A_{in} = 0 \tag{2.33}$$

$$\dot{b} = -\left(i\delta_{c,\mu} + \frac{\kappa_\mu}{2}\right)b - i\sum_k g_{\mu,k}(a\rho_{a,21,k} + b\rho_{b,21,k}) - \sqrt{\kappa_{\mu,in}}B_{in} = 0. \tag{2.34}$$

To simplify this expression, we can define $S_{a,12} = \sum_k g_{\mu,k}\rho_{a,12,k}$ and similarly for the other summation terms. Importantly, these equations result in a linear coupling between the two cavity modes and can be expressed in matrix form:

$$\begin{bmatrix} -\sqrt{\kappa_{o,in}}A_{in} \\ -\sqrt{\kappa_{\mu,in}}B_{in} \end{bmatrix} = \begin{bmatrix} i\delta_{c,o} + \frac{\kappa_o}{2} + iS_{a,31} & iS_{b,31} \\ iS_{a,21} & i\delta_{c,\mu} + \frac{\kappa_\mu}{2} + iS_{b,21} \end{bmatrix} \begin{bmatrix} a \\ b \end{bmatrix}. \tag{2.35}$$

We can solve this system of equations analytically and find the transduction efficiency equation:

$$\eta = \left|\frac{A_{out}}{B_{in}}\right|^2 = \left|\frac{iS_{b,31}\sqrt{\kappa_{o,in}\kappa_{\mu,in}}}{S_{a,21}S_{b,31} + (i\delta_{c,o} + \frac{\kappa_o}{2} + iS_{a,31})(i\delta_{c,\mu} + \frac{\kappa_\mu}{2} + iS_{b,21})}\right|^2. \tag{2.36}$$

This calculation can be solved relatively quickly by first solving for ρ and then Equation 2.36, which does not require any iterations.

Also, it is worth noting that when running these simulations, it is often desired to find the highest efficiency for a given system, where our experimental degrees of freedom are the four detunings (i.e. two atom-light detunings and two light-cavity detunings). In this model, the light-cavity detunings that maximize the efficiency can be found to be $\delta_{c,\mu,max} = -\mathrm{Re}(S_{b,21})$ & $\delta_{c,o,max} = -\mathrm{Re}(S_{a,31})$ when κ_o is the fastest rate in the system. In comparison, these detuning parameters need to be optimized in the numerical simulation in order to find the optimal conditions that give the higest efficiency. Therefore, to find the highest efficiency requires optimizing over two detuning parameters in the linear model compared to four detunings in the numerical model, which makes the linear model more straightforward to work with.

In the linear approximation model, the main limitation is that it assumes that the cavity fields are sufficiently small that the atomic coupling is linear. However, in the case of quantum transduction of single photons, this should be a good approximation. In other words, this model should break down at very high power, which is not the important regime for quantum transduction anyway.

2.4 Analytical Efficiency Equation from the Density Matrix Formalism

In this section, we will look at deriving an analytical transduction efficiency equation from the density matrix formalism shown above. The intention here is to find an efficiency equation that is more general compared to the adiabatic model, but is still analytical, so it is still fairly intuitive. The numerical models are the most precise, and contain the most physics, but it is not very obvious how all the input parameters affect the efficiency.

In order to find the steady state cavity field amplitudes, we need to know ρ_{21} and ρ_{31} (see Equation 2.27 and 2.28). As shown before, we can write down the equations of motion of these terms for each atom in the steady state:

$$\dot{\rho_{31}} = -iA\rho_{11} - i\Omega_o\rho_{21} - i\tilde{\delta_o}\rho_{31} + i\Omega_\mu\rho_{32} + iA\rho_{33} = 0 \tag{2.37}$$

$$\dot{\rho_{21}} = -i\Omega_\mu\rho_{11} - i\tilde{\delta_\mu}\rho_{21} + i\Omega_\mu\rho_{22} + iA\rho_{23} - i\Omega_o^*\rho_{31} = 0 \tag{2.38}$$

where we have defined $\tilde{\delta_\mu} = \delta_\mu - i\frac{\gamma_\mu(2n_b+1)+\gamma_{2d}}{2}$ and $\tilde{\delta_o} = \delta_o - i\frac{\gamma_\mu n_b+\gamma_{31}+\gamma_{32}+\gamma_{3d}}{2}$. We can write down an equation for ρ_{21} by taking [(Eq 2.37)$\cdot\Omega_o$] – [(Eq 2.38)$\cdot\tilde{\delta_o}$], such that:

$$\rho_{21} = -\frac{1}{\tilde{\delta_o}\tilde{\delta_\mu} - \Omega_o^2} \cdot \left[g_\mu \tilde{\delta_o} b(\rho_{22} - \rho_{11}) + g_o \Omega_o a(\rho_{33} - \rho_{11}) + \tilde{\delta_o} g_o a \rho_{23} + g_\mu \Omega_o b \rho_{32} \right], \tag{2.39}$$

and similarly for ρ_{31} by taking (Eq 2.37) x $\tilde{\delta_\mu}-$ (Eq 2.38) x Ω_o, such that:

$$\rho_{31} = \frac{1}{\tilde{\delta_o}\tilde{\delta_\mu} - \Omega_o^2} \cdot \left[-g_\mu \Omega_o b(\rho_{22} - \rho_{11}) + g_o \tilde{\delta_\mu} a(\rho_{33} - \rho_{11}) + \tilde{\delta_\mu} g_\mu b \rho_{32} + g_o \Omega_o a \rho_{23} \right]. \tag{2.40}$$

For simplicity, we will assume that ρ_{32} is sufficiently small, which should be true in the weak-excitation or adiabatic regime, such that we can neglect some of the terms. We can substitute these equations into our cavity equations of motion (Equations 2.27 and 2.28) in the steady state and get:

$$0 = (-i\delta_{c,o} - \kappa_o)a + -i\widetilde{S_{21}}b + i\widetilde{\omega_a}a - \sqrt{\kappa_{o,in}}A_{in} \tag{2.41}$$

$$0 = (-i\delta_{c,\mu} - \kappa_\mu)b + -i\widetilde{S_{31}}a + i\widetilde{\omega_b}b - \sqrt{\kappa_{o,in}}B_{in} \tag{2.42}$$

where $\widetilde{S_{31}} = \sum_k^N \frac{\Omega_{o,k} g_{\mu,k} g_{o,k}}{\widetilde{\delta_{o,k}\delta_{\mu,k}}}(\rho_{11,k} - \rho_{33,k})$ and $\widetilde{S_{21}} = \sum_k^N \frac{\Omega_{o,k} g_{\mu,k} g_{o,k}}{\widetilde{\delta_{o,k}\delta_{\mu,k}}}(\rho_{11,k} - \rho_{22,k})$ is the effective linear coupling strength and $\widetilde{\omega_a} = \sum_k^N \frac{\delta_{\mu,k}|g_{o,k}|^2}{\widetilde{\delta_{o,k}\delta_{\mu,k}} - |\Omega_{o,k}|^2}(\rho_{11,k} - \rho_{33,k})$, $\widetilde{\omega_b} = \sum_k^N \frac{\delta_{o,k}|g_{\mu,k}|^2}{\widetilde{\delta_{o,k}\delta_{\mu,k}} - |\Omega_{o,k}|^2}(\rho_{11,k} - \rho_{22,k})$ are the mode pulling terms of each cavity, where the imaginary part is given by the atomic energy decay and decoherence terms.

We can then find the transduction efficiency using input-output theory in the same way as before and arrive at:

$$\eta = \left| \frac{4i\widetilde{S_{21}}\sqrt{\kappa_o \kappa_\mu}}{4\widetilde{S_{21}}\widetilde{S_{31}} + (2i(\delta_{c,o} - \widetilde{\omega_a}) + \kappa_o)(2i(\delta_{c,\mu} - \widetilde{\omega_b}) + \kappa_\mu)} \right|^2 \cdot \frac{\kappa_{o,in}}{\kappa_o} \cdot \frac{\kappa_{\mu,in}}{\kappa_\mu} \tag{2.43}$$

This equation looks a lot like the efficiency equation derived in the adiabatic model (Equation 2.8). If all the atoms are in the ground state, $\mathrm{Im}(\widetilde{\delta_{\mu,k}}) = 0$ and $\mathrm{Im}(\widetilde{\delta_{o,k}}) = 0$, then this is exactly Equation 2.8. We can see that imperfect atom polarization effectively decreases our effective linear coupling strength between the microwave and optical cavity. It also effectively decreases the mode pulling terms. Energy decay or dephasing losses of the atom act to decrease the linear coupling strength and will also look like an effective cavity decay channel. Therefore, if this model is applicable to a given system, then in order for the atomic energy decay and decoherence to have minimal effect on the transduction efficiency, we require that $\mathrm{Re}(\widetilde{\delta_{o,k}}) \gg \mathrm{Im}(\widetilde{\delta_{o,k}})$,$\mathrm{Re}(\widetilde{\delta_{\mu,k}}) \gg \mathrm{Im}(\widetilde{\delta_{\mu,k}})$, $\kappa_o \gg \mathrm{Im}(\widetilde{\omega_a})$, and $\kappa_\mu \gg \mathrm{Im}(\widetilde{\omega_b})$.

2.5 Transduction in the Excited State

In the previous sections, the theoretical calculation of the transduction efficiency was for transduction using the atomic ground state for coupling to the rare-earth ion ensemble to the microwave cavity field. Transduction can also be performed by coupling the microwave cavity field to microwave transitions in the excited state of the rare-earth ion ensemble (Figure 2.3). Excited state transduction offers some useful practical advantages.

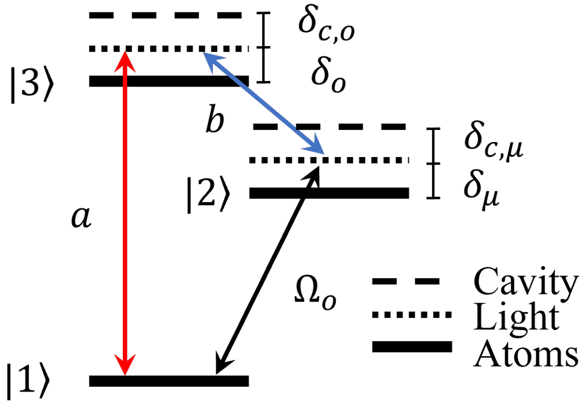

Figure 2.3: Three level atomic system for excited state transduction, where the optical pump is connected to the lowest level in the transducer and the microwave field is coupled to the excited state spin.

One important difference comes from the spins that will couple to the microwave cavity, but are not coupled to the optical cavity. We will refer to these spins as *parasitic spins*. These spins can absorb microwave photons, but will not contribute for transduction and will lower the transduction efficiency. For ground state transduction, it is not easy to separate the parasitic spins from the spins used for transduction. However, in excited state transduction only the spins that are excited from the optical pump can interact with the microwave photons, which is a natural way to filter out these parasitic spins. Also, the parasitic spins will cause power, temperature, and detuning dependent mode pulling of the microwave cavity, which can make transduction in the ground more tricky to implement experimentally compared to the excited state.

One disadvantage of the excited state is that the optical pump is on a transition that has significant population difference. This means the optical pump is more likely to move population, which could result in more spontaneous emission noise photons. However, these noise photons should not be at the transduced signal frequency (i.e. the frequency difference should be equal to the microwave photon frequency) if the excited state T_1 is sufficiently long, which will make them possible to filter at the output of the transducer.

The Hamiltonian for the excited state can be expressed as:

$$\begin{aligned} H_{excited}/\hbar = {} & \delta_{c,o}\hat{a}^\dagger\hat{a} + \delta_{c,\mu}\hat{b}^\dagger\hat{b} + \\ & \sum_k^N(\delta_{o,k} - \delta_{\mu,k})\sigma_{22,k} + \delta_{o,k}\sigma_{33,k} + (g_{\mu,k}\hat{b}\sigma_{32,k} + \Omega_{o,k}\sigma_{21,k} + g_{o,k}\hat{a}\sigma_{31,k} + HC). \end{aligned} \tag{2.44}$$

We can calculate the excited state transduction efficiency using the same master equation treatment while using the Hamiltonian for the excited state and modifying the loss/dephasing terms accordingly.

Chapter 3

ER^{3+}:YVO$_4$ SPECTROSCOPY

This chapter will cover the spectroscopic parameters that need to be considered for REI transduction and introduce the spectroscopy of Er-doped yttrium orthovanadate to help determine its viability for an REI transducer. The spectroscopy of Er-doped yttrium orthovanadate was published in [103].

As shown in Chapter 2, in the adiabatic limit the transduction should scale as $\eta \propto \zeta = \left|\frac{d_{31}d_{32}\mu_{21}\rho}{\Delta_o\Delta_\mu}\right|^2$. When using a zero nuclear spin isotope, the microwave transitions in the ground and excited state are created by breaking the degeneracy of the Kramer's doublet with a magnetic field. In this way, the zero field transition strength is split between four transitions. In order to maximize the transduction efficiency in this system, it is best to have equal transition strengths between the two optical transitions of the lambda or V system (i.e. such that $d_{31} = d_{32}$), which typically involves applying the static magnetic field along an optimal direction.

Although not strictly required, it is also beneficial to work with a system that has a relatively large g-factor such that the static magnetic field required to generate microwave spin transitions is minimized. For reference, an ion with g$\sim$2 will reach a transition frequency of 5 GHz at $\sim$180 mT.

3.1 Er^{3+}:YVO$_4$ Properties

Yttrium orthovanadate (YVO$_4$) is a zircon tetragonal crystal with D$_{4h}$ symmetry. Erbium dopant ions replace the yttrium ions in sites of local D$_{2d}$ point group symmetry. The crystal c-axis aligns with the z-axis of the site. The unaxial symmetry simplifies the characterization of parameters needed to describe the system (i.e. typically parameters only need to be characterized parallel and perpendicular to the c-axis).

Er^{3+} ions have 11 electrons in their 4f shell and the lowest two energy spin-orbit multiplets can be labelled as ^{4}I$_{15/2}$ and ^{4}I$_{13/2}$ from the free ion Hamiltonian [65, 66]. The YVO$_4$ crystal field splits the spin-orbit multiplets into J+1/2 Kramers doublets (i.e. 8 levels for the ground state ^{4}I$_{15/2}$ and 7 levels for ^{4}I$_{13/2}$). The 8 ground state levels can be labelled Z_1 through Z_8 and the 7 excited state levels can be labelled Y_1 through Y_7.

The energy splitting between Z_i and Y_j are at optical frequencies near $\sim$1530 nm (see Figure 3.1a). This is an important wavelength range as optical fibers exhibit the lowest loss at this frequency band, which can enable long distance communication of quantum light at these frequencies.

The crystal field energy splitting between Z_1 and Z_2 is $\sim$1.1 THz [67], so at cryogenic temperatures only Z_1 is populated. The energy splitting between Y_1 and Y_2 is only $\sim$55 GHz, which is relatively small splitting in the excited state amongst the different rare-earth ion and crystal host combinations, but not entirely unique as 35 GHz splittings are observed for Tb^{3+}:YAG [68].

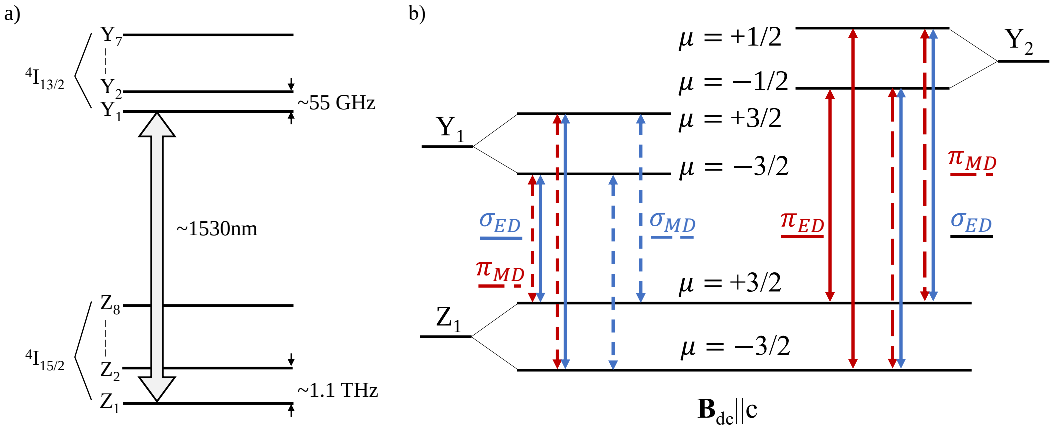

Figure 3.1: Er^{3+}:YVO_4 energy levels and optical selection rules. a) Energy level diagram of Er^{3+}:YVO_4 at zero magnetic field focusing on the lowest two spin-orbit manifolds and their lowest crystal field levels that have telecom optical transitions. b) Energy diagram for the crystal field levels Z_1, Y_1 and Y_2 and each of their two Zeeman levels denoted by their crystal field quantum numbers. The selection rules are shown for an external magnetic field along the crystal symmetry c-axis. π (red) and σ (blue) polarizations correspond to $E||c$ and $E||a$, respectively. The dotted lines correspond to the magnetic dipole transitions (MD) and the solid lines correspond to the electric dipole transitions (ED).

These levels can be labelled with the irreducible representations Γ_6 or Γ_7 and can be described by the crystal field quantum number $\mu = \pm\frac{1}{2}, \pm\frac{3}{2}$ according to the D_{2d} point group [65]. Z_1 and Y_1 can be labelled by $\mu = \pm\frac{3}{2}$ and Y_2 can be labelled by $\mu = \pm\frac{1}{2}$. From the irreducible representations, the selection rules for both Z_1-Y_1 and Z_1-Y_2 for both σ and π polarization can be determined [66, 104] as shown in Figure 3.1b and summarized in Table 3.1. For reference, σ polarization corresponds to the optical electric field polarized along the a-axis (E||a) and π corresponds to the optical electric field polarized along the c-axis (E||c).

Table 3.1: Er^{3+}:YVO_4 selection rules

μ	-3/2	+3/2	-1/2	+1/2
-3/2	σ_{MD}	σ_{ED},π_{MD}	σ_{ED},π_{MD}	π_{MD}
+3/2	σ_{ED},π_{MD}	σ_{MD}	π_{ED}	σ_{ED},π_{MD}

For a small magnetic field (i.e. small such that the Zeeman splitting is small compared to the crystal field splitting), we can model each Kramer's doublet using the effective spin Hamiltonian with S=1/2:

$$H_{eff,1/2} = \mu_0 \mathbf{B} \cdot \mathbf{g} \cdot \mathbf{S} \tag{3.1}$$

where **B** is the applied magnetic field, **g** is the electronic Zeeman g-tensor and **S** are the spin-1/2 operators. For Er^{3+}:YVO_4, **g** only has non-zero elements along the diagonal labelled as $g_{\|}$ and $g_{\perp}$ which correspond to the components parallel and perpendicular with respect to the crystal c-axis. The non-zero components of the **g**-tensor for Z_1, Y_1, and Y_2 are shown in Table 3.2 using values from Ref. [105] for Z_1 and values from Ref. [103] for Y_1 and Y_2.

Table 3.2: Er^{3+}:YVO_4 g-factors

	$g_{\|}$	$g_{\perp}$
Z_1	3.544	7.085
Y_1	4.51	4.57
Y_2	2.74	6.74

Another important parameter of Er^{3+}:YVO_4 is the microwave loss tangent which will set the upper bound for the microwave quality factors we can achieve that are integrated with this material. There hasn't been an extensive study on this to the best of my knowledge, but there is some literature that shows undoped YVO_4 has a loss tangent of $\tan(\theta) \sim 2 \cdot 10^{-5}$ [106, 107], which is likely an upper bound.

3.2 Bulk Spectroscopy Setup

Samples were cut and polished from YVO_4 boules doped with a natural abundance of Er^{3+} grown by Gamdan Optics. The first samples we looked at had a total erbium concentrations of 180 ppm and the even isotope Er^{3+} concentration was 140 ppm (measured by Secondary Ion Mass Spectrometry). A 200 μm thick a-cut crystal was used for optical measurements and a 2 mm thick sample was used for microwave measurements. The samples were mounted within a 2.4 GHz loop-gap microwave resonator (Q = 860) machined from oxygen-free copper sitting on the still plate (base temperature of 1 K) of a dilution refrigerator.

The loop-gap resonator sat on a fiber coupled U-bench (Thorlabs FBC-1550-APC) with two fiber collimators (Thorlabs PAF-X-2-C) for optical transmission measurements. The total optical coupling efficiency through the U-bench setup was 35% at 1 K, limited by misalignment due to thermal contraction during cooldown. As an aside, unfortunately the newer Thorlabs fiber collimators, which are supposed to have better operation at least at room temperature, tend to drift more when cooling down, which makes replicating this setup a bit more challenging.

The light propagation direction was along the a-axis of the crystal, which allowed measurement of both π and σ polarization spectra. A DC magnetic field ($\mathbf{B}_{dc}$) was applied to the crystal along the c-axis using a home-built split coil superconducting magnet that generated fields up to 120 mT.

3.3 Bulk Spectroscopy

In this section, I will present the spectroscopy of the optical and spin transitions of $Er^{3+}:YVO_4$ at cryogenic temperatures (T = 1 K unless noted otherwise), and then summarize some additional spectroscopy at different erbium concentrations.

Optical Absorption Spectroscopy

Our first characterization of the optical transitions of $Er^{3+}:YVO_4$ was with optical absorption spectroscopy. From this, we can determine the transition wavelength, transition linewidths, and transition strengths.

In order to measure the absorption strength and linewidth for the different transitions, we applied a magnetic field of 90 mT along the c-axis and swept the laser frequency across the optical transitions (Figure 3.2). For Z_1-Y_1 under σ polarized excitation, there are four well-resolved transitions with an average inhomogeneous linewidth of 184±10 MHz, as shown in Figure 3.2a. The number of allowed transitions is consistent with the theoretical calculation, where four (two) lines are observed under σ (π) polarization. For Z_1-Y_2 with π polarized excitation (Figure 3.2b), we observed four highly absorbing transitions with an average inhomogeneous linewidth of 163±14 MHz.

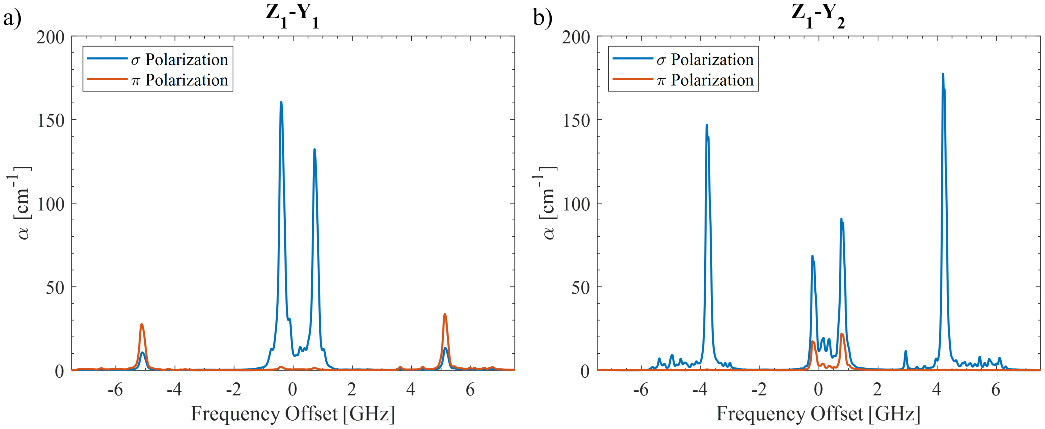

Figure 3.2: The optical absorption spectrum of (a) Z_1-Y_1 and (b) Z_1-Y_2 at an applied magnetic field of 90 mT and temperature of 1 K.

Using the integrated absorption coefficient spectrum, we can calculate the electric dipole (ED) and magnetic dipole (MD) absorption oscillator strength $f_{ij,q}$ [62, 108]:

$$f_{ij,q}^{ED} = 4\pi\epsilon_0 \frac{m_e c}{\pi e^2} \frac{1}{N} \frac{n_q}{\chi_L} \int \alpha_q^{ED}(\nu) d\nu \tag{3.2}$$

$$f_{ij,q}^{MD} = 4\pi\epsilon_0 \frac{m_e c}{\pi e^2} \frac{1}{N} \frac{1}{n_q} \int \alpha_q^{MD}(\nu) d\nu \tag{3.3}$$

where ϵ_0 is the vacuum permittivity, m_e is the mass of an electron, c is the speed of the light, e is the charge of an electron, N is the number density, q is the polarization, n_q is the refractive index along the q polarization direction, $\chi_L = \left(\frac{n_q^2+2}{3}\right)^2$ is the local electric field correction factor using the virtual cavity model, and α_q is the absorption coefficient for the q polarization direction. For YVO_4, the refractive index along the c (a) axis is 2.15 (1.95) [109]. With the doping concentration equal to 140 ppm, the even isotope erbium dopant number density is $N = 1.75 \times 10^{18}$ cm^{-3}, distributed between the two Zeeman levels.

The corresponding dipole moment was calculated from the oscillator strength using:

$$d_{i,j,q}^2 = \frac{\hbar e^2}{2m\omega} f_{i,j,q}. \tag{3.4}$$

It should be noted that there is a speed of light factor missing for a magnetic dipole transition using Equation 3.4 (i.e. $d \leftrightarrow c\mu$), but that is ignored here for now so we can conveniently compare the dipole strengths of electric and magnetic dipole transitions.

The radiative lifetime can be calculated using [62, 108]:

$$\frac{1}{\tau_{rad,q}^{ED}} = \frac{2\pi e^2}{\epsilon_0 m_e c} \frac{\chi n_q^2}{\lambda_0^2} \frac{f_{ij,q}^{MD}}{3} \tag{3.5}$$

$$\frac{1}{\tau_{rad,q}^{ED}} = \frac{2\pi e^2}{\epsilon_0 m_e c} \frac{n_q^3}{\lambda_0^2} \frac{f_{ij,q}^{MD}}{3} \tag{3.6}$$

where λ_0 is the transition wavelength in vacuum. The calculated absorption coefficient integral, oscillator strength, radiative lifetime, and dipole moment for different transitions are listed in Table 3.3. From these numbers, we obtained the total oscillator strength ($f_{ij,tot} = \sum_q f_{ij,q}$) as $f_{ED,tot} = 1.7 \times 10^{-7}$ and $f_{MD,tot} = 1.3 \times 10^{-6}$ for the Z_1-Y_1 transition, and $f_{ED,tot} = 1 \times 10^{-6}$ and $f_{MD,tot} = 1 \times 10^{-6}$ for the Z_1-Y_2 transition, respectively. The measured MD transition oscillator strength agreed with the theoretical calculation in [69] within a factor of two. The total oscillator strength of Er^{3+}:YVO_4 is relatively stronger compared to other erbium doped crystals as summarized in [71], which are mostly $f \sim 10^{-7}$. From the calculated radiative lifetimes shown in Table 3.3, we obtained the total radiative rate $\frac{1}{\tau_{rad}} = \sum_q \left(\frac{1}{\tau_{rad,q}^{ED}} + \frac{1}{\tau_{rad,q}^{MD}}\right)$ to be 1/8.1 ms for Y_1-Z_1 and 1/6.2 ms for Y_2-Z_1 transitions, respectively.

Table 3.3: Er^{3+}:YVO_4 optical properties

	Z_1-Y_1			Z_1-Y_2		
Wavelength, λ [nm]	1529.21			1528.78		
Optical Inhomogeneity, Δ_o [MHz]	184±10			163±14		
Polarization	σ		π	σ	π	
Dipole Type	ED	MD	MD	ED	ED	MD
$\int \alpha d\nu$ [GHz·cm^{-1}]	7.3	89.9	18.0	10.7	79.5	45.5
Oscillator Strength, f [10^{-7}]	0.8	9.0	2.0	1.2	7.6	5.1
Dipole Moment [10^{-32} C·m]	1	3.3	1.6	1.2	3.0	2.5
$1/\tau_{rad}$ [Hz]	5.7	85	13.9	8.3	75.2	35.3

Next, we measured the $Z_1 - Y_1$ fluorescence decay lifetime in order to determine the branching ratio of the transition. To minimize the impact of radiation trapping [110], which is present in the center of the inhomogeneous line, we excite the ensemble with the laser frequency detuned by two inhomogeneous linewidths from the center of the absorption peak. The fluorescence data detected on the SNSPD is shown in Figure 3.3. We extract a fluorescence lifetime, τ_{f,Y_1}, to be 3.34±0.01 ms. Given the 55 GHz energy splitting between Y_1 and Y_2, the phonon relaxation between the states will significantly modify the branching ratios to Z_1 as the temperature is varied. In the low temperature limit (i.e. $k_B T/\hbar \ll 55$ GHz), phonon absorption from Y_1 to Y_2 is supressed and the branching ratio for Y_1 to Z_1 will be at least $\beta_{Y_1} = \tau_{fY_1}/\tau_{radY_1} = 41.5\text{‰}$.

Initial measurements of the Y_2 lifetime gave nearly an identical fluorescence decay lifetime, which could be real or a sign that Y_2 decays quickly to Y_1 and we are just measuring the Y_1 lifetime. Further measurements indicated that there may be a fast relaxation rate of ~1-10 μs out of the Y_2 level, but verifying that is still the subject of future experiments.

EPR Measurement

We conducted electron paramagnetic resonance (EPR) on our bulk Er^{3+}:YVO_4 crystal by placing a 2-mm-thick (10x thicker than the optical measurements) sample within a loop-gap resonator with B_{ac} ||a to determine the spin inhomogeneous linewidth. When the Z_1 spin transition is near resonance of the microwave cavity from tuning an external magnetic field (B_{dc} ||c), we measure a small shift in the cavity frequency from the dispersive coupling to the spin ensemble.

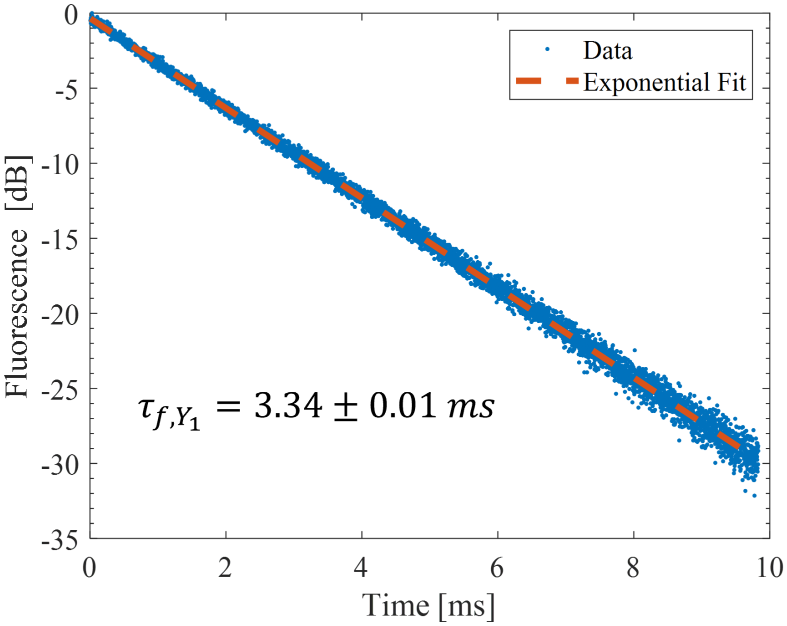

Figure 3.3: Y_1 optical lifetime measurement via fluorescence detection at 1 K. An exponential fit is showed by the red dashed line with a decay constant of τ_{f,Y_1} = 3.34 ± 0.01 ms.

The ensemble spin coupling, $g_{tot} = \mu_{21}\sqrt{\frac{\rho \Delta N \eta_m \omega_{\mu,0}\mu_0}{2\hbar}}$, where μ_{21} is the spin magnetic dipole moment ($g_\perp$ of the Z_1 level in this configuration), ρ is the number density of the ions, ΔN is the population difference between the spin levels, $\omega_{\mu,0}$ is center frequency of the resonator, η_m is the magnetic energy fraction in the $Er^{3+}:YVO_4$ crystal. From the simulation of the microwave cavity, we predict $\eta_m \approx 2\%$, corresponding to an ensemble coupling of $g_{tot} \approx 2.3$ MHz at 1 K. In the weak coupling regime, the maximum dispersive shift is proportional to g_{tot}^2/Δ_μ [90], where Δ_μ is the spin inhomogeneity.

To increase our measurement sensitivity for dispersive shifts smaller than the linewidth of the microwave cavity ($\kappa_\mu = 2.8$ MHz), we implemented a FM microwave tone to monitor small changes in the microwave cavity resonance frequency [101]. To determine the spin inhomogeneity, we follow the analysis from Diniz et al. [96], where a cavity with frequency $\omega_{\mu,0}$ couples to a distribution of N two-level systems in the weak excitation regime (i.e. similar to Equation 1.13). The cavity transmission function is given by:

$$t(\omega) = \frac{\kappa_\mu/2i}{\omega - \omega_{\mu,0} + i\kappa_\mu/2 - W(\omega)}. \tag{3.7}$$

The transmitted FM microwave field was measured on a microwave power meter at the modulation frequency, ω_m:

$$P_t = \text{DC term} + P_0\beta\{\text{Re}[\chi(\omega)]\cos(\omega_m t) + \text{Im}[\chi(\omega)]\sin(\omega_m t)\} + \text{O}(2\omega_m) \quad (3.8)$$

where β is the modulation strength and $\chi(\omega) = t(\omega)t^*(\omega+\omega_m) - t^*(\omega)t(\omega-\omega_m)$. When $\omega_m \ll \kappa_\mu$ and $\kappa_\mu \ll \Delta_\mu$, $\chi(\omega)$ has the shape of the derivative of $|t(\omega)|^2$, which transforms the resonance peak to a zero-crossing point. We measured the beat-note signal on a spectrum analyzer to take advantage of the large detection dynamic range so we can maximize our frequency sensitivity. Using this technique, we were able to measure kilohertz frequency shifts that were ~1000 times smaller than the resonator linewidth.

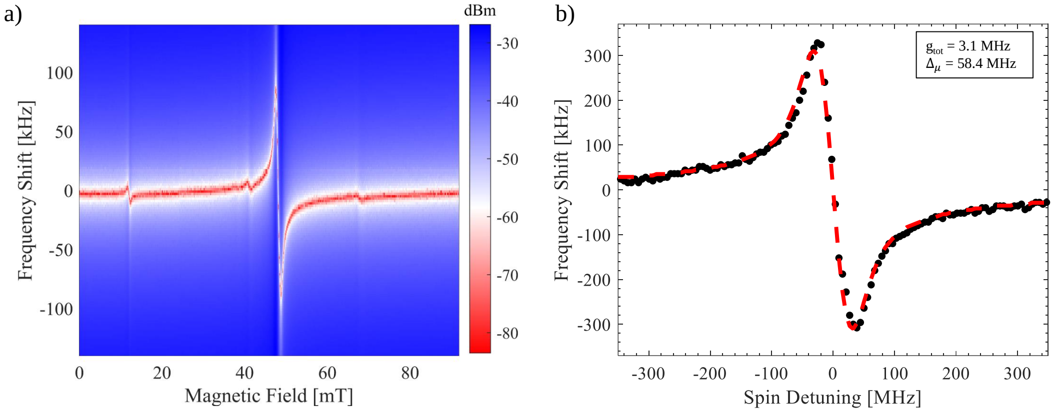

Figure 3.4: a) EPR spectrum taken at 4 K. The dispersive shift of the microwave resonator frequency indicates the coupling between the ensemble of ions and the resonator. The coupling at 48 mT was contributed from the even isotope of erbium with zero nuclear spin. The other three couplings located at 12, 41, and 68 mT are attributed to ^{167}Er hyperfine transitions. b) A detailed scan of the spin ensemble-cavity coupling centered at 48 mT taken at a temperature of 1 K. Each data point is obtained by a minimum search of the beat note signal at the corresponding magnetic field strength. The red dashed line is the fitting result using the model in Ref. [96].

As shown in Figure 3.4a, we observed a dispersive response of the microwave resonator frequency when the spin frequency crossed the bare cavity frequency. This measurement was done at T = 4 K. The strong signal at 48 mT was from the even erbium isotopes and the other coupling point at $B_{dc} = 12, 41$ and 68 mT were attributed to resonances with the ^{167}Er isotope hyperfine transitions.

We then took a finer scan around 48 mT at T = 1 K to characterize the even isotope transition. We calculated the Z_1 electron spin inhomogeneity to be Δ_μ =58.4 MHz with an ensemble coupling of g_{tot} =3.1 MHz, where we assume a Gaussian line shape for the spin inhomogeneity to fit the data (see Figure 3.4b). The small coupling strength observed here is expected due to the small size of the sample used and can be further improved by using a larger crystal to increase the filling factor [58]. The fitted 58.4 MHz spin inhomogeneity is an upper bound, given that we expect some spatial magnetic field inhomogeneity from our homemade magnet over the 3.5 x 2.5 x 2 mm sample volume within the microwave resonator.

Concentration Dependence

After the initial results with 180 ppm Er^{3+}:YVO_4, we tested a couple other high concentrations boules to see if their inhomogeneous linewidths were similar. The spectroscopy results are summarized in Table 3.4. Recall that from the adiabatic model, the efficiency should scale as $\eta \propto \frac{\rho}{\Delta_o \Delta_\mu}$.

Here, we measured the optical linewidths in a similar way as before (i.e. at 1 K and using the optical transmission spectrum of thin samples). For the microwave spin transition linewidths, we used a different setup. We used a patterned superconducting microwave coplanar waveguide on the Er^{3+}:YVO_4 surface and measured the linewidth from the waveguide absorption at a temperature of 40 mK (compared to 1 K previously). Due to the smaller interaction volume compared to the loop-gap resonator, we are less susceptible to magnetic field inhomogeneity from the magnet, but we are sensitive to flux-focusing at the edges superconducting film. In any case, we were able to measure more narrow spin linewidths in this setup and represents a better upper bound of the spin linewidth compared to the previous loop-gap measurements at 1 K.

Table 3.4: Er^{3+}:YVO_4 transition linewidths vs concentration

Er Conc.	Z_1-Y_1[MHz]	Z_1-Y_2[MHz]	Z_1 Spin [MHz]
180 ppm	184	163	30
560 ppm	260	225	65
2000 ppm	270	250	110

3.4 Magnetic Field Orientation

For a transduction experiment, one important degree of freedom is the magnetic field orientation. We define B_θ to be the magnetic field angle from the c-axis in the a-c plane. The choice of this orientation will determine g_{dc} and g_{ac} for both the ground and excited states and the optical transition branching ratio. g_{dc} is the effective g-factor strength for a given magnetic field direction such that $g_{dc} = \frac{\Delta E}{\mu_0 B_{dc}}$, where ΔE is the energy difference between the two Zeeman levels at a magnetic field strength, B_{dc}.

Ideally, we can have a magnetic field orientation where we can have large g-factors and have an even branching ratio between the two optical transitions, such that we have a good λ and V systems for transduction in the ground and excited state, respectively. It is also preferential to have the ground and excited states to have sufficiently different g_{dc}, such that the different λ and V systems can be isolated from each other.

Another practical restriction comes from our planar superconducting microwave resonators, whose quality factors will degrade significantly for out-of-plane magnetic fields required to generate GHz frequency Zeeman splitting, which limits us to in-plane magnetic field directions. This also limits our ac microwave magnetic field to be in the out-of-plane direction. In order to maximize our degrees of freedom, we use an a-cut sample such that we have the freedom to apply a magnetic field at an angle between the in-place a-axis and c-axis.

The g_{dc} for Z_1, Y_1 and Y_2 as a function of the magnetic field angle from the c-axis are shown in Figure 3.5. We see that Z_1 and Y_2 have a similar angle dependence, which is expected as their g-tensors are very similar (see Table 3.2). Y_1 has very little angular dependence as its g-factor is nearly isotropic. Z_1 and Y_1 have the same g factor for an angle of 27.2° from the c-axis, so angles near this value should be avoided to ensure that we have relatively isolated three level systems among the four levels within the ground and excited states.

The g_{ac} can be calculated as: $g_{ac} = \frac{|\langle -|\mathbf{H}_{AC}|+\rangle|}{\mu_B |\mathbf{B}_{AC}| S}$, where $|-\rangle$ and $|+\rangle$ are the eigenstates of the effective spin-1/2 system determined by the static magnetic field direction using Equation 3.1 and $\mathbf{H}_{AC} = \mu_B \cdot \mathbf{B}_{AC} \cdot \mathbf{g} \cdot \mathbf{S}$, where $\mathbf{B}_{AC}$ is the ac microwave magnetic field. Given our restriction of applying an in-plane DC magnetic field and an out-of-plane microwave magnetic field, g_{ac} does not have any dependence on the in-plane DC magnetic field angle and can be calculated to be $g_{ac,Z_1} = 7.09$, $g_{ac,Y_1} = 4.57$ and $g_{ac,Y_2} = 6.74$ for the ground and excited state transitions.

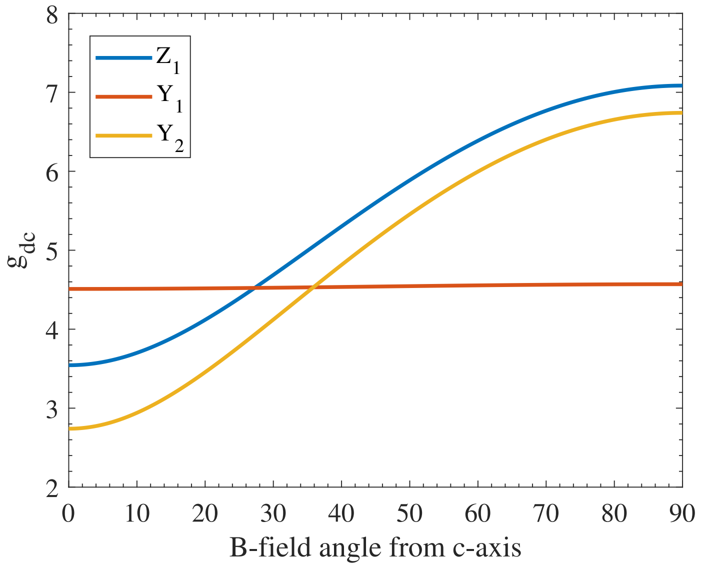

Figure 3.5: g_{dc} for Z_1, Y_1 and Y_2 as a function of the magnetic field angle from the c-axis.

Lastly, magnetic field orientation for the branching ratio of the optical transitions dipoles can be determined. We will use an effective spin Hamiltonian approach as previously shown in the literature that has matched quite well to their experiments [111–113]. We can use the effective spin Hamiltonian for the ground and excited state (Equation 3.1) to determine the states at a given magnetic field orientation.

First we can write down the states:

$$|\Psi_{+,Z_1}\rangle = -\beta * |\Phi_{-3/2,Z_1}\rangle + \alpha^* |\Phi_{+3/2,Z_1}\rangle \tag{3.9}$$

$$|\Psi_{-,Z_1}\rangle = -\alpha^* |\Phi_{-3/2,Z_1}\rangle + \beta |\Phi_{+3/2,Z_1}\rangle \tag{3.10}$$

$$|\Psi_{+,Y_1}\rangle = -\delta^*_{Y_1} |\Phi_{-3/2,Y_1}\rangle + \gamma^*_{Y_1} |\Phi_{+3/2,Y_1}\rangle \tag{3.11}$$

$$|\Psi_{-,Y_1}\rangle = -\delta_{Y_1} |\Phi_{-3/2,Y_1}\rangle + \gamma_{Y_1} |\Phi_{+3/2,Y_1}\rangle \tag{3.12}$$

$$|\Psi_{+,Y_2}\rangle = -\delta^*_{Y_2} |\Phi_{-1/2,Y_2}\rangle + \gamma^*_{Y_2} |\Phi_{+1/2,Y_2}\rangle \tag{3.13}$$

$$|\Psi_{-,Y_2}\rangle = -\delta_{Y_2} |\Phi_{-1/2,Y_2}\rangle + \gamma_{Y_2} |\Phi_{+1/2,Y_2}\rangle \tag{3.14}$$

where $|\Phi_{i,j}\rangle$ are the labels of the states with a magnetic field along the c-axis and i is the crystal field quantum number. $|\Psi_{i,j}\rangle$ is the label of the state when a static magnetic field is applied in the a-c plane. α, β, δ_{Y_1}, γ_{Y_1}, δ_{Y_2}, and γ_{Y_2} are the state overlap coefficients.

We can then apply the transition selection rules (see Table 3.1) and transition operator time-reversal symmetry properties [66, 112] to estimate the relative transition strengths for the electric and magnetic dipole transitions for Z_1-Y_1:

$$R_{Y_1,B\|c,\perp} = |\langle\Psi_{+,Z_1}|\,\hat{P}_{B\|c}\,|\Psi_{-,Y_1}\rangle|^2 = |\alpha\delta + \gamma\beta|^2 \tag{3.15}$$

$$R_{Y_1,B\|c,\|} = |\langle\Psi_{+,Z_1}|\,\hat{P}_{B\|c}\,|\Psi_{+,Y_1}\rangle|^2 = |\alpha\delta^* - \beta\gamma^*|^2 \tag{3.16}$$

$$R_{Y_1,E\|a,\perp} = |\langle\Psi_{+,Z_1}|\,\hat{P}_{E\|a}\,|\Psi_{-,Y_1}\rangle|^2 = |\alpha\delta + \beta\gamma|^2 \tag{3.17}$$

$$R_{Y_1,E\|a,\|} = |\langle\Psi_{+,Z_1}|\,\hat{P}_{E\|a}\,|\Psi_{+,Y_1}\rangle|^2 = |\alpha\gamma^* - \beta\delta^*|^2 \tag{3.18}$$

$$R_{Y_1,B\|a,\perp} = |\langle\Psi_{+,Z_1}|\,\hat{P}_{B\|a}\,|\Psi_{-,Y_1}\rangle|^2 = |\alpha\delta - \beta\gamma|^2 \tag{3.19}$$

$$R_{Y_1,B\|a,\|} = |\langle\Psi_{+,Z_1}|\,\hat{P}_{B\|a}\,|\Psi_{+,Y_1}\rangle|^2 = |\alpha\gamma^* + \beta\delta^*|^2 \tag{3.20}$$

where E/B correspond to magnetic and electric dipoles, $\|\ a/c$ refers to the polarization of the dipole, $\|\ /\perp$ correspond to transitions between sign-preserving (i.e. $|\Psi_{+,Z_1}\rangle \leftrightarrow |\Psi_{+,Y_1}\rangle$) or sign-flipping transitions (i.e. $|\Psi_{+,Z_1}\rangle \leftrightarrow |\Psi_{-,Y_1}\rangle$), and $\hat{P}$ is the transition dipole operator.

We can do the same thing for Z_1-Y_2:

$$R_{Y_2,E\|c,\perp} = |\langle\Psi_{+,Z_1}|\,\hat{P}_{E\|c}\,|\Psi_{-,Y_2}\rangle|^2 = |\beta\delta + \alpha\gamma|^2 \tag{3.21}$$

$$R_{Y_2,E\|c,\|} = |\langle\Psi_{+,Z_1}|\,\hat{P}_{E\|c}\,|\Psi_{+,Y_2}\rangle|^2 = |\alpha\delta^* - \beta\gamma^*|^2 \tag{3.22}$$

$$R_{Y_2,E\|a,\perp} = |\langle\Psi_{+,Z_1}|\,\hat{P}_{E\|a}\,|\Psi_{-,Y_2}\rangle|^2 = |\alpha^*\delta^* - \beta^*\gamma^*|^2 \tag{3.23}$$

$$R_{Y_2,E\|a,\|} = |\langle\Psi_{+,Z_1}|\,\hat{P}_{E\|a}\,|\Psi_{+,Y_2}\rangle|^2 = |\alpha^*\gamma + \beta^*\delta|^2 \tag{3.24}$$

$$R_{Y_2,B\|a,\perp} = |\langle\Psi_{+,Z_1}|\,\hat{P}_{B\|a}\,|\Psi_{-,Y_2}\rangle|^2 = |\alpha^*\delta^* + \beta^*\gamma^*|^2 \tag{3.25}$$

$$R_{Y_2,B\|a,\|} = |\langle\Psi_{+,Z_1}|\,\hat{P}_{B\|a}\,|\Psi_{+,Y_2}\rangle|^2 = |\alpha^*\gamma - \beta^*\delta|^2. \tag{3.26}$$

We can then define the branching ratio for each dipole transition as:

$$B_{i,j} = \frac{R_{i,j,\perp}}{R_{i,j,\perp} + R_{i,j,\|}} \tag{3.27}$$

for transition i (i.e. Z_1-Y_1 or Z_1-Y_2) and j dipole type and polarization. The branching ratio is defined in such a way that an ideal (or even) branching ratio gives a value of 1/2 which results in even mixing between the states, while a branching ratio of 0 or 1 corresponds to no mixing.

The branching ratio for the three different possible transition dipoles for Z_1-Y_1 are shown in Figure 3.6a. When the DC magnetic field is along either the c-axis or the a-axis, the branching ratio for all transitions dipoles is either 0 or 1. Only the $E \parallel a$ (σ_{ED}) transition dipole can reach an even branching ratio at a magnetic field angle of 35° from the c-axis. $B||a$ (π_{MD}) and $B||c$ (σ_{MD}) can reach non-zero branching ratios, but the mixing is far from even (97% and 3%, respectively).

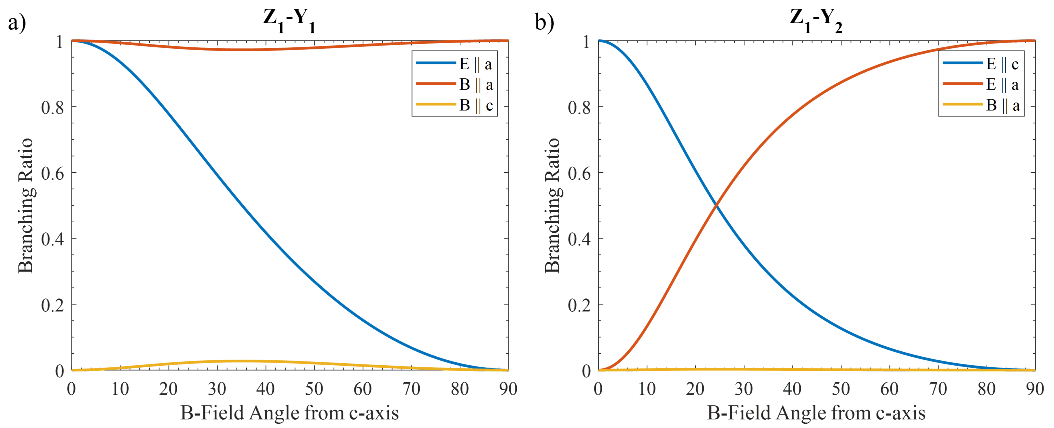

Figure 3.6: Branching ratio for a) Z_1-Y_1 and b) Z_1-Y_2 optical transitions for the different dipole operators (i.e. electric or magnetic) and orientations (i.e. parallel to the a-axis or c-axis).

Similarly, we can look at the branching ratios for Z_1-Y_2 in Figure 3.6b. Both orientation of the electric dipole can achieve an even branching ratio at a magnetic field angle 24° from the c-axis. The branching ratio for $B \parallel a$ (π_{MD}) reaches a maximum value of $3 \cdot 10^{-3}$ which is very small.

For transduction, we care about the branching ratio, but we also need to consider the overall strength of the transition dipole. In other words, if the branching ratio is not even, but the total strength is much larger, that can still be the better transition dipole to use. We can calculate the transition dipole moments as:

$$d^2_{i,j,\perp} = d^2_{i,j} \frac{R_{i,j,\perp}}{R_{i,j,\perp} + R_{i,j,\|}} \tag{3.28}$$

$$d^2_{i,j,\|} = d^2_{i,j} \frac{R_{i,j,\|}}{R_{i,j,\perp} + R_{i,j,\|}} \tag{3.29}$$

where we are using the same notation as the branching ratio. The transduction efficiency scales as $\eta \propto |d_{i,j,\perp} d_{i,j,\|}|^2$ if we assume that we are only able to use one of the transition dipole moments (i.e. only electric or only magnetic dipole) for the transduction process. This is the case for us in our standing wave optical cavities and will be mentioned again in the optical cavity design section in Chapter 4.

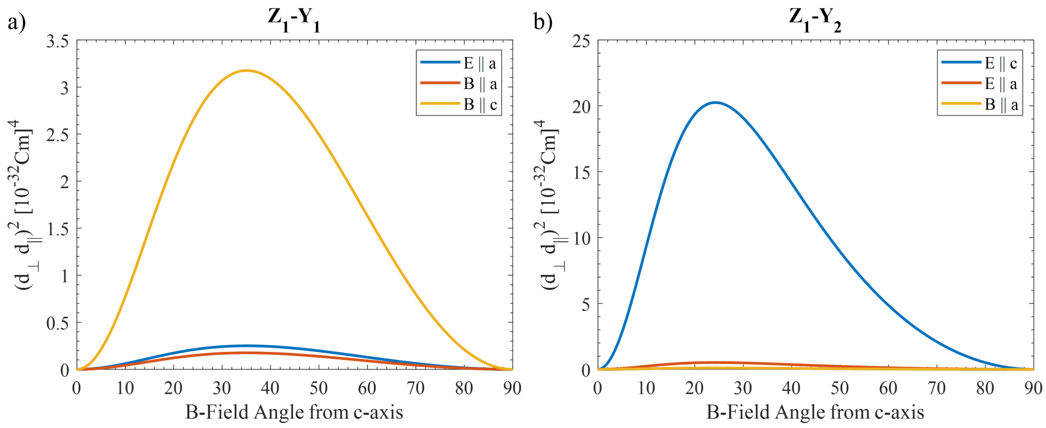

Figure 3.7: Dipole moment product for a) Z_1-Y_1 and b) Z_1-Y_2 for different transition dipole operators (i.e. electric or magnetic) and orientations (i.e. parallel to the a-axis or c-axis).

The dipole product factor for Z_1-Y_1 is shown in Figure 3.7a. The strongest transition dipole product for Z_1-Y_1 is the magnetic dipole along the c-axis (σ_{MD}) even though the branching ratio is far from even. Similarly, the dipole product for Z_1-Y_2 is shown in Figure 3.7b. Here, the strongest transition dipole for Z_1-Y_2 is the electric dipole along the c-axis (π_{ED}), which has both a strong dipole strength and an even branching ratio. Comparing the two different transitions, we would expect ~7x larger transduction signal for Z_1-Y_2 relative to Z_1-Y_1 based on the optical transition dipole strengths and assuming all other parameters are constant.

Initial devices we made were designed to couple to Z_1-Y_2 optical transitions, but after some worry about the optical coherence due to the close proximity of Y_1 and Y_2, we switched to devices coupled to Z_1-Y_1 optical transitions. Both transitions should be usable for transduction, but our Z_1-Y_1 devices had better performance. This is likely most attributed to more device iterations and improvements, while our Z_1-Y_2 device was made in the early days of our fabrication process development and did not have the luxury of improvements that were made over the years.

Table 3.5: Z_1-Y_1 spectroscopic parameters at $B_\theta = 50°$

Parameter	Value
g_{dc}, Z_1	5.89
g_{dc}, Y_1	4.55
$d_{B\|\|c,\perp}$ [10^{-32} C·m]	0.48
$d_{B\|\|c,\|\|}$ [10^{-32} C·m]	3.26
$d_{B\|\|a,\perp}$ [10^{-32} C·m]	1.58
$d_{B\|\|a,\|\|}$ [10^{-32} C·m]	0.23
$d_{E\|\|a,\perp}$ [10^{-32} C·m]	0.52
$d_{E\|\|a,\|\|}$ [10^{-32} C·m]	0.86

Best Magnetic Field Orientation for Z_1-Y_1

Based on the dipole moment product, for Z_1-Y_1 the best magnetic field is at an angle of 35° from the c-axis. However, it is also beneficial to have the g_{dc} for the ground and excited state to differ as much as possible which occurs at larger magnetic field angles (see Figure 3.5). Therefore, we decide to use a magnetic field angle of 50° as a balance of these two effects. At an angle of 50° from the c-axis, the dipole moment product is still near its maximum, so we only expect a decrease in transduction efficiency of ~25%, which is a small factor.

A summary of the magnetic field dependent Z_1-Y_1 spectroscopic parameters for a magnetic field angle of 50 ° are summarized in Table 3.5. The Y_1 label for the dipole moments was dropped, since we are only including the Z_1-Y_1 transitions here.

3.5 Calculated α Parameter

As mentioned in Chapter 2, we can summarize relevant spectroscopic parameters for REI transduction into a parameter α (see Equation 2.13). Having summarized the relevant parameters above, we can estimate α for both Z_1-Y_1 and Z_1-Y_2 transduction. Given that there are several different dipoles and orientations possible, we will only show the values for the highest efficiency configurations in Table 3.6. The erbium ion density is for 560 ppm. The spin dipole moment in the bracket is for Y_1 and Y_2 in the excited state in Table 3.6. For the detunings term in α, we take the center of the detunings to be 3 standard deviations as was used in [98].

Table 3.6: Er^{3+}:YVO_4 α parameters

	Z_1-Y_1	Z_1-Y_2
Density, ρ [cm^{-3}]	$5.4 \cdot 10^{18}$	$5.4 \cdot 10^{18}$
Optical Inhomogeneity, Δ_o [MHz]	260	225
Spin Inhomogeneity, Δ_μ [MHz]	65	65
Optical Dipole Type	σ_{MD}	π_{ED}
Optical Dipole Strength [C·m]	$3.26 \cdot 10^{-32}$	$2.08 \cdot 10^{-32}$
Spin Dipole Strength [μ_B]	3.55 (2.29)	3.55 (3.37)
α [s^{-1}]	$1.54 \cdot 10^{-10}$	$1.14 \cdot 10^{-10}$

The α parameter for Z_1-Y_1 and Z_1-Y_2 are very similar, with Z_1-Y_1 being slightly larger. It should be noted again that there is another optical dipole strength term in the optical Rabi frequency term, which makes Z_1-Y_2 slightly more favorable. Another difference is the dipole type. Z_1-Y_1 is best with a σ_{MD} optical dipole, while Z_1-Y_2 is best with a π_{ED} optical dipole. Therefore, the coupling to the optical resonator will require different designs, which will be discussed more in Chapter 4.

Comparison to Other Materials

It is useful to compare the α value we get for Er^{3+}:YVO_4 with other rare-earth ion materials. Unfortunately, it is not necessarily very straight forward to find the optimal α for a given material. As shown above, several parameters have strong dependence on the magnetic field direction used for the experiment. Also, $\alpha \propto \frac{\rho}{\Delta_o \Delta_\mu}$, which means it is important to find the highest density possible that also has most narrow linewidths. This complete type of analysis has not really been done on many (if any) materials, so we can only compare with experimental data we are aware about. In other words, there are possibly (or likely) other rare-earth ion/host materials that perform even better and using them will only improve things, but additional spectroscopy is needed to identify them.

In terms of known materials, we can compare to ^{171}Yb:YVO$_4$ [57, 108] and Er^{3+}:YSO [54, 98]. For ^{171}Yb:YVO$_4$, $\alpha = 1.6 \cdot 10^{-8}$ using the spectroscopic parameters provided in the references [57, 108]. This shows that ^{171}Yb:YVO$_4$ is another promising material. However, it should be noted that most of the improvement is due to the narrow spin inhomogeneity of ^{171}Yb:YVO$_4$ (0.1 MHz compare to 30 MHz). When coupling with an on-chip superconducting microwave resonator, the spin inhomogeneity tends to increase due to magnetic field inhomogeneity from the gaps in the superconducting film. ^{171}Yb:YVO$_4$ can operate at small magnetic fields if a small microwave frequency is acceptable, so potentially there are regimes where this is not a problem.

For Er^{3+}:YSO, $\alpha = 1.4 \cdot 10^{-10}$ using the spectroscopic parameters assumed in the reference [98] or $\alpha = 5.4 \cdot 10^{-13}$ using the spectroscopic parameters in [54]. The difference in these values largely arises from the difference in the spin linewidth, which is a factor of 25. We should also note that these Er^{3+}:YSO parameters assume a much smaller Er density (10 ppm), which is a factor of 56 smaller than our Er^{3+}:YVO$_4$ calculations.

3.6 ^{167}Er:YVO$_4$ Hyperfine Transitions

Although we do not intend to use ^{167}Er isotopes for transduction, their presence in natural abundance Er^{3+}:YVO$_4$ crystals can result in their transitions overlapping or being near transitions of interest. Therefore, it is useful to determine their transition frequencies and see how close they are to the even isotope spin transitions that we intend to use. ^{167}Er has a nuclear spin I =7/2, which increases the number of states from two (in the case of zero nuclear spin isotopes) to 16 states and makes it much more complicated.

The ground state ^{167}Er can be modelled using the following Hamiltonian [66]:

$$H_{eff} = \mu_B \mathbf{B} \cdot \mathbf{g} \cdot \mathbf{S} + \mathbf{I} \cdot \mathbf{A} \cdot \mathbf{S} + \mathbf{I} \cdot \mathbf{P} \cdot \mathbf{I} \tag{3.30}$$

where the first term is the electron spin term, the second term represents the hyperfine interaction between the electron and nuclear spin, and the last term describes the nuclear quadrupole interaction.

Due to the axial site symmetry, the spin Hamiltonian can be simplified to [66, 105]:

$$\begin{aligned} H_{eff} =& \mu_B \left[g_{\|} B_z S_z + g_{\perp}(B_x S_x + B_y S_y) \right] \\ &+ A_{\|} S_z I_z + A_{\perp}(S_x I_x + S_y I_y) + P_{\|} \left[I_z^2 - \frac{1}{3} I(I+1) \right] \end{aligned} \tag{3.31}$$

where $g_{\|} = 3.544$, $g_{\perp} = 7.085$, $|A_{\|}| = 1.226 \cdot 10^6\,[\mathrm{cm}^{-1}]$, $|A_{\perp}| = 2.491 \cdot 10^6\,[\mathrm{cm}^{-1}]$ and $|P_{\|}| = 1.39 \cdot 10^5\,[\mathrm{cm}^{-1}]$ for $^{167}\mathrm{Er}^{3+}$:YVO$_4$ using values from Ranon et al. [105].

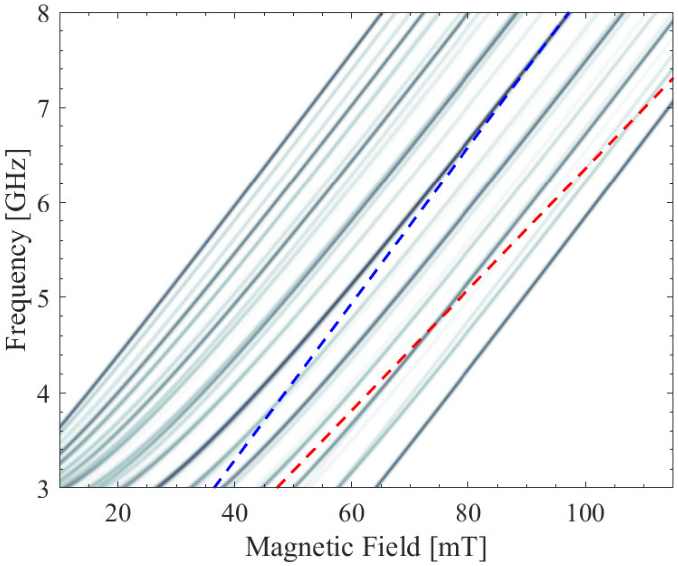

Figure 3.8: $^{167}\mathrm{Er}^{3+}$:YVO$_4$ hyperfine transitions for B_{dc} 50° from the c-axis. The blue line is the Z_1 electron spin transition and the red line is the Y_1 electron spin transition.

Solving the Hamiltonian, we can determine the energy of all the states. The hyperfine transitions for B_{dc} being 50° from the c-axis are shown in Figure 3.8. The transition strengths was evaluated by taking the inner product of the initial and final states mediated by both a $\sigma_x \otimes I_N$ (and $\sigma_z \otimes I_N$) operator to account for the selection rules for B_{ac} $\|$a (and B_{ac} $\|$c) [66, 103]. In our on-chip resonator, we expect B_{ac} to be along both crystal directions, so we consider both direction here.

The blue line is the Z_1 electron spin transition and the red line is the Y_1 electron spin transition to show the proximity of these transitions to the hyperfine transitions. It is evident that at particular magnetic fields and particular microwave frequencies, we have overlap between the even isotope spin transitions and hyperfine transitions. This will be important later when we do the experiment, so this will be referred to again in that section and does suggest that there can be improvements for an isotopically purified zero spin Er^{3+}:YVO$_4$ material.

3.7 YVO_4 Crystal Axis Orientation

One practical important factor for working with YVO_4 crystals is orienting the crystals that we have in the lab. Typically our crystals were cut along a crystal axis and it was useful to experimentally distinguish between the a-axis and c-axis. We can use the YVO_4 crystal birefringence to do this. Others have proposed using the crystal birefringence to orient YSO crystals [114], and we are using a similar concept here.

Our measurement method requires a linearly-polarized light source and a camera to image the light travelling through the crystal and reflected off the back surface. We can see the images for light polarized along each crystal axis in Figure 3.9. For light polarized along the a-axis, we see a typical circular image of the beam of light. We see the Airy rings as the light is slightly defocused from the YVO_4 back surface. Conversely, for light polarized along the c-axis, we see a more irregular pattern from the birefringence of the crystal. For us, this was a relatively quick, easy, and convenient way to orient our crystals if there was any doubt from a supplier.

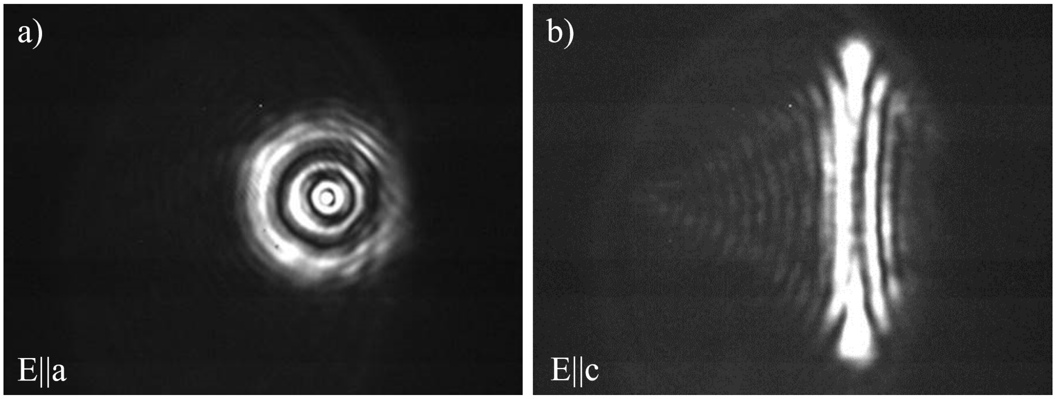

Figure 3.9: YVO_4 crystal axis alignment for a) light polarized with $E \parallel a$ and b) light polarized with $E \parallel c$.

Chapter 4

TRANSDUCER DESIGN AND SIMULATION

In this chapter, I will discuss the design of the transducer and the electromagnetic simulations of the optical and microwave resonator used to evaluate the theoretical transducer performance.

Some parts of the transducer (i.e. optical resonator polarization) depend on the optical transition used. In this chapter, I will include results for our transducer with Z_1-Y_1 transitions as those are the transitions we used most extensively. Similar optical simulations were done for Z_1-Y_2 and also Er^{3+}:YSO. Those designs are in Appendix B.

4.1 Transducer Design Figure of Merits

For the design of our transducer, we will consider several figures of merit that were previously introduced in Chapter 2. These include the mode overlap, the optical and microwave resonator quality factors, and the optical pump Rabi frequency. In this section, these figures of merit will be discussed in the context of our on-chip transducer.

Mode Overlap – F

In principle, we can find the electromagnetic fields of all three modes using an electromagnetic solver and calculate F directly (see Equation 2.14), but it will be convenient to decouple the microwave and optical contributions such that the two simulations can be optimized separately by independent figures of merit. In the spirit of this, we can assume that the microwave field is constant across the optical cavity. This is not strictly true in general, but is a reasonable approximation for our geometry. In this limit, we can define the approximated mode overlap as:

$$\begin{aligned} F &= \frac{1}{\sqrt{V_o V_\mu}} \left| \int_{YVO} \frac{B_{m,\mu}(r) B_{m,o,1}(r) B_{m,o,2}(r)}{B_{\mu,max} B_{o,1,max} B_{o,2,maxYVO}} dV \right| \\ &\approx \left[\frac{B_{m,\mu}(r_o)}{\sqrt{\int_{YVO} |B_\mu(r)|^2 dV}} \right] \left[\frac{\int B_{m,o,1}(r) B_{m,o,2}(r) dV}{B_{m,o,2,maxYVO} \sqrt{\int |B_{o,1}(r)|^2 dV}} \right] \\ &\approx F_\mu F_o \end{aligned} \tag{4.1}$$

where $F_\mu = \left[\frac{B_{m,\mu}(r_o)}{\sqrt{\int |B_\mu(r)|^2 dV}}\right]$ and $F_o = \left[\frac{\int_{YVO} B_{m,o,1}(r) B_{m,o,2}(r) dV}{B_{m,o,2,maxYVO}\sqrt{\int |B_{o,1}(r)|^2 dV}}\right]$ are the mode overlap contributions from the microwave and optical cavity design, respectively.

We have assumed for mode overlap that the microwave field is coupled to a magnetic dipole transition and the optical field is also coupled to magnetic dipole transitions of Z_1-Y_1.

Optical Rabi Frequency

Another figure of merit is the optical pump Rabi frequency, which can be expressed as:

$$\begin{aligned}\Omega_{max} &= \sqrt{\langle n_o \rangle}\sqrt{\frac{\omega\mu_0}{2\hbar}}\frac{\mu_{32}}{\sqrt{V_m}}\frac{B_{m,o,2,maxYVO}(r)}{\sqrt{(|B_{o,2}|^2)_{max}}} \\ &= \sqrt{\frac{P_o}{\hbar\omega}\frac{\kappa_{o,in}}{\kappa_o^2/4+\delta_c^2}}\sqrt{\frac{\omega\mu_0}{2\hbar}}\mu_{32}\frac{B_{m,o,2,maxYVO}}{\sqrt{\int |B_{o,2}(r)|^2 dV}}.\end{aligned} \tag{4.2}$$

From a geometric perspective of the optical cavity, the optical Rabi frequency will increase as we decrease the mode volume of the optical cavity. Also, we can increase the optical Rabi frequency by having $\frac{\kappa_{o,in}}{\kappa} \longrightarrow 1$ and $\delta_c \ll \kappa$. If those parameters are constrained, we can increase the optical pump power to increase the Rabi frequency, but this can also increase the temperature of the transducer (see Chapter 7 for more details).

If we want to stay within the constraints of the adiabatic model, we reach a limit on the maximum optical Rabi frequency we want to apply (i.e. $\left|\delta_{\mu,k}\delta_{o,k}\right| \gg \left|\Omega_{o,k}\right|^2$), which means there are two different regimes. In one regime, we can assume that we can arbitrarily set the optical pump power to the value that maximizes the optical Rabi frequency, and in this case we can ignore the Rabi frequency dependence on the other terms in Equation 4.1.

In the second regime, we assume that we cannot arbitrarily set the optical power to a given value, and thus we should maximize the other terms in order to maximize the optical Rabi frequency. For us, we elected to consider the second case, and thus we include the geometric contribution of the optical Rabi frequency in our figure of merit.

If we combine the two geometric factors from the mode overlap and the optical Rabi frequency to get a total optical geometric dependence on the transducer efficiency, we arrive at:

$$\begin{aligned} F_G &= \Omega_F F_o \\ &= \left[\frac{\int_{YVO} B_{m,o,1}(r) B_{m,o,2}(r) dV}{\sqrt{\int |B_{o,1}(r)|^2 dV \int |B_{o,2}(r)|^2 dV}} \right] \\ &\approx \left[\frac{\int_{YVO} B_{m,o,1}(r)^2 dV}{\int |B_{o,1}(r)|^2 dV} \right]. \end{aligned} \tag{4.3}$$

This is the energy filling fraction of the magnetic mode in the YVO_4 that aligns with the erbium dipole moment compared to the total magnetic mode energy. The last approximation in Equation 4.3 is considered in the case that the optical pump field and the transducer optical signal share the same optical mode, which is the case for our transducer design.

Resonator Quality Factors

Another important parameter to design for are the optical and microwave quality factors. Simply put, having higher quality factors (especially internal quality factors) is generally helpful for increasing the efficiency. It is worth noting that the cavity with the more narrow linewidth (in this case most likely the microwave cavity) will set the bandwidth of the transducer, so higher microwave quality factors will result in a trade-off between the transducer efficiency and bandwidth.

For the optical quality factor, since our design has an optical pump and transduction signal within the same optical mode, decreasing the optical linewidth well beyond the microwave frequency (i.e. $\omega_\mu \approx 2\pi \cdot 5$ GHz) is not helpful, since this will result in less pump photons circulating within the optical cavity. Having said this, we target a microwave and optical quality factors of $Q \approx 10{,}000$.

4.2 Transducer Design

In this section, I will discuss the design of the transducer we chose to implement and some factors we considered for those decisions. Our transducer consists of a rare-earth ion doped substrate (YVO_4) where resonators are patterned on the surface. We are interested to take an integrated circuits approach for our resonators within the transducer, where we expect to have advantages in integration with other planar superconducting components, relative ease of fabrication and also larger optical Rabi frequencies of our pump due to smaller optical mode volumes compared bulk resonators.

There are two main parts to this, which are the optical resonator and the microwave resonator, so those will be discussed independently.

Choice of Optical Resonator Design

The main figures of merit for our optical resonator is to maximize the coupling between the optical fields and the rare-earth ions and to obtain large quality factors. In general, to fabricate our optical resonator, we decided between two different approaches.

The first one is to pattern our resonator directly into our rare-earth ion host. To date, there are very limited ways to accomplish this with the currently available technology. YVO_4 (and most other common rare-earth ion hosts) can only be obtained commercially as bulk substrates and not single-crystal thin-films (i.e. silicon on insulator (SOI) or lithium niobate on insulator (LNOI)), which are typically required to pattern photonic resonators and confine light within a higher refractive index region of the material stack.

Research groups have overcome this limitation in some materials like diamond or silicon carbide by using non-conventional etching techniques [115, 116] or polishing of a bulk substrate to a thin film [117–119]. Another challenge for YVO_4 fabrication is that there is not a known dry-etching chemistry to pattern YVO_4. Until that is realized, one can only hope to pattern YVO_4 using a milling process to physical remove material instead of chemically removing material.

In the Faraon group, we developed a focused ion milling technique to pattern photonic crystal structures directly into the surface of YVO_4 substrates [74, 75]. However, fabricating these resonators is slow and tedious. Further, it is not straight forward to make a long optical resonator (typically the resonators we made had a total length of $< 20\ \mu$m including the mirror length) which is helpful for mode overlap with the microwave resonator, which tends to confine its field over larger distances ($\sim 100\ \mu$m or larger typically). More details of this fabrication process is in Appendix A.

The second method is to pattern the optical resonator in another high refractive index material that is added to the surface of the YVO_4 substrate. This approach has been done by the Faraon group and others for coupling to rare-earth ions [77–79, 120] and also other materials as well [121, 122]. In this method, we are able to overcome the challenges of YVO_4 fabrication by patterning a different material instead that is easier to pattern. We are also limited to materials that have low optical losses and should have a high refractive index relative to YVO_4 in order to confine the light to the high index material.

The main drawback of this method is that the coupling to the atoms is achieved using the evanescent optical field, which limits the fraction of the optical energy that interacts with the rare-earth ions in the substrate. Typically, the energy fraction that interacts with the rare-earth ions is $\sim 10\%$, while a resonator patterned directly in YVO_4 can have an energy fraction $> 50\%$.

For this project, we decided to implement the second method for the reasons stated above. We chose to use amorphous silicon (a-Si) as our high index optical material to make the optical cavity. Amorphous silicon can be deposited directly using PECVD onto the YVO_4 substrate using facilities at CalTech, it can be etched using conventional silicon etching processes, and it is relatively low loss at 1550 nm.

Our group has previously shown quality factors using a-Si on YSO to be above 100,000 [78], while others have shown optical waveguide losses < 1 dB/cm^{-1} and material absorption coefficients 0.04 dB/cm^{-1} [123], which indicates that even higher quality factors should be achievable with a more optimized deposition process. The refractive index is $n \sim 3.5$, which is significantly higher than YVO_4 and most rare-earth ion host substrates, which would allow the same concept to be applied to other rare-earth ion host materials if another host is determined to be more beneficial in the future.

In terms of the geometry of the optical resonator, we chose to fabricate a Fabry-Perot-like optical resonator, where we have an optical waveguide between two photonic crystal mirrors. This cavity is relatively easy to design as the different components (i.e. mirrors and waveguide) can be designed mostly independently. Also, the optical waveguide pattern is easy to integrate next to the microwave cavity. One challenge here is that we need to design low loss photonic crystal mirrors, but since we do not require a small mode volume, we can adiabatically taper to the mirror mode from the waveguide mode over as many periods as we need to have low scattering losses.

Microwave Resonator Design Considerations

For the superconducting microwave, the two main design considerations are the superconducting material that is used and the geometry of the resonator. We will focus on the superconducting materials first and then discuss the geometry afterwards.

For the superconducting material for our REI transducer device, our main priority was using a material that can be deposited using conventional thin-film deposition techniques (i.e. evaporation or sputtering) while maintaining high quality factors/low losses at microwave frequencies in the context of our transducer operation (i.e. in the presence of a magnetic field and nearby circulating optical power).

Our plan was to deposit the superconducting films at facilities within CalTech, so we wanted to use a material that many groups have had general success with. From this consideration, we limited our comparisons to aluminum, niobium and niobium alloys (NbN, NbTiN), which are listed here in order of relative ease of fabrication.

Table 4.1 is a summary of the relevant material properties from the literature that we need to determine which material is best suited for our transducer. Only NbTiN is included in the table among the niobium alloys, but NbN largely has similar properties to NbTiN. The penetration depth in Table 4.1 is calculated from the other parameters using Equation 4.14. It is worth noting that these values are not necessarily the case for all superconducting thin-films of these materials since the superconducting deposition parameters can impact the film properties significantly. However, it is still useful as a general comparison, especially when the values are orders of magnitude different between different materials. In the following discussions, only these materials will be looked at.

The main factors we will introduce for the different materials are how quasi-particles and magnetic fields limited quality factors and also the kinetic inductance of the different materials. The included references for each topic can be used for a more extensive understanding or analysis. As a principle resource for superconducting microwave device physics, I would recommend Jiansong Gao's thesis [124].

Table 4.1: Superconducting material properties

Parameters	Al	Nb	NbTiN	References
Critical Temperature, T_c[K]	1.1	9.2	14.5	[125]
Energy Gap, Δ [μeV]	168	1395	2200	[125]
Normal State Resistivity, ρ_N[$\mu\Omega\cdot$ cm]	0.8	6	100	[125]
Penetration depth, λ [nm]	89	92	276	
Coherence length, ζ [nm]	1600	40	4	[126]
Critical magnetic field, H_{c1}/H_{c2}[T]	0.01	0.17/0.4	0.03/14	[126]
Quasi-particle timescale, τ_o[ns]	438	0.149	-	[127]

Optical Photon Induced Quasi-Particle Quality Factor

Here we will consider the effects of optical photons inducing quasi-particles that degrade the quality factor of the microwave resonator. This is especially a concern for our transducer as we require optical photons to circulate in an optical resonator very close to the superconducting resonator. The effects of high-energy radiation on superconducting resonators has been well-studied in the context of microwave kinetic inductance detectors (MKIDs) [124, 125, 128], and superconducting quantum circuits [129, 130]. The general picture is that high energy photons (i.e. photons with energy larger than the superconducting gap) that impact the superconducting material can break Copper pairs into quasi-particles and the dissipation from the quasi-particles can lower the quality factor of the microwave resonator.

The quasi-particle limited quality factor of the microwave resonator can be expressed as [124]:

$$Q_{\mu,qp} = \frac{1}{\alpha\gamma}\frac{\sigma_2}{\sigma_1} \tag{4.4}$$

where α is the kinetic inductance fraction, $\sigma = \sigma_1 - i\sigma_2$ is the complex conductivity of the superconducting film [131, 132] and γ is a coefficient depending on the type of superconducting film (i.e. $\gamma = 1$ in the thin film limit, $\gamma = 1/2$ in the local dirty limit and $\gamma = 1/3$ in the extreme anomalous limit).

Using Mattis-Bardeem theory, in the low temperature (i.e. $T \ll T_c$, where T_c is the critical temperature of the superconducting film and $k_B T \ll \hbar\omega$), the complex conductivity ratio can be expressed as [130]:

$$\frac{\sigma_2}{\sigma_1} = \frac{\pi}{\sqrt{2}}\sqrt{\frac{\hbar\omega}{\Delta}}\frac{D(E_F)\Delta}{n_{qp}} \tag{4.5}$$

where Δ is the superconducting energy gap, $D(E_F)$ is the two-spin density of states, and n_{qp} is the quasi-particle density. If we assume a simple pair-breaking and recombination model for the light-induced quasi-particle density, we can express this density as [133]:

$$n_{qp} = \frac{1}{V}\sqrt{\frac{P}{\Delta R}} \tag{4.6}$$

where V is the volume, P is the optical power absorbed by the superconductor and R is the recombination rate. Therefore, using this simple model, the light-induced quasi-particle limited quality factor can be expressed as:

$$Q_{\mu,qp} = \frac{\pi}{\alpha\gamma}\sqrt{\frac{\hbar\omega}{2}}D(E_F)V\Delta\sqrt{\frac{R}{P}}. \tag{4.7}$$

From Equation 4.7, we can determine several factors that can contribute to the light-induced quasi-particle limited quality factor. The parameter that varies the most between the different materials is the recombination rate R, which is related to the quasi-particle timescale, τ_0. The recombination timescale has been shown to be several orders magnitude slower for Al (~100 μs) [128, 134] compared to Nb or NbTiN (~1 ns)[135].

We can also see that a smaller kinetic inductance fraction and a larger volume is beneficial, which suggests that the superconducting film should not be too thin or narrow. After all, that is how one can make a superconducting nanowire single photon detector (SNSPD), which is not what we are going for here. Lastly, we want to minimize the optical power absorbed by the superconductor, which can be achieved by using less optical power for the transducer itself or minimizing the absorption by reducing scattering or increasing the distance between the two components.

We compare the quasi-particle density and quasi-particle limited quality factor in Figure 4.1 for aluminum, niobium and NbTiN films using Equation 4.7. We can see that niobium and NbTiN are ~ 2 orders of magnitude better compared to aluminum, which is mostly attributed to the faster recombination timescale. NbTiN is slightly worse than Nb in the model due to the larger kinetic inductance fraction.

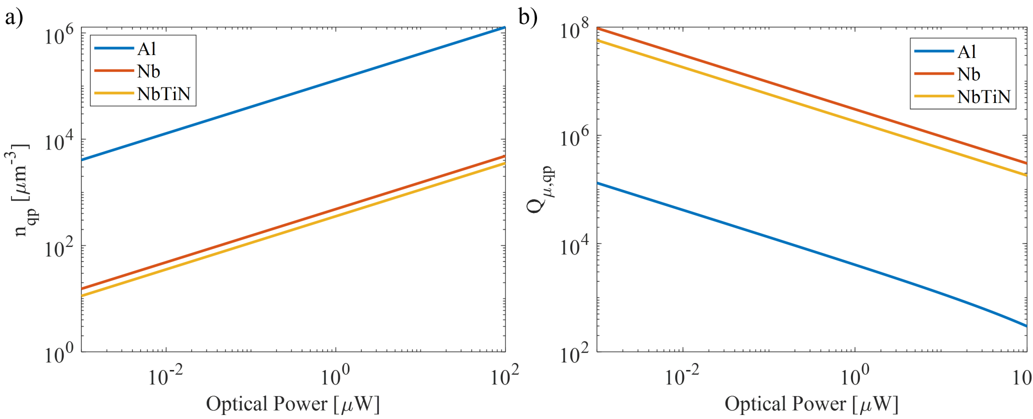

Figure 4.1: a) Estimated quasi-particle density and b) quasi-particle limited quality factor as a function of the applied optical power for different superconducting materials.

Microwave Resonators in Magnetic Fields

Here we will consider the effects of a magnetic field on the microwave resonator. In the REI transducer scheme with even isotope ions, we require a magnetic field (~ 100 mT) in order to have a microwave spin transition at GHz frequencies. Therefore, it is important that we have a superconducting resonator that can withstand magnetic fields of this magnitude. External magnetic fields that are sufficiently large can create vortices in the superconducting film, which can move using the energy of the circulating microwave photons and acts as a source of dissipation [136]. Therefore, to reduce the effects of an external magnetic field on the superconducting resonator, it is important to reduce the density of vortices and/or to prevent them from moving using a vortex trap.

Broadly speaking, there are a few approaches one can take to minimize the superconducting resonator degradation from the external magnetic field. The first is the orientation of the magnetic field with respect to the resonator plane. Magnetic fields that are out-of-plane with respect to the planar superconducting microwave resonator tend to degrade the quality factor of the microwave resonator much more quickly compared to magnetic field that are in-plane [137]. Secondly, one can chose a material with a large critical magnetic field value so even without any geometry ploys, one can still can still repel magnetic fields. See Table 4.1 for the critical field values of some common superconducting film materials.

Lastly, one can design the geometry of the superconducting resonator to make the resonator more resilient to magnetic fields. It has been shown that thinner superconducting films and narrower superconducting traces are more resilient [138–140]. The critical in-plane magnetic field in the thin film limit is $B_{c,||} = 2\sqrt{6}\frac{B_c\lambda}{t}$, where t is the film thickness [140]. The threshold field for vortex expulsion is $B_o = \frac{\pi}{4}\frac{\Phi_o}{w_\mu^2}$, where $\Phi_o = \frac{h}{2e}$ and w_μ is the trace width [138]. This suggests that even if the critical field of the material is not too large, no vortices will form in the superconducting traces if the trace widths are sufficiently narrow. However, it is worth noting that the ground plane can still have vortices, which may cause dissipation if there is sufficient current flowing in those regions.

One can also add vortex traps (effectively holes in the superconducting film) to improve the magnetic field induced quality factor [141, 142], however if too many holes are introduced, the quality factors can also decrease from increased dielectric losses at the superconductor's surface [143].

Using the approaches listed above, it has been shown that superconducting microwave resonators can achieve quality factors above 100,000 with in-plane magnetic fields above 100 mT [136, 137, 144–146]. Although these resonators have fairly extreme geometries (i.e. very thin films and narrow trace widths) that may not be best suited for our REI transducer, but do show that high-Q thin-film superconducting microwave resonators are achievable.

Kinetic Inductance

Another important parameter of the superconducting resonator is the kinetic inductance or the kinetic inductance fraction. The kinetic inductance fraction, α, can be defined as:

$$\alpha = \frac{L_k}{L_m + L_k} \tag{4.8}$$

where L_k is the kinetic inductance per unit length and L_m is the magnetic inductance per unit length. Kinetic inductance arises from the kinetic energy stored in the supercurrent of Cooper pairs [147]. Importantly, the kinetic inductance is not associated with the magnetic field that persists outside the superconductor, which means that the kinetic inductance of the superconductor acts as a *parasitic inductance* when we are trying to use the magnetic inductance to couple to the ions in the transducer. Therefore, it is important that our kinetic inductance fraction is small so that we can still couple to the erbium ion spin transitions with the superconducting resonator's magnetic field.

In order to calculate the kinetic inductance fraction, we need to determine both the magnetic inductance and the kinetic inductance, which can be derived from their respective inductive energy equations. The energy stored in the magnetic inductance per unit length is [148]:

$$E_m = \frac{1}{2} L_m I^2 = \frac{1}{2}\mu_0 \int \mathbf{H} \cdot \mathbf{H}^* dA. \tag{4.9}$$

Therefore the magnetic inductance per unit length is:

$$L_m = \frac{\mu_0 \int \mathbf{H} \cdot \mathbf{H}^* dA}{I^2}. \tag{4.10}$$

This magnetic inductance will depend on the geometry, but for reference the magnetic inductance per unit length for a co-planar waveguide can be derived from a conformal-mapping technique to be [149]:

$$L_m = \frac{\mu_0 K(k')}{4K(k)} \tag{4.11}$$

where K is the complete elliptic integral of the first kind, $k = \frac{w_\mu}{w_\mu + 2g_\mu}$ and $k' = \sqrt{1-k^2}$. The parameter, w_μ, is the co-planar waveguide center strip width and g_μ is the gap between the center strip and the ground plane. This expression can be approximated to be $L_m \approx \frac{\mu_0}{2\pi}(\ln(4/k) - (k/2)^2)$ for small k or approximated to be $L_m \approx \frac{\pi\mu_0}{4}/\ln(\frac{8w_\mu}{2g_\mu})$ when k approaches unity [150].

The energy stored in the kinetic inductance per unit length is [151, 152]:

$$E_k = \frac{1}{2} L_k I^2 = \frac{1}{2}\mu_0 \lambda^2 \int j^2 dA \tag{4.12}$$

where j is the current density and λ is the penetration depth. The kinetic inductance for unit length is then:

$$L_k = \frac{\mu_0 \lambda^2 \int j^2 dA}{I^2}. \tag{4.13}$$

From this equation, we can see there are contributions to the kinetic inductance from material properties from λ and also the geometry from the term $\frac{\int j^2}{I^2} dA$.

The penetration depth relates to the surface impedance of the superconductor as $Z_s = R_s + i\omega\mu_0\lambda$, where Z_s is the surface impedance and R_s is the surface resistance [124]. λ refers to the length-scale at which magnetic fields exponentially decay into the superconductor. Calculating λ in general is not simple, but analytical equations exist for certain limits. For instance, in the local limit [153]:

$$\lambda = \sqrt{\frac{\bar{\rho}_N}{\pi \Delta \mu_0}} \tag{4.14}$$

where ρ_N is the normal state resistivity and Δ is the superconducting energy gap.

We can simplify Equation 4.13 for two limiting cases of a superconducting strip [152]. First, in the limit that $w_\mu \gg t \gg \lambda$, where w_μ is the superconducting strip width and t is the thickness, the kinetic inductance per unit length is:

$$L_k = \frac{1}{2} \frac{\mu_0 \lambda}{w_\mu}. \tag{4.15}$$

Alternatively, in the limit that $w \gg \lambda \gg t$, the kinetic inductance per unit length is:

$$L_k = \frac{\mu_0 \lambda^2}{w_\mu t}. \tag{4.16}$$

As stated above, for the REI transducer we want to minimize the kinetic inductance fraction. This requires, in part, that the superconducting film thickness, t, is sufficiently large compared the penetration depth, λ. Also, as w_μ and g_μ increase, the kinetic inductance fraction also decreases. Therefore, generally speaking, devices with larger dimensions in the cross-section will have a smaller kinetic inductance fraction and using materials with smaller penetration depths will also result in a smaller kinetic inductance fraction.

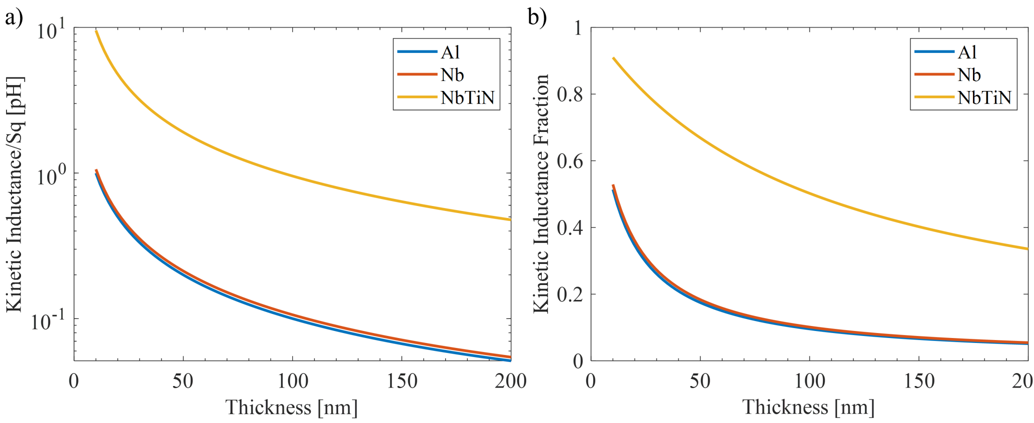

Figure 4.2: a) Kinetic inductance per square and b) the kinetic inductance fraction of different superconducting film materials as a function of the film thickness.

In Figure 4.2, we show the kinetic inductance per square and kinetic inductance fraction of aluminum, niobium and NbTiN films. To determine the kinetic inductance fraction, we obtain the geometric inductance of a co-planar waveguide with $w_\mu = 1$ μm and $g_\mu = 10$ μm. We can see that aluminum and niobium both have similarly low kinetic inductance fractions for relatively thick films (i.e. $t \gg 100$ nm), while the kinetic inductance fraction of NbTiN is substantially higher due to the larger penetration depth.

Microwave Resonator Material of Choice

For our REI transducer, we decided to use a niobium microwave resonator, which generally gives a respectable balance for all the figures of merit. Compared to aluminum, niobium should have significantly better performance in magnetic fields and under optical photon illumination, while it should have a similarly low kinetic inductance fraction. Aluminum should be easier to fabricate, since film-stress is less detrimental to the superconducting film quality and the oxide is less complicated and lossy. This allows aluminum to be deposited using evaporation or sputtering and does not require as much deposition parameter optimization. Conversely, niobium films can suffer more significantly from film-stress and impurity defects, which requires more work to fine tune the deposition parameters. However, we have the infrastructure to do this, so it was not a significant limitation for us.

Compared to niobium alloys (i.e. NbTiN or NbN), niobium resonators will have a smaller kinetic inductance fraction for the same geometry. The performance under optical illumination should be relatively similar since both exhibit very fast quasi-particle recombination rates. The niobium alloys should perform better in magnetic fields compared to niobium devices due to their higher critical field values. Also, niobium alloys are trickier to fabricate compared to niobium and require fine tuning of a reactive sputtering process. If we require very high microwave quality factors in a magnetic field or require to work in very high magnetic fields (i.e. $\gg 100$ mT), then NbTiN may become a much more attractive candidate.

Microwave Resonator Geometry

For the microwave resonator geometry, we took inspiration from previous works for coupling low impedance lumped-element microwave resonators to spins [154–157]. The general idea is to have a narrow superconducting wire which can act as the *inductor* of the resonator and have a interdigitated capacitor shunt this wire with a certain capacitance to obtain the desired resonance frequency. The circuit is designed to confine the magnetic field/inductance of the resonator to the wire and minimize the *parasitic inductance* of the interdigitated capacitor or, in other words, increasing the self-resonance of the capacitor.

Our geometry requires a few modifications from the previous works referenced. Firstly, in more recent works they are working with very narrow inductive wires ($w_{ind} < 1\mu$m), which may challenging in an REI transducer where optical power is required to be circulating nearby. In our geometry, we kept the inductive wire $w_{ind} > 1\mu$m for this reason. Secondly, they have their interdigitated capacitor on both sides of the inductive wire. Since we will have an optical circuit on one side of the inductive wire, we only have the interdigitated capacitor on one side of the inductive wire.

4.3 Optical Cavity Modelling

The optical cavity for the transducer consists of two photonic crystal mirrors separated by an optical waveguide. The photonic crystal mirrors are formed by patterning the amorphous silicon waveguide to form a photonic bandgap. There are several useful equations to describe our Fabry-Perot cavity that we can introduce [158].

The round-trip lifetime is $\tau_{RT} = \frac{2n_g L_o}{c}$, where n_g is the group index of the waveguide, L_o is the length of the cavity and c is the speed of light. The free-spectral range is $\Delta\nu = \frac{1}{\tau_{RT}}$. The cavity decay rate from the mirrors is $\kappa_{o,m} = \sum_i -\frac{\ln(R_i)}{\tau_{RT}}$, where R_i is the mirror reflectivity of mirror i. When we are coupling through a single mirror, we can define $\kappa_{o,in} = -\frac{\ln(R_{in})}{\tau_{RT}}$.

In practice the cavity mirrors may have some small scattering losses associated with them and we can model the scattering decay rate as $\kappa_{o,s_i} = -\frac{\ln(1-S_i)}{\tau_{RT}}$, where S_i is the scattering of the mirror. The cavity decay rate for propagation loss is $\kappa_a = \frac{\alpha c}{n_g}$, where α is the propagation decay constant, which can include both scattering or absorption losses from the waveguide. We can relate the cavity decay rate to a quality factor using $Q_i = \frac{\omega}{\kappa_i}$.

In order to have a high quality Fabry-Perot cavity, it is important to reduce both the mirror scattering losses and also to minimize the propagation losses of the waveguide between the mirrors. The propagation losses of the waveguide will be a result of the quality of the amorphous silicon films and the etching of the waveguides. The mirror scattering will be determined by the photonic crystal mirror design and also the fabrication process.

Another aspect of the optical cavity is the coupling to the rare-earth ion optical transitions. Since we are working with an amorphous silicon optical resonator on the Er^{3+}:YVO_4 surface, we are relying on evanescent coupling. Depending on the orientation of the optical dipole moment of the optical transition of interest, we will need to design a transverse-electric (TE) or transverse-magnetic (TM) polarized cavity. For Z_1-Y_1 transduction, we are interested in coupling to the σ_{MD} ($B_o \parallel c$) polarized transitions, which couple to the magnetic field of a TM mode resonator.

The optical cavity was simulated using COMSOL. The optical waveguides in the middle of the cavity were simulated using the 2D cross-section mode analysis. For simulating the photonic crystal mirrors, a combination of 3D band structure simulations of the individual unit cells and frequency domain analysis was done for the entire photonic crystal mirror.

The refractive index of YVO_4 was assumed to be 2.15 (1.95) along the c (a) crystal axis and the refractive index for amorphous silicon was assumed to be 3.45. The amorphous silicon is made in the lab here at CalTech and the precise refractive index at cryogenic temperatures is not precisely known. However, in the fabrication we can slightly bias certain geometric parameters of the photonic crystal mirrors (i.e. waveguide width and hole radii) to compensate for small deviations in refractive index, which makes this uncertainty not a significant issue.

2D Optical Simulations

Given that most of the field of the optical resonator resides within the optical waveguide, we can determine most of the field profile of the resonator from a 2D simulation of the optical waveguide cross-section. We chose a waveguide width, w_o, of 600 nm to prevent higher order waveguide modes. The electric and magnetic fields of the fundamental TM optical waveguide mode are shown in Figure 4.3. For coupling to the erbium optical transitions, we use the evanescent field that penetrates into the YVO_4 substrate. We can increase the amount of the field that penetrates into the YVO_4 substrate by decreasing the height of the amorphous silicon waveguide.

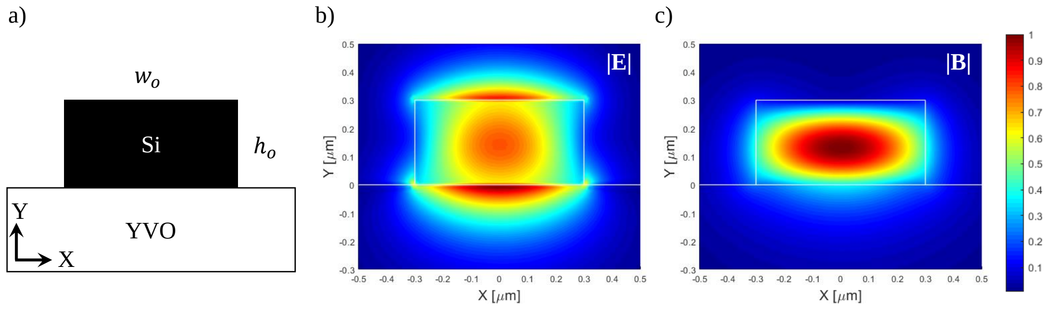

Figure 4.3: a) Cross section of the amorphous silicon optical waveguide on a YVO_4 substrate. b) The normalized electric field, |E|, and c) the magnetic field, |B|, are shown for the fundamental TM mode of the waveguide.

The waveguide effective index and group index of the TM mode as a function of the waveguide thickness are shown in Figure 4.4. The group index only accounts for waveguide dispersion and ignores the material dispersion. In order to have a well-confined optical mode, the effective index should be sufficiently higher than the substrate index. The group index is useful to determine the cavity free-spectral range.

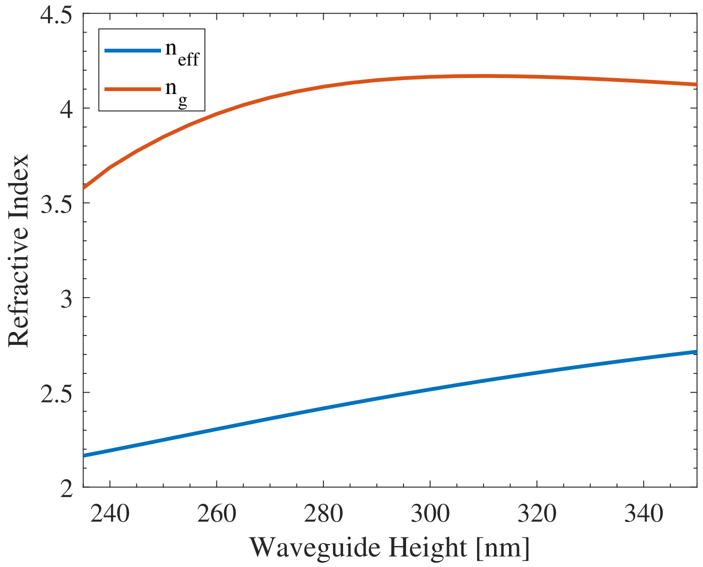

Figure 4.4: Effective index, n_{eff} and group index, n_g, of the amorphous silicon waveguide on the YVO_4 substrate as a function of the amorphous silicon waveguide height.

The waveguide height is important for determining the mode overlap term of the transduction efficiency. The contribution of the waveguide height to the mode overlap can be determined from Equation 4.3 and is shown in Figure 4.5. Here the magnetic dipole orientation is along the c-crystal axis (x-axis for position in Figure 4.3), so we consider the energy within the B_x magnetic field component. The electric field along the y-direction is also shown as it will be used later on.

We chose to use a waveguide height of 300 nm as a conservative value. By reducing the height, the energy fraction can increase by a factor of ~2-3x, however in this case the mode confinement becomes significantly less. This will likely reduce the quality factor of the resonator as the field intensity at the material surface will increase. Also it is more challenging to design large band gap, low loss photonic crystal mirrors as the height decreases. 300 nm was a conservative place to start and potential future devices can push limit further for potential improved performance.

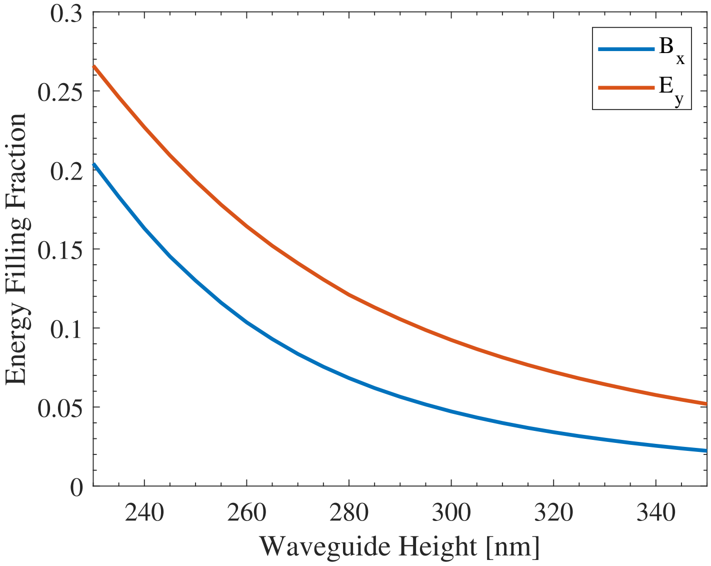

Figure 4.5: Filling factor of the TM magnetic energy along the c-axis (x-direction) and the TM electric field energy along the a-axis (y-direction) as a function of the waveguide height.

3D Optical Cavity Simulations

In this section, we look at the 3D optical cavity simulations with a main focus on the photonic crystal mirrors. One additional parameter introduced in the 3D simulations is the waveguide length between the two photonic crystal mirrors. Increasing the waveguide length will help match the modes between the optical modes and the microwave modes and in the limit of losses limited by the mirror, increasing the length of the cavity will increase the quality factor. However, as we increase the length, the optical Rabi frequency decreases and the free spectral range of the optical cavity decreases. We decided to use a waveguide length of 100 μm as a balance between these different factors.

Our photonic crystal mirrors consist of a one dimensional lattice of ellipse holes that are patterned into the amorphous silicon waveguide. The hole size and lattice spacing is tapered at the edges to reduce scattering with the waveguide component as shown in Figure 4.6. The mirror period is denoted by a_0 and the two ellipse radii are labelled $r_{\|,0}$ & $r_{\perp,0}$. The mirror period and radii are linearly tapered over N_t tapering periods to a final period of a_t and ellipse radii of $r_{\|,t}$ & $r_{\perp,t}$.

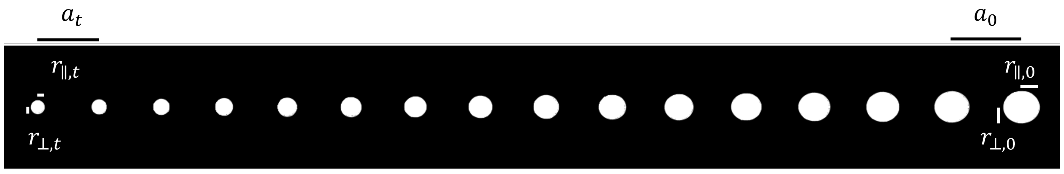

Figure 4.6: The photonic crystal mirror parameters including the mirror period and radii and the final taper period and radii.

We first design the mirror parameters to have a large photonic bandgap centered at the erbium $Z_1 - Y_1$ optical transitions, as shown in Figure 4.7. The red line refers to the erbium $Z_1 - Y_1$ optical transitions, the dotted black line is the light line and the two blue lines are the optical modes. The geometric parameters are set to a_0 = 350 nm, $r_{\parallel,0}$ = 95 nm and $r_{\perp,0}$ = 105 nm in order to get a band gap of 5.89 THz (~46 nm). A large bandgap is helpful to reduce the number of periods required for the mirror and also provides a larger fabrication tolerances as there will be more cavity modes that can be used even if the bandgap center is detuned from the $Z_1 - Y_1$ optical transitions.

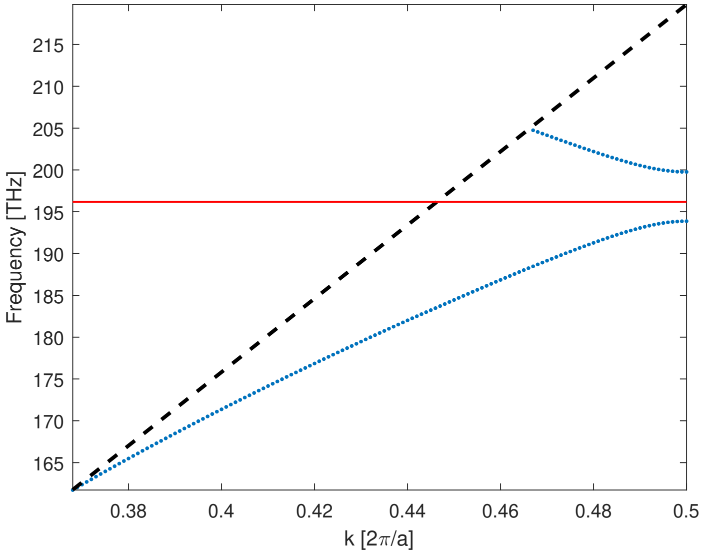

Figure 4.7: Bandstructure of the photonic crystal mirror. The blue points are the modes that can propagate through the photonic crystal, the black dotted line is the light line (i.e. $2\pi f = c \cdot k$) and the red line is the Z_1-Y_1 optical transition frequency for reference.

Once we have the cavity mirror determined, we designed the taper to minimize the scattering from the cavity waveguide mode and the cavity mirror mode. This tapering was done linearly over $N_t = 15$ periods to a final period of $a_t = 315$ nm and ellipse radii of $r_{\|,t} = r_{\perp,t} = 20$ nm. In order to change the mirror reflectivity, we can change the number of periods of the mirror holes. We want to have one mirror with a smaller reflectivity to allow us to couple into the cavity efficiently and a second mirror with high reflectivity to reduce any transmission losses from that mirror.

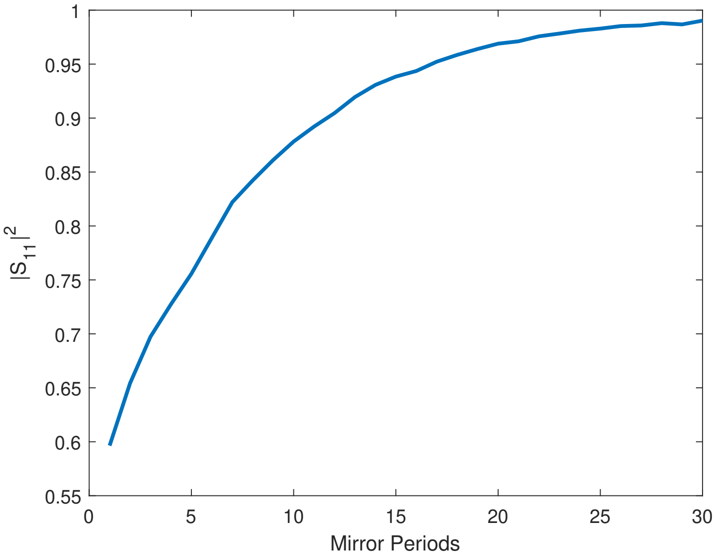

Figure 4.8: Mirror reflectivity as a function of the number of the mirror periods, N_m.

We first sweep the number of mirror periods and plot the mirror reflectivity in Figure 4.8 at the $Z_1 - Y_1$ optical transition wavelength. We then assign $N_m = 2$ and $N_m = 25$ for the low and high reflectivity mirrors to obtain a mirror reflectivity of 65% and 98%, respectively.

In order to characterize the mirror, we can look at the mirror S-parameters as a function of optical wavelength to determine the mirror reflectivity and also the losses. The S-parameters of the high reflectivity mirror are shown in Figure 4.9a. We observe peak reflectivity of 98.4% and a FWHM of 6.7 THz (52.5 nm). The S-parameters of the low reflectivity mirror are shown in Figure 4.9b. We observe peak reflectivity of 65.7% and a FWHM of 7 THz (55 nm).

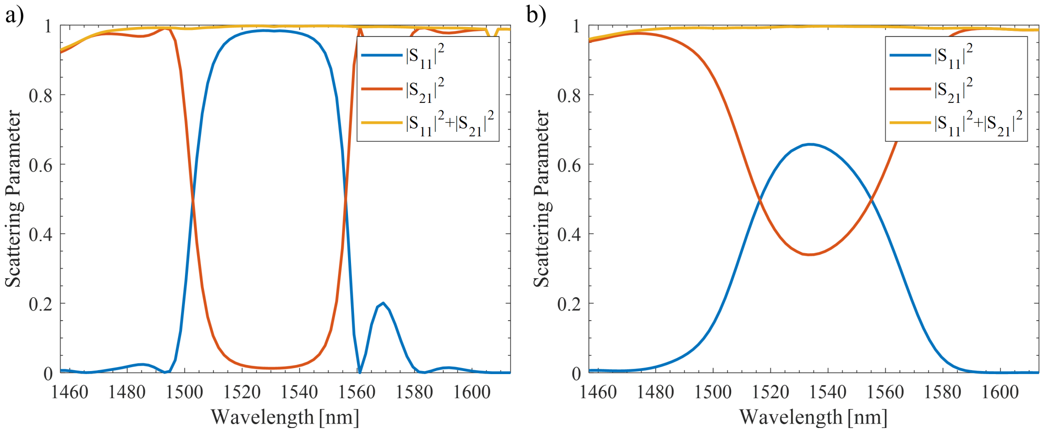

Figure 4.9: Scattering parameters for a) the high reflectivity photonic crystal mirror and b) the low reflectivity photonic crystal mirror.

Table 4.2: Optical cavity geometry parameters

Parameter	Value
Waveguide Height	300 nm
Waveguide Width	600 nm
Waveguide Length	100 μm
a_0	350 nm
$r_{\parallel,0}$	95 nm
$r_{\perp,0}$	105 nm
a_t	315 nm
$r_{\parallel,t}$	20 nm
$r_{\perp,t}$	20 nm
Mirror Periods	2, 25
Taper Periods	15

We can also quantify the mirror coupling quality factor (i.e. from the mirror transmission) and the mirror scattering quality factor for each mirror as shown in Figure 4.10. The mirror scattering quality factor is similar for both mirrors and ranges from $Q_{o,s} \approx 10^5 - 10^6$ depending on the wavelength. The low reflectivity mirror has a coupling quality factor of $Q_{o,in} \approx 10^4$ and the high reflectivity mirror has a maximum coupling quality factor of $Q_{in} \approx 10^5$. Given the limits of our fabrication, we do not expect these scattering losses of the design to be the limiting factor on the device quality factor and these values exceed the target quality factor of 10,000.

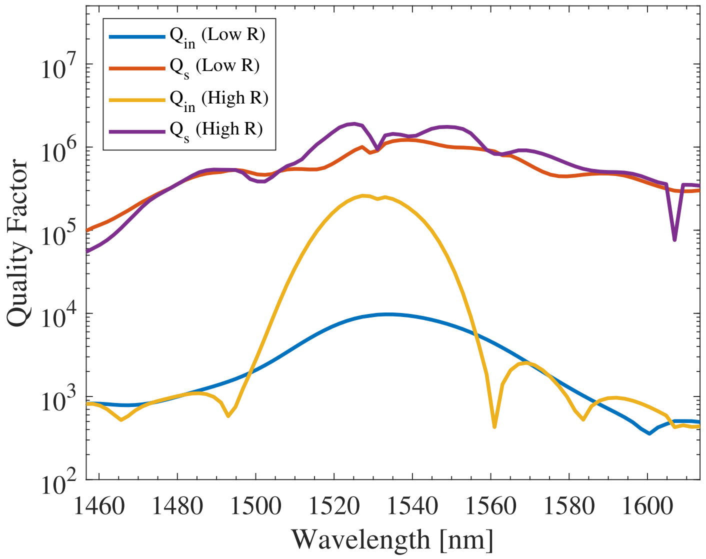

Figure 4.10: Quality factors of the high reflectiviy and low reflectivity mirrors for the optical cavity. $Q_{o,in}$ corresponds to the cavity decay rate via transmission through the mirror, while $Q_{o,s}$ corresponds to scattering losses from the mirror.

After characterizing the cavity mirrors and their theoretical quality factors, we can determine the parameters of the full optical cavity by simulating the full cavity (i.e. mirrors and 100 μm waveguide). The electric and magnetic fields of the cavity mode look like the waveguide mode in the center and the amplitude decays at the mirrors. The mode volume of the cavity is 7.6 μm^3 and an FSR of 350 GHz.

Due to the exponentially decaying electromagnetic fields within the YVO_4 substrate, the ion-cavity coupling strength is highly position dependent and can be calculated using Equation 1.1. The distribution of the single ion coupling strengths is shown in Figure 4.11 for the stronger optical dipole moment transition (i.e. $|-\rangle_g \leftrightarrow |-\rangle_e$, which is also denoted by a subscript, $\|$). The binsize is 0.0147 dB as the histogram is in logarithmic scale. There are many ions with small coupling strengths from the evanescent tail of the optical field.

We define the number of ions as the ions with the largest coupling rates that make up 99.9% of the total ensemble coupling. When modelling the system, we want to include as many ions within the transducer as possible to have the highest efficiency in the simulation. By this definition, we calculate the total number of ions to be $N_o \sim 2.1 \cdot 10^8$. Alternatively, if we define the number of ions as the $N \sim V_o \cdot \rho$, we estimate $\sim 4.1 \cdot 10^7$ ions in the cavity.

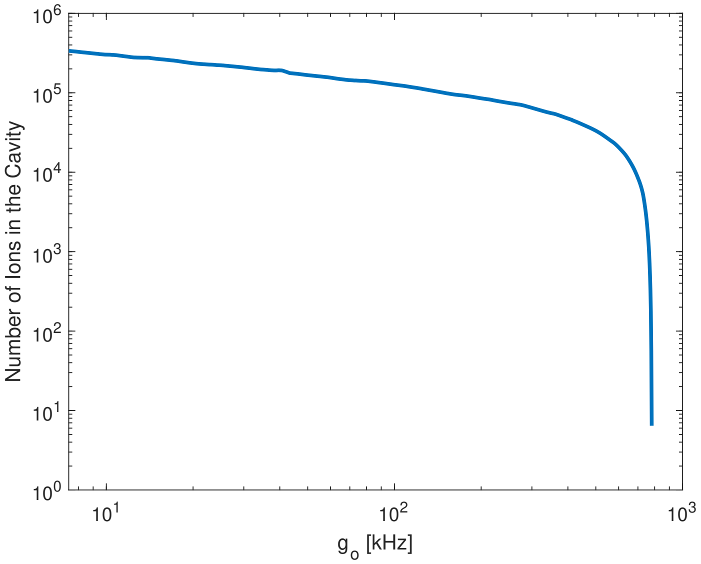

Figure 4.11: Histogram of the single ion coupling rate between the ions and the optical cavity. Each bin size is 0.0147 dB.

The maximum single ion coupling strength for transition $|-\rangle_g \leftrightarrow |-\rangle_e$ is $g_{o,max,\|}/(2\pi)$ = 783 kHz and for transition $|-\rangle_g \leftrightarrow |+\rangle_e$ is $g_{o,max,\perp}/(2\pi)$=115 kHz for the magnetic dipole moment along the a-axis. The subscripts on the state denote the ground and excited states. The ensemble coupling rate for transition $|-\rangle_g \leftrightarrow |-\rangle_e$ is $g_{o,tot,\|}/(2\pi)$=1.17 GHz, while the ensemble coupling rate for transition $|-\rangle_g \leftrightarrow |+\rangle_e$ is $g_{o,tot,\perp}/(2\pi)$=172 MHz for the magnetic dipole moment along the a-axis.

We can also account for the coupling to the other dipole moment directions, which will appear when we measure the ion-cavity coupling in experiment. The ensemble coupling rate for transition $|-\rangle_g \leftrightarrow |-\rangle_e$ is 1.85 GHz, while the ensemble coupling rate for transition $|-\rangle_g \leftrightarrow |+\rangle_e$ is 585 MHz if we account for all dipole moments and all directions of the optical cavity field.

We can also calculate the figures of merit for the transduction efficiency, $F_G = F_o \Omega_F$. The mode overlap figure of merit, $F_o = 4.14 \cdot 10^{-10}\mathrm{m}^{3/2}$ and the Rabi frequency term, $\Omega_F = 1.31 \cdot 10^{-4}\mathrm{m}^{-3/2}$, such that the total figure of merit of the optical cavity, $F_G = 0.0542$.

Table 4.3: Simulated optical cavity parameters

Parameter	Value
Mirror Scattering Q, $Q_{o,s}$	10^5
Mirror Reflection Q, $Q_{o,in}$	$10^4(10^5)$
Mode Volume	$7.6\mu m^3$
FSR	350 GHz
F_G	0.0542
# of Ions, N_o	$2.1 \cdot 10^8$
$g_{o,max,\parallel} = 2\pi$	783 kHz
$g_{o,max,\perp} = 2\pi$	115 kHz
$g_{o,tot,\parallel} = 2\pi$	1.04 GHz
$g_{o,tot,\perp} = 2\pi$	153 MHz

The full optical cavity device is shown in Figure 4.12. Light can be coupled into the optical cavity from the grating coupler (labelled G1) such that we couple through the low reflectivity mirror. The second grating coupler, labelled G2, is to allow for room temperature transmission measurements, but is not used once the device within the dilution fridge. The waveguide bend radius is 10 μm to ensure the waveguide is low loss. The grating coupler, G1, is tilted at angle of 40 degrees from the cavity section such that it is horizontally aligned when mounted in the fridge. The whole chip will be mounted at an angle to accommodate the magnetic field orientation that needs to be generated on the chip.

Figure 4.12: CAD image of the full optical cavity device including the two photonic crystal mirrors with a 100 μm waveguide in between. Two grating couplers are used for coupling into the cavity.

4.4 Microwave Cavity Modelling

Modelling of the microwave cavity was done in both COMSOL and Sonnet. The microwave cavity geometry consists of a narrow inductive wire that is shunted by an interdigitated capacitor, such that the magnetic field can be confined to the inductive wire that is patterned next to the optical cavity (see Figure 4.13).

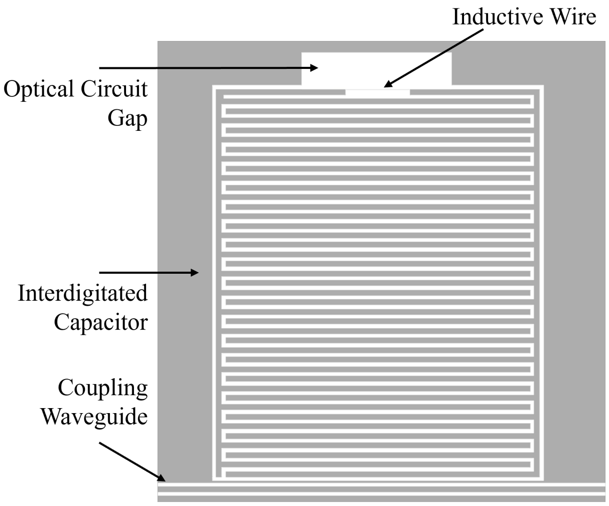

Figure 4.13: CAD image of the microwave resonator including the inductive wire next to the optical circuit, the interdigitated capacitor and the coupling waveguide.

Table 4.4: Microwave cavity geometry parameters

Parameter	Value
Inductive Wire Length, L_{ind}	100 μm
Inductive Wire Width, W_{ind}	1 μm
Capacitor Finger Length, L_{cap}	485 μm
Capacitor Finger Width, W_{cap}	10 μm
Capacitor Finger Gap, G_{cap}	5 μm
Capacitor Finger Number, N_{cap}	20
Optical Gap Width, $G_{o,w}$	235 μm
Optical Gap Height, $G_{o,h}$	55 μm
Waveguide Coupling Gap, $G_{wg,cou}$	4 μm
Waveguide Width, W_{wg}	10 μm
Waveguide Gap, G_{wg}	4.5 μm

The cavity geometry parameters are summarized in Table 4.4 and are shown in Figure 4.14. The length of the inductive wire length is 100 μm to match the length of the optical cavity and the inductive width is 1 μm. In order to change the resonance frequency of the microwave cavity, the length of the capacitor fingers and the number of capacitor fingers was adjusted, but the resonator that was used for the main experiments has its parameters in the Table 4.4. On a given sample, we fabricated 10 resonators and tune their resonance frequencies ~200-300 MHz apart from each other, such that they would span ~4.5-7 GHz.

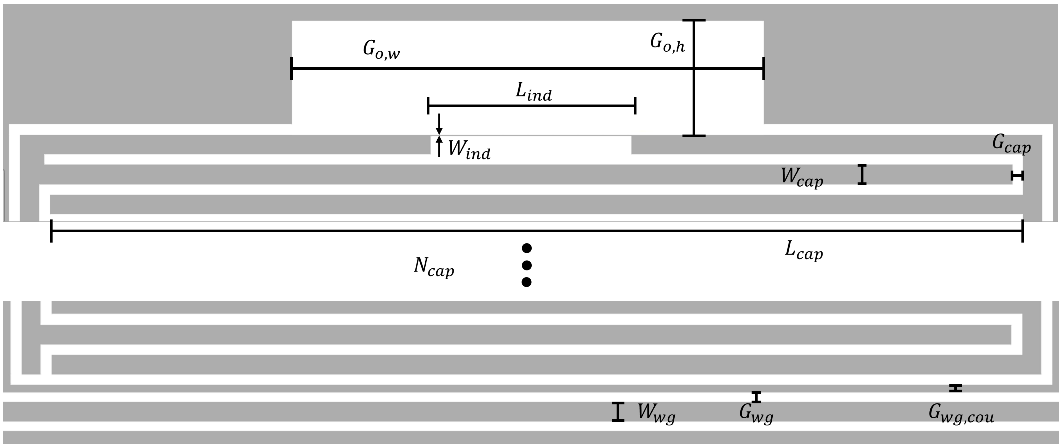

Figure 4.14: The geometric parameters that define the pattern of the microwave resonator including the parameters related to the inductive wire, the interdigitated capacitor, the coupling waveguide and the gap for the optical resonator.

The microwave cavity was modelled in COMSOL to determine the electromagnetic fields of its fundamental resonance mode. The normalized magnetic field distribution in log-scale is shown in Figure 4.15. In Figure 4.15a, the magnetic field is shown of the device plane, where the magnetic field is mostly confined to the inductive wire and the regions of the capacitor that are nearby. The maximum magnetic field is confined to the inductive wire (Figure 4.15b). The black line is a guide to the eye of the location of the optical resonator, where the magnetic field is near its peak value. We can also look at the cross-section of the mode in Figure 4.15c and see how the magnetic field strength decays away from the inductive wire.

From the magnetic field distribution, we can calculate a few different parameters. First, we determine the magnetic field mode volume to be 156 μm^3. Next, we can simulate how the magnetic field decays as a function of the distance from the inductive wire (Figure 4.16). The optical resonator will reside next to the inductive wire, so we can see how much we can improve by decreasing the distance between the inductive wire and the optical resonator. We observe a $B/B_{max} \sim 1/D$, where D is the distance from the inductive wire.

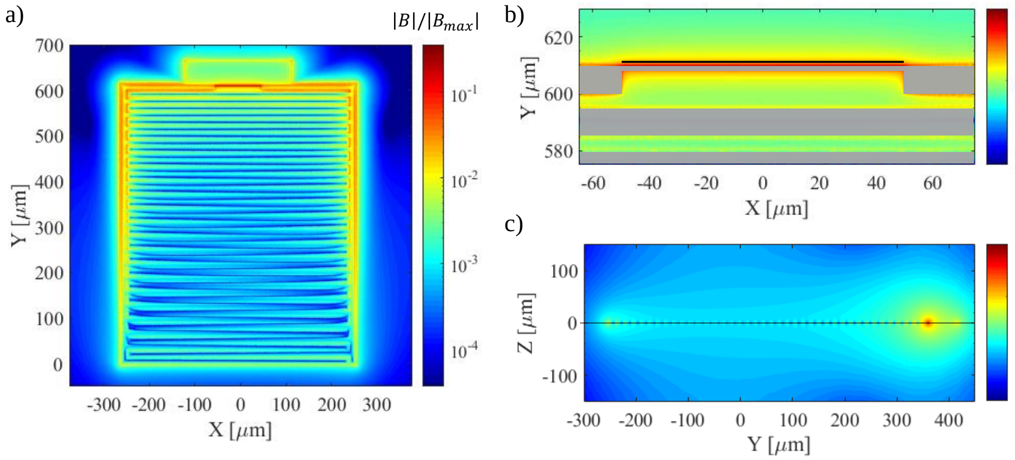

Figure 4.15: The normalized magnetic field distribution of the microwave resonator. a) The in-plane magnetic field distribution in the plane of the niobium resonator itself. b) A closer look at the magnetic field distribution near the inductive wire. The black line indicates the location of the optical resonator for reference. c) The cross-section of the microwave resonator magnetic field.

For our devices, we choose to center the optical cavity waveguide 1.5 μm away from the inductor (i.e. the nearest edges of the optical waveguide and the superconducting resonator is 1.2 μm apart), which results in a value of $B/B_{max} = 0.043$. In principle, we can decrease the gap and increase the microwave resonator magnetic field at the optical resonator, but we did not want to push this too extreme. If the distance between the two is too close, the niobium will induce optical losses on the optical resonator, the optical resonator losses will induce more quasi-particles in the superconductor and the fabrication process may start to get a bit trickier.

The next thing we can look at is the histogram of the different ion-cavity coupling rate to the Z_1 ground state spin as shown in Figure 4.17. The coupling rate bin size is 0.0086 dB. The ions right at the surface of the superconducting have a maximum coupling rate of $g_{\mu,max}/2\pi = 5.8$ kHz, while the ions at the position of the optical cavity have a coupling rate of $g_{\mu,o}/2\pi = 255$ Hz (as denoted by the red dotted line in the Figure 4.17). The excited state spins have a dipole moment that is $\mu_{21,Y_1} = 0.65\mu_{21,Z_1}$ for the out-of-plane magnetic field component, so the excited state spin coupling rates can be scaled by that factor.

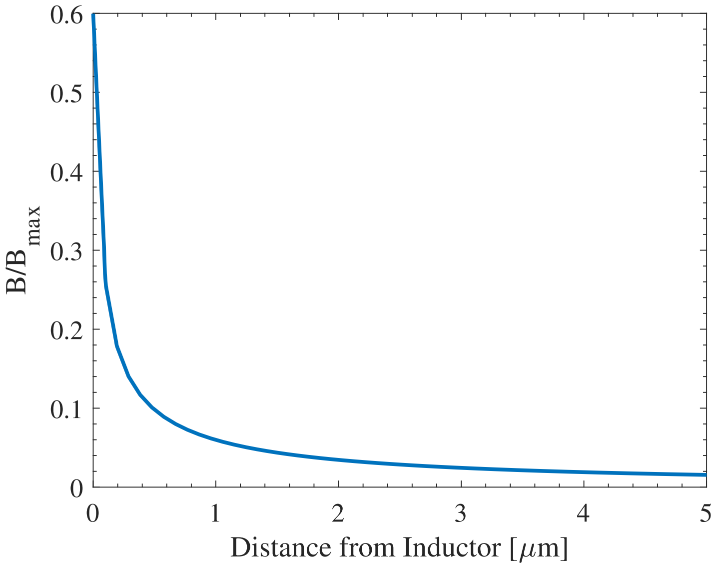

Figure 4.16: Microwave resonator normalized magnetic field strength as a function of the distance from the inductive wire.

Again, we define the number of ions as the ions with the largest coupling rates that make up 99.9% of the total ensemble coupling. This corresponds to $\sim 1.64 \cdot 10^{15}$ ions within the microwave cavity. Alternatively, if we define the number of ions as the $N \sim V_\mu \cdot \rho$, we estimate $\sim 8.4 \cdot 10^8$ ions in the cavity. This suggests that there are a lot weakly coupled ions to the microwave cavity.

The ensemble coupling between the ground state spin to cavity is calculated to be 120 MHz, where we have included contributions for all magnetic field directions and the associated dipole moments of the spin along each direction. 83 MHz of this coupling is along the out-of-plane direction. We expect there to be $\sim 2.1 \cdot 10^8$ ions within the optical cavity so the coupling of these spins to the microwave cavity is $\sim$ 3.6 MHz.

For the Y_1 excited state spin, we calculate a total ensemble coupling of 91 MHz with 53 MHz coming from the out-of-plane component. The contribution from ions within the optical cavity is ~2.3 MHz.

We can use the electromagnetic field distribution to determine the transduction figure of merit that relates to the microwave cavity as shown in Equation 4.1 and get $F_\mu = 3.55 \cdot 10^6$ m$^{-3/2}$.

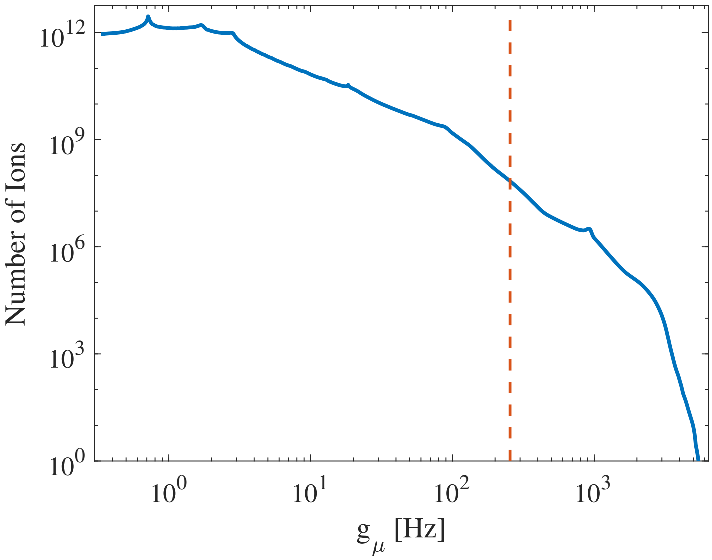

Figure 4.17: Histogram of the single ion coupling rate between the ions and the microwave cavity. Each bin size is 0.0086 dB. The red line indicates the coupling rate for the ions that are also positioned within the optical cavity.

We can also define the more canonical circuit parameters of the lumped element microwave resonator. We can model the resonator as typical LC resonator, where the inductance has contributions from the inductive wire, L_{wire}, and a parasitic inductance from the interdigitated capacitor, $L_{parasitic}$, such that $L = L_{parasitic} + L_{wire}$. The circuit parameters were determined in Sonnet by adding ideal lumped element components into the model, measuring the shift in the resonance frequency and using $\omega_{\mu,0} = \frac{1}{\sqrt{LC}}$, where $\omega_{\mu,0}$ is the resonance frequency, L is the inductance and C is the capacitance of the resonator.

From simulation, we determine that L = 964 pH, L_{wire} = 208 pH, $L_{parasitic}$ = 756 pH and C = 839 pF. This results in a characteristic impedance of $Z_0 = \sqrt{\frac{L}{C}} = 33.9$ Ω. The inductance fraction within the inductive wire (i.e. L_{wire}/L) is only 22% due to the parasitic inductance of the interdigitated capacitor. Reducing this parasitic capacitance would result in a smaller magnetic mode volume and increase the coupling rate of the spins to the microwave cavity.

Table 4.5: Simulated microwave cavity parameters

Parameter	Value
Magnetic Mode Volume, V_μ	156 μm^3
Spin-coupling rate at optical cavity $g_{\mu,o}/2\pi$	255 Hz (166 Hz)
$g_{\mu,max}/2\pi$	5.6 kHz (3.6 kHz)
Total spin-coupling rate, $g_{\mu,tot}$	120 MHz (91 MHz)
Inductance	964 pH
Capacitance	839 pF
Impedance	33.9 Ω
$L_{wire}/L_{parasitic}$	0.22
Coupling Q, $Q_{\mu,in}$	10414
F$_\mu$	$3.55 \cdot 10^6$m$^{-3/2}$

In Sonnet, we also simulated the coupling quality factor (or coupling capacitance) of the coplanar waveguide. There is a ground plane in between the waveguide and resonator, $G_{wg,cou}$ = 4 μm, to tune the coupling between the two. From simulation, we determine a coupling quality factor to be $Q_{\mu,in}$ = 10414. The coplanar waveguide is a convenient way to couple to the resonators as we can frequency multiplex several resonators. However, this does reduce the device efficiency by up to 2x as the microwave cavity cannot exceed critical coupling.

4.5 Transduction Efficiency Modelling

Now that we have our designs for the microwave and optical cavity, we can put them together as shown in Figure 4.18 with the optical cavity sitting next to the inductor of the microwave cavity. We also have the main spectroscopic parameters of Er^{3+}:YVO$_4$ that we need from Chapter 3, we can start to calculate the expected transduction efficiency of the device.

We do need to make a few assumptions at this point in order to calculate the efficiency. First, we need to assume the optical and microwave quality factors and how overcoupled the cavities are (i.e κ_{in}/κ). We set the microwave quality factors to be $Q_{\mu,in}$ = 10,000 and $Q_{\mu,i}$ = 10,000, where $Q_{\mu,in}$ accounts for coupling losses to both propagation directions of the microwave waveguide. We set the optical quality factors to be $Q_{o,in}$ = 10,000 and $Q_{o,i}$ = 20,000.

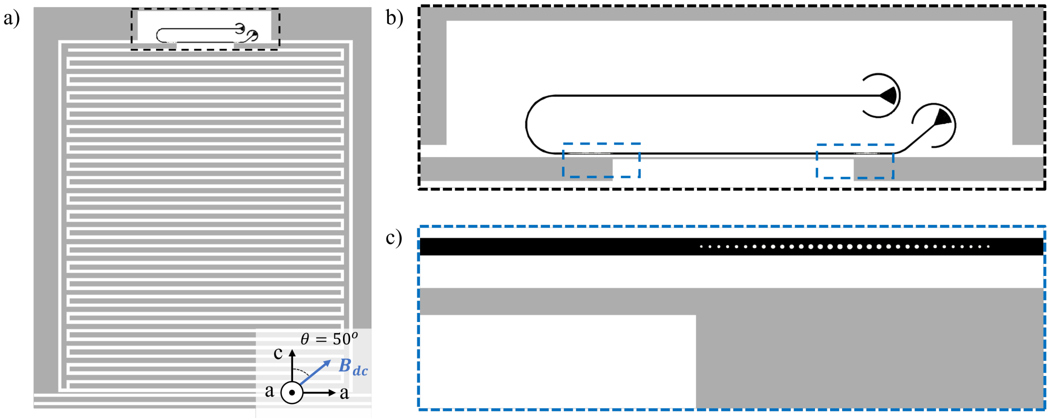

Figure 4.18: Schematic of a on-chip rare-earth ion transducer, where the microwave resonator inductive wire is patterned next to the optical cavity. The photonic crystal mirrors of the optical cavity are patterned by the end of the inductive wire. The YVO_4 crystal axis and the magnetic field angle relative to the microwave and optical patterns are highlighted.

We will assume that we can send in up to 100 μW of optical power for the pump. Using Equation 1.12, this would result in $\langle n \rangle = 9960$ for the case of the pump frequency detuned by 5 GHz from the optical cavity resonance. Also, we allow that all the experimentally flexible detunings (i.e. ion-cavity detunings and light-cavity detunings) are free parameters to optimize.

With that, we can use our different models to calculate the efficiency of the device. We will start with the adiabatic model, which is the easiest to calculate. We will also consider a few items within the context of this model for improving the efficiency.

Next, we will look at the linear numerical model where we can sweep more parameters to see the dependence on the efficiency. Here, much less assumptions are made, so we can take into more parameters of our device and see how that effects the efficiency.

Lastly, we will look at the iterative numerical model, which is similar to the linear numerical model, except we can now consider the effects of high input power, so we will look at that.

Adiabatic model

In order to calculate the efficiency from the adiabatic model, we use the equations from Chapter 2.1. We can determine the effective coupling strength, S, from $\alpha = 1.54 \cdot 10^{-10}$ (from Table 3.6 for 560 ppm erbium doping concentration), $F = F_\mu \cdot F_o = 9.5 \cdot 10^{-4}$ and $\Omega_{max} = \langle n \rangle \cdot g_{o,max} = 2\pi \cdot 11.5$ MHz, which gives us $S = 2\pi \cdot 6$ MHz. From S and our cavity quality factors, we can calculate $R = 0.011$ and give us an internal efficiency of $\eta_{int} = 4.6 \cdot 10^{-4}$ and a total efficiency of $\eta = 7.6 \cdot 10^{-5}$.

In terms of improving this efficiency within the adiabatic model framework, we can naively increase the cavity quality factors or increase the optical pump power to make $R = 1$ and reach an internal efficiency of unity.

We can also consider ways to improve the mode overlap term, F, and for that it is useful to consider a simpler form of Equation 2.14 that is more intuitive.

Mode Overlap Approximation

The mode overlap equation as originally presented in Equation 2.14 is a normalized integral over three parameters, which is not very intuitive to optimize, so it can be useful to further approximate it given our geometry and represent it in terms of more intuitive parameters.

In the most simplistic case, if we have spatially uniform modes, then the mode overlap is $F \approx \frac{V_o}{V_\mu}$, where we have assumed that the optical field is smaller than the microwave field. We can add an additional factor to account for the fact that not all of the optical energy of the mode is coupled to the ions by adding an optical energy filling factor term, such that $F \approx \frac{V_o}{V_\mu}\eta_m$, where we have assumed magnetic dipoles for the optical transitions. Lastly, if we can account for the spatial non-uniformity of the microwave mode by adding a term to relate the microwave mode field strength at the position of the optical cavity, we arrive at:

$$F = \frac{V_o}{V_\mu}\eta_m \frac{B(r_o)}{B_{max}}. \tag{4.17}$$

From Equation 4.17, we can see some intuitive ways to maximize the mode overlap. Firstly, we want the optical and microwave modes to have as similar mode volumes. This means we want to have a relatively large optical mode volume and minimize the microwave mode volume as much as possible. For the amorphous silicon optical resonators, we can increase the mode volume by making the cavity length longer. It is worth noting that increasing the optical mode volume will also decrease the optical Rabi frequency, so this is not the most straightforward way from improvements. For the microwave cavity, we can make the magnetic mode volume smaller by decreasing the parasitic inductance of the capacitor region within the resonator.

Secondly, we want to increase the optical mode filling factor, η_m, as much as possible, which means we want as much of the optical energy to be interacting with the rare-earth ions (see Figure 4.5). For the amorphous silicon hybrid resonators, this can be improved by decreasing the height of the amorphous silicon. This can be improved further by making the optical cavity directly out of YVO_4 instead of amorphous silicon, which should offer ~10x improvement in η_m.

Lastly, we want to have the optical resonator as close to the microwave resonator field maximum as possible (see Figure 4.16). Practically speaking, this corresponds to the distance between the microwave resonator inductor wire and the optical waveguide in the optical resonator. This distance cannot be too small as the metal film will induce losses in the optical cavity and the microwave cavity.

For our initial demonstrations, we did not try to improve the mode overlap further than the design detailed above, but there are ways to improve it as outlined above.

Transduction efficiency with Linear Numerical Model

As noted in Chapter 2, there are some limitations to the adiabatic model. These include neglecting dephasing or energy relaxation, parasitic spins and finite temperature. Also, it only applies to a far off-resonance case, which is not necessarily where the highest efficiency is expected to occur.

These limitations can be lifted by moving to a more general model. We will start with the linear numerical model, which is the regime that a quantum transducer should operate in (i.e. small cavity fields). The default parameters for the simulation are shown in Table 4.6.

Table 4.6: Simulation parameters

Parameter	Value
Temperature	100 mK
Optical lifetime	3.3 ms
Optical dephasing rate, $\gamma_{3d}/2\pi$	10 MHz
Optical inhomogeneous linewidth, Δ_o	300 MHz
Spin lifetime	1 ms
Spin dephasing rate, $\gamma_{2d}/2\pi$	10 MHz
Spin inhomogeneous linewidth, Δ_μ	65 MHz
Optical cavity coupling Q, $Q_{o,in}$	10,000
Optical cavity intrinsic Q, $Q_{o,in}$	20,000
Microwave cavity coupling Q, $Q_{\mu,in}$	10,000
Microwave cavity intrinsic Q, $Q_{\mu,in}$	10,000
Maximum optical pump Rabi frequency, $\Omega_{o,max}/2\pi$	11.5 MHz
Max optical ion cavity coupling, $g_{o,max}/2\pi$	783 kHz
Spin cavity coupling (ions in both cavities), $g_{\mu,o}/2\pi$	255 Hz (165 Hz)
Spin cavity coupling (other ions), $g_{\mu,p}/2\pi$	3.4 Hz (2.2 Hz)
Total spin cavity coupling, $g_{\mu,tot}/2\pi$	120 MHz (91 MHz)
Ions in optical cavity	$2.1 \cdot 10^8$
Ions in microwave cavity	$1.64{\cdot}10^{15}$
Simulated ions	10^6

We do make a few assumptions when implementing this model. First, we assume that the microwave coupling for the spins within the optical cavity is constant. Second, there are far too many ions to simulate all of them. To overcome this, we simulate $N_{sim} = 10^6$ unique ions and assume that these ions are representative enough of the inhomogeneity and scale their result (i.e. density matrix) for the rest of the ions. We also ignore all the other levels within the Er^{3+}:YVO_4 level structure for simplicity and assume that there are no ^{167}Er isotopes.

The inhomogeneity we consider is the spectral detunings of both the spin and optical transitions and also the inhomogeneity in the optical coupling g_o (and equivalently in the optical pump Rabi frequency Ω_o). We randomly sample the distributions of these three parameters over the N_{sim} number of ions that we simulate. The g_o distribution is shown in Figure 4.11 and we assume a Gaussian distribution for the optical and microwave transition inhomogeneities.

In order to pick the detunings, we use numerical optimization to find the optimal atom-light detunings (for both the microwave and optical transitions) and then set the cavity-light detunings to maximize the efficiency.

With this methodology and the parameters in Table 4.6, we obtain a maximum total device efficiency of $\eta_d = 2.9 \cdot 10^{-7}$ for ground state transduction (internal efficiency of $\eta_{d,int} = 1.7 \cdot 10^{-6}$) and $\eta_d = 1.1 \cdot 10^{-5}$ for excited state transduction (internal efficiency of $\eta_{d,int} = 6.6 \cdot 10^{-5}$). The ground state efficiency is lower compared to the excited state due to the parasitic even isotope erbium ions that can absorb microwave photons.

Next, we look at how different parameters can influence the efficiency for both the excited state and the ground state. We first look at transduction using the excited state in Figure 4.19. We start by sweeping the various coupling rates between the three transitions Figure 4.19(a-c). The efficiency increases at first before eventually saturating and decreasing when the coupling is too large, especially for the optical ion cavity coupling. I attribute this to optical reabsorption of the transduced photons when the optical co-operativity is too large and our efficiency is mainly limited by the relatively weak spin cavity coupling rate for the ions within the transducer.

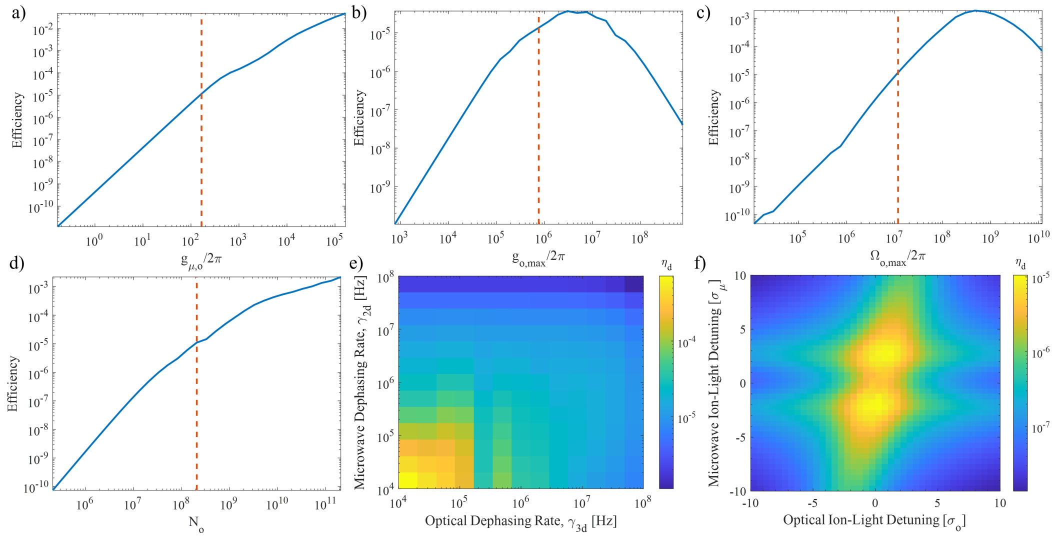

Figure 4.19: Excited state linear numerical model parameter sweeps for a) spin cavity coupling $g_{\mu,o}$, b) optical ion cavity coupling, $g_{o,max}$, c) optical pump Rabi frequency, $\Omega_{o,max}$, d) ions in the optical cavity, N_o, e) optical and spin dephasing rates, γ_{3d}&γ_{2d}, f) optical and microwave ion-light detunings (in units of the standard deviation of the inhomogeneous linewidths). The red dashed line is a reference to the default parameters.

We also look at the effect of the number of ions within the transducer in Figure 4.19d and observe a steady increase in the efficiency as the number of ions increases. In Figure 4.19e, we look at the efficiency as a function of the optical and spin dephasing rates. The efficiency decreases as these rates get larger, but it is a relatively weak dependence.

Lastly, we look at the efficiency as a function of the ion-light detuning for both the optical and microwave transition in Figure 4.19f. We do observe a splitting which indicates that higher efficiency is observed at a small detuning (i.e. around one linewidth).

In general, we do see that we cannot just tune a single parameter to improve the efficiency to unity, but need several terms to be improved.

Next, we looked at transduction using the ground state in Figure 4.20. We first consider the number of ions within the transducer in Figure 4.20a and again see a steady increase in the efficiency as we increase the number ions. We then look at the efficiency as a function of the number of parasitic spins (or effectively the total spin-cavity coupling of the parasitic spins) in Figure 4.20. We observe that the efficiency continuously decreases as we increase the number of parasitic spins. We note that when we remove all the parasitic spins the efficiency increases to $\eta_d = 1.1 \cdot 10^{-5}$, which indicates that the main difference in the efficiency between the ground and excited state, at least in the model, is the parasitic spins that couple to the ground state.

We then look at the optical pump Rabi frequency, the optical and spin dephasing rates and ion-light detunings in Figures 4.20(c-e). The dependence of the efficiency on the ion-light detuning is substantially different compared to the excited state, which we attribute to the parasitic spins. In the ground state, the highest efficiency is observe when the ion-light detunings is many linewidths away and does not decay quickly, but slowly decreases over tens of linewidths. This indicates that we can expect near equal efficiency for a large range of spin-light detunings.

Transduction efficiency with iterative numerical model

Here we look at the transduction efficiency simulation results using the iterative numerical model. As mentioned in Chapter 2, the iterative model allows us to look at the input power dependence of the transducer. In the transducer, there are a finite number of atoms, so they can only transduce a finite number of photons before they will saturate.

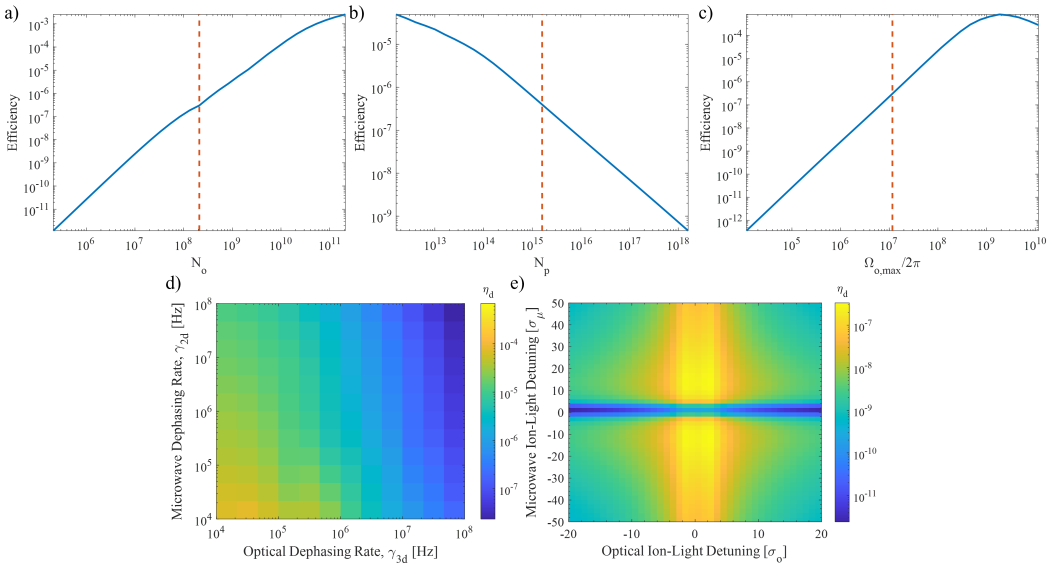

Figure 4.20: Ground state linear numerical model parameter sweeps for a) ions in the optical cavity, N_o, b) number of parasitic ions, N_p, c) optical pump Rabi frequency, $\Omega_{o,max}$, d) optical and spin dephasing rates, γ_{3d} & γ_{2d}, e) optical and microwave ion-light detunings (in units of the standard deviation of the inhomogeneous linewidths). The red dashed line is a reference to the default parameters.

Optimizing for four different detunings at each input microwave power to find the highest efficiency at each power is very slow, so for here we fix the ion-light detunings (i.e. center of inhomogeneous line equals the light frequency) and the light-cavity detuning of the optical cavity, while we sweep the light-cavity detuning of the microwave cavity.

The simulation results are shown in Figure 4.21 for both ground and excited transduction. At low microwave input power, the efficiency is constant and then above a specific microwave power (i.e. -100 dBm for the excited state and -50 dBm for the ground state), the efficiency begins to decrease due to saturation of the spin transition. We attribute the saturation of the transducer in the excited state at lower microwave power to the smaller number of spins that will be in the excited state compared to the ground state. It is also worth noting, the specific saturation power level will be sensitive to the exact pumping rates and also the decay rates of all the energy levels.

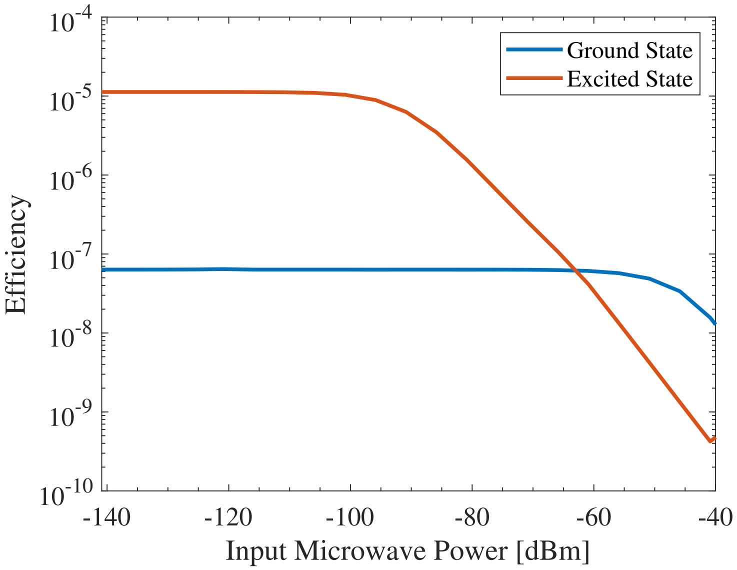

Figure 4.21: Transducer efficiency vs input microwave power for transduction in the ground and excited state.

Chapter 5

FABRICATION PROCESS

In this chapter, I will describe the device fabrication process used to make our REI transducer. The main steps are summarized in Figure 5.1. In brief, the fabrication process includes depositing an alumina etch stop layer, patterning the niobium microwave circuit, patterning the amorphous silicon optical circuit and finally removing the remaining mask material in hydrofluoric acid (HF). The CAD drawing of the full chip (excluding alignment markers) is shown in Figure 5.2.

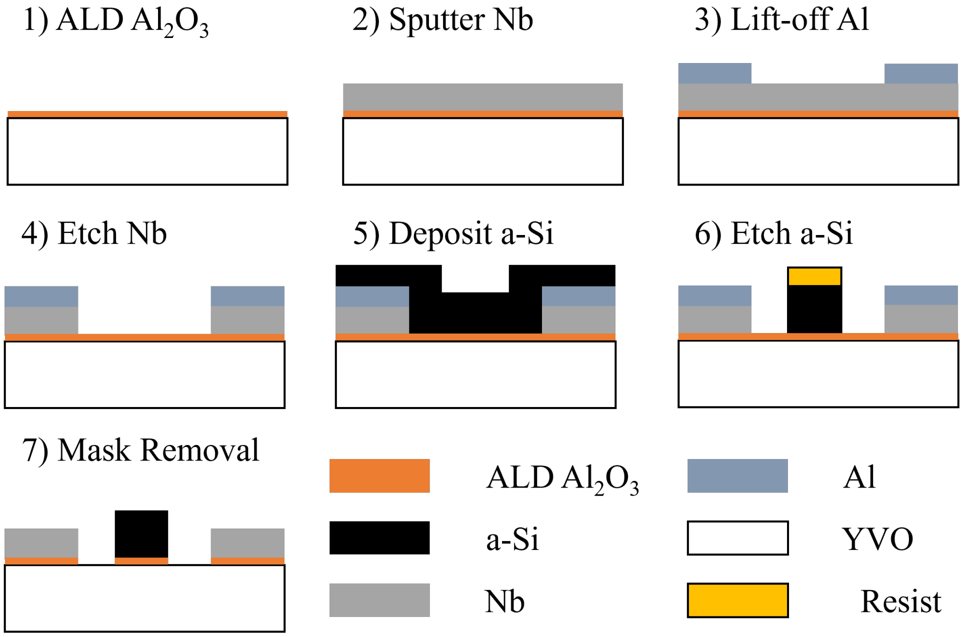

Figure 5.1: Fabrication process to make the niobium microwave resonators and the amorphous silicon optical resonators on the YVO_4 surface.

5.1 Sample and Surface Preparation

Our YVO_4 material was normally obtained as a boule with typical dimensions of ~1" x 1" x 1" (see Figure 5.3). Most of our YVO_4 boules come from Gamdan Optics, but we have some material from other commercial vendors as well. Typically the boules have a slight yellow hue that is independent of any rare-earth ion doping and is believed to be from oxygen vacancies formed during the crystal growth [159].

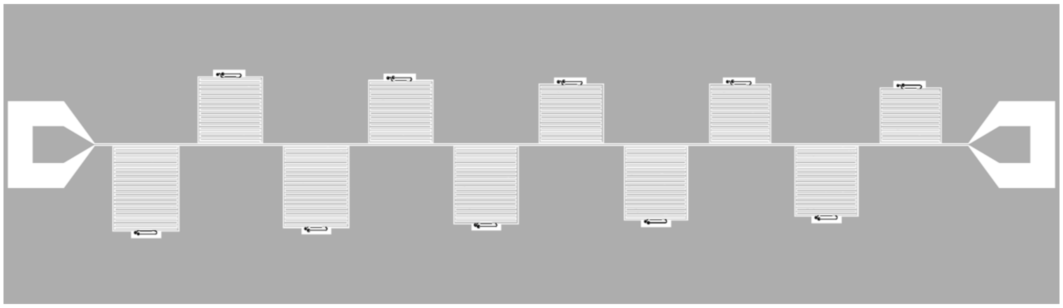

Figure 5.2: CAD file of the full chip, which contains ten microwave resonators (each with an optical resonator) that couple to a microwave coplanar waveguide in the center. The large pads at the end of the coplanar waveguide are for wirebonding.

Before device fabrication, the boule was sent out to Brand Laser Optics for orienting, dicing and polishing samples into chips for fabrication. The samples are oriented to within ±0.5° of the crystal axis. The diced chips are cut to dimensions of 8.5 mm x 9 mm x 0.5 mm (a,c,a). The YVO_4 surface roughness after polishing was measured using a Bruker Dimension Icon atomic force microscope (AFM) to be R_a ~0.3 nm. For testing the fabrication process, we also used 10 mm x 10 mm x 0.5 mm (a,c,a) undoped YVO_4 from MTI (YVO4a101005S1), since these are more abundant and cheaper than our doped samples.

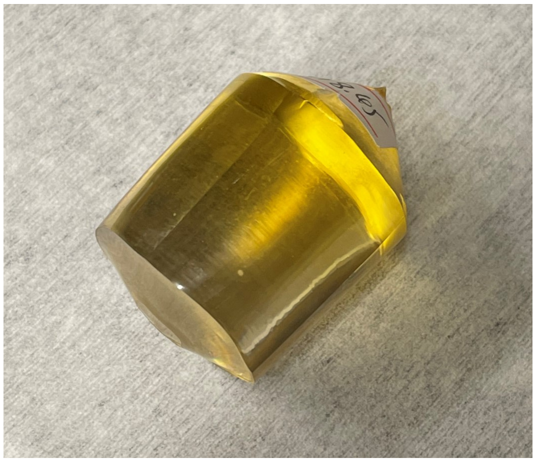

Figure 5.3: Typical YVO_4 boule from commercial growth.

Table 5.1: Niobium deposition parameters

Parameters	Value
Ar Flow Rate	50 sccm
Deposition Pressure	~7 mTorr
Deposition Rate	~ 7 Å/s
DC Power	200 W
Plasma Resistance	~ 350-400 Ω
Thickness	150 nm

After polishing, the samples are solvent cleaned in acetone and isopropyl alcohol and then rinsed in deionized (DI) water. The samples are coated with a ~5 nm thick alumina (Al_2O_3) film using an Oxford Instruments FlexAL ALD System. This film is used to protect the YVO_4 surface from subsequent etching processes. The alumina layer is thin to minimize the distance between the amorphous silicon photonic resonator and the YVO_4 substrate and also to minimize the additional losses it will introduce to the microwave resonator from the alumina dielectric losses.

5.2 Niobium Fabrication

The next step is the deposition of niobium thin films. The deposition was conducted using a home-built DC magnetron sputtering system. This system reached a base pressure of $\sim 2 \cdot 10^{-10}$ Torr and uses 6N argon gas in an effort to minimize the impurities in the niobium films.

The deposition was done using parameters in Table 5.1. The deposition pressure was chosen to minimize the film stress of the deposited films and was slightly adjusted over time to maintain low film stress (i.e. compressive film stress of ~100 MPa). The film stress was calculated using the Stoney equation [160] and the sample curvature was measured using a Dektak XT stylus profilometer. The niobium film surface roughness was measured using an AFM to be R_a ~1.4 nm.

The niobium thin films were then patterned to form the microwave resonators, microwave coupling waveguide, and alignment markers using an aluminum hard mask and ICP-RIE etching. The aluminum hard mask was patterned using a lift-off process with MaN-2403 electron beam resist. A negative tone resist is useful for lift-off in this case as most of the chip will be the ground plane (i.e. covered by the aluminum mask), so the negative-tone resist allows us to reduce the electron beam writing time.

MaN-2403 was spun directly on the niobium surface at 3000 rpm and baked at 90 °C for 5 minutes before exposure. Electron beam lithography was done using a Raith EBPG 5200 Electron Beam Writer with a beam current of 100 nA, shot size of 25 nm and an exposure dose of 300 μC/cm^2. A proximity effect correction was used to help compensate for the varying pattern density across the microwave resonator. Along the coupling waveguide, the write fields were interleaved over 500 nm to prevent stitching errors from causing shorts. After writing, the resist development was conducted using MF-319 and stopped with a DI water rinse. In order to remove the resist residue remaining on the niobium surface after development, a 1-minute O2 plasma descum was done at 150 W.

The aluminum hard mask was deposited using electron-beam evaporation (Lesker Labline). A 25 nm film was deposited at a rate of 1 Å/s and at a pressure typically between $\sim 5 \cdot 10^{-8} - 10^{-7}$ Torr. Lift-off was done using hot Remover PG (~75 °C) for 15 minutes and sonicated for 5 minutes. After lift-off, the Remover PG is rinsed off using DI water.

The niobium films were etched using an inductively coupled plasma reactive ion etching (ICP-RIE) process in an Oxford Plasmalab System 100 (III-V) etcher to transfer the pattern from the aluminum hard mask into the niobium film. Before etching the samples, the etching chamber was prepared using a 10 minute O_2 plasma cleaning step, a 5 minute SF_6 plasma cleaning step and conditioned with the niobium etching recipe for 10 minutes. This process was done to try and create a consistent chamber environment for the etching process over time as this etcher is commonly used for many different materials and etch chemistries. The samples were mounted on a silicon carrier wafer with thermal grease, which was removed after etching with acetone.

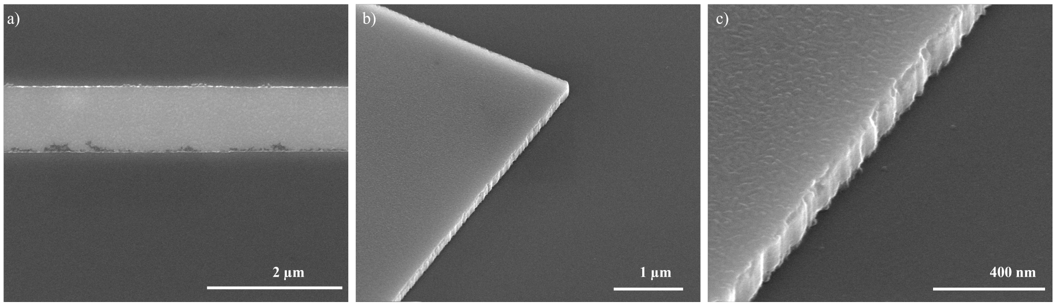

Figure 5.4: SEM images of the niobium fabrication process. a) Aluminum hard mask before etching. b-c) Edge of the niobium film after etching (tilt angle is set to 45°). The scale bars for each image are in the lower right corner.

Table 5.2: Niobium etching parameters

Parameters	Value
Pressure	10 mTorr
SF_6 Flow Rate	20 sccm
Ar Flow Rate	10 sccm
RF Forward Power	50 W
RF Reflected Power (typical)	1-2 W
DC Bias (typical)	110-120 V
ICP Forward Power	1200 W
ICP Reflected Power (typical)	8-10 W
Temperature	15 °C
Etch time	1 min 15 seconds

The niobium etching parameters are summarized in Table 5.2. The aluminum hard mask was etched less than 5 nm during the niobium etch. The etching time is chosen long enough to minimize the niobium material remaining on the YVO_4 surface, which will decrease the optical quality factor of the amorphous silicon resonators patterned next to the microwave resonator, but also short enough to minimize over-etching that can add roughness to the substrate surface which can also decrease the optical quality factors. Some SEM images of the niobium fabrication process are shown in Figure 5.4.

5.3 Amorphous Silicon Fabrication

The next part of the fabrication process involves the deposition and patterning of amorphous silicon to form the optical resonator. Before the amorphous silicon deposition, the sample was rinsed in DI water and baked on a hot plate to improve the adhesion of the amorphous silicon to the substrate. Amorphous silicon was deposited using plasma-enhanced chemical vapour deposition with a Oxford Plasmalab System 100 (PECVD). The deposition was done using parameters in Table 5.3. The amorphous silicon films had a surface roughness of R_a ~2.6 nm as measured by AFM.

A thin 10 nm layer of titanium was deposited on the amorphous silicon surface using an electron beam evaporator. This film can be helpful for electron beam lithography to ensure the height monitor works for transparent samples and prevent any charging effects for insulating samples. This is not required for patterning the full device (i.e. with Nb resonators), but it is required for making only-optical test devices, so it was used here for consistency.

Table 5.3: Amorphous silicon deposition parameters

Parameters	Value
Pressure	800 mTorr
5% SiH_4/Ar Flow Rate	250 sccm
RF Forward Power	10 W
Temperature	200 °C
Deposition Rate	26 nm/min
Deposition Thickness	300 nm

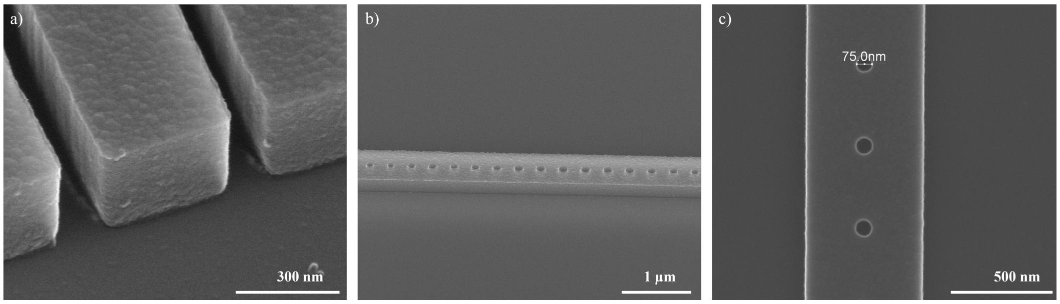

Figure 5.5: SEM images of the fabricated amorphous silicon devices. a) Grating coupler sidewall and surface roughness after etching. b) Photonic crystal pattern. a-b) have a tilt angle of 45°. c) Small holes patterned in the amorphous silicon for tapering from the mirror mode to the waveguide mode. The scale bars for each image are in the lower right corner.

The next step was patterning the amorphous silicon optical resonators. Hydrogen silsesquioxane (HSQ) was used as the resist for the lithography. A high-resolution negative tone resist was desired to make the small features of the photonic crystal structure and also to remove all the amorphous silicon on the niobium, while just leaving the amorphous silicon for the photonic resonator. HSQ resist (Dow Corning FOx 16) was diluted in methyl isobutyl ketone (MIBK) (2:1.2 HSQ:MIBK), spun at 5000 rpm and baked at 100 °C for 5 minutes before exposure. Electron beam lithography was done using a beam current of 300 pA, shot size of 1 nm and an exposure dose of 2000 μC/cm^2. The resist was developed using 25% TMAH for 20 seconds and stopped using DI water.

Table 5.4: Amorphous silicon etching parameters

Parameters	Value
Pressure	10 mTorr
SF_6 Flow Rate	15 sccm
C_4F_8 Flow Rate	25 sccm
RF Forward Power	23 W
RF Reflected Power (typical)	1-2 W
DC Bias (typical)	85-90 V
ICP Forward Power	1200 W
ICP Reflected Power (typical)	8-10 W
Temperature	15 °C
Etch time	3 min 50 seconds

The amorphous silicon films were etched using a pseudo-bosch process with parameters detailed in Table 5.4. A similar chamber preparation was used as described previously for the niobium etching, but here the chamber was conditioned with the pseudo-bosch process instead. The SF_6/C_4F_8 ratio was chosen to maintain vertical sidewalls in the amorphous silicon during etching. The etching time was chosen to slightly over-etch the amorphous silicon in order to remove the amorphous silicon at the niobium pattern sidewalls. Importantly, the aluminum hard mask on the niobium surface also protects the niobium film during the amorphous silicon etching.

Lastly, the sample was placed in 5% HF for 1 minute to remove the remaining HSQ resist, titanium adhesion layer and the remaining aluminum hard mask on the niobium films. The sample was rinsed in DI water and ready for packaging and characterization. Some SEM images of the fabricated amorphous silicon structures are shown in Figure 5.5.

A full fabricated device can be seen in Figure 5.6, which shows the microwave resonator and optical resonator and a zoom-in of the optical cavity and a photonic crystal mirror of the optical cavity.

5.4 Transducer Packaging

After device fabrication, the device was wire-bonded (Westbond 7476D Wire Bonder) to a microwave PCB launch board (Arlon AD1000) that was manufactured by Hughes Circuits. The launch board consists of a coplanar waveguide to connect an SMP connector (Fairview SC5371) to the microwave coupling waveguide on the chip.

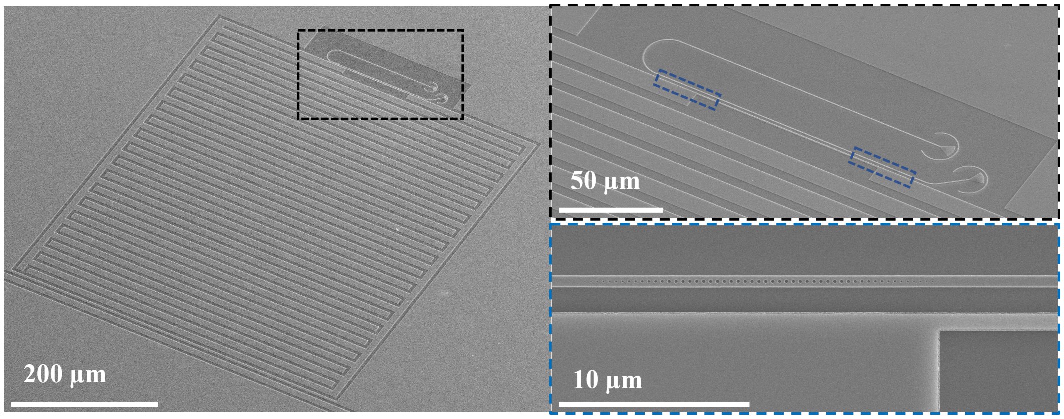

Figure 5.6: SEM images of the rare-earth ion transducer. The full device including the microwave resonator and optical resonator on the Er^{3+}:YVO_4 substrate are shown, while the zoom-in images show a close up of the optical resonator next to the inductive wire and a photonic crystal mirror.

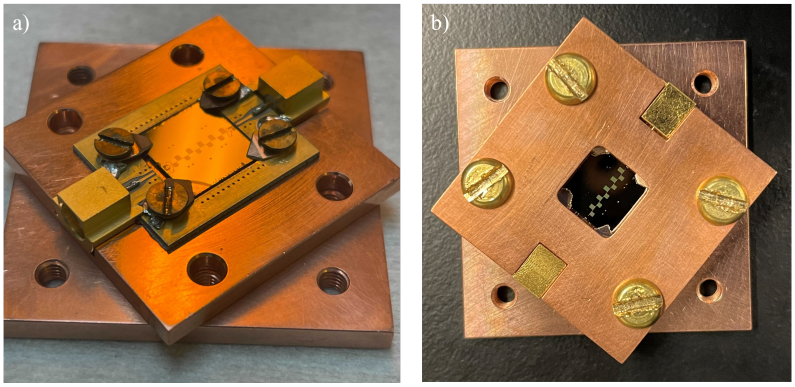

Figure 5.7: a) The device packaging without the copper lid to see inside and b) with the copper lid in place as it would be mounted in the fridge.

The PCB board was screwed onto a copper plate and a copper lid was placed over package with a hole in the middle to allow for optical coupling. An image of the package without the lid and with the lid are shown in Figure 5.7. The sample is mounted at an angle, such that the applied magnetic field can easily be applied in the correct direction with respect to the crystal axis of the sample.

5.5 Sputtering Tool

The niobium sputtering tool that we used was a home-built system in Professor Keith Schwab's laboratory. His most recent students had previously used the tool for sputtering superconducting aluminum devices and it had not been used for niobium depositions before or at least to my knowledge.

The system only has one target, so this was swapped from aluminum to niobium. We used a 3-inch diameter, 99.99% purity (excluding Ta) niobium target from Super Conductor Materials.

Depositing high quality superconducting films is not something the Faraon group had a lot (or any) expertise in, so we got advice from Matt Shaw and Rick LeDuc at JPL. The main suggestion was to minimize the impurities during deposition, which included ensuring a very low base pressure of the tool and ensuring the Ar gas was ultra-pure as well.

Given that the tool has relatively few parts and only deposits niobium getting a low base pressure was manageable after baking the tool and gettering by depositing niobium on the chamber sidewalls. After several months of pumping with the cryopump, the pressure would drop below the range of the ion gauage (i.e. down to $\sim 2 \cdot 10^{-10}$ Torr).

In order to ensure high purity argon entered the system, we started with 6N purity argon, used a high-purity gas regulator (Matheson 9001 Series Ultra-Line), added an inline gas purifier (Saes Pure Gas MC1), ensured all fittings were done with VCR metal gasket face seals and connected all parts with stainless steel tubing.

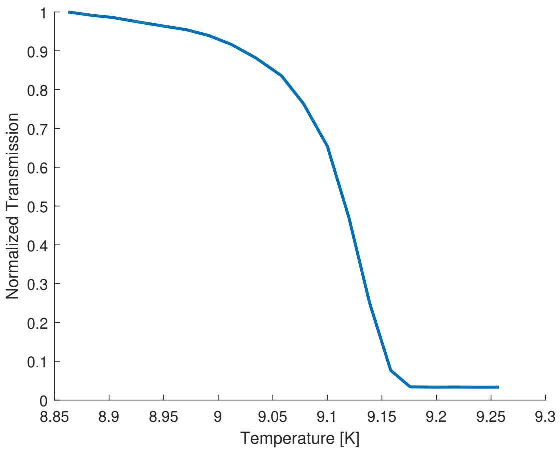

Figure 5.8: Transmission of a niobium waveguide to determine the critical temperature, Tc, of the superconducting films.

One way to determine the quality of the niobium films is to measure the critical temperature of the films. This was characterized by measuring the transmission through a microwave co-planar waveguide. Below the critical temperature, the transmission increases as the film losses decrease. This measurement was conducted in a Montana Instruments cryostat, which gave us easier control of the temperature around T ~9 K compared to the BlueFors dilution refrigerator that we used for all other low temperature measurements. The normalized waveguide transmission as a function of the temperature is shown in Figure 5.8. We denote the temperature where the transmission drops to half as the T_c and obtain $T_c = 9.12$ K.

Chapter 6

EXPERIMENTAL SETUPS

In this section, the experimental setups will be presented. These are focused on the cryogenic components inside the dilution refrigerator and also the accompanying room temperature components used for the device characterization and transduction measurements. This includes microwave, optical, and magnetic field components.

In general, a lot of the infrastructure for measurements is similar or derived from methods described by previous group members [161–163].

6.1 Dilution Fridge Set-Up

The transduction experiment set-up is mounted on the mixing chamber plate of a dilution fridge (BlueFors LD250) with a base temperature of ~35 mK with all components installed (see Figure 6.1). The set-up includes an OFHC copper post and mount for the transducer package, a two-axis home-built superconducting magnet, coaxial cable for microwave signals, an optical fiber coupling setup for optical signals and DC wiring for controlling a three-axis piezo stack. These components will be described in more detail in the proceeding sections.

Also, within the same fridge is a fiber-coupled SNSPD (courtesy of Matt Shaw's group at JPL) that sits on the cold plate (T~100 mK) for low noise photon counting measurements of small optical signals.

On the still plate (T~1 K) of the fridge, we used two Thorlabs U-bench setups which allowed for spectroscopy of bulk rare-earth doped crystals during the same cooldown [103].

A full set-up diagram for the transduction measurements and characterization is shown in Figure 6.2.

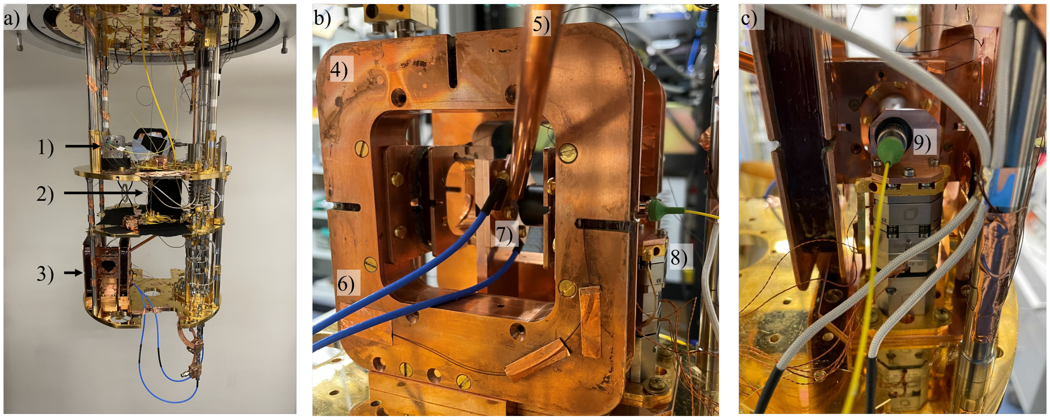

Figure 6.1: Fridge setup. a) Different setups on the different plates of the dilution fridge including 1) U-bench bulk spectroscopy setups on the still plate, 2) SNSPD on the cold plate, and 3) the transduction experiment on the mixing chamber plate. b) The transduction experimental setup includes 4) a superconducting magnet, 5) gas tuning line, 6) microwave coax, 7) sample and package, and 8) optical fiber and piezo stack. c) The optical fiber and lens tube are mounted on a holder (9) at an offset angle of 5° from normal to the sample. This angle is to improve the grating coupler efficiency.

6.2 Microwaves

Inside the dilution fridge, the microwave packaging for the device is coupled to two microwave coaxial cables for routing the input and output microwave signals. From room temperature to the mixing chamber stage, CuNi semi-rigid coaxial cable is used on the input line. In-line 10 dB attenuators (XMA 2082-6418-10-CRYO) are placed on the 4K, still, cold plate and the mixing chamber stages. From the mixing chamber plate to the sample package SMP connector, a copper coaxial cable is used (Fairview Microwave FMC0221085-18) on both the input and output lines.

On the output line, two cryogenic circulators (Low Noise Factory – LNF-CIC4-8A) are placed in series on the mixing chamber stage. Between the mixing chamber flange and the 4K stage, superconducting NbTi coaxial cable (CryoCoax NbTi 034) is used. On the 4K stage, a HEMT amplifier is used for low noise amplification (Low Noise Factory – LNF-LNC4-8C). From 4K to room temperature, CuNi coaxial cable is used.

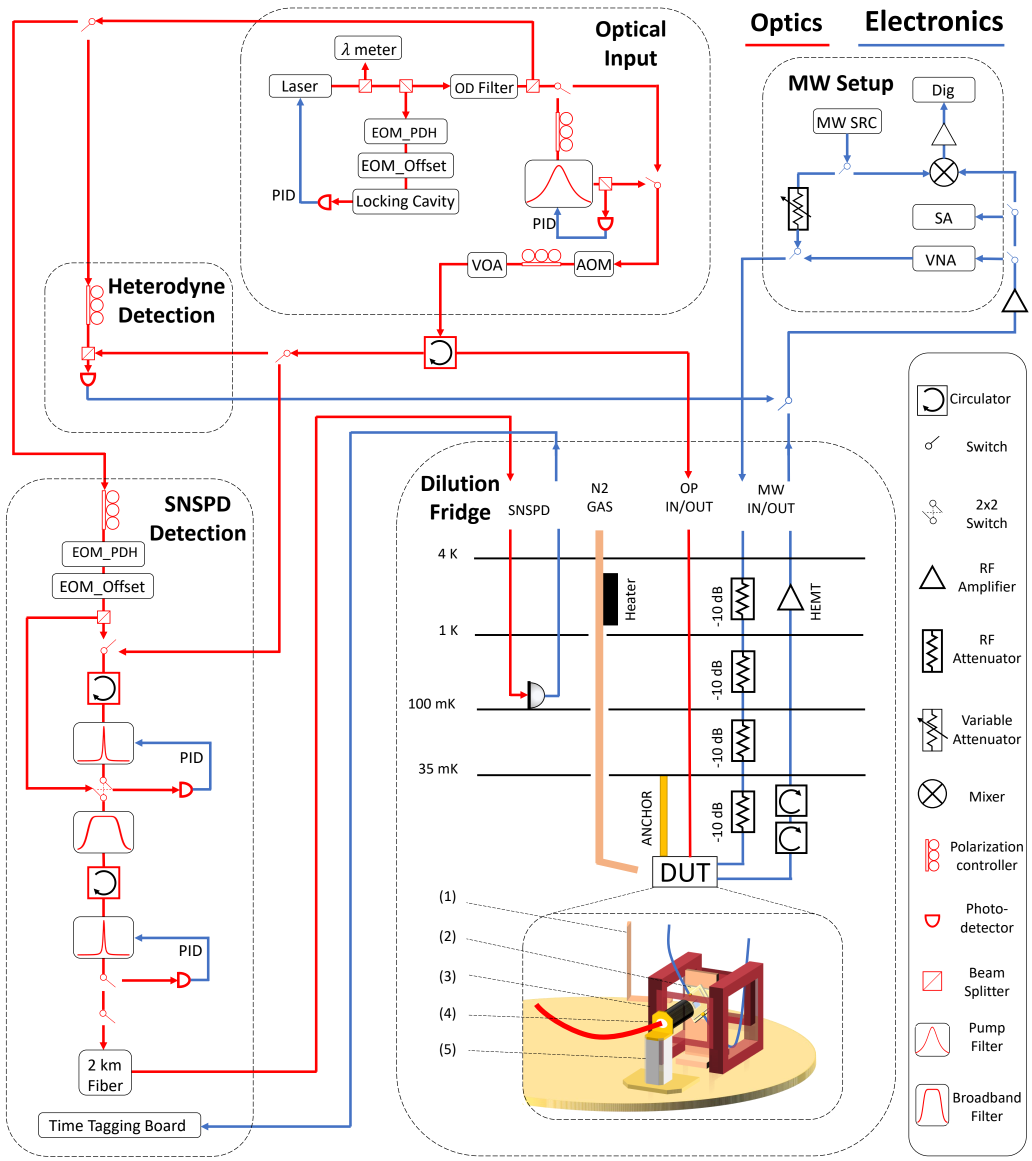

Figure 6.2: Diagram of the full experimental set-up. This includes the optical and microwave signal generation, the dilution fridge setup, and the optical and microwave signal detection. The device setup in the fridge consists of: 1) gas tuning line, 2) microwave coax, 3) superconducting magnet, 4) optical fiber and lens tube, and 5) three-axis piezo stack. Further details are in the text.

At room temperature, microwave signals were generated either from the network analyzer, spectrum analyzer, or a microwave signal generator (Berkeley Nucleonics Model 845). For pulsed measurements, the microwave input passed through a fast microwave switch (General Microwave E9114H) controlled by an AWG (Zurich Instruments HDAWG4).

The output microwave signal from the fridge is amplified with a LNA (WanTcom WBA2080-35A) at room temperature to further amplify the signal before detection on a network analyzer (Copper Mountain C1209), spectrum analyzer (Keysight FieldFox N9915A), or digitizer (AlazarTech ATS9130). All microwave sources and detectors were synced to a global reference clock (SRS FS725).

6.3 Optics

Inside the fridge, we coupled to the optical device using an optical fiber that focuses light through a lens pair (Thorlabs A260TM-C & A375TM-C) onto the grating coupler. The optical fiber and lens pair setup are mounted on a 3-axis piezo stack (Attocube ANPx101 (x2) & ANPz102) to control the position of the light. The lens pair is aligned with a 5° angle (relative to the normal of the sample surface) to best match the output mode of the grating coupler (see Figure 6.1c).

The external cavity diode laser (ECDL) (Toptica CTL 1500) is locked to a stable reference cavity (Stable Laser Systems) using the Pound-Drever-Hall (PDH) method for measurements where a precise and stable laser frequency is needed. A low frequency phase EOM (iXblue MPX) is used to generate sidebands for the PDH locking. A high frequency phase EOM (iXblue MPZ) is used so we can lock to the sideband in order to offset the main laser tone from the reference cavity frequency. The locking error signal is filtered by a laser servo (Vescent D2-125) and the generated feedback signal adjusts the laser current and piezo voltage to stabilize the laser frequency. For measurements that sweep the laser frequency several GHz, the laser is left unlocked and swept using the internal piezo actuator.

The input light path differs for the different experiments. For heterodyne measurements, the input light is split into a 90/10 fiber beamsplitter, where the 10% path acts as a LO for heterodyne detection and the 90% path passes through a 100 MHz fiber-coupled acousto-optical modulator (AOM) (Brimrose AMM-100-20-25), a polarization controller and a variable optical attenuator towards the device. The AOM acts as a fast optical switch for pulsed measurements and offsets the transduction pump laser frequency (and also the upconverted transduction signal) for heterodyne detection relative to the optical LO. The AOM switching is controlled by the AWG.

For SNSPD measurements, an additional Fabry-Perot cavity (Micron Optics FFP-TF), with finesse = 1,000 and free-spectral range = 100 GHz, is used to filter the laser noise at the input and is locked to the laser frequency with feedback to an internal piezo within the cavity.

A fiber circulator (OZ Optics) is used to input light to the optical fiber going into the fridge and route the output photons from the device to the detection path. The set-ups for transduction detection will be discussed in its own section.

6.4 Magnetic Fields

In order to generate a bias magnetic field for the transducer, we use a two-axis home-built split-pair superconducting electromagnetic mounted on the mixing chamber stage of the dilution refrigerator, where one axis is used to generate a large ($\sim$100 mT) in-plane magnetic field and the second smaller correction coil is used to minimize the out of plane magnetic field that the transducer microwave resonator experiences.

The large split-coil magnet consists of 1250 turns on each coil with an inner diameter of 85 mm and a gap of 40 mm between the two coils. We estimate the magnet coil coefficient to be $\sim$17.8 mT/A. The correction coil consists of 75 turns per coil with an inner diameter of 40 mm and a gap of 50 mm. We estimate the correction coil coefficient to be $\sim$1.5 mT/A. The superconducting magnet wire is made out of NbTi (SuperCon 430M-1A4B3A T48-M).

The superconducting electromagnets are each powered with a four-quadrant power supply (American Magnetics 4Q06125PS-430).

6.5 Gas Tuning

In order to tune the optical cavity into resonance with our atomic transitions, we use nitrogen gas condensation to red shift the optical cavities by taking advantage of the different refractive index between nitrogen and vacuum [164]. Gas is introduced to the fridge using a copper tube (OD 1/4 inch) with PTFE swagelock fittings between the stages before lastly being thermally lagged to the 4 K stage. Below the 4 K stage, the tube is positioned to maximize line of sight with the optical cavity without being in the way of any other components and without any physical contact with any cold components.

Due to the multimode nature of our optical cavities, we would have to tune the optical cavity up to ~3 nm at most. Gas tuning was done by introducing a set number of nitrogen gas pulses at a set pressure (30 psi) depending on the tuning range required, while the fridge remained at 4 K. The gas that enters the fridge freezes within the copper tube no optical resonance tuning is observed at first. In order to condense the gas onto the optical cavity, a resistive heater (typically set to ~8 W) is applied to the copper tube at the 4 K stage, which heats up the tube and allows some of the frozen gas to deposit on the optical resonator. For our set-up, we would typically start to observe tuning at ~12 K, as measured by the 4 K stage temperature sensor. In order to reach a specific optical resonance, we would control the duration of time the heater was turned on.

6.6 Transduction Detection Set-Ups

For heterodyne detection, the output signal is combined with the optical LO and mixed down to microwave frequencies on a photodetector (Alphalas UPD-35-IR2-FC). The photodetector output signal passes through a bias tee and the high frequency component is amplified using two LNAs before detection on a network analyzer or spectrum analyzer for continuous-wave transduction measurements.

For pulsed transduction measurements, we either mixed down the heterodyne signal and measured on digitizer or directly measured the transduction pulse on an SNSPD.

For pulsed heterodyne detection, heterodyne signal was mixed down to 21.4 MHz using an IQ mixer (Marki Microwave IQ-4509) and a microwave LO. The 21.4 MHz signal was amplified (SRS SR445A) and filtered (Mini-Circuits BBP-21.4+) before detection on a digitizer (AlazarTech ATS9130).

For SNSPD detection, the output light first passes through a filtering setup to attenuate the optical pump light. The filtering setup consisted of two high finesse fiber-coupled Fabry-Perot cavities (Stable Laser Systems) with finesse = 10,000 and free-spectral range = 20 GHz, a cascaded broadband bandpass filter assembly and two fiber circulators before each Fabry-Perot cavity and a series of optical MEMS switches (Serca SXLA-2X2-9N-10-FA) which were used to change the light path between the locking path and a detection path. The MEMS switches are controlled by a pulse generator (SpinCore PulseBlaster-ESR-PRO). This detection setup is shown in Figure 6.3.

The Fabry-Perot filters are frequency stabilized to the transduction light frequency using PDH locking by using a low frequency phase EOM on the laser and feedback from the laser servo is applied to the Fabry-Perot piezo through a high-voltage amplifier (Vescent SLICE-DHV) in a pulsed operation. Every 5 seconds, the light path switches from measuring transduced photons with the Fabry-Perot piezo voltage held at a constant value to a locking path where light at the transduction frequency is generated from the laser with a high-frequency phase EOM sideband and detected on a photodiode (Menlo Systems FPD510-FC-NIR) for PDH locking feedback. The locking path provides feedback to the cavity piezo for 0.1 s before switching back to the measurement path.

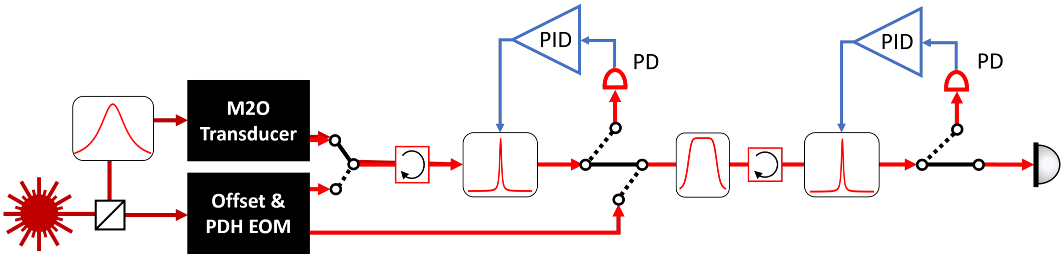

Figure 6.3: Detailed set-up diagram for single photon detection of transduced photons and the auxiliary components required to stabilize the frequency of the high finesse Fabry-Perot cavities. The same symbolic notation is used as in Figure 6.2.

Fiber circulators are used to prevent reflections or coupling between the different filters. The cascaded broadband bandpass filter assembly, consisting of one 30 GHz bandwidth filter (Coherent 114-ER456-003) and three 400 GHz bandwidth filters (Semrock NIR01-1535/3-25), is place between the two Fabry-Perot filters to prevent far detuned noise from propagating to the SNSPD.

After passing through the filtering setup and before entering the fridge, the light passes through a 2 km fiber to delay the transduction signal by ~11 μs. Our SNSPD and transduction device are in the same dilution fridge and we observe some small crosstalk, so the time delay allows us to filter the crosstalk in the time domain. After the fiber delay line, the light then goes back into the dilution fridge and passes through a coiled fiber (PhotonSpot) on the 4 K stage to filter IR photons before finally detecting on the SNSPD mounted on the cold plate (background counts ~ 5 counts/s). The voltages pulses generated from the SNSPD were processed on a time-tagging board (PicoQuant TimeHarp 260).

The filter setup insertion loss is 12 dB, where most of loss comes from the insertion loss of the two Fabry-Perot filters (~7.8 dB) and the remaining loss comes from the optical MEMS switches, fiber circulators, the 2 km delay fiber and all the fiber mating connections. The SNSPD has a total detection efficiency of 50%, which includes all losses from the fiber outside of the fridge to the detector itself (i.e. fiber losses from the coiled fiber in the fridge and splicing losses).

The detection noise floor of the SNSPD for transduction measurements is typically around $\sim$10 photons per second, which includes ~5 photons per second from laser leakage through the filtering setup when the laser output power to the filter setup is at 100 μW. Therefore, the laser attenuation from the insertion loss and the filtering is a total of $\sim$140 dB. We also note that depending on the pulse sequence duty cycle, we can also observe PL noise leakage. However, for low duty cycle measurements, this is not a dominant factor. This will be explored further in Chapter 7.

6.7 Filter Characterization

The high finesse Fabry-Perot filters were each initially characterized for their extinction far detuned from resonance. The pump laser that we will try and filter out is ~5 GHz detuned from the cavity resonance. The filter extinction measurement was done using heterodyne detection (i.e. mixing the transmitted laser light with a local oscillator offset by 100 MHz) and measuring the beatnote signal on a spectrum analyzer. The normalized filter transmission spectrum for both filters is shown in Figure 6.4. We observe extinction of ~60-70 dB per filter when measured individually. We note that this heterodyne method is only sensitive for detecting transmission of the main tone of the laser and is not sensitive to the broadband laser noise that can be associated with the diode laser.

We also observe several other cavity modes, but these modes are also narrow and only have measurable transmission $\sim$1-2 GHz detuned from the main resonance, which is well detuned from the pump laser we aim to attenuate at $\sim$5 GHz.

Also before we decided to PDH lock the filter setup, we characterized the filter frequency drift as shown in Figure 6.5. Each filter is in a temperature stabilized enclosure, but we still measured significant drift of the resonance frequency (i.e. much larger than the filter linewidth), which made any passive frequency stabilization solution infeasible without significant improvements. This is likely due to temperature fluctuations in our lab, which led to us using a locking method to stabilize the filter frequency as described above.

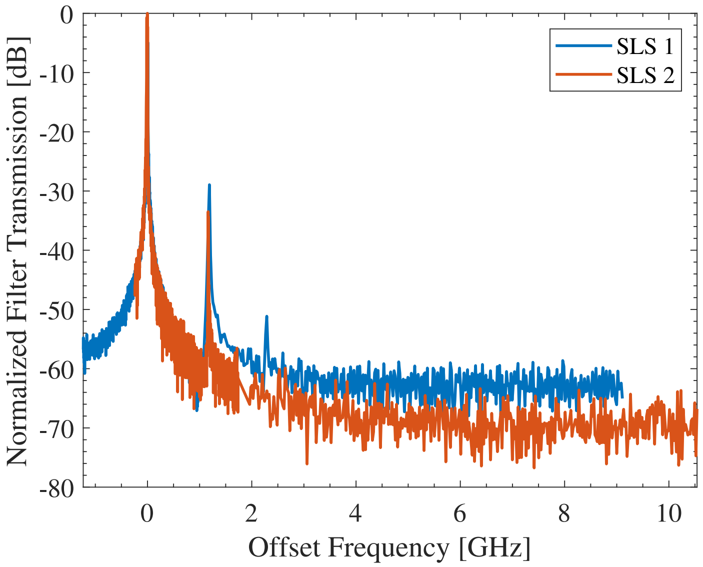

Figure 6.4: Extinction of the high finesse Fabry-Perot filters used to attenuate the laser. The different curves correspond to the two different filters. High extinction is observed for frequencies detuned ~3 GHz or more from the Fabry-Perot resonance.

Next, we characterized the locking of the SLS filters. Here, we are focused on maximizing the cavity transmission at the transduced photon frequency. We first characterize the normalized transmission (i.e. transmission of unity is the maximum transmission) when the SLS filter is actively being locked as shown in Figure 6.6. The black line corresponds to the mean transmission, the red area corresponds to one standard deviation of the measured transmission and the blue area corresponds to the difference between the maximum and minimum transmission measured. While the cavity is actively locked, the normalized transmission remains around 98.5 % of the maximum transmission for the duration of the measurement.

The next measurement involved first locking the SLS cavity and then holding the locking feedback and observing the transmission decrease as the cavity drifts over time as shown in Figure 6.7. The mean cavity transmission drops to 90 % within ~40 seconds and drops to 50% within 3 minutes. Based on this measurement, we determined we needed to have some feedback to the cavity frequency in a time period well under 40 seconds.

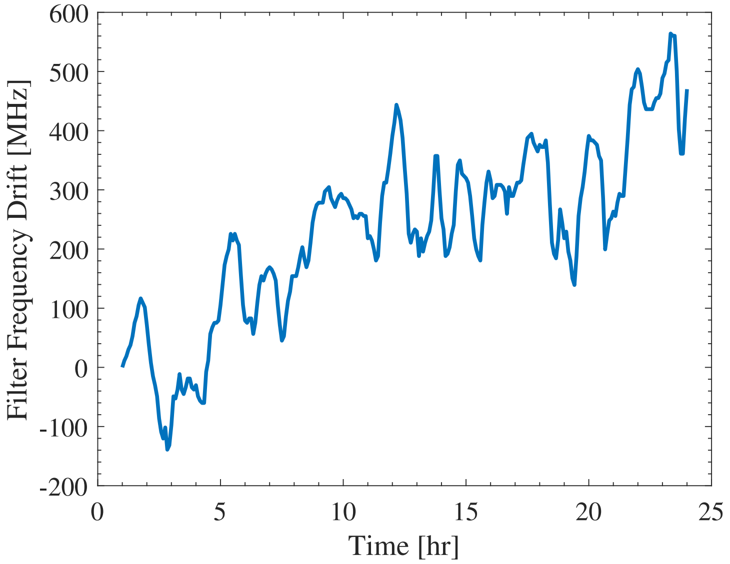

Figure 6.5: Drifting of the high finesse filter resonance frequency over time in the lab without any active feedback on the filter frequency.

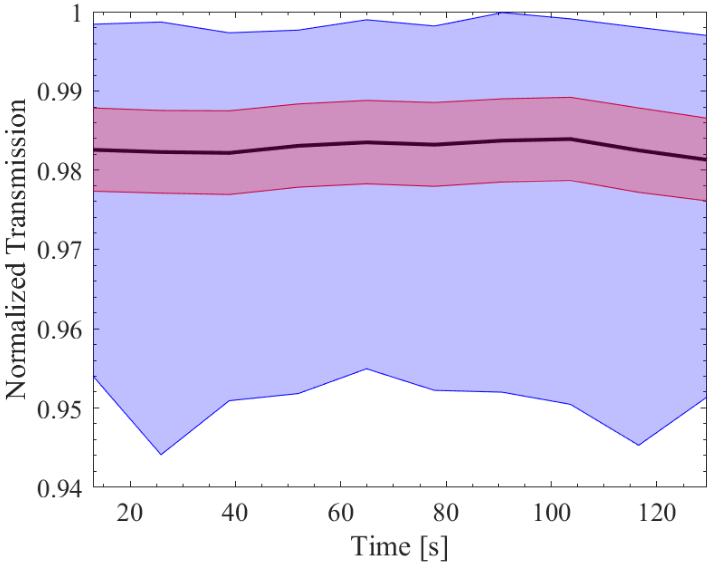

Figure 6.6: Normalized filter transmission while the filter is locked.

Based on the cavity drifting rate, we decided to implement our pulsed lock every 10 seconds. For 1 second, the cavity is actively locked using feedback from our PDH locking method. For the next 9 seconds, the cavity lock is held at a fixed value allowing us to conduct experiments. The results of this pulsed locking technique are shown in Figure 6.8. In this method, we are able to have a mean normalized cavity transmission of 97%. There are rare instances where the cavity transmission drops to ~70-80%, so there is still room for improvement in this method.

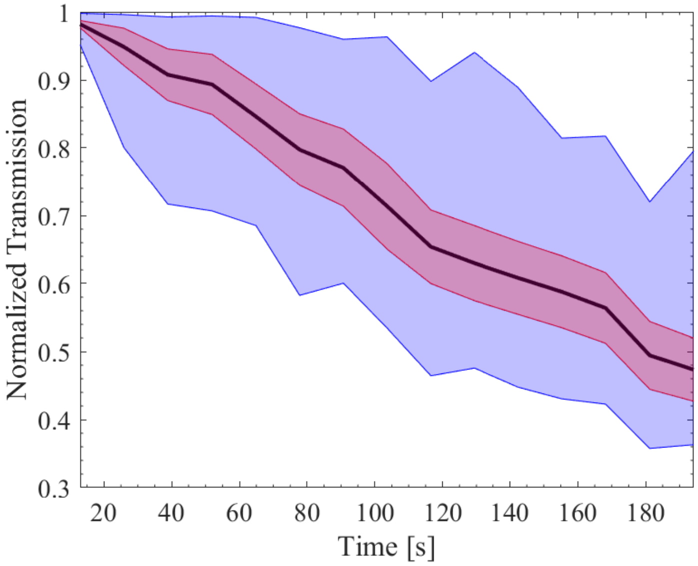

Figure 6.7: Normalized filter transmission while the filter was originally locked at the start and the locking piezo voltage is held constant after the initial time.

Lastly, when we started running the experiments, we switched the pulsed locking timing to 0.1 seconds of active locking and 4.9 seconds of measurement time while the lock is being held. This produced similar results in terms of cavity transmission.

6.8 Microwave Noise Measurements

Beyond transduction measurements, we also did some measurements on the microwave noise/temperature under optical illumination, which was detected on the output microwave coax line. Those measurements will be described in Chapter 7, but the set-up for those measurements will be described here. The measurement was done in two different ways. Either with CW optical illumination or pulsed optical illumination. For the CW case, the microwave signal exiting the fridge was first amplified before detection on a spectrum analyzer. In the pulsed case, the signal exiting the fridge was amplified, then mixed down to ~10-20 MHz with a mixer and a microwave LO. The signal was then amplified (SRS SR445A) before detection on a digitizer (AlazarTech ATS9130).

An important part of this measurement was the calibration of the output microwave amplification chain gain and added noise, which need to be subtracted from the signal in order to determine the noise from the resonator. The calibration was done by adding a heater to the mixing chamber plate and detecting the output microwave power on the spectrum analyzer or digitizer.

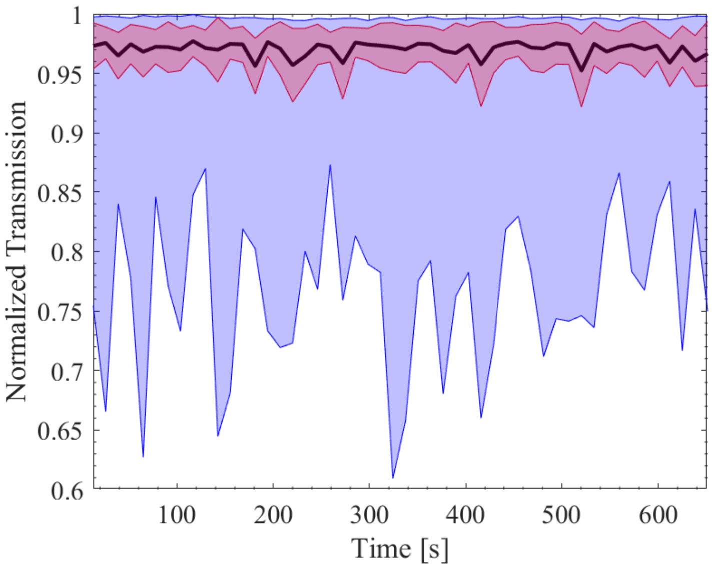

Figure 6.8: Normalized filter transmission while the filter is in pulsed lock mode, where the lock is implemented for a brief period and then held for an extended period of time.

The gain and added noise are determined by fitting to [46]:

$$GN_{out} = \frac{P_{out}}{\hbar\omega \mathrm{BW}} = G\left[\frac{1}{2}\coth\left(\frac{\hbar\omega}{2k_bT}\right) + N_{add}\right] \tag{6.1}$$

where P_{out} is the detected power on the spectrum analyzer or digitizer, N_{out} is the output noise photon number (referenced before the amplifier chain), BW is the detection bandwidth of the detector, G is the gain of the detection setup, T is the temperature, and N_{add} is the added noise of the detection setup.

The calibration for the digitizer is shown in Figure 6.9, where we fit to $G = 90.4 \pm 0.03$ dB and $N_{add} = 6.84 \pm 0.05$ $[\mathrm{s}^{-1}\mathrm{Hz}^{-1}]$. For reference, our HEMT amplifier (i.e. the first amplifier in our detection setup) has an added noise of $N_{add} = 6.33$ $[\mathrm{s}^{-1}\mathrm{Hz}^{-1}]$ according to the data sheet, which is fairly close to the level that we measure in the lab. This is the calibration for $\omega_\mu/2\pi$=4.933 GHz, but we observe similar parameters for nearby frequencies that we also calibrate.

When we do the same measurement but with the spectrum analyzer, we measure a similar N_{add}, but our gain is decreased to G = 70.5±0.06 dB, since we have less amplifiers in the output chain. This gain of 70.5 dB includes 33 dB of gain from our room temperature amplifier and an expected gain of 42 dB from the HEMT, which would correspond to 4.5 dB of cable loss from the coaxial cable inside the fridge and outside the fridge to the spectrum analyzer.

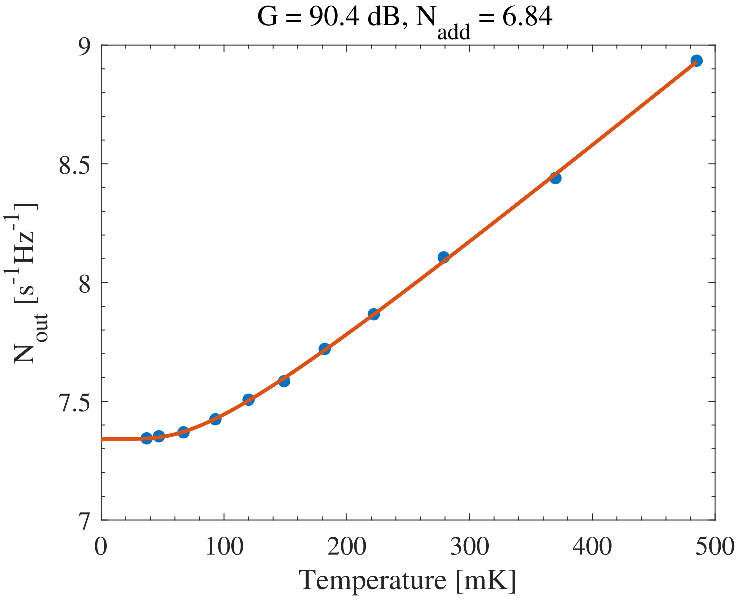

Figure 6.9: Microwave output amplification chain gain and added noise for the digitizer detection setup.

We note that N_{add} may contain additional noise corresponding to thermal photons in the microwave waveguide when the fridge is at the base temperature (35 mK). There are 40 dB in microwave attenuators on the input coaxial cable to attenuate thermal noise from warmer stages (see Figure 6.2), which may be insufficient to ensure the waveguide is in thermal equilibrium with the mixing chamber stage. Additional attenuators would require us to send in higher microwave power at the input for some transduction measurement, which we wanted to avoid. Therefore, in our later measurements, the thermal noise that we measure corresponds to the thermal occupation induced from the optical light within the transducer. The thermal noise of the waveguide introduced from the warmer stages in the fridge can be attenuated using additional attenuators or filtering and is a characterization of the set-up and not the transducer itself.

Chapter 7

TRANSDUCER MEASUREMENTS

In this chapter, the measurements of the rare-earth ions transducer will be presented. This will start with some preliminary device measurements at room temperature and then focus on the cryogenic device characterization and transduction measurements.

7.1 Preliminary Devices

In this section, preliminary devices toward the development of the transducer device will be shown. This will include both the optical devices and the microwave devices.

Preliminary Optical Devices

Before fabricating a full transducer device with a microwave cavity and an optical cavity on a Er^{3+}:YVO_4 substrate, we first fabricated each cavity independently to make sure they functioned by themselves. We also started by making devices on a sapphire substrate since it has a similar refractive index to YVO_4 ($n_{sapphire} \sim 1.75$), so although the designs could not be the exact same, they were similar. Also, sapphire is known to be a good substrate for superconducting microwave devices, while YVO_4 is not a standard substrate, so it was useful to make initial microwave devices on sapphire for testing. The designs for the additional optical devices (i.e. designs not shown in Chapter 3) are included in Appendix B.

After making devices on sapphire, we then used the same fabrication process to make the devices on YVO_4. After making all optical devices on YVO_4, we then added the microwave resonator step in the fabrication. While making test devices, we would make weakly coupled cavities (i.e. $\kappa_{o,in} \ll \kappa_{o,i}$) such that we could determine the intrinsic losses of the cavities.

A summary of these different optical cavity quality factors are shown in Figure 7.1. This measurement was done by using the laser piezo to scan the laser frequency over the cavity resonance and the transmitted light through the resonator was detected on a photodiode. Figure 7.1(a-c) show the optical cavities on YVO_4, which include a TE mode device (Q~160,000), a TM mode device (Q~105,000) and a TM mode device with a microwave resonator (Q~80,000). We were able to achieve higher quality factors for a TE mode device compared to a TM mode (note we need a TM mode device for the transducer). Adding the microwave resonator to the fabrication process degraded the TM mode quality factor by $\sim 25\%$ for the best devices. This required the addition of the ALD alumina step and precise timing of both the amorphous silicon and niobium etching. However, this was difficult to maintain for an extended period of time given the drift and inconsistency of the etching tools, so this process was constantly adjusted to make it as good as possible.

Figure 7.1(d-f) show the optical cavities on sapphire, which include a TE mode device (Q~185,000), a TM mode device (Q~135,000) and a TE mode device with a microwave resonator (Q~145,000). Generally, the optical devices on sapphire had a higher quality factor compared to YVO_4. This was partially attributed to the robustness of the sapphire substrate to our etching processes, which allowed us to overetch with little consequences and made timing the etching much easier. Importantly, it shows that with an optimized fabrication process, it should be possible to have optical quality factors above 100,000 with a microwave resonator present.

Although for the transducer we only care about a single optical cavity mode, the Fabry-Perot style optical cavities have many modes. This does make the measurements easier as there is always a mode within a few nm of the target wavelength, which makes the gas-tuning easier. The transmission and reflection spectrum of a YVO TM mode device are shown in Figure 7.2. These measurements were done in a room temperature confocal microscope set-up (more details of the setup can be found in Evan Miyazono's thesis [161]) using a erbium-doped fiber amplifier (EDFA) as the broadband source and a spectrometer (Princeton Instruments SP2750i) for the optical detection. As expected, we see many cavity modes within the photonic bandgap of the photonic crystal mirrors. The modes are separated by ~ 2.55 nm. The different amplitude of the modes and the envelope for the reflection measurement are given by the EDFA output power spectrum.

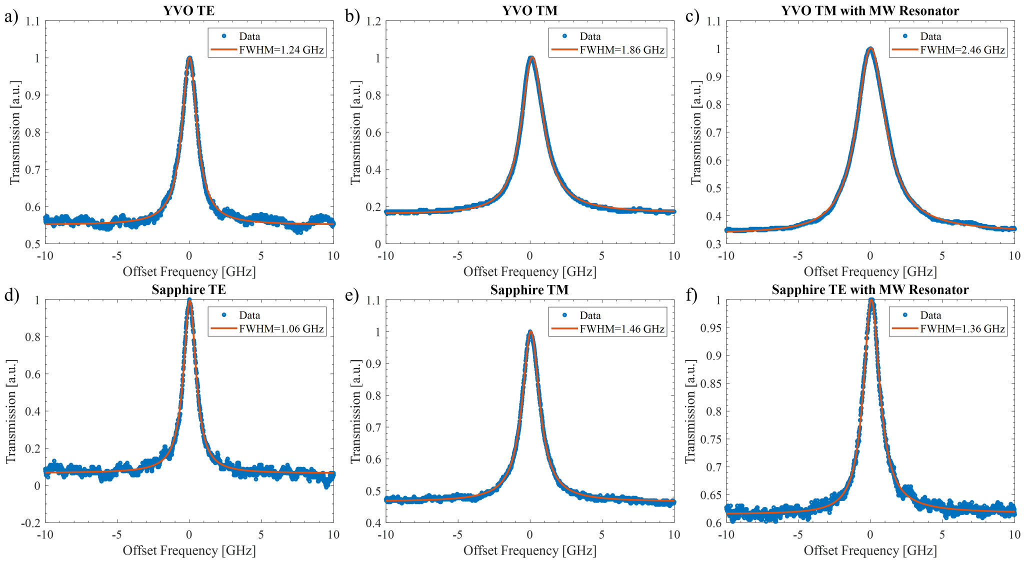

Figure 7.1: Linewidths of test optical resonators with modes near 1530 nm. a-c) Resonators fabricated on a YVO_4 substrate. d-f) Resonators fabricated on a sapphire substrate.

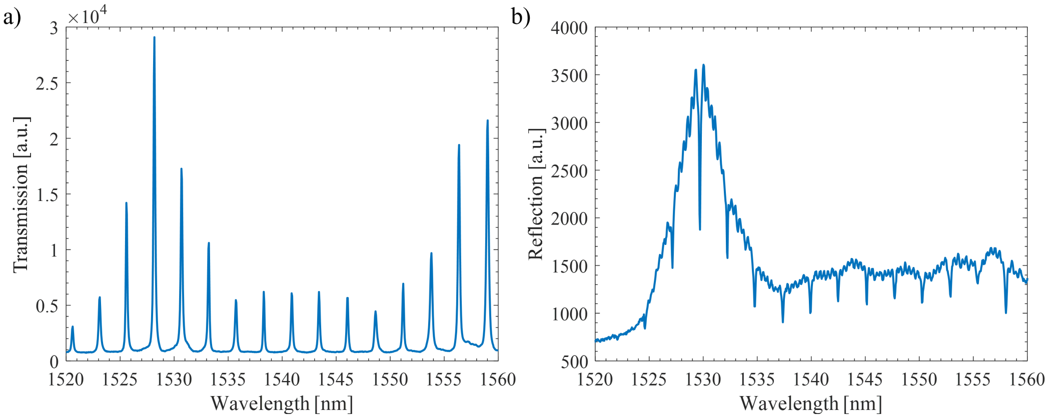

Figure 7.2: The a) transmission and b) reflection spectrum of the optical photonic crystal resonator.

Preliminary Microwave Devices

Like the optical devices, the initial microwave devices were done without the optical resonator fabrication and were initially done on sapphire. This project was the first time our group had worked with superconducting microwave resonators in any capacity, so we initially worked with more simple $\lambda/4$ co-planar waveguide resonators.

Our initial devices had quality factors around 5,000-10,000. Over the course of improving the sputtering deposition system, the device packaging and mounting, we were able to measure quality factors exceeding 100,000 at high microwave power. This puts an upper bound on the Er^{3+}:YVO_4 loss tangent of $tan(\theta) \sim 2 \cdot 10^{-5}$, which is similar to the literature value of undoped YVO_4 [106, 107]. This quality factor exceeds the need for our project, so we did not try to push this any further. Initial measurements were done before we had a HEMT amplifier, so we were restricted to high microwave power measurements.

Improvements to device packaging included improving the enclosure to a copper box and using a PCB launch board to connect from coax to the device. Improvements to the mounting involved switching from using silver paint to using copper clips to hold down the sample in place. The previous devices in our group had all been optical devices (or some with simple gold microwave waveguides). Silver paint worked quite well for mounting those as it is easy to implement and easy to remove. However, it did seem detrimental to the superconducting microwave resonators, so we stopped using it here.

7.2 Transducer Device Characterization

The final transducer device and the one that we characterized the most extensively was made on a Er^{3+}:YVO_4 substrate, where the erbium doping concentration was 560 ppm. The optical cavity was a TM mode amorphous silicon waveguide between two photonic crystal mirrors that was patterned on the the YVO_4 surface.

The microwave cavity consisted of a narrow inductive wire with a width of 1 μm that was shunted by an interdigitated capacitor. Further details of the design for the optical and microwave cavity within the transducer are in Chapter 4. There were a total of ten microwave resonators, each with an optical cavity, patterned on the chip. The optical devices were all relatively similar in terms of quality factor, so we used a device with a high microwave quality factor.

Initial Microwave Measurements

The transmission signal through the co-planar waveguide at base temperature (35 mK) is shown in Figure 7.3, where we observe ten dips corresponding to the ten microwave resonators. This measurement was done using a network analyzer and measuring $|S_{21}|^2$. The input microwave power here was relatively high ($P_\mu = -75$ dBm). This power was quoted as the power in the microwave coupling waveguide on the chip and all other microwave powers to the device are quoted in a similar way.

Since the coupling to the resonator is designed to be the same for all the resonators, the depth of the resonance dip is related to the resonances with the higher internal quality factors. For our transduction devices, we used the third lowest frequency resonator that has a resonance frequency, $\omega_{\mu,0}/2\pi = 4.94$ GHz.

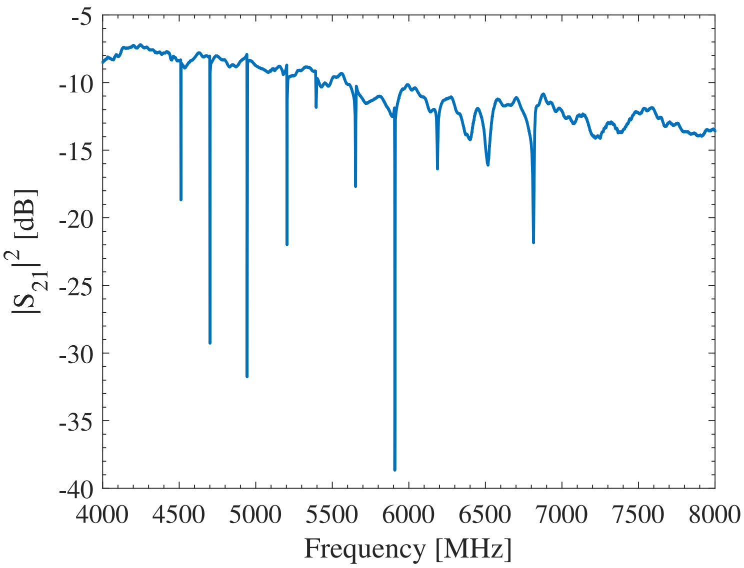

Figure 7.3: A broadband microwave coupling waveguide transmission spectrum at base temperature (35 mK), where the transmission dips correspond to coupling to the different microwave resonators on the chip.

The microwave resonator had a coupling quality factor of $Q_{\mu,in} = 5,676$, an internal quality factor of $Q_{\mu,i} = 2.36 \cdot 10^5$ at high microwave power and an internal quality factor of $Q_{\mu,i} = 50,878$ at low microwave power, as shown in Figure 7.4. The $|S_{21}|^2$ level is different here (compared to Figure 7.3) as an additional –40 dB attenuator was added to the input path and a 33 dB gain amplifier was added to the output path for measuring the signal at low microwave input power. We note that these are the initial quality factors at the start of the cooldown. The quality factor is determined by fitting the transmission spectrum near the cavity resonance to [165, 166]:

$$|S_{21}(\omega)|^2 = \left| \frac{1}{1 + \frac{Q_i}{Q_{in}} e^{i\phi} \frac{1}{1+i2Q_i\frac{\delta\omega}{\omega_{\mu,0}}}} \right|^2 + C \tag{7.1}$$

where $\omega_{\mu,0}$ is the cavity resonance frequency, $\delta\omega = \omega - \omega_{\mu,0}$, ϕ is a phase to account for reflections (i.e. impedance mismatch in the coupling transmission line), and C is a constant offset.

We observe a steady increase in the intrinsic quality factor as we increase the microwave power which is consistent with a model of saturating the microwave absorption of a loss mechanism. This is typically associated with two-level system (TLS) defects [167, 168]. A more detailed analysis of the internal quality factor is provided later on as we incorporate more experimental conditions that are required for transduction.

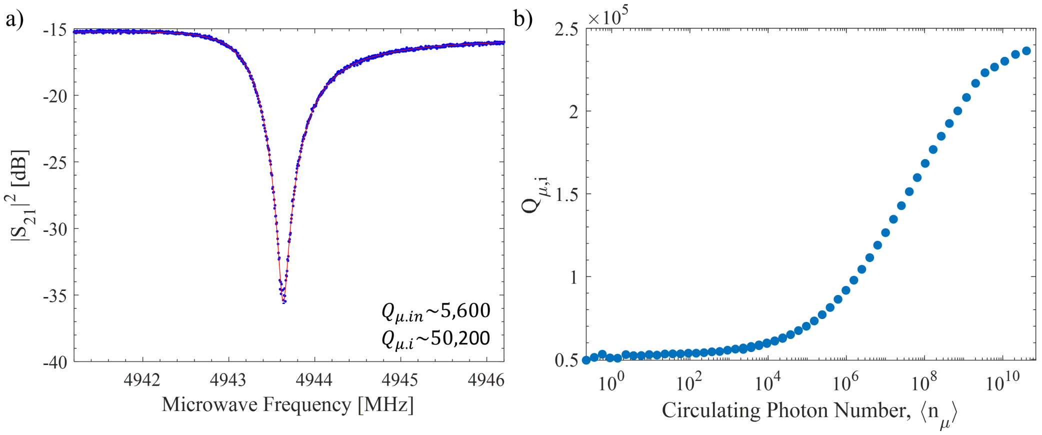

Figure 7.4: Microwave cavity spectrum before gas tuning. a) Cavity transmission spectrum and fitting at low microwave power to obtain the coupling and internal quality factor of the resonator. b) The microwave internal quality factor as a function of the circulating photon number in the microwave cavity.

Gas Tuning

After selecting the device on the chip, the next step was to gas tune the optical device, as mentioned in Chapter 6, to bring a optical cavity mode into resonance with the Z_1-Y_1 optical transitions. The cavity spectrum and reference Z_1-Y_1 transitions are shown in Figure 7.5 after gas tuning. The optical cavity is broader than the laser scan range (~ 20 GHz) so we only see part of the line shape here.

The cavity resonance is near to the zero magnetic field Z_1-Y_1 transition of a bulk crystal that was also mounted in the fridge and acts as our frequency reference in this measurement. The small dips next to the main Z_1-Y_1 transition are from ^{167}Er isotope ions. The small peak in the optical cavity is from coupling to the ions. This peak is relatively small here as this measurement was done with high optical power (P_o ~ 1 mW) which is convenient to have large signal for detection off the cavity reflection on a photodiode. We note that the optical power is quoted at the input fiber to fridge here and in all later references.

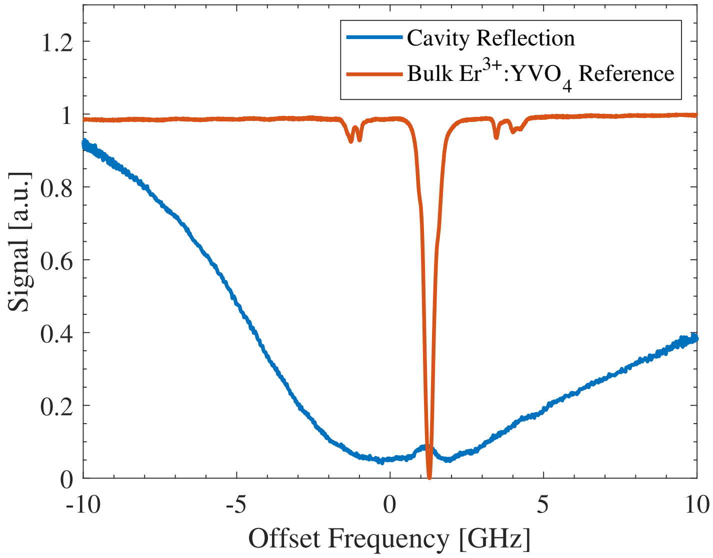

Figure 7.5: The optical cavity reflection spectrum (blue trace) and the reference Z_1-Y_1 optical transition (red trace) after gas tuning, which shows the cavity nearly resonant with the atomic transition.

Microwave Ion Cavity Coupling

After gas tuning the optical cavity into resonance with the Z_1-Y_1 optical transitions, the bias magnetic field is introduced to bring the ground state erbium spins into resonance with the microwave cavity. This process was monitored on a network analyzer. We have a small out-of-plane coil that we use to null the out-of-plane component of the magnetic field. This out-of-plane correction is introduced manually as we ramp the main coil and the amplitude of the correction field is chosen to maximize the quality factor. This does become challenging around certain magnetic fields where there is hyperfine coupling, which itself changing the microwave resonator line shape. Typically, we end up applying a magnetic field of ~ 0.1 mT in the correction coil, while the main coil reaches ~60-80 mT.

The microwave resonator spectrum as the spins cross the cavity resonance is shown in Figure 7.6. At a magnetic field of 60 mT, we observe an avoided-crossing due to the large ensemble coupling between the microwave cavity and the erbium ground state spin transition ($g_{\mu,tot}/2\pi$ ~105 MHz) at the base temperature, which we obtain by fitting the mode pulled cavity frequency to Equation 1.13. With $\kappa_\mu/2\pi = 2$ MHz, and $\Delta_\mu = 65$ MHz, we obtain a microwave ensemble co-operativity of $C_\mu = \frac{4g^2_{\mu,tot}}{\kappa_\mu \Delta_\mu} =$ 340.

We also observe coupling of the microwave resonator to several other spin transitions that we attribute to the ^{167}Er isotope. The small dip that sweeps through the anti-crossing is attributed to coupling of the even isotope erbium spins directly with the co-planar waveguide that we use for the transmission measurement. For reference, we expect the excited state erbium spins to be on resonance with the microwave cavity at 78mT.

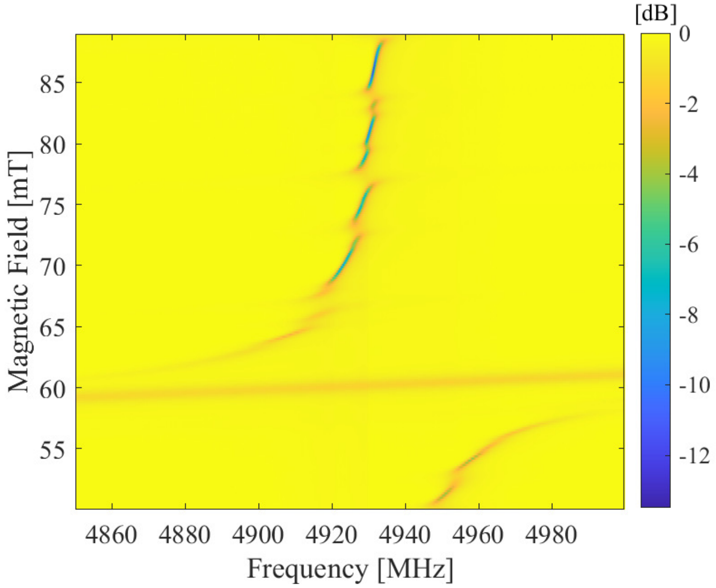

Figure 7.6: Ion-cavity coupling spectrum at microwave frequencies as a function of the applied magnetic field.

Optical Photoluminescence Spectrum

We then started to characterize the optical device. We first measured the optical transition linewidths by measuring the transition photoluminescence on a SNSPD as a function of the laser excitation frequency as shown in Figure 7.7. The measurement sequence used a 2 μs excitation laser pulse and a 10 ms wait time between the adjacent pulses at a magnetic field of 78 mT.

During this sequence the atoms are cold so we focus on transitions using level $|-\rangle_g$ in the ground state and both levels in the excited state. The linewidth of transition $|-\rangle_g \leftrightarrow |-\rangle_e$ is shown in Figure 7.7a) and gives a FWHM of 307 MHz. The linewidth of transition $|-\rangle_g \leftrightarrow |+\rangle_e$ is shown in Figure 7.7b) and gives a FWHM of 264 MHz.

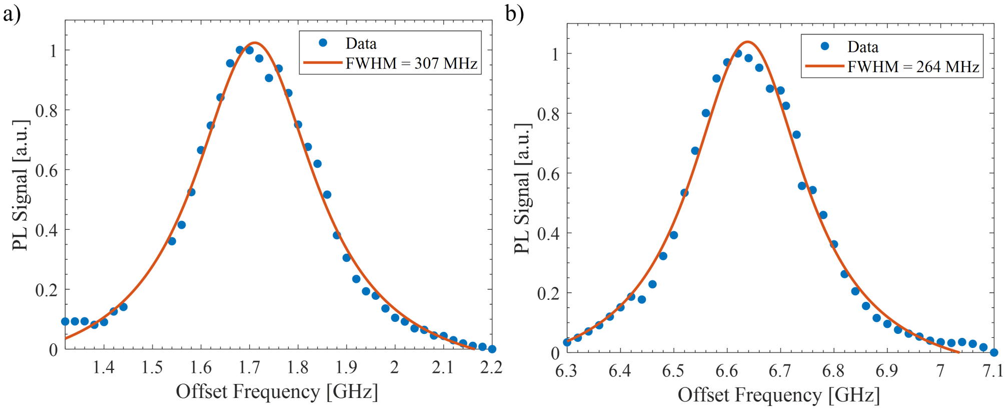

Figure 7.7: Optical photoluminescence spectrum for transition a) $|-\rangle_g \leftrightarrow |-\rangle_e$ and b) $|-\rangle_g \leftrightarrow |+\rangle_e$.

Optical Ion Cavity Coupling

The optical ion-cavity coupling is measured by sweeping the frequency of a weak probe laser (P_o ~1 pW) across the cavity resonance and detecting the light reflected from the cavity on a superconducting nanowire single-photon detector (SNSPD). A magnetic field of 76 mT was applied such that each optical transition is resolved and is the field used later for excited state transduction.

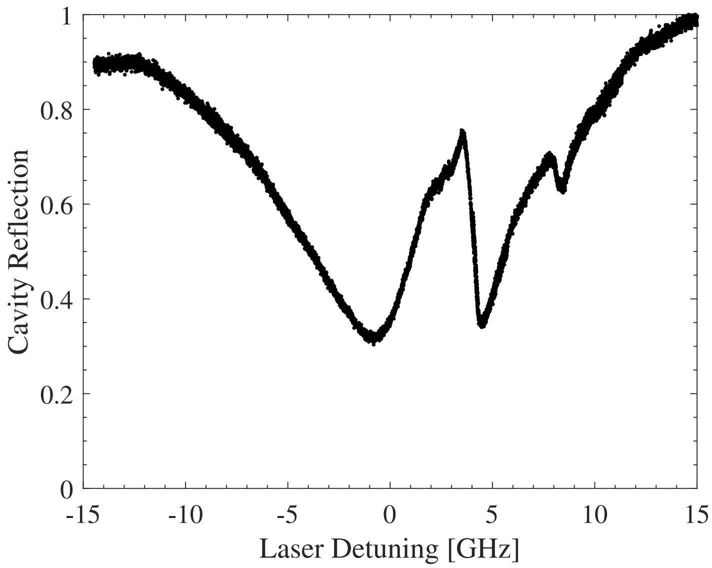

Figure 7.8: Ion cavity coupling spectrum at optical frequencies. The two coupling points correspond to coupling between $|-\rangle_g$ and both excited states. Transitions with coupling to level, $|+\rangle_g$, are not observed as the device is cold and this level has little population in it.

Due to the relatively large cavity linewidth (i.e. $\kappa_o > \omega_{\mu,0}$), all the optical transitions couple to the same optical cavity mode. Since $\kappa_o \gg g_{o,tot}, \Delta_o$, we observe a reflection peak within the cavity reflection spectrum corresponding to the ion-cavity coupling. From fitting of the spectrum, we obtain $\kappa_o/2\pi = 13.2$ GHz and $g_{o,tot,\parallel}/2\pi = 2.0$ GHz and $g_{o,tot,\perp}/2\pi = 0.98$ GHz for optical transitions $|-\rangle_g \leftrightarrow |-\rangle_e$ and $|-\rangle_g \leftrightarrow |+\rangle_e$, respectively. The inhomogeneous linewidth was measured in photoluminescence resulting in an optical ensemble co-operativity of $C_{o,\parallel} = \frac{4g^2_{o,tot,\parallel}}{\kappa_o\Delta_o} = 4.1$ and $C_{o,\perp} = 1.1$. As noted in Chapter 4, only part of this coupling is associated with the magnetic dipole moment that we predict to be the dominate dipole moment that can be used for transduction.

Microwave Cavity Quality Factor

During the transduction process, we require a magnetic field of $\sim 60 - 80$ mT and optical power circulating in the optical resonator. We also condensed nitrogen gas on the microwave resonator during the process of tuning the optical cavity in resonance with the Z_1-Y_1 transitions. It is useful to see how all these factors affect the internal quality factor of the microwave resonator.

The internal microwave quality factor as a function of the circulating photon number in the microwave cavity is shown in Figure 7.9 at four distinct configurations. First, the quality factor at the initial cool down to the base temperature (blue trace). Second, the quality factor after gas tuning (red trace). Third, the quality factor after ramping the magnetic field up to 78 mT. And lastly, the quality factor while the magnetic field is 78 mT and 1 mW of optical power is applied to the optical resonator.

After gas tuning the optical resonator, we see a decrease in the low microwave power internal quality factor from $Q_{\mu,i} \sim 50,000$ to $Q_{\mu,i} \sim 30,000$. We also observe a shift in the resonance frequency of ~ 1.5 MHz due to the permittivity of condensed nitrogen being slightly larger than vacuum. The high power quality factors are nearly identical, which indicates the additional losses from the nitrogen gas condensation can be saturated with microwave power. It is not clear if the losses from the gas tuning are a result of the loss tangent of condensed nitrogen itself or impurities in the nitrogen gas that we use.

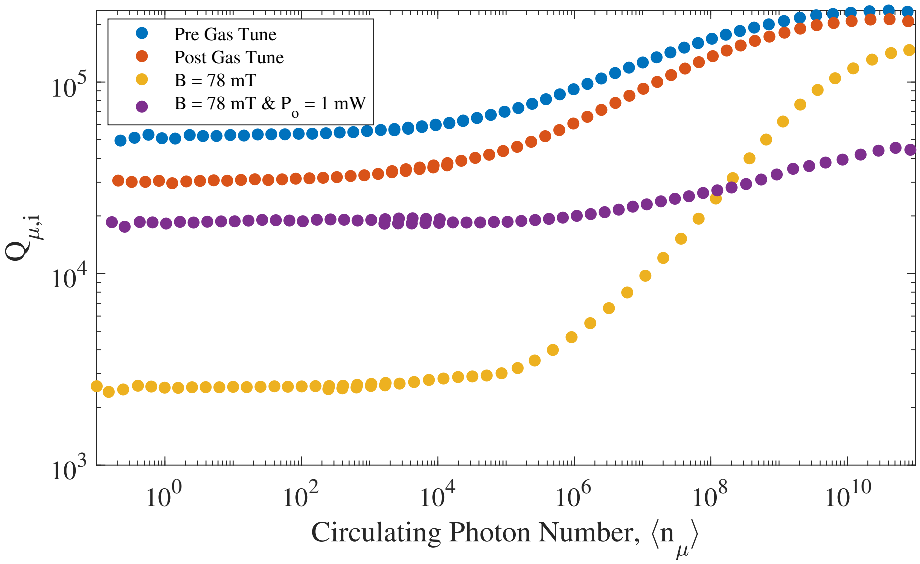

Figure 7.9: Microwave internal quality factor as a function of the circulating photon number in four distinct regimes. These include: before gas tuning the optical device (blue trace), after gas tuning the device (red trace), in a magnetic field of 78 mT (yellow trace) and in a 78 mT magnetic field and 1 mW of optical power applied to the optical device (purple trace).

After adding the 78 mT magnetic field, the internal quality factor drops significantly at low microwave power. We attribute this to the ^{167}Er isotopes that have hyperfine transitions that overlap with the microwave cavity frequency around this magnetic field (see Figure 3.8). These spins can be saturated away at high microwave power and we can recover a high internal quality factor.

Lastly, we added 1 mW of optical power at the same magnetic field. At low microwave power, we observe an increase in the internal quality factor compared to without applying any optical power. We attribute this to the optical power heating up the chip, which saturates the absorption that is limiting the quality factor. Although optical power does generate quasi-particles and microwave losses itself, it appears at low microwave power the heating that saturates the spin or TLS absorption is the dominate factor. At high microwave power, the internal quality factor is lower compared to no optical power. We attribute this to the fact that the high microwave power is used to saturate the absorption, so now the quasi-particle related losses from the optical power dominate and reduce the quality factor.

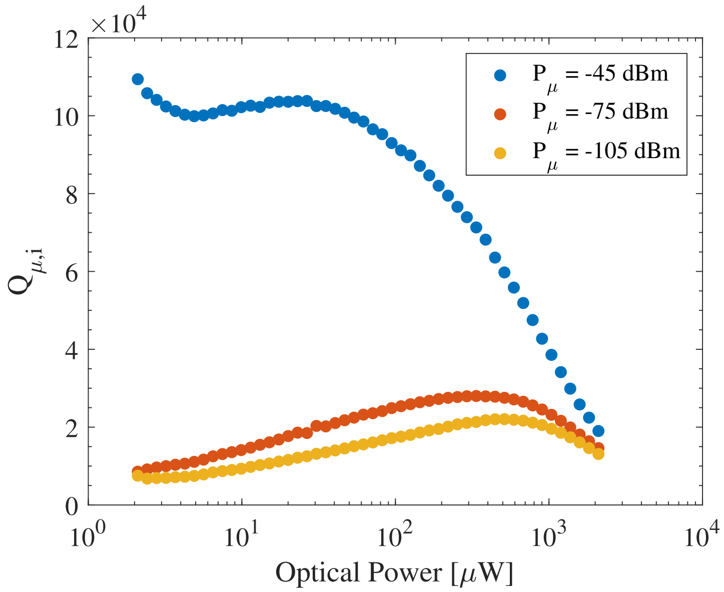

Figure 7.10: The microwave internal quality factor as a function of the input optical power to the optical device. The different traces correspond to different microwave powers applied to the microwave resonator.

Next, we looked at how the internal quality factor changed as a function of the optical power at three different microwave power levels as shown in Figure 7.10. The highest microwave power, $P_\mu = -45$ dBm, corresponds to a circulating photon number of $\langle n_\mu \rangle \sim 10^{10}$ photons, the middle microwave power, $P_\mu = -75$ dBm, corresponds to $\langle n_\mu \rangle \sim 10^7$ photons, and the lowest microwave power, $P_\mu = -105$ dBm, corresponds to $\langle n_\mu \rangle \sim 10^4$ photons.

At low microwave power, increasing the optical power up to $P_o \sim 500$ μW increases the internal microwave quality factor, which we attribute to a steady increase in the device temperature. The optical power increases the internal quality factor from $Q_{\mu,i} = 2,800$ at no optical power to a maximum value of $Q_{\mu,i} = 22,000$. Above $P_o \sim 500$ μW, the quasi-particle losses start to dominate and the quality factor starts to decrease again.

At high microwave power, increasing the optical power is not beneficial as the high microwave power is already saturating the absorption, so we just observe the quasi-particle related losses once they start to dominate above $P_o \sim 30$ μW and see the internal quality factor decrease.

Microwave Ion Cavity Coupling vs Optical Power

Next, we measured at the microwave ion-cavity coupling as a function of continuous-wave optical power, as shown in Figure 7.11, to determine the heating from the optical light. Figure 7.11(a-g) shows the ion-cavity coupling as a function of the magnetic field by measuring the cavity spectrum on the network analyzer. Increasing the temperature, decreases the population difference of the spins, which reduces the ensemble coupling and causes the mode splitting of the microwave cavity and spin system to decrease. Importantly, the coupling to the hyperfine transitions decreases significantly at higher optical power (or temperature) and this will be relevant in the transduction measurement section. Figure 7.11h) is summary of the fitted ensemble coupling, $g_{\mu,tot}$, for the different optical powers using Equation 1.13.

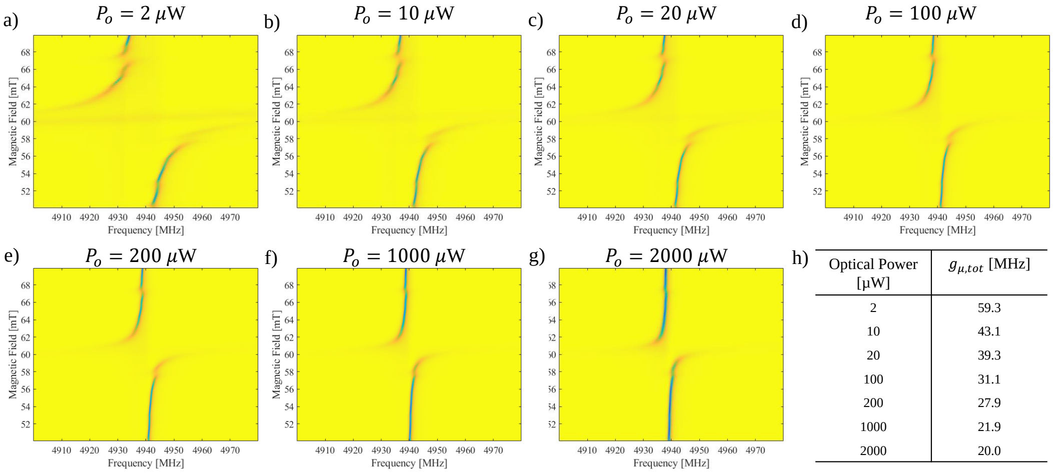

Optical Power [μW]	$g_{\mu,tot}$ [MHz]
2	59.3
10	43.1
20	39.3
100	31.1
200	27.9
1000	21.9
2000	20.0

Figure 7.11: a)-g) The spin-cavity coupling spectrum vs magnetic field for different optical powers. h) Table of the fitted ensemble coupling, $g_{\mu,tot}$, for the different optical powers.

Next, we infer the spin temperature by relating the ensemble coupling to the population inversion using $g_{\mu,tot} = \sqrt{\Delta N/N} g_{\mu,tot,max}$, where $g_{\mu,tot,max}$ is the ensemble coupling at zero optical power and $\Delta N/N$ is the normalized population difference between the two ground state spin levels. The normalized population difference between two levels separated in energy of, $\hbar\omega$, at temperature, T, is given by:

$$\frac{\Delta N}{N} = \frac{N_{|->_g} - N_{|+>_g}}{N_{|->_g} + N_{|+>_g}} = \frac{1 - e^{-\frac{\hbar\omega}{k_b T}}}{1 + e^{-\frac{\hbar\omega}{k_b T}}}. \tag{7.2}$$

We plot Equation 7.2 for $\omega/2\pi = 4.94$ GHz (i.e. the resonance frequency of our microwave cavity) in Figure 7.12a. The temperature is below 100 mK when the normalized population difference is above 90% and then increases rapidly as the population difference decreases.

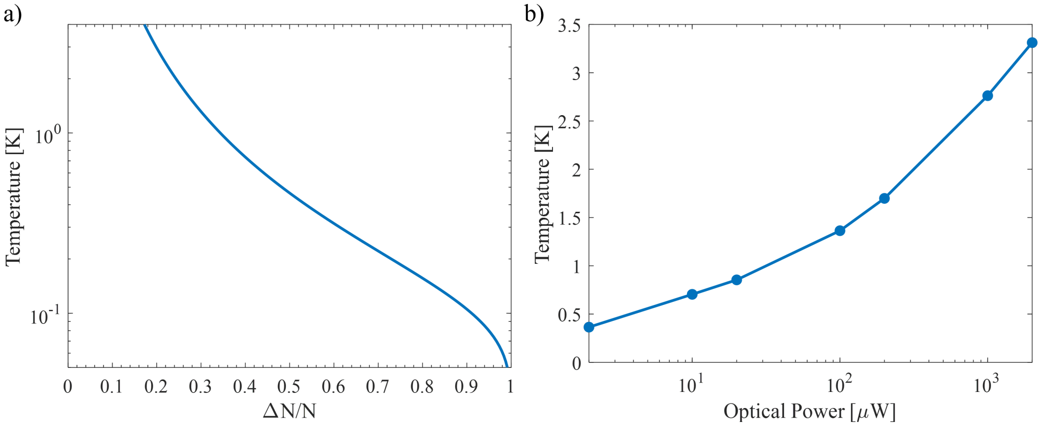

Figure 7.12: a) The spin temperature as a function of the normalized population difference between the two ground state spin levels (i.e. $|-\rangle_g$ and $|+\rangle_g$). b) The temperature of the spins coupled to the microwave resonator as a function of optical power.

Using the data in Figure 7.11 and Equation 7.2, we determine the spin temperature for each optical power as shown in Figure 7.12b. Even though the fridge reaches a base temperature of 35 mK, the spins heat up to T$\sim$ 3 − 4 K at high optical power. The mixing chamber stage temperature also increases up to a few hundred mK at the highest optical power we used. In order to have low temperature with continuous wave optical power, low optical power is required (likely $P_o \ll 1$ μW). Alternatively, pulsed optical power can lower the average power and potentially decrease the temperature that way.

Spin Relaxation Measurements

In order to measure the spin relaxation, we follow a similar procedure as King et al. [58], where we saturate the spins that are strongly coupled to the microwave cavity and monitor the polariton modes recovery as a function of time to determine the relaxation timescale. Importantly, this method is only sensitive to the net difference in population, so we are insensitive to spin-spin relaxation within the resonator volume.

One difference in our measurement is that we operate in a detuned regime between the spins and the cavity (i.e. $\omega_i - \omega_{\mu,0} \gg \kappa_\mu, \Delta_\mu, g_{\mu,tot}$) such that the coupled mode frequency shift from the spin coupling goes as $\sim \frac{g_{\mu,tot}^2}{\omega_i - \omega_{\mu,0}}$.

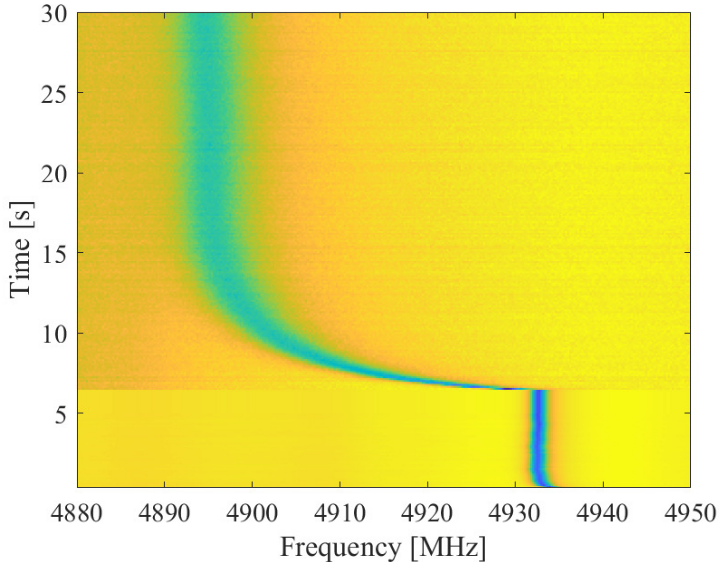

Figure 7.13: Network analyzer spectrum over time to observe the spin relaxation dynamics. The spins are initially saturated at high input microwave power before the power is reduced to observe the relaxation.

We first measure this relaxation at the base temperature and with no optical power. First, we apply P_μ = –40 dBm of microwave power as we sweep the network analyzer frequency for 5 seconds to saturate the spin transition. We then turn down the network analyzer power to P_μ = –75 dBm and monitor the spins returning to the ground state by measuring the mode pulling increase as shown in Figure 7.13.

We normalize the frequency shift and fit the decay to a stretched exponential function $f(t) = \exp[-\left(\frac{t}{\tau}\right)^x]$ and obtain a decay time constant, $\tau = 1.61$ s, and $x = 0.72$.

Next, we looked at the relaxation under the presence of optical power up to 1 mW. For optical power at or above $P_o = 50\ \mu$W, the relaxation is too fast for the network analyzer sweeping method, so we switch to using a digitizer to detect the signal. In this detection method, the network analyzer first applied a sweeping signal at with microwave power of P_μ = –40 dBm to saturate the spins. That signal is turned off and we then send in a weak microwave signal at P_μ = –75 dBm. We then mix the output signal with a local oscillator down to 21.4 MHz and detect the beat note on a digitizer. This is repeated for each microwave frequency to measure the cavity spectrum.

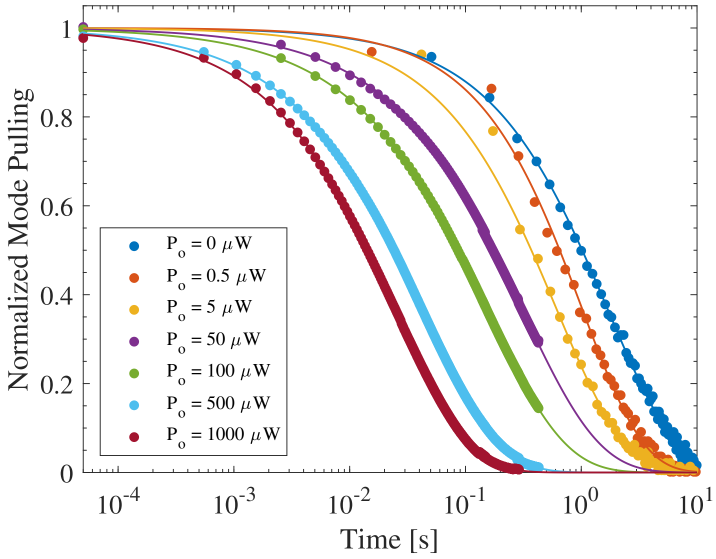

Figure 7.14: Spin relaxation dynamics as a function of the applied optical power. The frequency shift that is observed as the spins relax is normalized here for convenient comparison between the different optical powers.

A summary of the relaxation dynamics for different optical power are shown in Figure 7.14. Here, we normalize the frequency shift caused by the spin relaxation such that we can more easily compare the results. The data points (circles) correspond to the normalized mode frequency at a given time. The solid line corresponds to the stretched exponential fit.

We observe significant decrease in the relaxation timescale as the optical power increases from τ = 1.61 s at no optical power to τ = 25 ms at 1 mW of optical power. A summary of the fitted decay constants at different powers is shown in Table 7.1.

Table 7.1: Spin relaxation time constant vs optical power

Optical Power [μW]	τ [s]
0	1.61
0.5	1.02
5	0.612
50	0.306
100	0.152
500	0.042
1000	0.025

7.3 CW Microwave to Optical Transduction

Coherent microwave-to-optical conversion was initially measured in continuous-wave (CW) mode using a Raman heterodyne technique. The input microwave photons are transduced to optical photons which are then mixed with an optical local oscillator on a photodetector. The generated microwave beat note signal is measured with a network analyzer. This is shown in Figure 7.15a.

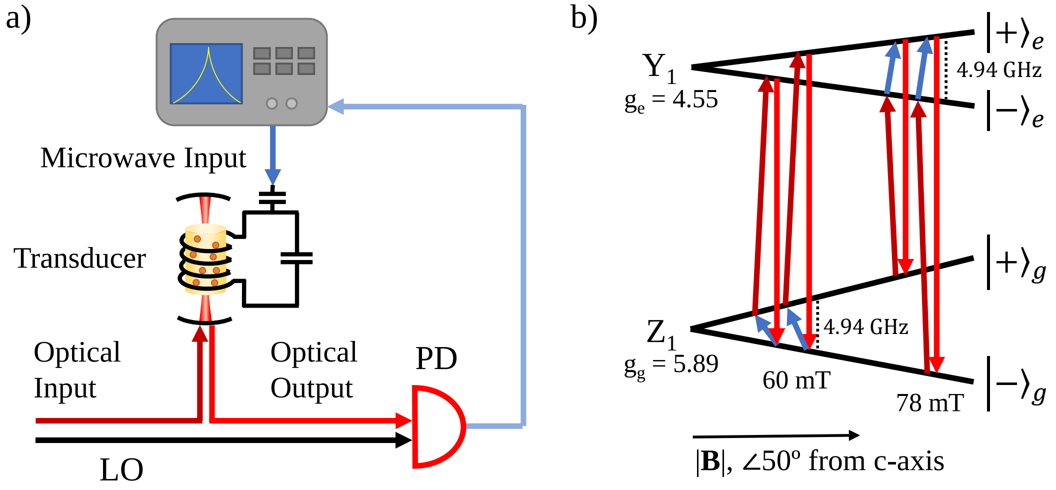

Figure 7.15: a) Heterodyne detection setup where the output transduced signal is mixed with an optical LO on a photodetector and measured on a network analyzer. b) Level structure of Z_1-Y_1 as a function of the magnetic field in the context of microwave to optical transduction. The upwards pointing arrows correspond to input photons and the downward arrow is the output optical photon. The blue arrow is for the microwave transition, the dark red arrow is for the optical pump and the light red arrow is for the output optical field. By changing the magnetic field strength, we can perform transduction in either the ground or excited state. g_{dc} for the Zeeman splitting of each doublet is labelled as g_g and g_e.

In order to observe all possible atomic configurations of our erbium ions that generate a transduction signal (Figure 7.15b), we first do a three parameter sweep. This includes a sweep of the magnetic field to bring either the ground state (or excited state) spin transitions into resonance with the microwave cavity, the pump laser frequency across different optical transitions and the input microwave frequency across the microwave cavity. We fix the optical and microwave power to be P_o=7 μW and P_μ= –51 dBm (as measured at the input of the device) to provide a high signal-to-noise ratio (SNR=18 dB) heterodyne spectra. At this optical power in CW mode the device temperature reaches T~700 mK, but the temperature can be reduced by operating in a pulsed regime.

In Figure 7.16a, we simplify this three dimensional parameter sweep by setting the microwave frequency to the microwave cavity (i.e. the microwave frequency with the highest efficiency) and sweep both the pump laser frequency and the magnetic field strength. There are four configurations for transduction which include two conditions that use the ground state spin (lambda systems) at ~60 mT and two conditions that use the excited state spin (V system) at ~76 mT. The laser frequency difference between the two λ systems corresponds to the excited state spin frequency and likewise the laser frequency difference between the two V systems corresponds to the ground state spin frequency. The slopes of the transduction signals correspond to the transition frequency shifts with the applied magnetic field. The transduction signal decreases when the microwave cavity is resonant with the ground state spin (60 mT) due to extra losses from the parasitic ions but can be increased 8 dB by detuning the spins ~150 MHz from the microwave cavity at 62 mT.

In Figure 7.16b, we select the laser frequency that provides the highest transduction efficiency and sweep the microwave frequency and the magnetic field. The transduction signal follows the microwave cavity resonance frequency. At ~60 mT, we observe a splitting in the signal that corresponds to the strong coupling of the ground state spins with the microwave cavity. We also observe the frequency shifts slightly at higher magnetic fields which we attribute to the microwave cavity coupling to various hyperfine transitions.

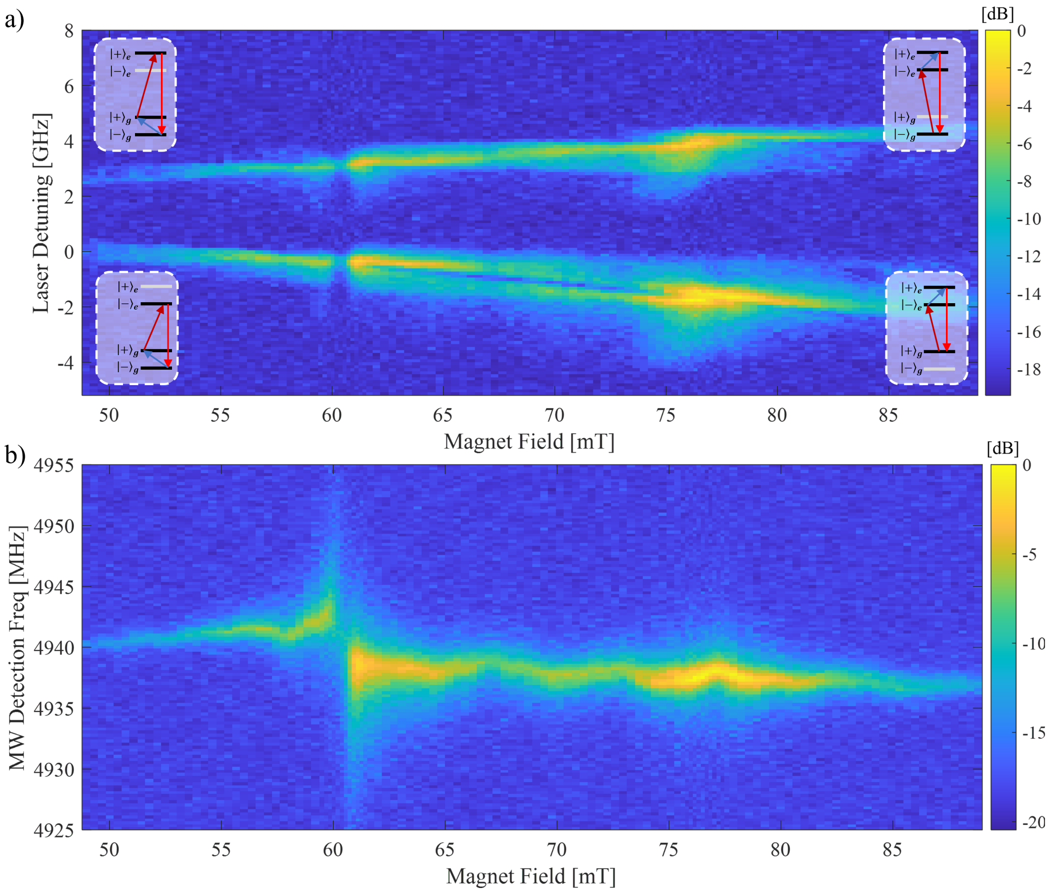

Figure 7.16: Normalized heterodyne spectrum where the applied bias magnetic field and the pump laser frequency are swept. The four configurations (as labelled in the inset level structure diagrams) for transduction with Er^{3+}:YVO_4 are identified. The microwave frequency is set to the microwave cavity resonance.

In Figure 7.17, we show the transduction device efficiency for both the ground state and excited state at P_o = 500 μW and P_μ = -51 dBm as a function of the input microwave frequency. We focus on the transduction configurations where the pump laser is coupled to the $|+\rangle_g \leftrightarrow |-\rangle_e$ transition as these configurations have higher efficiency in CW mode operation (i.e. the pump laser frequency is selected to maximize the efficiency and is near the center of the inhomogeneous line here and in all proceeding measurements). The bandwidth of the transduction signal is 1 MHz for excited state transduction and 1.2 MHz for ground state transduction, which matches the microwave cavity linewidth for each measurement.

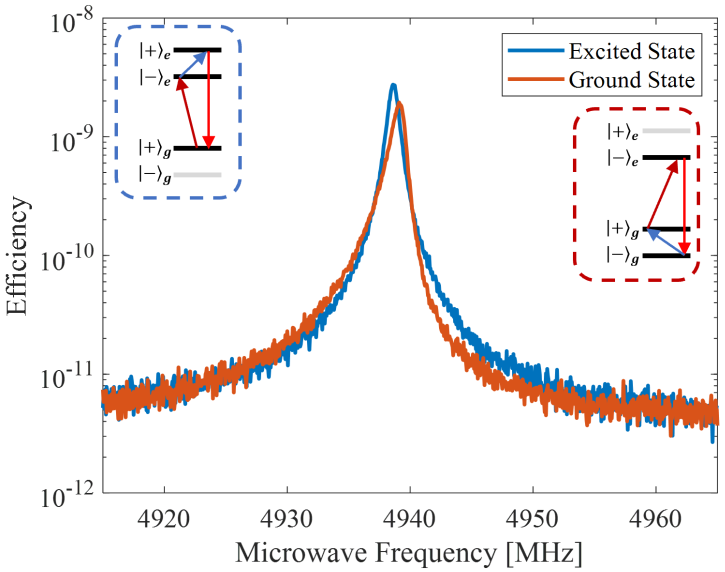

Figure 7.17: Transduction efficiency spectrum for the ground (red) and excited (blue) state spins as a function of the applied microwave frequency. The input optical power is $P_o = 500\ \mu$W and microwave power is P_μ= -51 dBm. The level structures used for the excited state transduction is shown in the left inset and the level structure used for the ground state transduction is shown in the right inset.

For the ground state, we measure an device efficiency of $\eta_d = 2 \cdot 10^{-9}$ at 62 mT magnetic field and for the excited state we measure an efficiency of $\eta_d = 3 \cdot 10^{-9}$ at 76 mT under CW optical and microwave power. We define device efficiency as the photons into the optical fiber at the output compared to the input microwave photons into the microwave coupling waveguide. The ground state signal has an asymmetric line shape due to the large microwave power that drives the spins during the measurement.

Next, we measure the efficiency dependence on both the optical and microwave power for ground and excited state transduction in Figure 7.18. Typically for M2O transducers increasing the optical pump power increases the transduction efficiency until the optical power induces a detrimental effect such as device heating or microwave cavity degradation. In our on-chip REI transducer, the CW device efficiency reaches a maximum at P_o=500 μW before it decreases primarily due to device heating, which limits the spin population difference, and saturation of the optical transition being driven by the pump field.

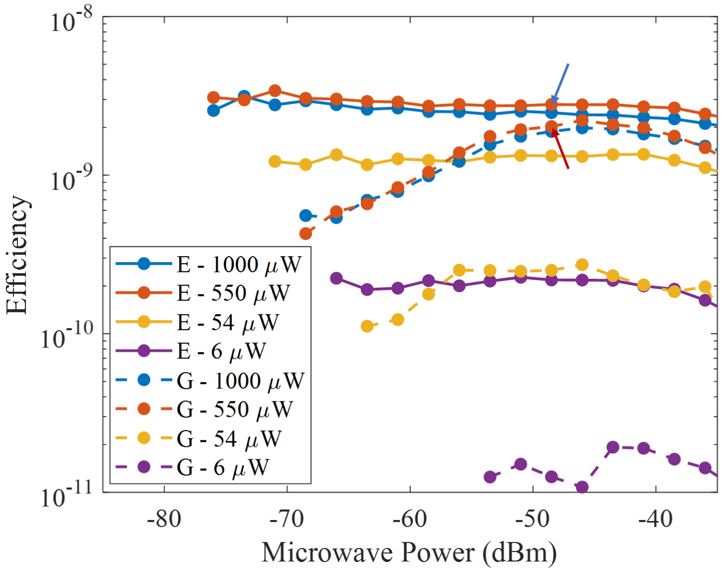

Figure 7.18: Transduction efficiency for the ground state (dotted lines) and the excited state (solid lines) at different input optical and microwave power. The arrows correspond to the power parameters used in Figure 7.17, where the arrow color matches the trace colors in the figure. In the legend, E denotes transduction with the excited state and G denotes transduction with the ground state.

As the microwave power is reduced (i.e. $P_\mu < -50$ dBm), the ground state efficiency decreases as the input microwave tone is no longer saturating the absorption from the parasitic spins that diminish the transducer efficiency. This makes excited state transduction more promising in the low microwave power, low temperature regime. We should note that excited state transduction is likely to be favored in most atomic systems, but ground state transduction should also work well in a more optimized transducer.

Calibrating CW Efficiency

The detected device efficiency is determined by the ratio of the output optical photons in the optical fiber compared to the input photons in the superconducting microwave coupling waveguide. On the photon output side, we need to convert from heterodyne power to optical power incident on the detector and then account for optical losses of the detection setup. For the microwave input, we need to calibrate the microwave losses of the input microwave signal from the microwave source to the superconducting coupling waveguide.

The detected heterodyne power on the network analyzer can be related to the output optical power from the transducer using:

$$P_h = G\mathcal{R}^2 P_{LO} P_t R_{50\Omega}/2 \tag{7.3}$$

where P_h is the detected heterodyne power, G is the gain, $\mathcal{R}$ is the photodetector responsivity, P_{LO} is the power of the optical local oscillator (typically $\sim$ 1 mW), P_t is the transduced power at the detector and $R_{50\Omega}$ is the impedence of the analyzer. We divide by 2, since the setup is not phase stable so we measure the time-average beat note between the transduced signal and local oscillator, which is half of the maximum.

The responsivity of the detector is $\mathcal{R} = 0.9$ A/W. The gain of our amplification chain after the photodetector is 66 dB (i.e. 33 dB for each of two amplifiers). We account for the losses of the 50/50 fiber beamsplitter and fibers that we use to combine the transduced signal and the local oscillator (which is the –3 dB loss of the 50/50 beamsplitter and –1.5 dB of excess loss). We also account for electrical losses of the bias tee and coaxial cable from the photodetector to the amplifiers and network analyzer (–1.65 dB).

For the microwave input losses, we first naively calculate the expected losses from component data sheets. This includes –40 dB in loss from the 4x -10 dB attenuators. The coaxial cable from the mixing chamber stage to the chip (Fairview FMC0221085-18) should give –0.5 dB of loss. From the coaxial cable from the 4 K stage to the mixing chamber stage (SC-086/50-SCN-CN), we expect –2.3 dB of loss. The coax from the 4 K stage to room temperature inside the fridge should add –1.7 dB of loss. The room temperature cable from the VNA output to the top of the fridge (PE341-200CM) should have –1.8 dB of loss. This all combines for –46.3 dB of loss from the network analyzer output to the superconducting coupling waveguide.

We can also compare the microwave transmission from a network analyzer $|S_{21}|^2$ measurement and the calibrated output gain of the output line to infer the input line losses. We measure –8.3 dB of loss of the total microwave circuit (this includes the input and output gain and losses). From the calibrated output gain of 70.5 dB, 33 dB of this is from the room temperature microwave amplifier that is not used in the network analyzer output measurement, so we should remove that factor. Therefore, we can infer the input losses to be –45.8 dB, which is very close to the expectation from the component data sheets.

7.4 Pulsed Excited Transduction with Single Photon Detection

Next, we looked at pulsed operation of the transducer to reduce the device temperature and increase the device efficiency. Short transduction pulses and small duty cycles are helpful in the pulse regime to lower the device temperature and minimize optical transition saturation effects due to large driving fields, which limited the device efficiency when the transducer is operated in CW mode.

We also switched our transduction detection setup from the heterodyne detection scheme used in the CW mode to direct photon detection of the transduced photons. Here, we use our filtering set-up to remove the pump laser noise photons in the frequency domain from our transduced signal photons before detection on a SNSPD (Figure 7.19a). Photon detection is advantageous due to the decreased noise floor, especially for short pulses/high bandwidth measurements, and it is the more natural detection setup for measuring transduced single photons [42]. In heterodyne detection, the noise floor power increases linearly with the bandwidth (i.e. SNR decreases at shorter pulses). Conversely, with single photon detection the noise photon rate is independent of the pulse length (i.e. SNR is constant with pulse length, assuming constant efficiency), so it is better suited for detecting short pulses.

For the pulsed experiments, we use square optical and microwave pulses as shown in Figure 7.19b. We refer to the duration of the pulse as τ_{pulse}, while the wait time between adjacent pulses is referred to as τ_{wait}. We did also experiment with Gaussian pulses, but that offered no substantial difference in the transducer performance and was more complicated to implement, so we reverted back to square pulses.

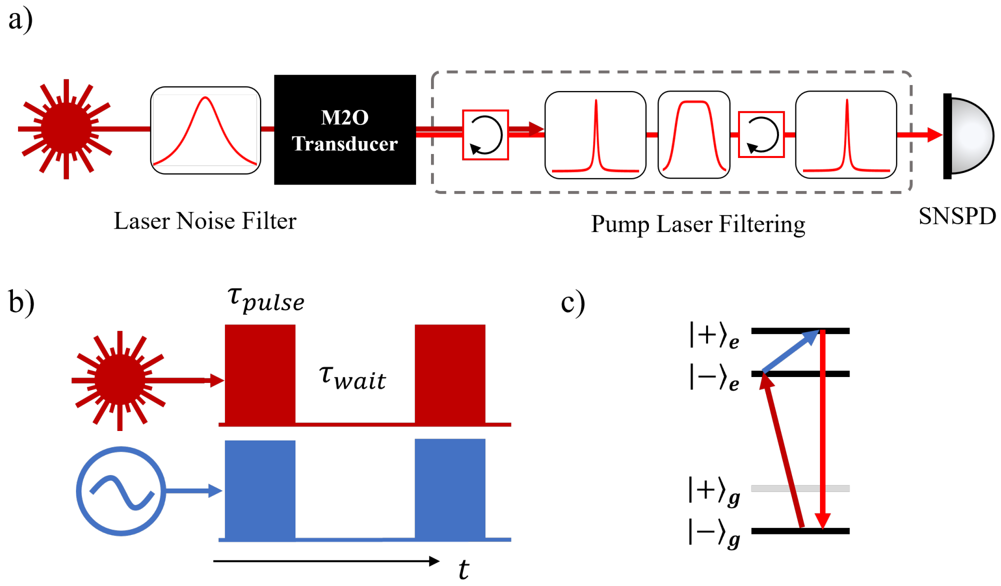

Figure 7.19: a) Single photon transduction detection set-up for measuring transduction signals. The laser source is filtered to remove its broadband noise before the transducer. After the transducer, the main tone of the laser is filtered with high-finesse Fabry-Perot cavities before detection on a SNSPD. b) Pulse sequence configuration, where we have a square pulse of length, τ_{pulse}, and a wait time between pulses of length, τ_{wait}, for both the optical and microwave pulses simultaneously. c) The level structure used for the pulsed excited state transduction process used in this section.

For measuring pulsed M2O transduction, we focus primarily on using the excited state spin transition so that we can reduce the effects of the parasitic ions that couple to the microwave cavity that are especially detrimental in the ground state. There are ^{167}Er ground state spin transitions near the excited state spin transition of the even isotopes, so we choose a magnetic field of 76 mT to best avoid those parasitic transitions. Future devices can use isotopically purified even isotopes of erbium to avoid this issue.

Compared to the previous CW excited state transduction, we move the pump frequency to the $|-\rangle_g \leftrightarrow |+\rangle_e$ transition such that the population in the involved ground state only increases as we decrease the temperature. The level structure that we used for excited state pulsed transduction is shown in Figure 7.19c.

We first characterize the transducer bandwidth by measuring the transduced pulse as a function of the pulse duration at a fixed duty cycle (duty cycle = τ_{pulse}/τ_{wait}) of 0.01% with P_μ = –60 dBm microwave power and P_o =550 μW optical power (Figure 7.20a). This is the microwave and optical power used for pulsed transduction experiments unless otherwise noted. We only consider relatively short pulses (i.e. τ_{pulse} < 10 μs) to avoid significant heating during the transduction pulse. The efficiency reaches –3 dB of the maximum efficiency as the pulse length decreases to τ_{pulse}=630 ns, which matches the microwave cavity bandwidth. The maximum efficiency in this parameter sweep is $\eta_d = 6 \cdot 10^{-8}$.

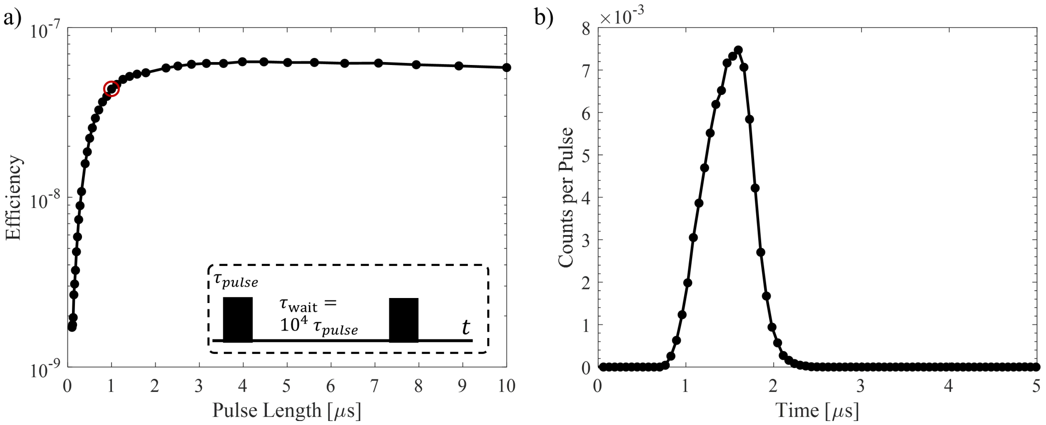

Figure 7.20: a) Pulsed transduction efficiency as a function of the pulse length with a fixed duty cycle (τ_{pulse}/τ_{wait} =0.01%, as shown in the inset). b) The output counts per pulse for a pulse duration of 1 μs as a function of time. The bin size is 64 ns.

A time trace of the 1 μs transduced pulse is shown in Figure 7.20b. The timing resolution is 64 ns. The total output photon rate per pulse (referenced to the fiber at the output of the transducer and before the pump filtering) is 0.08 photons per pulse. The noise photons per pulse in this experiment is $\sim 10^{-5}$ photons per pulse, which results in SNR$\sim$ 40 dB. Using this significantly improved SNR ratio (i.e. compared to heterodyne measurements), we can explore the parameter space more deeply. We note that although the SNR is high, the acquisition time is slower compared to heterodyne detection. With SNSPD detection, we need to measure every microwave frequency independently and lock the filtering setup for each frequency, while with heterodyne detection we can sweep the frequency on the network analyzer and collect data more quickly. We fix our transduction pulse length to τ_{pulse} =1 μs for all subsequent pulsed measurements, as noted by the red circle in Figure 7.20a. The red circles in the different plots refer to a common set of experimental parameters for the different parameter sweeps. Shorter pulses help reduce the heating from the optical pulse.

Next, we measure the transducer efficiency as a function of the wait time between adjacent transduction pulses (Figure 7.21). We also sweep the microwave input frequency, since as the wait time increases, the device becomes colder and the microwave cavity frequency shifts (Figure 7.21a). As the ground state spins become colder, the dispersive shift of the microwave resonator from the detuned ground state spins increases. The maximum expected dispersive shift of the ground state spin at the magnetic field for excited state transduction is $\frac{g_{\mu,tot}^2}{\omega_i-\omega_{\mu,0}} = (105\text{ MHz})^2/1.3\text{ GHz} = 8.6\text{ MHz}$. At long wait times (i.e. τ_{wait} >100 ms), the experimental acquisition time becomes very long, so we only sweep the microwave frequency near the maximum value.

For each wait time, we select the microwave frequency that results in the highest efficiency as shown in Figure 7.21b. As we increase the wait time from $\tau_{wait} = 30\ \mu$s to 100 ms, we observe an increase in efficiency from $\eta_d = 9 \cdot 10^{-9}$ to $\eta_d = 7 \cdot 10^{-8}$. We attribute the increase in efficiency to a reduction in the device temperature and limiting the atomic transition saturation that limited the CW transduction efficiency. The wait time of τ_{wait}=10 ms is used for subsequent measurements as the longer wait times require longer acquisition times and the increase in efficiency is modest.

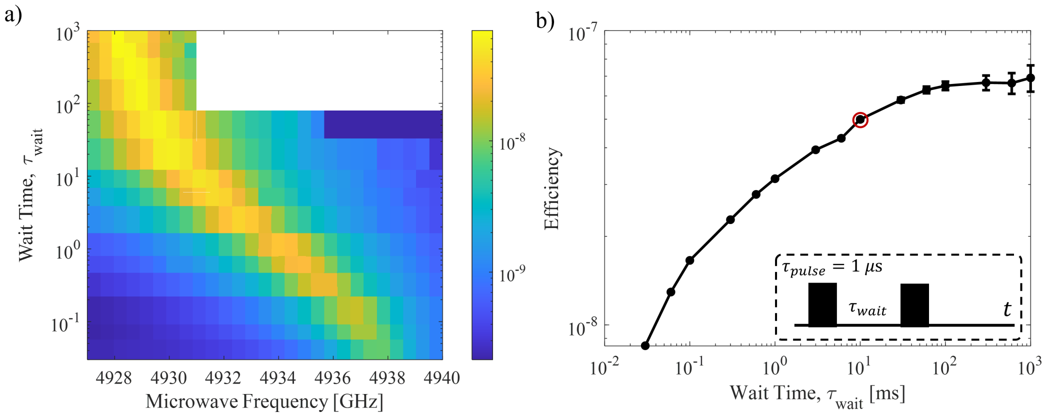

Figure 7.21: Transduction efficiency as a function of the wait time between transduction pulses. a) 2D scan showing the transduction signal frequency shift as the wait time increases. b) The maximum transduction efficiency for each wait time. The pulse duration is 1 μs as shown in the inset.

Next, we sweep the optical pump power and observe a continuous increase in the efficiency up to $\eta_d = 2 \cdot 10^{-7}$ with a maximum optical pump power of $P_o = 5$ mW (Figure 7.22a). This differs from the CW operation where the efficiency reached a maximum at $P_o = 500\ \mu$W. The rate of efficiency increase with optical power (i.e. $d\eta_d/dP$) decreases at the highest optical power in the pulsed mode, which does suggest that we are approaching the highest efficiency for this device in the pulsed operation.

We also measured the pulsed transduction efficiency as a function of the input microwave power (Figure 7.22b). Ideally, we could characterize the transducer at the single photon level where a quantum transducer would operate. Here, we are limited by the modest device and detection efficiency and the finite measurement noise of the setup to measure input microwave pulses with at least $\sim 10^4$ photons. At P_μ= −100 dBm ($\sim 10^4$ microwave photons per pulse), we observe a maximum pulsed excited state transduction efficiency of $\eta_d = 6 \cdot 10^{-8}$. There is an efficiency roll-off at $P_\mu \sim -55$ dBm ($\sim 10^9$ microwave photons per pulse) that we attribute to saturation of the microwave transition. Notably, we do not see the efficiency drop at lower microwave power indicating that we could expect similar performance at the single photon level as the 10^4 photon level that we were able to measure.

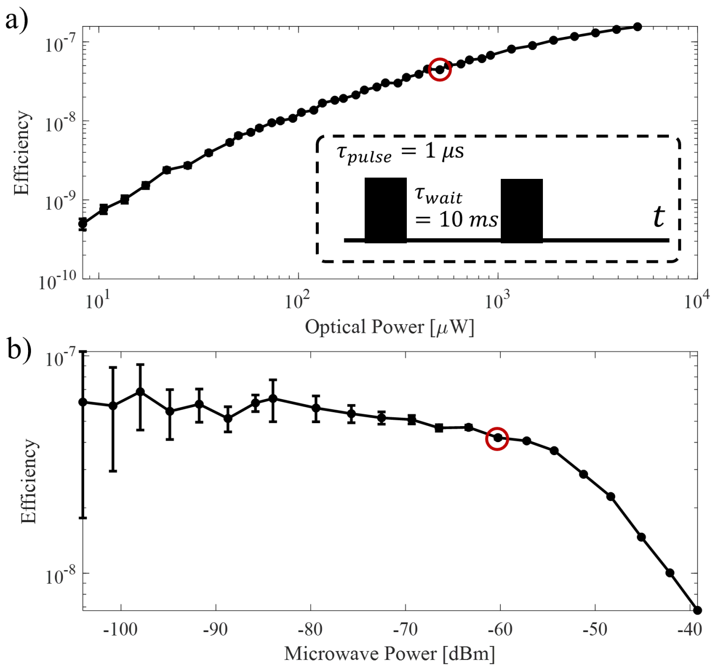

Figure 7.22: Transduction efficiency as a function of the a) microwave power and b) optical power. The pulse sequence used for these parameter sweeps is shown in the inset.

Next, we looked at the transduction efficiency as a function of the magnetic field in Figure 7.23a. We obtain the highest efficiency at a magnetic field of 76 mT, which is the field chosen for the other pulsed excited state transduction measurements. The signal has a complicated and asymmetric line shape that we attribute to the ^{167}Er hyperfine transitions that can absorb microwave photons.

As shown in Figure 7.23b, we expect several hyperfine transitions around the microwave resonator frequency near the magnetic field for excited state transduction. This is a closer look of the hyperfine simulation previously shown in Figure 3.8. Therefore, in order to have high efficiency in the excited state, the excited state spin should be near resonant with the microwave cavity and the hyperfine transitions should be far away from the microwave cavity resonance. This effect should not be a problem in future devices that use isotopically purified erbium instead of the natural abundance erbium used here.

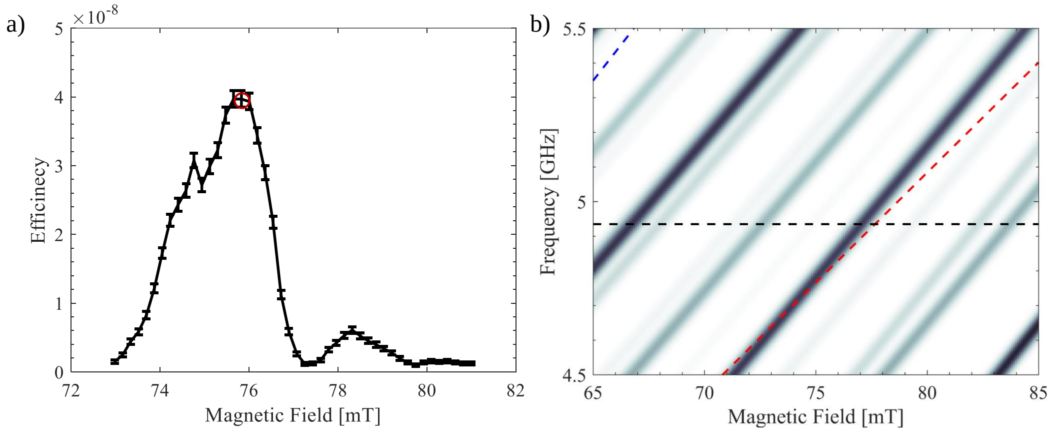

Figure 7.23: a) The transduction efficiency as a function of the magnetic field. The peak efficiency is at 76 mT. b) Simulation of the ^{167}Er hyperfine transitions. The red dashed line is the excited state spin and the black dashed line is the microwave resonator frequency. The blue dash line is the ground state spin.

Lastly for excited state transduction, we looked at the transduction efficiency as a function of the pump laser frequency in Figure 7.24. The maximum efficiency is within 100 MHz of the maximum photoluminescence signal from this transitions (Figure 7.7), so the maximum efficiency corresponds to the case that the optical pump frequency is near resonance of the $|-\rangle_g \leftrightarrow |+\rangle_e$ transition.

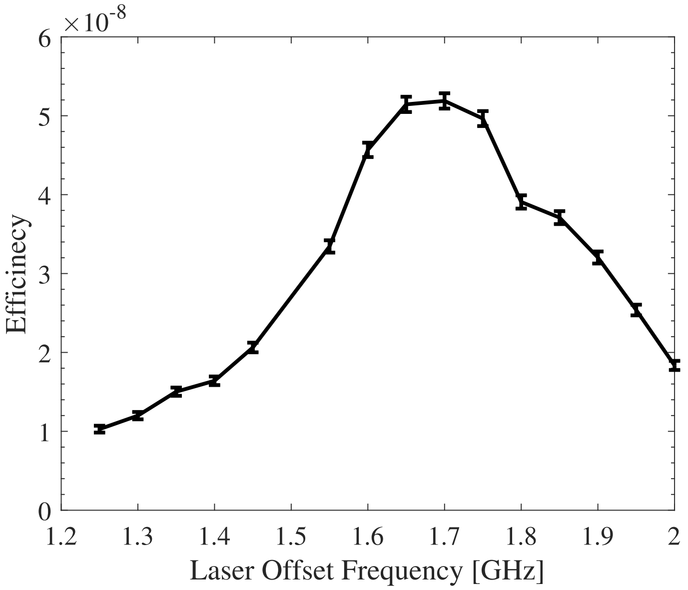

Figure 7.24: Transduction efficiency as a function of the optical pump laser frequency.

Calibrating SNSPD detection efficiency

In order to calculate the pulsed transduction device efficiency from SNSPD detection, we compare the detected photon counts to the input photon number given the input power level, pulse duration and the number of input pulses. We then account for the filter detection losses and SNSPD detection efficiency (i.e. -15 dB as detailed in Chapter 6) to determine the device efficiency. The input microwave loss is 4 dB larger compared to the previous CW heterodyne measurements as we have added a microwave switch here and an additional coaxial cable. In order to determine the detected photon number, we integrate the transduction signal over the time bins associated with the transduction pulse. The noise level is negligible for most measurements, but for the lower SNR measurements, the noise level is subtracted out.

Internal Efficiency

In order to estimate the device internal efficiency from the total device efficiency, we need to take into account the optical and microwave cavity coupling strength compared to all loss channels (i.e. κ_{in}/κ) and the grating efficiency. The optical cavity coupling ratio is $\kappa_{o,in}/\kappa_o = 0.22$. The optical grating coupler efficiency was measured to be 30% by measuring the reflected light from the device.

The microwave cavity coupling ratio depends on the measurement regime as the microwave internal quality factor varies, but ranges between $\kappa_{\mu,in}/\kappa_\mu = 0.25 - 0.4$, where $\kappa_{\mu,in}/\kappa_\mu$ is closer to 0.25 in the colder device temperature experiments and is closer to 0.4 in the higher device temperature experiments. This makes the difference between the internal device efficiency and the total device efficiency to be $\eta_d/\eta_{d,int} \sim 1.7\% - 2.6\%$ (i.e. we estimate the internal efficiency is roughly a factor of 50x larger than the device efficiency).

Simulated Efficiency

From the simulations in Chapter 4, there are some parameters that are slightly different in the experiment compared to the simulation. These are mainly the internal and coupling quality factors. If we account for these difference and account for the 30% grating coupler efficiency, we obtain a simulated excited state device transduction efficiency of $\eta_d = 1.1 \cdot 10^{-7}$ compared to the measured value of $\eta_d = 8 \cdot 10^{-8}$ for $P_o = 550\ \mu$W.

This difference can be attributed to several possible factors. First, we are not accounting for the ^{167}Er hyperfine transitions in the simulation, which could degrade the efficiency slightly, even though we choose the magnetic field to minimize their effect. Also, the optical and spin dephasing rates used in the simulation (i.e. $\gamma_{2d}/2\pi = \gamma_{3d}/2\pi = 10$ MHz) and the excited state spin inhomogeneous linewidth (i.e. $\Delta_\mu = 65$ MHz) are assumed values and further spectroscopy is needed to verify their values in the precise experimental configuration used here.

Having said that, the difference in simulation and experiment is not too large given the uncertainty in a few parameters of the simulation.

7.5 Pulsed Ground State Transduction with Single Photon Detection

We also did some pulsed measurements using the ground state spin with SNSPD detection. The pulsed transduction efficiency using the ground state spin as a function of the magnetic field strength to show the transduction signal following the microwave polariton frequency (see Figure 7.25). This was done for the sequence $\tau_{pulse} = 1$ μs and $\tau_{wait} = 1$ ms. The pump frequency was set to the $|+\rangle_g \leftrightarrow |+\rangle_e$ transition. Although longer wait time would result in a lower temperature, it also makes the data acquisition much slower and would require us to sweep an even larger microwave frequency range to capture the signal.

We observe a splitting in the transduction signal when the ground state spins are resonant with the microwave cavity. We also observe that the transducer efficiency is greater at higher magnetic fields (i.e. 62-64 mT) compared to lower magnetic fields (i.e. 57-59 mT). This asymmetry may be due to hyperfine transitions at the lower magnetic field values that absorb microwave photons and lower the efficiency.

Since ground state transduction was shown to have lower efficiency and was trickier to optimize the parameters, we did not explore it much further with this device. The different experimental parameters of the transducer (i.e. wait time, microwave frequency, magnetic field, etc) are more coupled to each other so its not as straightforward to find an optimal regime to experiments. This is due to the presence of the parasitic even isotope spins that can provide significant mode pulling and modify the transducer frequency or absorption that can lower the efficiency.

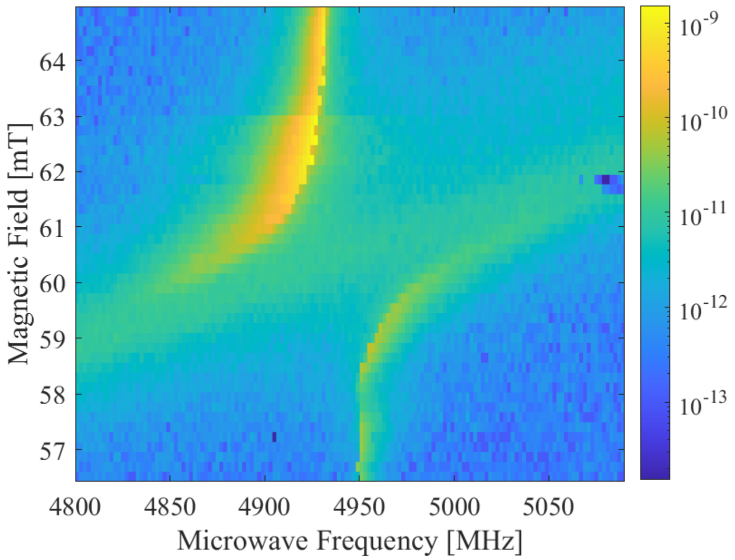

Figure 7.25: Pulsed transduction efficiency using the ground state spins as a function of the magnetic field.

7.6 Transducer Temperature and Noise Measurements

In this section, we take a more detailed look at the temperature and noise of the transducer. During the transduction process, heating from the optical pump (or other mechanisms) can induce noise photons which can pollute the transducer output field. Ideally, to characterize the noise, we would measure the generated noise photons directly at the transducer output. Here, with limited device efficiency and detection noise floor, some noise sources (i.e. thermal microwave excitations) are heavily suppressed, so we cannot faithfully determine reliable noise contributions from those sources from directly measuring the noise at the output. Instead, we follow a similar approach of others to quantify the temperature of different components of the transducer as a way to infer the transducer noise when the transducer efficiency is low [41, 46, 50].

Here, we measure the temperature of the erbium ions and the microwave resonator noise to quantify the optical heating effects during the transduction process, which we suspect to be the dominate noise source for our REI transducer.

Erbium Spin Temperature

For the erbium spins, there are two ensembles that we can characterize. These include all the erbium ions that couple to the microwave resonator and the erbium ions that are used for transduction (i.e. ions within both the optical and microwave modes).

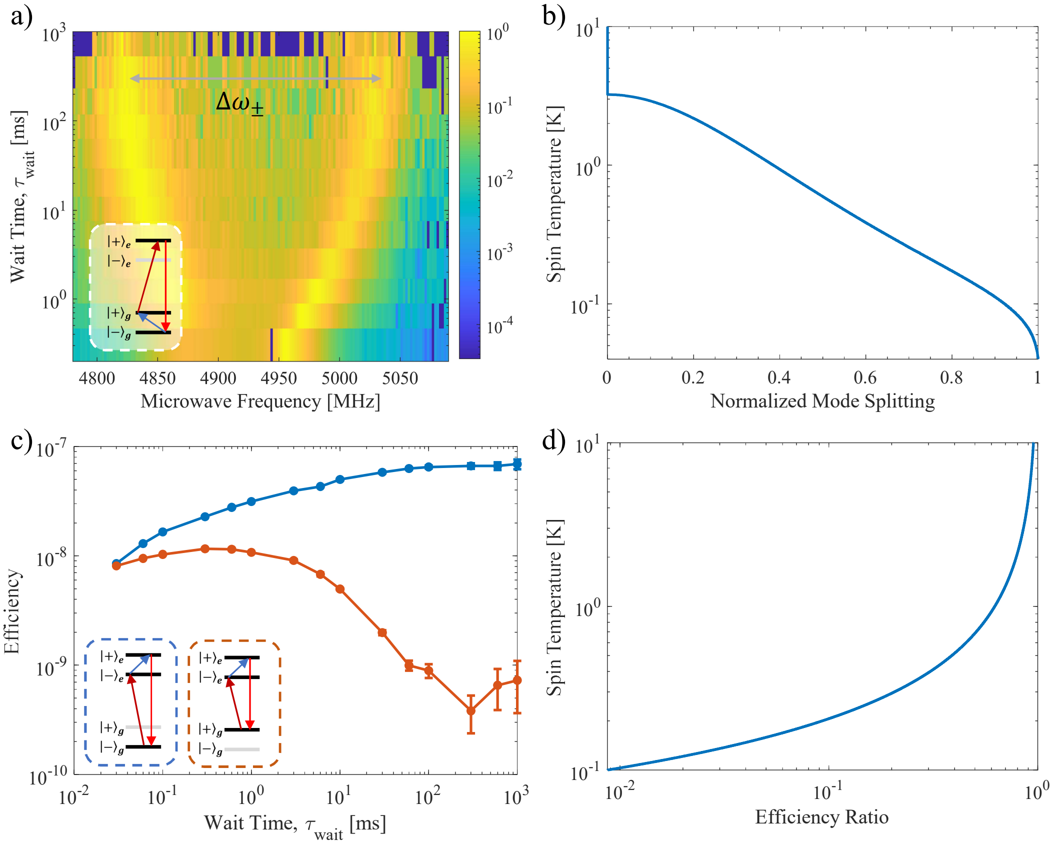

Figure 7.26: Transduction measurements to determine the temperature of the erbium spins. a) Ground state transduction (level structure utilized in the inset) as a function of the wait time between pulses. b) Simulation of the normalized mode splitting (i.e. splitting of the signal in (a)) and the associated spin temperature to determine the temperature of all the spins coupled to the microwave cavity. c) Excited state transduction for both V-systems (level structures utilized are in the inset) as a function of the wait time. d) Simulation to correlate the measured efficiency ratio between the two V-systems and the associated temperature of the spins within the transducer.

The average temperature of the ensemble of erbium spins that couple to the microwave cavity was determined by measuring the microwave frequency dependence of the transduction signal (Figure 7.26a). Optical heating decreases the population difference between the erbium spins as the temperature increases. This subsequently decreases the microwave cavity mode pulling that determines the microwave frequency that has the highest transduction signal and allows us to infer the spin temperature.

We measure the microwave frequency spectrum of the transduction signal for the ground state spin at a magnetic field of 60 mT (i.e. the magnetic field to make ground state spins resonant with the microwave cavity), P_o= 550 uW, P_μ= -60 dBm and a pulse length of τ_{pulse} =1 μs. We then sweep the microwave frequency and the wait time between the pulses to change the average optical power incident on the device and monitor the mode splitting in the transduction signal. The plot in Figure 7.26a shows the normalized signal strength at each wait time to more conveniently show the change in the splitting.

The efficiency is as high as $\eta_d = 8 \cdot 10^{-10}$ at the shorter wait times and decreases to $\eta_d = 10^{-10}$ at the longer wait times. Lower spin temperature allows more parasitic spins to absorb microwave photons (especially when the spins are resonant with the microwave cavity) and that decreases the efficiency. Higher efficiency can be achieved in the ground state when the spins are detuned from the microwave cavity (see Figure 7.25).

The theoretical spin temperature that corresponds to the normalized mode splitting (i.e. normalized to the maximum mode splitting at base temperature) is shown in Figure 7.26b using Equation 1.4. We have fairly strong sensitivity to the spin temperature from ~0.1-1 K by measuring the change in the mode splitting. Below 100 mK, the change in mode pulling is small as the spins are nearly fully polarized, while above ~3 K, the system leaves the strong coupling regime and there is no mode splitting.

We observe an increase in the transduction signal splitting, corresponding to a decrease in the resonator temperature, as we increase the wait time. An average spin temperature of ~100 mK is reached at a wait time of 100 ms for the spins coupled to the microwave resonator (blue trace in Figure 7.27).

The temperature of the erbium spins within the transducer was estimated by measuring the excited state transduction efficiency for the two excited state transduction configurations that interact with each ground state spin level (i.e. $|-\rangle_g$ and $|+\rangle_g$). In the regime where the ion dynamics evolve linearly, the transduction efficiency scales as N^2, so by measuring the efficiency ratio between the two configurations (i.e. $\eta_{|+\rangle_g}/\eta_{|-\rangle_g} \sim \exp(-2\hbar\omega/k_BT)$, where the subscripts indicates which ground state is used for the transduction process), we can deduce the ground state spin population distribution and thus the erbium spin temperature.

Since we are measuring the ratio in the efficiency, any common change in the efficiency (i.e. different coherence times at different temperatures) will not effect this measurement. The only factor we account for is that the two different configurations have a pump at a different laser frequency (i.e. $|-\rangle_g \leftrightarrow |-\rangle_e$ and $|+\rangle_g \leftrightarrow |-\rangle_e$) which have different detunings from the optical cavity. This results in a different circulating photon number for the same optical power and thus a different optical pump Rabi frequency. This difference in detunings should lead to the configuration using the $|-\rangle_g \leftrightarrow |-\rangle_e$ pump transition to have 1.2x higher efficiency, so we account for this small factor when calculated the temperature.

We measure the transduction efficiency for both V-systems at a magnetic field of 76 mT and keep the input power (Figure 7.26c) and pulse sequence the same as the previous microwave resonator spin temperature measurement. Figure 7.26d shows the theoretical spin temperature as a function of the measured transduction efficiency ratio. In order to measure a spin temperature of below 100 mK, this requires an efficiency ratio of 20 dB. This does make this measurement a bit tricky as we need high SNR to measure the large efficiency ratio so we cannot operate in regimes that have more modest SNR even if they may be colder. However, using this technique, if we do have sufficient SNR, we become exponentially sensitive to the spin temperature at low temperatures.

As the wait time increases, the transducer spin temperature decreases which results in the V system involving the $|+\rangle_g$ state to have decreased efficiency, while the V system involving the $|-\rangle_g$ state efficiency only increases due to increased population and low device temperature (Figure 7.27). As the wait time increases to 300 ms, we measure an efficiency ratio up to 20 dB which corresponds to a transducer spin temperature of 100 mK.

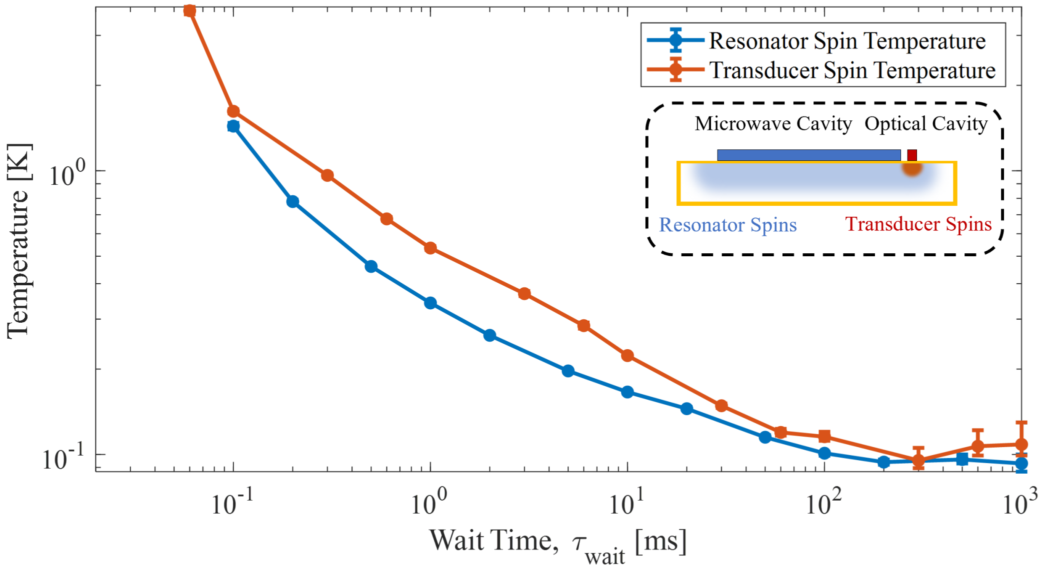

Figure 7.27: The temperature of the spins within the microwave resonator and the transducer as a function of the wait time. The temperature is determine from the data and models shown in Figure 7.26. The transducer spins occupy the volume within the optical cavity (i.e. red area in substrate in the inset diagram), while the resonator spins occupy the entire volume of the microwave cavity (i.e. blue area in the substrate in the inset diagram).

We conclude that the transducer spins and the microwave resonator spins have similar temperatures as shown in Figure 7.27, when measured using entirely independent techniques. The temperature of the spins within the transducer was measured to be slightly higher than the ensemble of spins coupled to the microwave resonator, which we attribute to closer proximity to the optical heating source.

Microwave Resonator Noise

In order to measure the thermal noise of the microwave resonator induced by optical light during the transduction process, we detected the noise from microwave cavity of the transducer that radiates into the coupling waveguide and was measured through a low noise microwave readout line [46, 50, 52, 169]. This method has been applied by a few groups and the theory has been detailed already [169], so we will only highlight the main points here.

Our system involves a microwave resonator that is coupled to its environment through the intrinsic cavity decay rate and a co-planar waveguide via the coupling cavity decay rate as shown in Figure 7.28a. One end of the co-planar waveguide is connected to our microwave amplification readout chain consisting of a low noise HEMT and a room-temperature microwave amplifier for detection. The other end of the co-planar waveguide is connected to the input microwave line, which is thermally-lagged to the mixing chamber stage with a microwave attenuator.

The output thermal noise from the transducer coupled to the co-planar waveguide can be determined to be:

$$N_{out} = \tau(\omega)(N_{env} - N_{wg}) + N_{wg} + N_{add} + 0.5 \tag{7.4}$$

where $\tau(\Delta\omega) = \frac{2\kappa_{\mu,i}\kappa_{\mu,in}}{(\kappa_{\mu,i}+\kappa_{\mu,in})^2+4\Delta\omega^2}$ and $N_{out} = \frac{P_{out}}{G\hbar\omega\mathrm{BW}}$ relates the detected power level to photon number. N_{env} and N_{wg} are the thermal occupations of the environment the resonator is coupled with and the coupling waveguide, respectively. N_{out} is the output noise photon level after the amplification chain, N_{add} is the added noise from the amplification chain and G is the gain of the microwave amplification chain.

We note that the resonator is coupled to a co-planar waveguide and can radiate into both propagation directions of the waveguide, but we only detect one direction (i.e. $\kappa_{\mu,in}$ accounts for the resonator coupling to both propagation directions).

We can understand Equation 7.4 in the following way. Once we subtract the added noise from the amplifier, the white noise level provides us the thermal occupation of the waveguide. At the cavity resonance frequency, we can observe a peak or dip in the noise spectrum depending on if the resonator environment is hotter or colder than the waveguide. We can quantify the thermal occupation of the resonator environment after accounting for the relative cavity decay rates (i.e. $\tau(\omega)$) and the size of the peak or dip in the noise spectrum at the cavity frequency.

Once N_{wg} and N_{env} have been determined, we can calculate the thermal occupancy of the resonator mode, N_{mode}, which is coupled to both baths:

$$N_{mode} = \frac{\kappa_{\mu,in}N_{wg} + \kappa_{\mu,i}N_{env}}{\kappa_{\mu,in} + \kappa_{\mu,i}}. \tag{7.5}$$

For our setup, $N_{add} \sim 6.8$ photons (i.e. as shown in Chapter 6), and we are trying to measure small additional thermal noise from the resonator. In other words, we are trying to measure a small resonance of thermal noise of the resonator over a large white noise background. This requires precise calibration of the background noise level (i.e. N_{add} and G of the microwave amplification chain) and sufficient averaging to make the trace noise sufficiently small. This measurement is also sensitive to any drifts in the microwave amplification chain parameters, so these need to calibrated often to ensure the setup calibration is as reliable as possible.

We first look at the microwave resonator noise induced from optical light as a function of the continuous-wave optical power on the spectrum analyzer as shown in Figure 7.28b. All noise measurements were done at the excited state transduction magnetic field of 76 mT. We observe a peak in the noise spectrum at the microwave resonator frequency, which indicates that the microwave resonator environment is hotter than the microwave waveguide. As the optical power increases, the noise peak increases and the white noise level increases, which indicates that the microwave resonator environment and microwave coupling waveguide are getting hotter. We also observe that the resonance shifts to higher frequencies as the optical power increases. We attribute this to heating of the device that saturates the spin coupling and shifts the cavity resonance closer to its natural frequency.

We fit the noise spectra to Equation 7.4 to determine the resonator environment noise, the coupling waveguide noise and the microwave resonator mode noise as a function of the optical power in Figure 7.28c. The error bars correspond to the 95% confidence interval from the fitting. The resonator mode thermal occupancy is quite high, $N_{mode} = 3.3$ photons, at the nominal optical power (i.e. $P_o = 550\ \mu$W) used in the transduction experiments. The mode thermal occupancy is below unity at $P_o = 35\ \mu$W and below 1/2 at $P_o = 8.5\ \mu$W. The thermal occupancies have a power law dependence of $N_{wg} \propto P_o^{0.53}$, $N_{env} \propto P_o^{0.34}$ and $N_{mode} \propto P_o^{0.44}$. The waveguide thermal occupancy power law dependence is very similar to the result of Hease et al. [46], who measure $N_{wg} \propto P_o^{0.55}$ for their system.

This measurement indicates that we can achieve low thermal noise with CW optical excitation if the optical power is sufficiently small, but these low optical powers will also decrease the transduction efficiency. However, our transducer is most efficient in the pulsed regime anyway, so we next measure the microwave resonator noise in the presence of optical pulses.

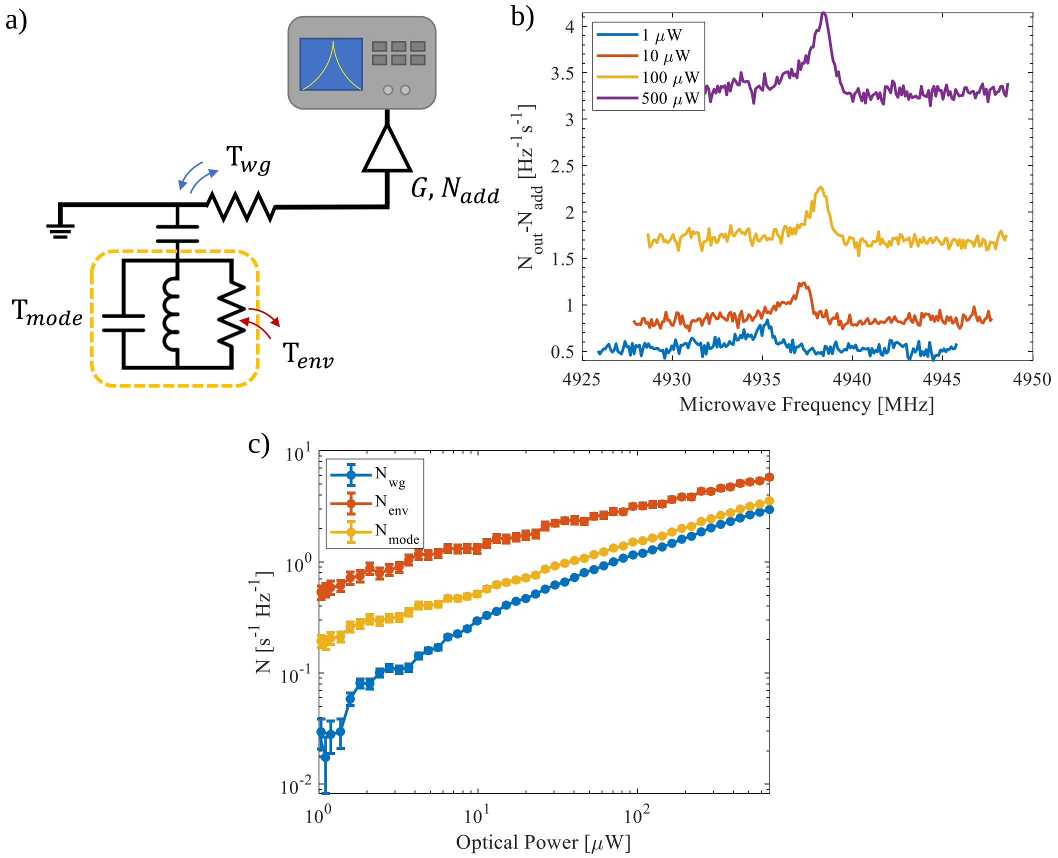

Figure 7.28: Microwave resonator noise under continuous-wave optical excitation. a) The measurement set-up to detect the noise photons from the device. b) Noise spectra of the device for different optical power. c) Thermal occupancy for the microwave waveguide, N_{wg}, the resonator environment, N_{env} and the resonator mode, N_{mode} as a function of the optical power.

In order to measure the resonator noise induced from optical light in the presence of optical pulses, we change our detection setup slightly (see Figure 7.29a). We add a mixer to shift the resonator noise down to 10-20 MHz and detect it on a digitizer. This allows us to time-resolve our noise detection for the optical pulses.

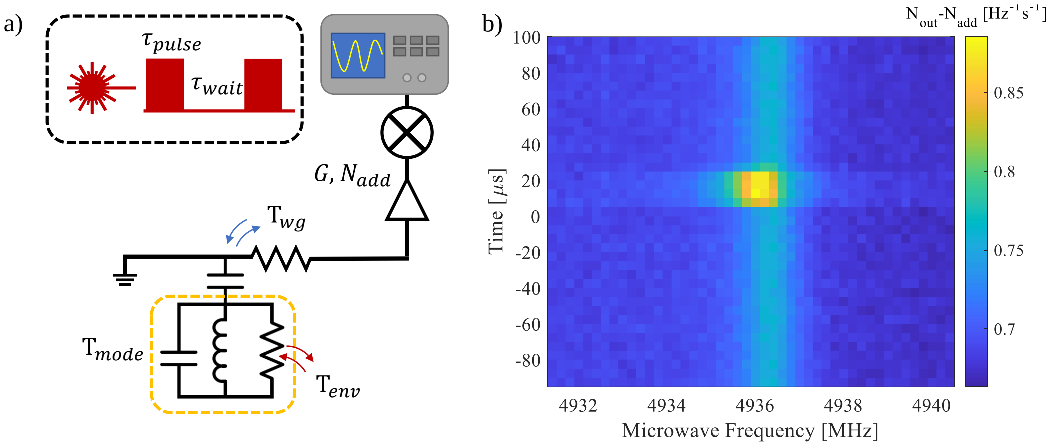

Figure 7.29: a) Measurement set-up for measuring the microwave resonator noise under pulsed optical power. The resonator noise is mixed down to lower frequency for detection on a digitizer. The optical pulse sequence is shown in the inset. b) Time resolved noise spectra of the microwave resonator under pulsed optical light.

We first measure single pulse sequence of P_o = 550 μW, τ_{pulse} = 20 μs and τ_{wait} = 5 ms as shown in Figure 7.29b. We observe a relatively small peak in the noise spectra at all times and then a larger peak when the optical pulse is on (i.e. from 0-20 μs). We attribute the sudden rise in the resonator noise to be associated with coupling to a fast bath, which we believe is the quasi-particle bath, which should have fast dynamics in the niobium resonator. We also believe that there is a slow bath that keeps the resonator hot even when the optical pulse is turned off. We believe this slow bath has a decay time of longer than 100 ms as we do not observe any significant decay of the noise signal up to that time. One potential candidate for this bath is the erbium spins themselves, which we know have long lifetimes as measured previously (see Figure 7.14). Others have measured the timescale of the slow bath in their system and it was several minutes for their system [52].

We also observe a small shift in the frequency when the optical pulse is on relative to off. We attribute this to the optical power breaking quasi-particles in the superconducting resonator and increasing the kinetic inductance, which shifts the resonance frequency. We note that this has been observed by others [50], but the shift they observe is significantly larger (i.e. >10 MHz), which we attribute to their larger kinetic inductance fraction of their microwave resonator.

Next, we looked at how the different parameters of the optical pulse sequence impact the resonator noise during the optical excitation pulse. These parameters include the pulse length, τ_{pulse}, the wait time between pulses, τ_{wait}, and the optical power, P_o.

First, we looked at the microwave noise as a function of the wait time between pulses (Figure 7.30). This was done for P_o = 550 μW and τ_{pulse} = 20 μs. The thermal occupancies have a power law dependence of $N_{env} \propto \tau_{wait}^{-0.28}$ and $N_{mode} \propto \tau_{wait}^{-0.39}$ for wait times less than 20 ms and $N_{env} \propto \tau_{wait}^{-0.23}$ and $N_{mode} \propto \tau_{wait}^{-0.16}$ for wait times larger than 20 ms. $N_{wg} \propto \tau_{wait}^{-0.54}$ for all wait times. At long wait times (i.e. τ_{wait}>100 ms), we can bring the resonator thermal occupancy down 0.2 photons, which results in a mode temperature of 120 mK.

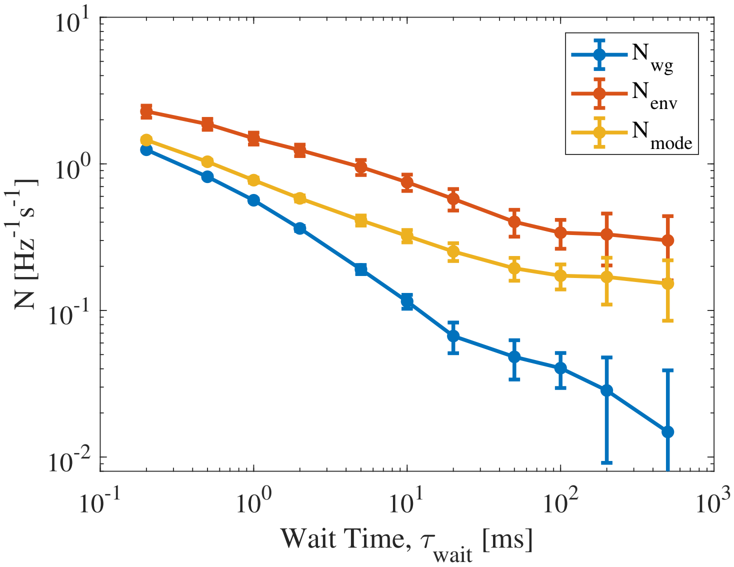

Figure 7.30: The thermal occupation of the device as a function of the wait time between adjacent optical pulses.

Next, we measured the microwave noise as a function of the pulse length (Figure 7.31). This was done for P_o = 550 μW and τ_{wait} = 10 ms. The thermal occupancies have a power law dependence of $N_{wg} \propto \tau_{pulse}^{0.65}$, $N_{env} \propto \tau_{pulse}^{0.37}$ and $N_{mode} \propto \tau_{pulse}^{0.4}$. Here we were limited to pulse lengths greater than 10 μs, but we could expect N_{mode} to be ~2-3x smaller for 1 μs pulses (i.e. the pulse length used for the transduction measurements) based on the power law dependence. N_{mode} has similar, but inverse, power law dependencies for τ_{pulse} and τ_{wait} (i.e. for τ_{wait} < 20 ms), which indicates that the thermal occupancy of the mode scales roughly as the average power for the pulse sequences with a duty cycle greater than 0.1%.

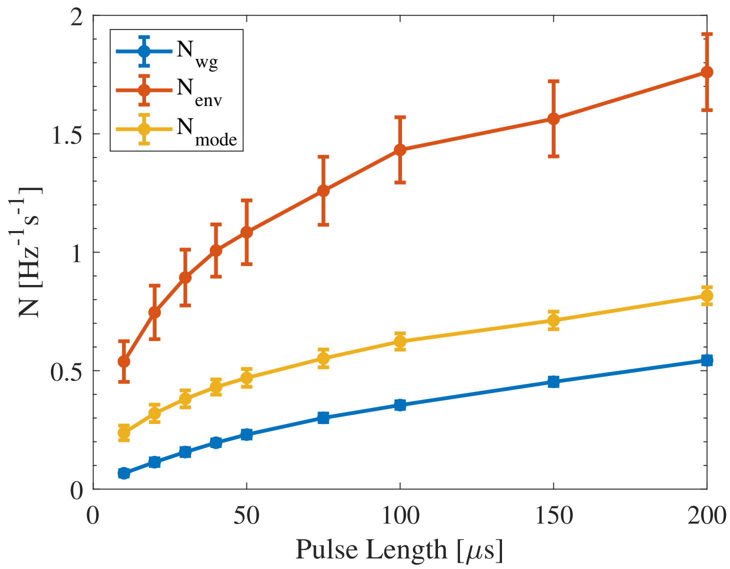

Figure 7.31: The thermal occupation of the device as a function of the pulse length of the optical excitation.

Lastly, we looked at the microwave noise as a function of the optical pulse power (Figure 7.32). This was done for τ_{pulse} = 20 μs and τ_{wait} = 1 ms. The thermal occupancies have a power law dependence of $N_{wg} \propto P_o^{0.69}$, $N_{env} \propto P_o^{0.58}$ and $N_{mode} \propto P_o^{0.55}$ in the pulsed operation, which differ from the continuous wave operation. The average power is 50x smaller compared to the CW experiment (i.e. 2% duty cycle), which may attribute to the different power law scaling. We note that Fu et al. [50] also observed an increased power law dependence for their pulsed measurements compared to their CW measurements when they swept the optical power.

In order to obtain $N_{mode} < 0.5$, the optical power should be $P_o < 55$ μW. This is roughly a factor of ~7x more optical power compared to the CW case with a 2% pulse duty cycle to achieve the same thermal occupancy of the resonator.

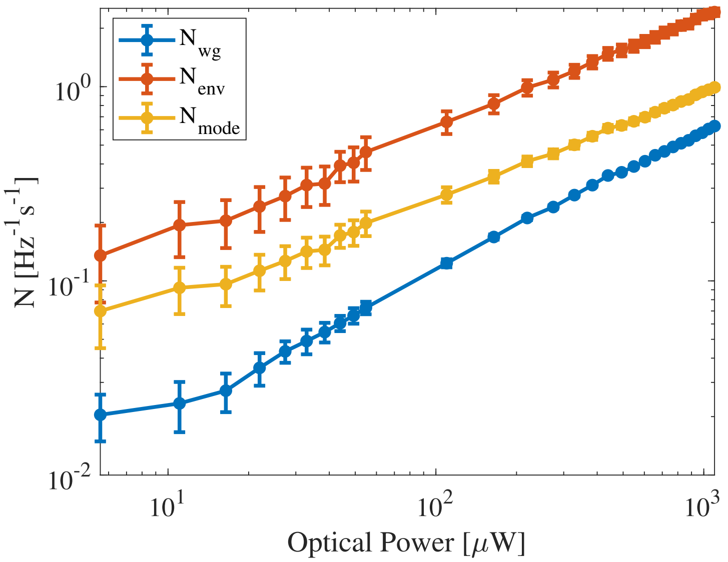

Figure 7.32: The thermal occupation of the device as a function of the power of the optical excitation pulse.

The internal microwave quality factor changes significantly when we change the parameters of the optical pulse sequence, which modifies which bath that the microwave resonator mode is more coupled to between the coupling waveguide and the resonator environment baths. To illustrate that more clearly, the internal microwave quality factors for the three parameter sweeps (i.e. wait time, pulse length and optical power) are shown in Figure 7.33. $Q_{\mu,i}$ ranges from as low as 6,000 to as high as 23,000 depending on the exact sequence. For reference, $Q_{\mu,in} \sim 5,800$. This causes the resonator mode to be more coupled to the waveguide in the pulse sequences that result in higher temperatures.

In summary, we identify regimes where we expect the microwave resonator noise is low (i.e. $N_{mode} \ll 1$), but these require long wait times or low optical power. Improvements to the device for more efficient use of optical power can allow for lower input pump powers and lower temperature at shorter wait times.

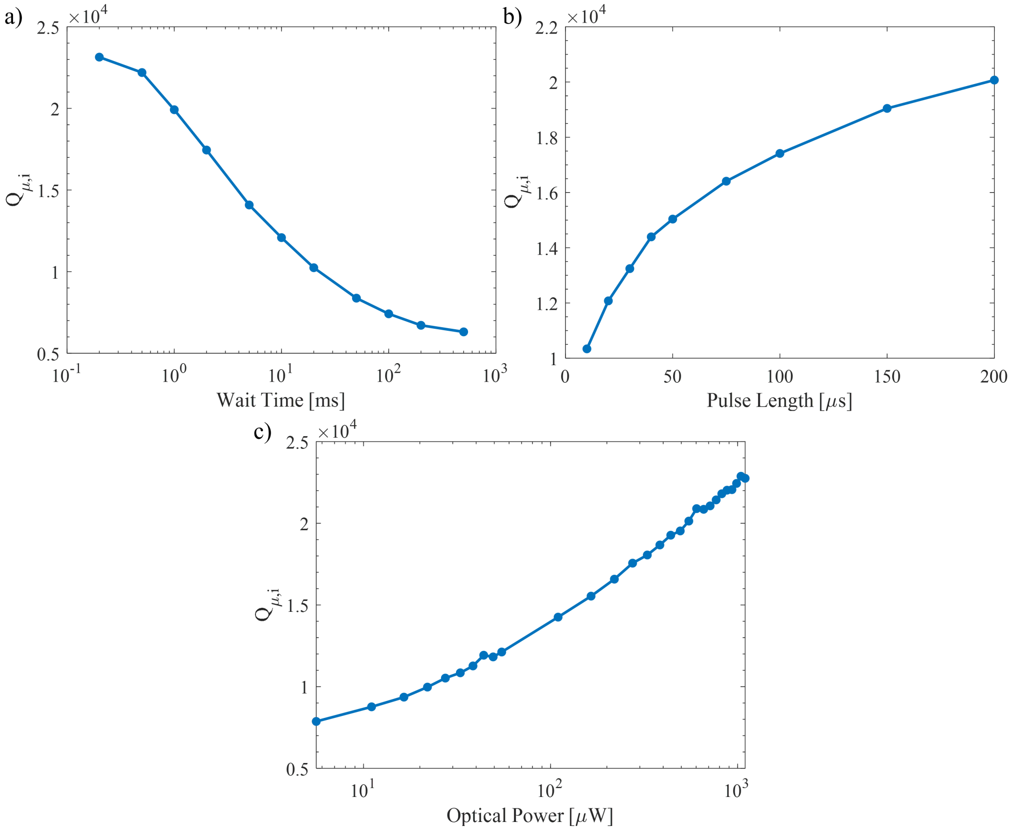

Figure 7.33: Internal microwave quality factor for the different pulsed resonator noise parameter sweeps including a) the wait time sweep, b) the pulse length sweep and c) the optical power sweep.

Photoluminescence Noise

One concern specific for transduction with atomic systems is the addition of photoluminescence noise photons during our transduction pulse. That is, the optical pump will excite ions to the excited state and when they decay spontaneously to the ground state, the emitted photon can act as noise at the transducer optical output. We quantify this noise in Figure 7.34, where we measure the detected noise photons per pulse as a function of the wait time for our pulsed transduction measurements. This is done for 1 μs optical pulses and with 550 μW of optical power.

We measure the noise photons down to $\sim 4{\cdot}10^{-5}$ photons per pulse in the transduction pulse window when the wait time is longer than the optical lifetime of 3 ms. The red line is the detection noise floor of our setup which includes SNSPD background counts and laser leakage from the filtering. After accounting for detection losses, the photoluminescence noise referred to the output of the optical device is 15 dB higher (or $\sim 10^{-3}$ photons per pulse).

We also determined that this noise corresponds to photoluminescence from ions in the bulk of the crystal (i.e. not from our cavity), so this is not fundamental to a REI transducer and not a problem if we remove those ions in future devices. Nonetheless, the value is already quite small due to the high extinction of the filtering that removes most of the photoluminescence noise and the time domain filtering associated with short transduction pulses (i.e. pulse length is much shorter than the optical lifetime).

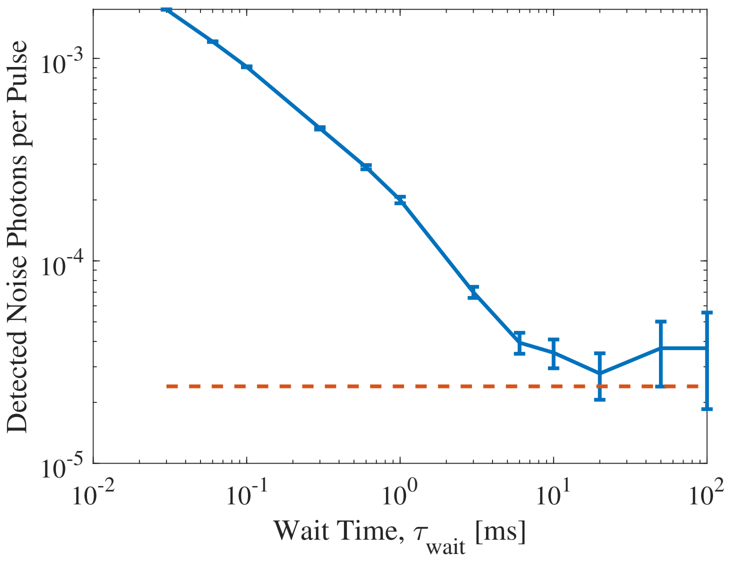

Figure 7.34: Detected photoluminescence noise per transduction pulse as a function of the wait time between adjacent pulses. The red dashed line is the detection noise floor.

7.7 Other Transducer Device Results

Although not detailed here, on the path to the transducer that was presented above, several other devices were tested beforehand with worse performance. Due to the architecture of this platform (i.e. patterned amorphous silicon and niobium resonators on a rare-earth ion substrate), it was relatively easy to make devices on different materials and target different transitions.

This included a TE mode optical cavity for coupling to Z_1-Y_2 transitions in Er^{3+}:YVO$_4$ (180 ppm), a TM mode optical cavity for coupling to Z_1-Y_1 transitions in Er^{3+}:YSO (50 ppm) and previous TM mode optical cavities for coupling to Z_1-Y_1 transitions in Er^{3+}:YVO$_4$ (180, 560 and 1000 ppm), which were measured over a 1-2 year period. During this time the experimental set-up was being built up so certain measurements were not possible at the time (i.e. SNSPD detection of transduced signals). Also, the fabrication process was continuously being optimized during the fabrication of these different devices.

These previous devices all exhibited much lower efficiency (i.e. $\eta_d \sim 10^{-12} - 10^{-9}$), but they were not measured nearly as carefully as the current device. Therefore, it is a bit difficult to assign a precise reason for the difference in the efficiency, but we largely attribute it to better fabrication and more optimized measurements.

For the Er^{3+}:YSO device, the erbium concentration was smaller, which we would expect to decrease the efficiency by an order of magnitude roughly. Also, the magnetic field angle that we used is best for maximizing the optical dipole moments but it has a small g_{dc} in the optically excited state (B_{dc} angle was 30° from D_1 on the $D_1 - D_2$ plane). This prevented us from looking at excited state transduction on this device, since the electromagnet that was used for these experiments could not provide a field that large.

Chapter 8

CONCLUSIONS

8.1 Summary of Results

In this thesis, we presented our progress towards a microwave-to-optical transducer using rare-earth ions simultaneously coupled to a microwave and optical cavity. We identified a promising material in Er^{3+}:YVO_4 and performed spectroscopy and simulations to characterize its performance.

We then designed the transducer using a Er^{3+}:YVO_4 substrate with a superconducting microwave resonator and photonic crystal optical resonator patterned on the substrate. The design was optimized to maximize the efficiency and relative ease of fabrication.

A new nanofabrication process was developed to deposit and pattern both the optical and microwave resonators on the Er^{3+}:YVO_4 substrate. A microwave, optical, and cryogenic measurement set-up was assembled for characterizing the transducers. These included optical, microwave, and magnetic field control within a dilution fridge, a heterodyne detection setup for transduction readout, narrowband optical filtering for single photon detection of transduced photons, and microwave device readout with a network analyzer, spectrum analyzer, and digitizer.

The rare-earth ion microwave-to-optical transducer was then characterized in the dilution fridge. This included characterization of the optical and microwave cavity independently and also the effects of co-localizing the two resonators. Next, the transducer efficiency was characterized. We measured continuous-wave transduction efficiency up to $\eta_d = 3 \cdot 10^{-9}$. In pulsed operation, the efficiency increased up to $\eta_d = 2 \cdot 10^{-7}$ when $P_o = 5$ mW and $\eta_d = 8 \cdot 10^{-8}$ when $P_o = 550$ μW for 1 μs pulses and 10 ms wait time between pulses. Based on the cavity coupling rates and grating coupler efficiency, an internal efficiency of $\eta_{d,int} \sim 1 \cdot 10^{-5}$ could be achieved at the highest optical power.

We also characterized the temperature of the erbium spins and the microwave resonator during transduction and identified regimes where the spin and microwave resonator temperatures reach 100 mK while the transducer operates in a pulsed mode. This involved either long wait times (i.e. t_{wait}> 100 ms) or low optical power power (i.e. P_o< 10 μW).

8.2 Future Works

The main improvements needed for a future device include increasing the transduction efficiency and achieving low noise operation with higher duty-cycle transduction pulses at the same time. Part of this can be solved at the same time by more efficient use of the optical photons with a significantly over-coupled optical cavity and on/off chip coupling with near unity efficiency. This would allow for lower optical power to be used for similar optical Rabi frequencies to reduce the noise and higher efficiency due to better collection of the transduced photons.

Another issue with the current device is the parasitic spins. This included the even isotope erbium spins that were within the microwave cavity, but not the optical cavity that impacted the ground state transduction efficiency and the ^{167}Er spins that impacted the excited state transduction. The ^{167}Er spins are easier to avoid by moving to an isotopically purified sample.

Removing the parasitic even isotope spins likely involves moving to a different fabrication platform, where the erbium spins are only within the optical cavity. This could be achieved with ion implantation (although some initial attempts at this with Er^{3+}:YVO_4 were unsuccessful) or by changing the platform more substantially and patterning the optical resonator directly out of the Er^{3+}:YVO_4 material instead of relying on patterning amorphous silicon. This would also increase the number of spins by ~10x and the optical pump Rabi frequency by ~3x (i.e. we are no longer just relying on evanescent optical coupling). Using the adiabatic model formalism, we would expect the device mode overlap to increase by a factor of ~10x. We would expect a factor of ~100x improvement in the device efficiency for the excited state and a factor of $\sim 10^4$x for the ground state from simulation with the linear numerical model to reach an efficiency of $\eta_{d,int} \sim 10^{-2}$. Its worth noting that currently there is not a straight forward way to do this in a way that is readily available and easy to integrate with superconducting microwave resonators, so that is still an area of active research.

Another way to improve the efficiency by improving the mode overlap is to decrease the parasitic inductance of the capacitor that shunts the inductive wire. One possible solution is to change from an interdigitated capacitor to a parallel plate capacitor, which will have negligible parasitic inductance. A concern of this type of capacitor is a significant reduction in the microwave quality factor due to dielectric losses, but for our transducer, we do not require very high quality factors, and others have shown reasonable quality factors with an amorphous silicon dielectric between the parallel plate capacitor [170]. We should also note that this would require more lithography steps and would complicate the fabrication process, but we could expect a $\sim$ 5x improvement in the mode overlap with this implementation.

It is also worth noting that potentially another rare-earth ion/host system can offer better performance compared to $\mathrm{Er^{3+}{:}YVO_4}$. However, at this point it is unclear to us exactly what that would be and it does require a significant amount of spectroscopy to find a better material.

Once a high efficiency and low noise transducer can be achieved, the next step is to integrate it with superconducting qubits. This may be a bit tricky since in the current implementation a high magnetic field of 76 mT was used and traditional superconducting qubits are not known to function within magnetic fields of that magnitude.

One possible solution is to switch to another rare-earth ion/isotope that exhibits GHz microwave transitions at zero or near zero magnetic field [57, 171].

Another possible solution is to use a *novel* type of superconducting qubit that can operate in relatively large magnetic fields [172–174]. Admittedly, these are not state-of-the-art qubits as of now, but they could be used for some initial proof-of-principle demonstrations as sources of non-classical light. Potentially, the performance of certain sueprconducting qubits in magnetic fields improves as more work is developed.

Assuming those two solutions are not feasible, another approach would be to have the superconducting qubit spatially decoupled from the transducer and have sufficient magnetic shielding in between the two components, while coupling them with superconducting coaxial cable for a low loss interconnect. This approach is maybe not scalable for larger integration, but could be configured for single device proof-of-principle quantum transduction with rare-earth ions.

BIBLIOGRAPHY

1. Dowling, J. P. & Milburn, G. J. Quantum technology: The second quantum revolution. *Philosophical Transactions of the Royal Society of London. Series A: Mathematical, Physical and Engineering Sciences* **361** (ed MacFarlane, A. G. J.) 1655–1674. `https://doi.org/10.1098/rsta.2003.1227` (June 2003).
2. Gisin, N. & Thew, R. Quantum communication. *Nature Photonics* **1,** 165–171. `https://doi.org/10.1038/nphoton.2007.22` (Mar. 2007).
3. Van Enk, S. J., Cirac, J. I. & Zoller, P. Ideal quantum communication over noisy channels: A quantum optical implementation. *Physical Review Letters* **78,** 4293–4296. `https://doi.org/10.1103/physrevlett.78.4293` (June 1997).
4. Preskill, J. Quantum Computing in the NISQ era and beyond. *Quantum* **2,** 79. `https://doi.org/10.22331/q-2018-08-06-79` (Aug. 2018).
5. Ladd, T. D., Jelezko, F., Laflamme, R., Nakamura, Y., Monroe, C. & O'Brien, J. L. Quantum computers. *Nature* **464,** 45–53. `https://doi.org/10.1038/nature08812` (Mar. 2010).
6. Steane, A. Quantum computing. *Reports on Progress in Physics* **61,** 117–173. `https://doi.org/10.1088/0034-4885/61/2/002` (Feb. 1998).
7. Polino, E., Valeri, M., Spagnolo, N. & Sciarrino, F. Photonic quantum metrology. *AVS Quantum Science* **2,** 024703. `https://doi.org/10.1116/5.0007577` (June 2020).
8. Giovannetti, V., Lloyd, S. & Maccone, L. Quantum Metrology. *Physical Review Letters* **96.** `https://doi.org/10.1103/physrevlett.96.010401` (Jan. 2006).
9. Simon, C. Towards a global quantum network. *Nature Photonics* **11,** 678–680. `https://doi.org/10.1038/s41566-017-0032-0` (Oct. 2017).
10. Wehner, S., Elkouss, D. & Hanson, R. Quantum internet: A vision for the road ahead. *Science* **362.** `https://doi.org/10.1126/science.aam9288` (Oct. 2018).
11. Cacciapuoti, A. S., Caleffi, M., Tafuri, F., Cataliotti, F. S., Gherardini, S. & Bianchi, G. Quantum internet: Networking challenges in distributed quantum computing. *IEEE Network* **34,** 137–143. `https://doi.org/10.1109/mnet.001.1900092` (Jan. 2020).
12. Barz, S., Kashefi, E., Broadbent, A., Fitzsimons, J. F., Zeilinger, A. & Walther, P. Demonstration of Blind Quantum Computing. *Science* **335,** 303–308. `https://doi.org/10.1126/science.1214707` (Jan. 2012).

13. Bruzewicz, C. D., Chiaverini, J., McConnell, R. & Sage, J. M. Trapped-ion quantum computing: Progress and challenges. *Applied Physics Reviews* **6,** 021314. `https://doi.org/10.1063/1.5088164` (June 2019).

14. Stephenson, L. *et al.* High-rate, high-fidelity entanglement of qubits across an elementary quantum network. *Physical Review Letters* **124.** `https://doi.org/10.1103/physrevlett.124.110501` (Mar. 2020).

15. Humphreys, P. C., Kalb, N., Morits, J. P. J., Schouten, R. N., Vermeulen, R. F. L., Twitchen, D. J., Markham, M. & Hanson, R. Deterministic delivery of remote entanglement on a quantum network. *Nature* **558,** 268–273. `https://doi.org/10.1038/s41586-018-0200-5` (June 2018).

16. Krantz, P., Kjaergaard, M., Yan, F., Orlando, T. P., Gustavsson, S. & Oliver, W. D. A quantum engineer's guide to superconducting qubits. *Applied Physics Reviews* **6,** 021318. `https://doi.org/10.1063/1.5089550` (June 2019).

17. Blais, A., Grimsmo, A. L., Girvin, S. & Wallraff, A. Circuit quantum electrodynamics. *Reviews of Modern Physics* **93.** `https://doi.org/10.1103/revmodphys.93.025005` (May 2021).

18. Wallraff, A. *et al.* Strong coupling of a single photon to a superconducting qubit using circuit quantum electrodynamics. *Nature* **431,** 162–167. `https://doi.org/10.1038/nature02851` (Sept. 2004).

19. Arute, F. *et al.* Quantum supremacy using a programmable superconducting processor. *Nature* **574,** 505–510. `https://doi.org/10.1038/s41586-019-1666-5` (Oct. 2019).

20. Wu, Y. *et al.* Strong quantum computational advantage using a superconducting quantum processor. *Physical Review Letters* **127.** `https://doi.org/10.1103/physrevlett.127.180501` (Oct. 2021).

21. Place, A. P. M. *et al.* New material platform for superconducting transmon qubits with coherence times exceeding 0.3 milliseconds. *Nature Communications* **12.** `https://doi.org/10.1038/s41467-021-22030-5` (Mar. 2021).

22. Somoroff, A., Ficheux, Q., Mencia, R. A., Xiong, H., Kuzmin, R. V. & Manucharyan, V. E. Millisecond coherence in a superconducting qubit. eprint: `arXiv:2103.08578` (2021).

23. Fowler, A. G., Mariantoni, M., Martinis, J. M. & Cleland, A. N. Surface codes: Towards practical large-scale quantum computation. *Physical Review A* **86.** `https://doi.org/10.1103/physreva.86.032324` (Sept. 2012).

24. Krinner, S. *et al.* Engineering cryogenic setups for 100-qubit scale superconducting circuit systems. *EPJ Quantum Technology* **6.** `https://doi.org/10.1140/epjqt/s40507-019-0072-0` (May 2019).

25. Rosenberg, D. *et al.* 3D integrated superconducting qubits. *npj Quantum Information* **3.** `https://doi.org/10.1038/s41534-017-0044-0` (Oct. 2017).

26. Gold, A. *et al.* Entanglement across separate silicon dies in a modular superconducting qubit device. *npj Quantum Information* **7.** `https://doi.org/10.1038/s41534-021-00484-1` (Sept. 2021).

27. Magnard, P. *et al.* Microwave quantum link between superconducting circuits housed in spatially separated cryogenic systems. *Physical Review Letters* **125.** `https://doi.org/10.1103/physrevlett.125.260502` (Dec. 2020).

28. Hu, L. *et al.* Quantum error correction and universal gate set operation on a binomial bosonic logical qubit. *Nature Physics* **15,** 503–508. `https://doi.org/10.1038/s41567-018-0414-3` (Feb. 2019).

29. Zeuthen, E., Schliesser, A., Sørensen, A. S. & Taylor, J. M. Figures of merit for quantum transducers. *Quantum Science and Technology* **5,** 034009 (2020).

30. Lambert, N. J., Rueda, A., Sedlmeir, F. & Schwefel, H. G. L. Coherent conversion between microwave and optical photons—An overview of physical implementations. *Advanced Quantum Technologies* **3,** 1900077. `https://doi.org/10.1002/qute.201900077` (Jan. 2020).

31. Lauk, N., Sinclair, N., Barzanjeh, S., Covey, J. P., Saffman, M., Spiropulu, M. & Simon, C. Perspectives on quantum transduction. *Quantum Science and Technology* **5,** 020501. `https://doi.org/10.1088/2058-9565/ab788a` (Mar. 2020).

32. Andrews, R. W., Peterson, R. W., Purdy, T. P., Cicak, K., Simmonds, R. W., Regal, C. A. & Lehnert, K. W. Bidirectional and efficient conversion between microwave and optical light. *Nature Physics* **10,** 321–326. `https://doi.org/10.1038/nphys2911` (Mar. 2014).

33. Arnold, G., Wulf, M., Barzanjeh, S., Redchenko, E. S., Rueda, A., Hease, W. J., Hassani, F. & Fink, J. M. Converting microwave and telecom photons with a silicon photonic nanomechanical interface. *Nature Communications* **11.** `https://doi.org/10.1038/s41467-020-18269-z` (Sept. 2020).

34. Higginbotham, A. P. *et al.* Harnessing electro-optic correlations in an efficient mechanical converter. *Nature Physics* **14,** 1038–1042. `https://doi.org/10.1038/s41567-018-0210-0` (July 2018).

35. Han, X. *et al.* Cavity piezo-mechanics for superconducting-nanophotonic quantum interface. *Nature Communications* **11.** `https://doi.org/10.1038/s41467-020-17053-3` (June 2020).

36. Vainsencher, A., Satzinger, K. J., Peairs, G. A. & Cleland, A. N. Bi-directional conversion between microwave and optical frequencies in a piezoelectric optomechanical device. *Applied Physics Letters* **109,** 033107. `https://doi.org/10.1063/1.4955408` (July 2016).

37. Peairs, G. *et al.* Continuous and time-domain coherent signal conversion between optical and microwave frequencies. *Physical Review Applied* **14.** `https://doi.org/10.1103/physrevapplied.14.061001` (Dec. 2020).

38. Jiang, W., Sarabalis, C. J., Dahmani, Y. D., Patel, R. N., Mayor, F. M., McKenna, T. P., Laer, R. V. & Safavi-Naeini, A. H. Efficient bidirectional piezo-optomechanical transduction between microwave and optical frequency. *Nature Communications* **11.** `https://doi.org/10.1038/s41467-020-14863-3` (Mar. 2020).

39. Shao, L. *et al.* Microwave-to-optical conversion using lithium niobate thin-film acoustic resonators. *Optica* **6,** 1498. `https://doi.org/10.1364/optica.6.001498` (Dec. 2019).

40. Hönl, S., Popoff, Y., Caimi, D., Beccari, A., Kippenberg, T. J. & Seidler, P. Microwave-to-optical conversion with a gallium phosphide photonic crystal cavity. eprint: `arXiv:2105.13242` (2021).

41. Forsch, M. *et al.* Microwave-to-optics conversion using a mechanical oscillator in its quantum ground state. *Nature Physics* **16,** 69–74. `https://doi.org/10.1038/s41567-019-0673-7` (Oct. 2019).

42. Mirhosseini, M., Sipahigil, A., Kalaee, M. & Painter, O. Superconducting qubit to optical photon transduction. *Nature* **588,** 599–603. `https://doi.org/10.1038/s41586-020-3038-6` (Dec. 2020).

43. Stockill, R., Forsch, M., Hijazi, F., Beaudoin, G., Pantzas, K., Sagnes, I., Braive, R. & Gröblacher, S. Ultra-low-noise microwave to optics conversion in gallium phosphide. eprint: `arXiv:2107.04433` (2021).

44. Witmer, J. D. *et al.* A silicon-organic hybrid platform for quantum microwave-to-optical transduction. *Quantum Science and Technology* **5,** 034004 (2020).

45. Xu, Y. *et al.* Bidirectional interconversion of microwave and light with thin-film lithium niobate. *Nature Communications* **12.** `https://doi.org/10.1038/s41467-021-24809-y` (July 2021).

46. Hease, W., Rueda, A., Sahu, R., Wulf, M., Arnold, G., Schwefel, H. G. & Fink, J. M. Bidirectional electro-optic wavelength conversion in the quantum ground state. *PRX Quantum* **1.** `https://doi.org/10.1103/prxquantum.1.020315` (Nov. 2020).

47. Holzgrafe, J. *et al.* Cavity electro-optics in thin-film lithium niobate for efficient microwave-to-optical transduction. *Optica* **7,** 1714. `https://doi.org/10.1364/optica.397513` (Dec. 2020).

48. McKenna, T. P. *et al.* Cryogenic microwave-to-optical conversion using a triply resonant lithium-niobate-on-sapphire transducer. *Optica* **7,** 1737. `https://doi.org/10.1364/optica.397235` (Dec. 2020).

49. Rueda, A. *et al.* Efficient microwave to optical photon conversion: An electro-optical realization. *Optica* **3,** 597. `https://doi.org/10.1364/optica.3.000597` (June 2016).

50. Fu, W. *et al.* Cavity electro-optic circuit for microwave-to-optical conversion in the quantum ground state. *Physical Review A* **103.** `https://doi.org/10.1103/physreva.103.053504` (May 2021).

51. Fan, L., Zou, C.-L., Cheng, R., Guo, X., Han, X., Gong, Z., Wang, S. & Tang, H. X. Superconducting cavity electro-optics: A platform for coherent photon conversion between superconducting and photonic circuits. *Science Advances* **4,** eaar4994. `https://doi.org/10.1126/sciadv.aar4994` (Aug. 2018).

52. Sahu, R., Hease, W., Rueda, A., Arnold, G., Qiu, L. & Fink, J. Quantum-enabled operation of a microwave-optical interface. *Nature Communications* **13,** 1276 (2022).

53. Tretiakov, A., Potts, C. A., Lee, T. S., Thiessen, M. J., Davis, J. P. & LeBlanc, L. J. Atomic microwave-to-optical signal transduction via magnetic-field coupling in a resonant microwave cavity. *Applied Physics Letters* **116,** 164101. `https://doi.org/10.1063/1.5144616` (Apr. 2020).

54. Fernandez-Gonzalvo, X., Horvath, S. P., Chen, Y.-H. & Longdell, J. J. Cavity-enhanced Raman heterodyne spectroscopy in Er^{3+}:Y_2SiO_5 for microwave to optical signal conversion. *Physical Review A* **100.** `https://doi.org/10.1103/physreva.100.033807` (Sept. 2019).

55. Han, J., Vogt, T., Gross, C., Jaksch, D., Kiffner, M. & Li, W. Coherent microwave-to-optical conversion via six-wave mixing in rydberg atoms. *Physical Review Letters* **120.** `https://doi.org/10.1103/physrevlett.120.093201` (Mar. 2018).

56. Vogt, T., Gross, C., Han, J., Pal, S. B., Lam, M., Kiffner, M. & Li, W. Efficient microwave-to-optical conversion using Rydberg atoms. *Physical Review A* **99.** `https://doi.org/10.1103/physreva.99.023832` (Feb. 2019).

57. Bartholomew, J. G., Rochman, J., Xie, T., Kindem, J. M., Ruskuc, A., Craiciu, I., Lei, M. & Faraon, A. On-chip coherent microwave-to-optical transduction mediated by ytterbium in YVO_4. *Nature Communications* **11.** `https://doi.org/10.1038/s41467-020-16996-x` (June 2020).

58. King, G. G. G., Barnett, P. S., Bartholomew, J. G., Faraon, A. & Longdell, J. J. Probing strong coupling between a microwave cavity and a spin ensemble with Raman heterodyne spectroscopy. *Physical Review B* **103.** `https://doi.org/10.1103/physrevb.103.214305` (June 2021).

59. Welinski, S., Woodburn, P. J., Lauk, N., Cone, R. L., Simon, C., Goldner, P. & Thiel, C. W. Electron spin coherence in optically excited states of rare-earth ions for microwave to optical quantum transducers. *Physical Review Letters* **122.** `https://doi.org/10.1103/physrevlett.122.247401` (June 2019).

60. Zhu, N., Zhang, X., Han, X., Zou, C.-L., Zhong, C., Wang, C.-H., Jiang, L. & Tang, H. X. Waveguide cavity optomagnonics for microwave-to-optics conversion. *Optica* **7,** 1291. `https://doi.org/10.1364/optica.397967` (Sept. 2020).

61. MacCabe, G. S., Ren, H., Luo, J., Cohen, J. D., Zhou, H., Sipahigil, A., Mirhosseini, M. & Painter, O. Nano-acoustic resonator with ultralong phonon lifetime. *Science* **370,** 840–843. `https://doi.org/10.1126/science.abc7312` (Nov. 2020).

62. Liu, G. & Jacquier, B. *Spectroscopic properties of rare earths in optical materials* (Springer Science & Business Media, 2006).

63. Bottger, T., Thiel, C. W., Sun, Y. & Cone, R. L. Optical decoherence and spectral diffusion at1.5μ Er^{3+}:Y2SiO5 versus magnetic field, temperature, and Er^{3+} concentration. *Physical Review B* **73.** `https://doi.org/10.1103/physrevb.73.075101` (Feb. 2006).

64. Bartholomew, J. G. *Investigation of the scalability of rare-earth-ion quantum hardware.* PhD thesis (Australian National University. Laser Physics Centre, 2014).

65. Luo, Z. & Huang, Y. *Physics of Solid-State Laser Materials* `https://doi.org/10.1007/978-981-32-9668-8` (Springer Singapore, 2020).

66. Abragam, A. & Bleaney, B. *Electron paramagnetic resonance of transition ions* (OUP Oxford, 2012).

67. Capobianco, J., Kabro, P., Ermeneux, F., Moncorge, R., Bettinelli, M. & Cavalli, E. Optical spectroscopy, fluorescence dynamics and crystal-field analysis of Er^{3+} in YVO$_4$. *Chemical Physics* **214,** 329–340 (1997).

68. Lutz, T., Veissier, L., Woodburn, P. J. T., Cone, R. L., Barclay, P. E., Tittel, W. & Thiel, C. W. Modification of relaxation dynamics in Tb^{3+}:Y$_3$Al$_5$O$_{12}$ nanopowders. *Physical Review B* **98.** `https://doi.org/10.1103/physrevb.98.054308` (Aug. 2018).

69. Dodson, C. M. & Zia, R. Magnetic dipole and electric quadrupole transitions in the trivalent lanthanide series: Calculated emission rates and oscillator strengths. *Physical Review B* **86.** `https://doi.org/10.1103/physrevb.86.125102` (Sept. 2012).

70. Koster, G. F., Dimmock, J. O. & Wheeler, R. G. *Properties of the thirty-two point groups* (MIT press, 1963).

71. Thiel, C., Böttger, T. & Cone, R. Rare-earth-doped materials for applications in quantum information storage and signal processing. *Journal of Luminescence* **131,** 353–361. `https://doi.org/10.1016/j.jlumin.2010.12.015` (Mar. 2011).

72. Ahlefeldt, R., Hush, M. & Sellars, M. Ultranarrow optical inhomogeneous linewidth in a stoichiometric rare-earth crystal. *Physical Review Letters* **117.** `https://doi.org/10.1103/physrevlett.117.250504` (Dec. 2016).

73. Wesenberg, J. H., Mølmer, K., Rippe, L. & Kröll, S. Scalable designs for quantum computing with rare-earth-ion-doped crystals. *Physical Review A* **75.** `https://doi.org/10.1103/physreva.75.012304` (Jan. 2007).

74. Zhong, T., Kindem, J. M., Miyazono, E. & Faraon, A. Nanophotonic coherent light-matter interfaces based on rare-earth-doped crystals. *Nature Communications* **6.** `https://doi.org/10.1038/ncomms9206` (Sept. 2015).

75. Zhong, T., Rochman, J., Kindem, J. M., Miyazono, E. & Faraon, A. High quality factor nanophotonic resonators in bulk rare-earth doped crystals. *Optics Express* **24,** 536. `https://doi.org/10.1364/oe.24.000536` (Jan. 2016).

76. Wang, S., Yang, L., Cheng, R., Xu, Y., Shen, M., Cone, R. L., Thiel, C. W. & Tang, H. X. Incorporation of erbium ions into thin-film lithium niobate integrated photonics. *Applied Physics Letters* **116,** 151103. `https://doi.org/10.1063/1.5142631` (Apr. 2020).

77. Dibos, A., Raha, M., Phenicie, C. & Thompson, J. Atomic Source of Single Photons in the Telecom Band. *Physical Review Letters* **120.** `https://doi.org/10.1103/physrevlett.120.243601` (June 2018).

78. Miyazono, E., Craiciu, I., Arbabi, A., Zhong, T. & Faraon, A. Coupling erbium dopants in yttrium orthosilicate to silicon photonic resonators and waveguides. *Optics Express* **25,** 2863. `https://doi.org/10.1364/oe.25.002863` (Feb. 2017).

79. Yang, L., Wang, S., Shen, M., Xu, Y., Xie, J. & Tang, H. X. Photonic integration of Er^{3+}:Y2SiO5 with thin-film lithium niobate by flip chip bonding. *Optics Express* **29,** 15497. `https://doi.org/10.1364/oe.423659` (May 2021).

80. Ding, D. *et al.* Multidimensional Purcell effect in an ytterbium-doped ring resonator. *Nature Photonics* **10,** 385–388. `https://doi.org/10.1038/nphoton.2016.72` (Apr. 2016).

81. Bartholomew, J. G., de Oliveira Lima, K., Ferrier, A. & Goldner, P. Optical line width broadening mechanisms at the 10 kHz Level in Eu^{3+}:$\mathrm{Y}_2\mathrm{O}_3$ nanoparticles. *Nano Letters* **17,** 778–787. `https://doi.org/10.1021/acs.nanolett.6b03949` (Jan. 2017).

82. Serrano, D., Kuppusamy, S. K., Heinrich, B., Fuhr, O., Hunger, D., Ruben, M. & Goldner, P. Ultra-narrow optical linewidths in rare-earth molecular crystals. *Nature* **603,** 241–246 (Mar. 2022).

83. Serrano, D., Karlsson, J., Fossati, A., Ferrier, A. & Goldner, P. All-optical control of long-lived nuclear spins in rare-earth doped nanoparticles. *Nature Communications* **9.** `https://doi.org/10.1038/s41467-018-04509-w` (May 2018).

84. Kumar, K. S., Serrano, D., Nonat, A. M., Heinrich, B., Karmazin, L., Charbonnière, L. J., Goldner, P. & Ruben, M. Optical spin-state polarization in a binuclear europium complex towards molecule-based coherent light-spin interfaces. *Nature Communications* **12.** `https://doi.org/10.1038/s41467-021-22383-x` (Apr. 2021).

85. Merkel, B., Ulanowski, A. & Reiserer, A. Coherent and purcell-enhanced emission from erbium dopants in a cryogenic high- Q resonator. *Physical Review X* **10.** `https://doi.org/10.1103/physrevx.10.041025` (Nov. 2020).

86. Siyushev, P. *et al.* Coherent properties of single rare-earth spin qubits. *Nature Communications* **5.** `https://doi.org/10.1038/ncomms4895` (May 2014).

87. Probst, S., Rotzinger, H., Wünsch, S., Jung, P., Jerger, M., Siegel, M., Ustinov, A. V. & Bushev, P. A. Anisotropic rare-earth spin ensemble strongly coupled to a superconducting resonator. *Physical Review Letters* **110.** `https://doi.org/10.1103/physrevlett.110.157001` (Apr. 2013).

88. Wisby, I., de Graaf, S. E., Gwilliam, R., Adamyan, A., Kubatkin, S. E., Meeson, P. J., Tzalenchuk, A. Y. & Lindström, T. Coupling of a locally implanted rare-earth ion ensemble to a superconducting micro-resonator. *Applied Physics Letters* **105,** 102601. `https://doi.org/10.1063/1.4894455` (Sept. 2014).

89. Staudt, M. U. *et al.* Coupling of an erbium spin ensemble to a superconducting resonator. *Journal of Physics B: Atomic, Molecular and Optical Physics* **45,** 124019. `https://doi.org/10.1088/0953-4075/45/12/124019` (June 2012).

90. Dold, G. *et al.* High-cooperativity coupling of a rare-earth spin ensemble to a superconducting resonator using yttrium orthosilicate as a substrate. *Physical Review Applied* **11.** `https://doi.org/10.1103/physrevapplied.11.054082` (May 2019).

91. Probst, S. *et al.* Hybrid quantum circuit with implanted erbium ions. *Applied Physics Letters* **105,** 162404. `https://doi.org/10.1063/1.4898696` (Oct. 2014).

92. Probst, S., Rotzinger, H., Ustinov, A. V. & Bushev, P. A. Microwave multimode memory with an erbium spin ensemble. *Physical Review B* **92.** `https://doi.org/10.1103/physrevb.92.014421` (July 2015).

93. Farr, W. G., Goryachev, M., Creedon, D. L. & Tobar, M. E. Strong coupling between whispering gallery modes and chromium ions in ruby. *Physical Review B* **90.** `https://doi.org/10.1103/physrevb.90.054409` (Aug. 2014).

94. Tkalčec, A. *et al.* Strong coupling of anEr3-dopedYAlO3 crystal to a superconducting resonator. *Physical Review B* **90.** `https://doi.org/10.1103/physrevb.90.075112` (Aug. 2014).

95. Bushev, P. *et al.* Ultralow-power spectroscopy of a rare-earth spin ensemble using a superconducting resonator. *Physical Review B* **84.** `https://doi.org/10.1103/physrevb.84.060501` (Aug. 2011).

96. Diniz, I., Portolan, S., Ferreira, R., Gérard, J. M., Bertet, P. & Auffèves, A. Strongly coupling a cavity to inhomogeneous ensembles of emitters: Potential for long-lived solid-state quantum memories. *Physical Review A* **84.** `https://doi.org/10.1103/physreva.84.063810` (Dec. 2011).

97. O'Brien, C., Lauk, N., Blum, S., Morigi, G. & Fleischhauer, M. Interfacing superconducting qubits and telecom photons via a rare-earth-doped crystal. *Physical Review Letters* **113.** `https://doi.org/10.1103/physrevlett.113.063603` (Aug. 2014).

98. Williamson, L. A., Chen, Y.-H. & Longdell, J. J. Magneto-optic modulator with unit quantum efficiency. *Physical Review Letters* **113.** `https://doi.org/10.1103/physrevlett.113.203601` (Nov. 2014).

99. Blum, S., O'Brien, C., Lauk, N., Bushev, P., Fleischhauer, M. & Morigi, G. Interfacing microwave qubits and optical photons via spin ensembles. *Physical Review A* **91.** `https://doi.org/10.1103/physreva.91.033834` (Mar. 2015).

100. Li, B., Li, P.-B., Zhou, Y., Ma, S.-L. & Li, F.-L. Quantum microwave-optical interface with nitrogen-vacancy centers in diamond. *Physical Review A* **96.** `https://doi.org/10.1103/physreva.96.032342` (Sept. 2017).

101. Fernandez-Gonzalvo, X., Chen, Y.-H., Yin, C., Rogge, S. & Longdell, J. J. Coherent frequency up-conversion of microwaves to the optical telecommunications band in an Er:YSO crystal. *Physical Review A* **92.** `https://doi.org/10.1103/physreva.92.062313` (Dec. 2015).

102. Barnett, P. S. & Longdell, J. J. Theory of microwave-optical conversion using rare-earth-ion dopants. *Physical Review A* **102.** `https://doi.org/10.1103/physreva.102.063718` (Dec. 2020).

103. Xie, T. *et al.* Characterization of Er^{3+}:YVO_4 for microwave to optical transduction. *Physical Review B* **104.** `https://doi.org/10.1103/physrevb.104.054111` (Aug. 2021).

104. Marino, R., Lorgeré, I., Guillot-Noël, O., Vezin, H., Toncelli, A., Tonelli, M., Gouët, J.-L. L. & Goldner, P. Energy level structure and optical dephasing under magnetic field in Er^{3+}:$LiYF_4$ at 1.5 μm. *Journal of Luminescence* **169,** 478–482. `https://doi.org/10.1016/j.jlumin.2015.03.003` (Jan. 2016).

105. Ranon, U. Paramagnetic resonance of Nd^{3+}, Dy^{3+}, Er^{3+} and Yb^{3+} in YVO_4. *Physics Letters A* **28,** 228–229. `https://doi.org/10.1016/0375-9601(68)90218-1` (Nov. 1968).

106. Jacob, M. V., Mazierska, J. & Krupka, J. Dielectric properties of yttrium vanadate crystals from 15 K to 295 K. *Journal of Electroceramics* **15,** 237–241. `https://doi.org/10.1007/s10832-005-3302-z` (Dec. 2005).

107. Jacob, M. V., Mazierska, J. E., Krupka, J., Ledenyov, D. O. & Takeuchi, S. Microwave properties of Yttrium Vanadate at cryogenic temperatures. eprint: `arXiv:1209.5255` (2012).

108. Kindem, J. M., Bartholomew, J. G., Woodburn, P. J. T., Zhong, T., Craiciu, I., Cone, R. L., Thiel, C. W. & Faraon, A. Characterization of $^{171}Yb^{3+}$:YVO_4 for photonic quantum technologies. *Physical Review B* **98.** `https://doi.org/10.1103/physrevb.98.024404` (July 2018).

109. Hong-sheng, S., Ge, Z. & Hong-yuan, S. Measurement of principal refractive indices and the thermal refractive index coefficients of yttrium vanadate. *Journal of Synthetic Crystals* **30,** 85–88 (2001).

110. Sumida, D. S. & Fan, T. Y. Effect of radiation trapping on fluorescence lifetime and emission cross section measurements in solid-state laser media. *Optics Letters* **19,** 1343. `https://doi.org/10.1364/ol.19.001343` (Sept. 1994).

111. Afzelius, M. *et al.* Efficient optical pumping of Zeeman spin levels in. *Journal of Luminescence* **130,** 1566–1571. `https://doi.org/10.1016/j.jlumin.2009.12.026` (Sept. 2010).

112. Raha, M., Chen, S., Phenicie, C. M., Ourari, S., Dibos, A. M. & Thompson, J. D. Optical quantum nondemolition measurement of a single rare-earth ion qubit. *Nature Communications* **11.** `https://doi.org/10.1038/s41467-020-15138-7` (Mar. 2020).

113. Louchet, A. *et al.* Branching ratio measurement of a Λ system in Tm^{3+}:YAG under a magnetic field. *Physical Review B* **75.** `https://doi.org/10.1103/physrevb.75.035131` (Jan. 2007).

114. Woodburn, P. J. T., Marsh, A. D., Cone, R. L. & Thiel, C. W. Using birefringence to orient crystals for classical and quantum information applications. unpublished.

115. Burek, M. J. *et al.* High quality-factor optical nanocavities in bulk single-crystal diamond. *Nature Communications* **5.** `https://doi.org/10.1038/ncomms6718` (Dec. 2014).

116. Khanaliloo, B., Mitchell, M., Hryciw, A. C. & Barclay, P. E. High-Q/V monolithic diamond microdisks fabricated with quasi-isotropic etching. *Nano Letters* **15,** 5131–5136. `https://doi.org/10.1021/acs.nanolett.5b01346` (July 2015).

117. Latawiec, P., Venkataraman, V., Burek, M. J., Hausmann, B. J. M., Bulu, I. & Lončar, M. On-chip diamond Raman laser. *Optica* **2,** 924. `https://doi.org/10.1364/optica.2.000924` (Oct. 2015).

118. Faraon, A., Barclay, P. E., Santori, C., Fu, K.-M. C. & Beausoleil, R. G. Resonant enhancement of the zero-phonon emission from a colour centre in a diamond cavity. *Nature Photonics* **5,** 301–305. `https://doi.org/10.1038/nphoton.2011.52` (Apr. 2011).

119. Lukin, D. M. *et al.* 4H-silicon-carbide-on-insulator for integrated quantum and nonlinear photonics. *Nature Photonics* **14,** 330–334. `https://doi.org/10.1038/s41566-019-0556-6` (Dec. 2019).

120. Craiciu, I., Lei, M., Rochman, J., Bartholomew, J. G. & Faraon, A. Multifunctional on-chip storage at telecommunication wavelength for quantum networks. *Optica* **8,** 114. `https://doi.org/10.1364/optica.412211` (Jan. 2021).

121. Wang, C., Miyazono, E., Craiciu, I. & Faraon, A. Hybrid silicon on silicon carbide integrated photonics platform. *Applied Physics Letters* **115,** 141105. `https://doi.org/10.1063/1.5116201` (Sept. 2019).

122. Gould, M., Schmidgall, E. R., Dadgostar, S., Hatami, F. & Fu, K.-M. C. Efficient extraction of zero-phonon-line photons from single nitrogen-vacancy centers in an integrated GaP-on-diamond platform. *Physical Review Applied* **6.** `https://doi.org/10.1103/physrevapplied.6.011001` (July 2016).

123. Takei, R., Manako, S., Omoda, E., Sakakibara, Y., Mori, M. & Kamei, T. Sub-1 dB/cm submicrometer-scale amorphous silicon waveguide for backend on-chip optical interconnect. *Optics Express* **22,** 4779. `https://doi.org/10.1364/oe.22.004779` (Feb. 2014).

124. Gao, J. *The Physics of Superconducting Microwave Resonators* PhD thesis (California Institute of Technology, 2008). `https://resolver.caltech.edu/CaltechETD:etd-06092008-235549`.

125. De Visser, P. *Quasiparticle dynamics in aluminium superconducting microwave resonators.* PhD thesis (Delft University of Technology, 2014). `http://resolver.tudelft.nl/uuid:eae4c9fc-f90d-4c12-a878-8428ee4adb4c`.

126. De Graaf, S. E. *Fractal superconducting resonators for the interrogation of two-level systems* PhD thesis (Chalmers University of Technology, 2014). `https://publications.lib.chalmers.se/records/fulltext/190808/190808.pdf`.

127. Kaplan, S. B., Chi, C. C., Langenberg, D. N., Chang, J. J., Jafarey, S. & Scalapino, D. J. Quasiparticle and phonon lifetimes in superconductors. *Physical Review B* **14,** 4854–4873. `https://doi.org/10.1103/physrevb.14.4854` (Dec. 1976).

128. Barends, R. *Photon-detecting superconducting resonators.* PhD thesis (TU Delft, 2009). `https://repository.tudelft.nl/islandora/object/uuid$%5C%$%203A574944e6-c3ce-4c86-a511-a88385b22379`.

129. Martinis, J. M., Ansmann, M. & Aumentado, J. Energy decay in superconducting josephson-junction qubits from nonequilibrium quasiparticle excitations. *Physical Review Letters* **103.** `https://doi.org/10.1103/physrevlett.103.097002` (Aug. 2009).

130. Barends, R. *et al.* Minimizing quasiparticle generation from stray infrared light in superconducting quantum circuits. *Applied Physics Letters* **99,** 113507. `https://doi.org/10.1063/1.3638063` (Sept. 2011).

131. Mattis, D. C. & Bardeen, J. Theory of the anomalous skin effect in normal and superconducting metals. *Physical Review* **111,** 412–417. `https://doi.org/10.1103/physrev.111.412` (July 1958).

132. Glover, R. E. & Tinkham, M. Conductivity of superconducting films for photon energies between 0.3 and 40 *k*Tc. *Physical Review* **108,** 243–256. `https://doi.org/10.1103/physrev.108.243` (Oct. 1957).

133. Rothwarf, A. & Taylor, B. N. Measurement of recombination lifetimes in superconductors. *Physical Review Letters* **19,** 27–30. `https://doi.org/10.1103/physrevlett.19.27` (July 1967).

134. Day, P. K., LeDuc, H. G., Mazin, B. A., Vayonakis, A. & Zmuidzinas, J. A broadband superconducting detector suitable for use in large arrays. *Nature* **425,** 817–821. `https://doi.org/10.1038/nature02037` (Oct. 2003).

135. Lobo, R. P. S. M. *et al.* Photoinduced time-resolved electrodynamics of superconducting metals and alloys. *Physical Review B* **72.** `https://doi.org/10.1103/physrevb.72.024510` (July 2005).

136. Borsoi, F. Magnetic field resilient superconducting circuit elements for Majorana parity detection. (2015).

137. Kroll, J. *et al.* Magnetic-Field-Resilient Superconducting Coplanar-Waveguide Resonators for Hybrid Circuit Quantum Electrodynamics Experiments. *Physical Review Applied* **11.** `https://doi.org/10.1103/physrevapplied.11.064053` (June 2019).

138. Stan, G., Field, S. B. & Martinis, J. M. Critical field for complete vortex expulsion from narrow superconducting strips. *Physical Review Letters* **92.** `https://doi.org/10.1103/physrevlett.92.097003` (Mar. 2004).

139. Meservey, R. & Tedrow, P. M. Properties of very thin aluminum films. *Journal of Applied Physics* **42,** 51–53. `https://doi.org/10.1063/1.1659648` (Jan. 1971).

140. Tinkham, M. *Introduction to Superconductivity* (Courier Corporation, 2004).

141. Song, C., DeFeo, M. P., Yu, K. & Plourde, B. L. T. Reducing microwave loss in superconducting resonators due to trapped vortices. *Applied Physics Letters* **95,** 232501. `https://doi.org/10.1063/1.3271523` (Dec. 2009).

142. Bothner, D., Gaber, T., Kemmler, M., Koelle, D. & Kleiner, R. Improving the performance of superconducting microwave resonators in magnetic fields. *Applied Physics Letters* **98,** 102504. `https://doi.org/10.1063/1.3560480` (Mar. 2011).

143. Chiaro, B. *et al.* Dielectric surface loss in superconducting resonators with flux-trapping holes. *Superconductor Science and Technology* **29,** 104006 (2016).

144. Samkharadze, N., Bruno, A., Scarlino, P., Zheng, G., DiVincenzo, D., DiCarlo, L. & Vandersypen, L. High-kinetic-inductance superconducting nanowire resonators for circuit QED in a magnetic field. *Physical Review Applied* **5.** `https://doi.org/10.1103/physrevapplied.5.044004` (Apr. 2016).

145. De Graaf, S. E., Davidovikj, D., Adamyan, A., Kubatkin, S. E. & Danilov, A. V. Galvanically split superconducting microwave resonators for introducing internal voltage bias. *Applied Physics Letters* **104,** 052601. `https://doi.org/10.1063/1.4863681` (Feb. 2014).

146. Zollitsch, C. W., O'Sullivan, J., Kennedy, O., Dold, G. & Morton, J. J. L. Tuning high-Q superconducting resonators by magnetic field reorientation. *AIP Advances* **9,** 125225. `https://doi.org/10.1063/1.5129032` (Dec. 2019).

147. Meservey, R. & Tedrow, P. M. Measurements of the Kinetic Inductance of Superconducting Linear Structures. *Journal of Applied Physics* **40,** 2028–2034. `https://doi.org/10.1063/1.1657905` (Apr. 1969).

148. Pozar, D. M. *Microwave Engineering* (John Wiley & Sons, 2011).

149. Rauch, W., Gornik, E., Sölkner, G., Valenzuela, A. A., Fox, F. & Behner, H. Microwave properties of $YBa_2Cu_3O_7$-xthin films studied with coplanar transmission line resonators. *Journal of Applied Physics* **73,** 1866–1872. `https://doi.org/10.1063/1.353173` (Feb. 1993).

150. Clem, J. R. Inductances and attenuation constant for a thin-film superconducting coplanar waveguide resonator. *Journal of Applied Physics* **113,** 013910. `https://doi.org/10.1063/1.4773070` (Jan. 2013).

151. Beck, M. A., Isaacs, J. A., Booth, D., Pritchard, J. D., Saffman, M. & McDermott, R. Optimized coplanar waveguide resonators for a superconductor-atom interface. *Applied Physics Letters* **109,** 092602. `https://doi.org/10.1063/1.4962172` (Aug. 2016).

152. Doyle, S. *Lumped Element Kinetic Inductance Detectors.* PhD thesis (Cardiff University, 2008). `https://orca.cardiff.ac.uk/54728/1/U585117.pdf`.

153. Zmuidzinas, J. Superconducting microresonators: Physics and applications. *Annual Review of Condensed Matter Physics* **3,** 169–214. `https://doi.org/10.1146/annurev-conmatphys-020911-125022` (Mar. 2012).

154. Haikka, P., Kubo, Y., Bienfait, A., Bertet, P. & Mølmer, K. Proposal for detecting a single electron spin in a microwave resonator. *Physical Review A* **95.** `https://doi.org/10.1103/physreva.95.022306` (Feb. 2017).

155. Eichler, C., Sigillito, A., Lyon, S. & Petta, J. Electron spin resonance at the level of 10^4 spins using low impedance superconducting resonators. *Physical Review Letters* **118.** `https://doi.org/10.1103/physrevlett.118.037701` (Jan. 2017).

156. Probst, S. *et al.* Inductive-detection electron-spin resonance spectroscopy with 65 spins/ Hz sensitivity. *Applied Physics Letters* **111,** 202604. `https://doi.org/10.1063/1.5002540` (Nov. 2017).

157. Bienfait, A. *et al.* Reaching the quantum limit of sensitivity in electron spin resonance. *Nature Nanotechnology* **11,** 253–257. `https://doi.org/10.1038/nnano.2015.282` (Dec. 2015).

158. Ismail, N., Kores, C. C., Geskus, D. & Pollnau, M. Fabry-Pérot resonator: spectral line shapes, generic and related Airy distributions, linewidths, finesses, and performance at low or frequency-dependent reflectivity. *Optics Express* **24,** 16366. `https://doi.org/10.1364/oe.24.016366` (July 2016).

159. Garces, N. Y., Stevens, K. T., Foundos, G. K. & Halliburton, L. E. Electron paramagnetic resonance and optical absorption study of V^{4+}centres in YVO_4 crystals. *Journal of Physics: Condensed Matter* **16,** 7095–7106. `https://doi.org/10.1088/0953-8984/16/39/040` (Sept. 2004).

160. The tension of metallic films deposited by electrolysis. *Proceedings of the Royal Society of London. Series A, Containing Papers of a Mathematical and Physical Character* **82,** 172–175. `https://doi.org/10.1098/rspa.1909.0021` (May 1909).

161. Miyazono, E. T. *Nanophotonic Resonators for Optical Quantum Memories based on Rare-Earth-Doped Materials* PhD thesis (California Institute of Technology, 2017). `https://resolver.caltech.edu/CaltechTHESIS:03152017-114949088`.

162. Kindem, J. M. *Quantum Nanophotonics with Ytterbium in Yttrium Orthovanadate* PhD thesis (California Institute of Technology, 2019). `https://resolver.caltech.edu/CaltechTHESIS:03132019-062905529`.

163. Craiciu, I. *Quantum Storage of Light Using Nanophotonic Resonators Coupled to Erbium Ion Ensembles* PhD thesis (California Institute of Technology, 2020). `https://resolver.caltech.edu/CaltechTHESIS:06012020-134801698`.

164. Mosor, S. *et al.* Scanning a photonic crystal slab nanocavity by condensation of xenon. **87,** 141105. `https://doi.org/10.1063/1.2076435` (Oct. 2005).

165. Megrant, A. *et al.* Planar superconducting resonators with internal quality factors above one million. *Applied Physics Letters* **100,** 113510. `https://doi.org/10.1063/1.3693409` (Mar. 2012).

166. Mazin, B. A. *Microwave Kinetic Inductance Detectors* PhD thesis (California Institute of Technology, 2005). `https://resolver.caltech.edu/CaltechETD:etd-10042004-120707`.

167. Pappas, D. P., Vissers, M. R., Wisbey, D. S., Kline, J. S. & Gao, J. Two level system loss in superconducting microwave resonators. *IEEE Transactions on Applied Superconductivity* **21,** 871–874. `https://doi.org/10.1109/tasc.2010.2097578` (June 2011).

168. Goetz, J. *et al.* Loss mechanisms in superconducting thin film microwave resonators. *Journal of Applied Physics* **119,** 015304. `https://doi.org/10.1063/1.4939299` (Jan. 2016).

169. Xu, M., Han, X., Zou, C.-L., Fu, W., Xu, Y., Zhong, C., Jiang, L. & Tang, H. X. Radiative cooling of a superconducting resonator. *Physical Review Letters* **124.** `https://doi.org/10.1103/physrevlett.124.033602` (Jan. 2020).

170. Gely, M. F., Kounalakis, M., Dickel, C., Dalle, J., Vatré, R., Baker, B., Jenkins, M. D. & Steele, G. A. Observation and stabilization of photonic Fock states in a hot radio-frequency resonator. *Science* **363,** 1072–1075. `https://doi.org/10.1126/science.aaw3101` (Mar. 2019).

171. Chen, Y.-H., Fernandez-Gonzalvo, X. & Longdell, J. J. Coupling erbium spins to a three-dimensional superconducting cavity at zero magnetic field. *Physical Review B* **94.** `https://doi.org/10.1103/physrevb.94.075117` (Aug. 2016).

172. Luthi, F. *et al.* Evolution of nanowire transmon qubits and their coherence in a magnetic field. *Physical Review Letters* **120.** `https://doi.org/10.1103/physrevlett.120.100502` (Mar. 2018).

173. Schneider, A., Wolz, T., Pfirrmann, M., Spiecker, M., Rotzinger, H., Ustinov, A. V. & Weides, M. Transmon qubit in a magnetic field: Evolution of coherence and transition frequency. *Physical Review Research* **1.** `https://doi.org/10.1103/physrevresearch.1.023003` (Sept. 2019).

174. Kringhøj, A. *et al.* Magnetic-field-compatible superconducting transmon qubit. *Physical Review Applied* **15.** `https://doi.org/10.1103/physrevapplied.15.054001` (May 2021).

175. Zhong, T. *et al.* Nanophotonic rare-earth quantum memory with optically controlled retrieval. *Science* **357,** 1392–1395. `https://doi.org/10.1126/science.aan5959` (Sept. 2017).

176. Craiciu, I. *et al.* Nanophotonic quantum storage at telecommunication wavelength. *Physical Review Applied* **12.** `https://doi.org/10.1103/physrevapplied.12.024062` (Aug. 2019).

177. Ruskuc, A., Wu, C.-J., Rochman, J., Choi, J. & Faraon, A. Nuclear spin-wave quantum register for a solid state qubit. *Nature* **602,** 408–413. `https://doi.org/10.1038/s41586-021-04293-6` (Feb. 2022).

178. Zhong, T. *et al.* Optically addressing single rare-earth ions in a nanophotonic cavity. *Physical Review Letters* **121.** `https://doi.org/10.1103/physrevlett.121.183603` (Oct. 2018).

179. Bartholomew, J. G., Zhong, T., Kindem, J. M., Lopez-Rios, R., Rochman, J., Craiciu, I., Miyazono, E. & Faraon, A. Controlling rare-earth ions in a nanophotonic resonator using the ac Stark shift. *Physical Review A* **97.** `https://doi.org/10.1103/physreva.97.063854` (June 2018).

Appendix A

FIB NANOBEAM FABRICATION

Before starting the transduction project described in the thesis, I had worked on the design and fabrication of optical photonic crystal cavities in YVO_4 and YSO substrates using focused ion beam (FIB) milling. This work started as an undergraduate internship in the Faraon group. At that time, the group had only tried to make cavities using FIB with YSO (led by a previous postdoc, Dr. Tian Zhong, and some work also by Evan Miyazono), and my work involved extending those efforts into YVO_4. Generally speaking, making FIB cavities in YVO was relatively successful, and we were quickly able to get higher quality factors in YVO_4 compared to YSO for cavities at the same wavelength. This was largely thought to be due to the higher refractive index of YVO_4 compared to YSO.

The photonic crystal cavities consist of a triangular waveguide cross-section where the photonic crystal pattern is achieved by milling thin slots across the beam. We could control the photonic bandgap by the waveguide width, the slot depth, the slot width and the lattice constant between adjacent slots. The defect mode in the center of the cavity was introduced by perturbing the mirror lattice constant. The lattice constant was by far the most reliable parameter from the fabrication process since it was introduced in the milling pattern file and did not depend on any user input. The simulated electric field distribution of a TM cavity mode is shown in Figure A.1.

This design would result in simulated intrinsic quality factors nearing one million, so the fabricated device quality factors were not limited by this, but more by our ability to perfectly reproduce the design using the FIB. The simulated cavity mode volumes were around 1 cubic wavelength.

Using this fabrication technique, I fabricated devices using FIB for different projects including optical quantum memories [175, 176], single rare-earth ions [108, 177, 178] and microwave-to-optical transduction [57], and others [179] during my time as a PhD student. This included devices for Er^{3+}:YSO ($\lambda \sim 1536$ nm), Nd^{3+}:YVO_4 ($\lambda \sim 880$ nm), and Yb^{3+}:YVO_4 ($\lambda \sim 984$ nm). SEM images of a fabricated nanobeam cavity are shown in Figure A.2.

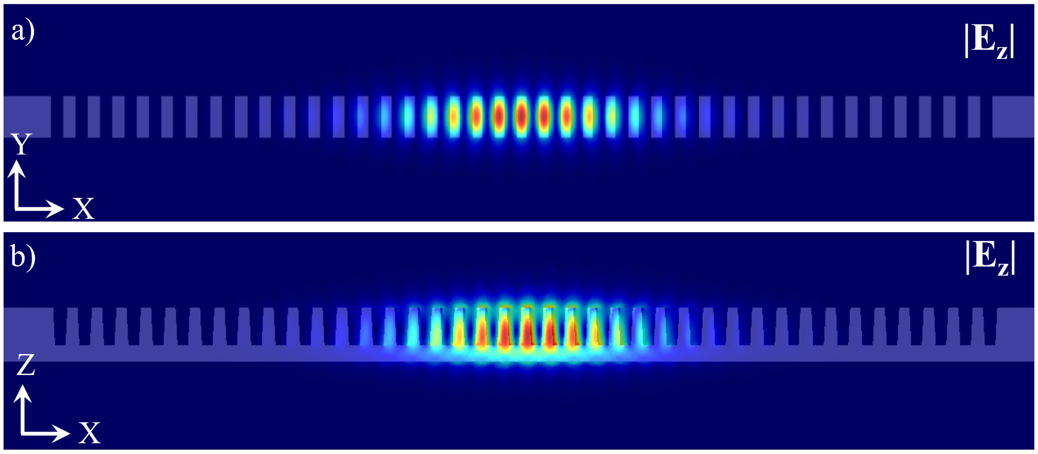

Figure A.1: Simulated electric field of the nanobeam cavity. a) Top view of the cavity field. b) Side view of the cavity field.

The general recipe for fabricating these resonators is provided in reference [75], but I will provide some additional insight here. On a given chip, normally 9 devices would be fabricated at a time before the devices were tested. It would take ~3-4 hours to mill three triangular waveguides at a time. The time was on the longer side for the longer wavelength cavities (i.e. for coupling to erbium) since they required longer waveguides (25 μm compared to 15 μm for shorter wavelengths).

Typically each milling step was kept below 10 minutes to ensure that the sample would not drift to much during the step. There were a minimum of 6 milling steps for each beam. This includes milling on both sides of the waveguide and first starting at a high beam current (~ 1 nA) to remove material quickly and then finishing at a low beam current (~ 30 pA) to precisely shape the waveguide. The additional time was to align each beam current as we switched between them and for moving between devices. To create all 9 devices, this process would be repeated two additional times.

It was important to make sure the waveguide was milled to the correct width (typically within 10 nm of the design target). One convenient aspect of the FIB is that there is a SEM in the same tool so it was relatively easy to measure the waveguide width and make the required corrections to make it more narrow.

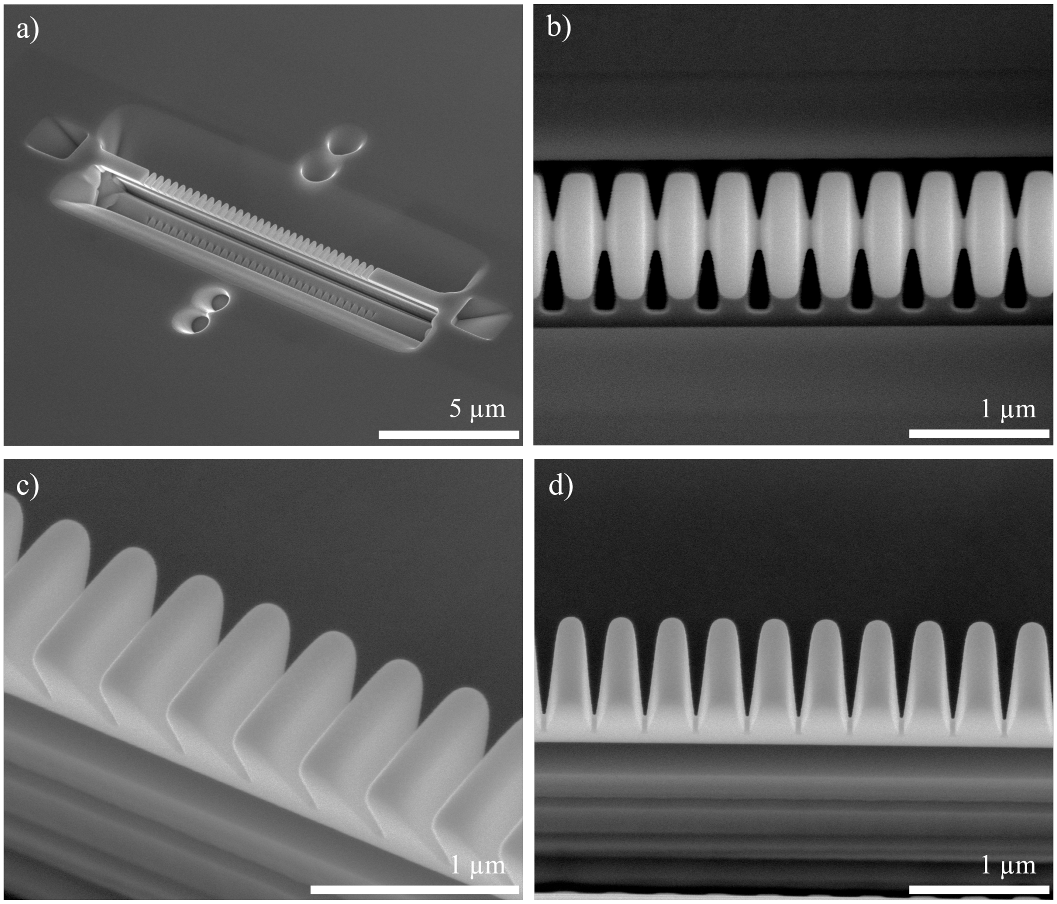

Figure A.2: SEM images of optical resonators from FIB milling. a) full nanobeam cavity. b-d) close up images of the photonic crystal patterns of the cavity.

Another important aspect of milling the triangular waveguides was the angle. We targeted to create an equilateral triangle cross-section. Naively, one would set the focused ion beam at that angle and mill the structure. However, the focused ion beam has a Gaussian beam shape, so the tails of the beam can also mill material and can change the angle by ~5° (i.e. interior angles at the top of the triangle was ~65° if not corrected). The FIB angle was adjusted accordingly to minimize the deviation of nanobeam angle. It is also worth noting that this angle is sensitive to the alignment and focus of the FIB, so it is important to optimize this consistently every time.

The photonic crystal pattern and the 45° end couplers would then all be patterned in a single 3-4 hour session. So typically it would take a total of at least 12 hours to fabricate 9 devices. The milling of the slots would be recalibrated for every device as the shape of the slots highly depends on how well the FIB is focused, which was aligned by the user. For alignment, typically one waveguide was sacrificed for test milling the slots to make sure the dimensions were as perfect as possible. Again, we took advantage of the SEM to optimize this step.

Another issue during the milling of the photonic crystal slots was the drifting of the FIB relative to the sample. Typically, we would let the sample stage settle for some time until we did not notice any more movement. Also, in order to prevent any drift from charging effects, the SEM was left on at the correct current to null the additional positive charge from the FIB.

The 45° end couplers would be milled as the last FIB step, which was our method for coupling light into and out of the photonic crystal cavities. The devices were then placed in chrome etchant for one minute to remove the 50 nm chrome hard mask used during the milling process.

In terms of the highest quality factors, we measured Q's up to ~25,000 and ~50,000 at wavelengths of ~900 nm and ~1050 nm, respectively, in YVO_4. We also measured Q's up to 70,000 at a wavelength of ~1500 nm in YSO.

Appendix B

TRANSDUCER DESIGN AND SIMULATION

For Z_1-Y_2 transduction, we used a TE mode resonator (parameters are in Table B.1). The designs for TE and TM mode cavities on sapphire are shown in Table B.2 and Table B.3.

Table B.1: Optical cavity geometry parameters—YVO TE mode

Parameter	Value
Waveguide Height	225 nm
Waveguide Width	600 nm
Waveguide Length	100 μm
a_0	312.5 nm
$r_{\|\|,0}$	50 nm
$r_{\perp,0}$	50 nm
a_t	275 nm
$r_{\|\|,t}$	20 nm
$r_{\perp,t}$	20 nm
Mirror Periods	0, 25
Taper Periods	15

Table B.2: Optical cavity geometry parameters—sapphire TE mode

Parameter	Value
Waveguide Height	225 nm
Waveguide Width	600 nm
Waveguide Length	100 μm
a_0	325 nm
$r_{\|\|,0}$	60 nm
$r_{\perp,0}$	70 nm
a_t	280 nm
$r_{\|\|,t}$	20 nm
$r_{\perp,t}$	20 nm
Mirror Periods	0, 25
Taper Periods	15

Table B.3: Optical cavity geometry parameters—sapphire TM mode

Parameter	Value
Waveguide Height	300 nm
Waveguide Width	600 nm
Waveguide Length	100 μm
a_0	370 nm
$r_{\parallel,0}$	125 nm
$r_{\perp,0}$	115 nm
a_t	310 nm
$r_{\parallel,t}$	20 nm
$r_{\perp,t}$	20 nm
Mirror Periods	4, 25
Taper Periods	15

Appendix C

CW TRANSDUCTION AT HIGH MICROWAVE POWER

Although not important for quantum transduction, we also characterized the transducer under high microwave input power and observed some interesting structure in the signal. We also note that at high microwave input power, the efficiency is lower compared to lower microwave input power.

The CW transduction signal as function of the input microwave and optical frequency for a set of optical and microwave powers is shown in Figure C.1. The data is for ground state transduction and the magnetic field is 60 mT. Figure C.1a-c shows the signal at P_o=15 μW for different microwave powers, while Figure C.1d-f shows the signal at P_o=150 μW. We do not observe a significant change in the signal shape for the different optical power.

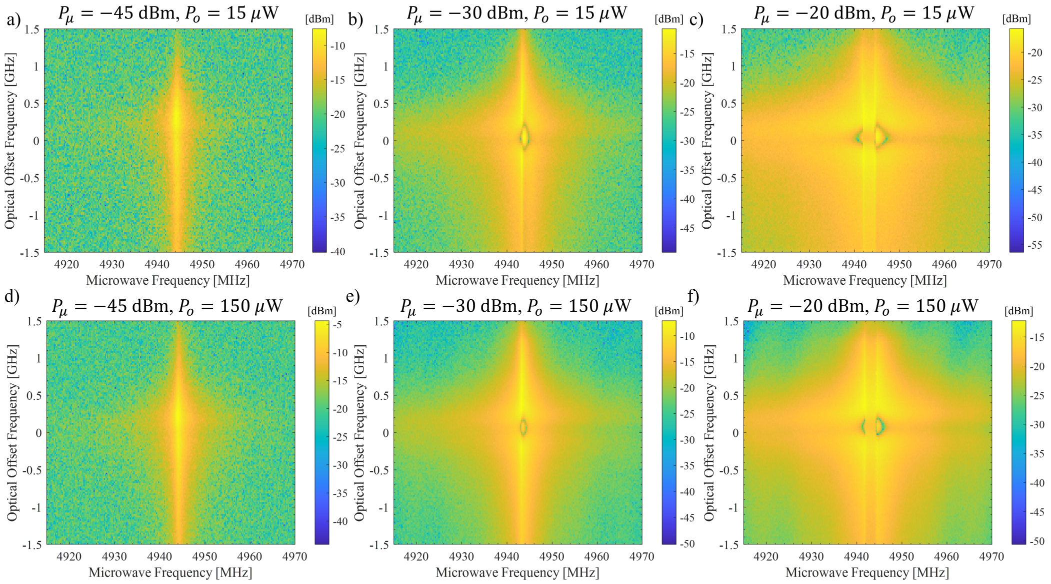

Figure C.1: CW transduction as a function of the input microwave and optical frequencies at different microwave and optical powers, with a focus on high microwave input power.

We do observe a significant change for sweeping the microwave power. At the lower microwave power of P_μ =–45 dBm (Figure C.1a), the signal has a single peak at the microwave cavity frequency, while at the high microwave power of P_μ =–20 dBm (Figure C.1c), the signal splits in the microwave frequency domain and there develops some narrow features that exhibit very low signal. We note that we only see this structure in the transduction signal and not just in the microwave cavity line shape when we send in high microwave power.

The signal at a fixed laser frequency for different microwave powers and P_o=15 μW is shown in Figure C.2a. The frequencies that null the signal has an increased splitting at larger microwave power and the efficiency decreases. The transduction signal as a function of the microwave frequency at two different laser offsets is shown in Figure C.2b-c for P_μ=–30 dBm and P_μ=–20 dBm, respectively. We observe that the signal has a complicated structure when the laser offset is 0 GHz, while a more Lorentzian lineshape emerges at larger frequency offsets.

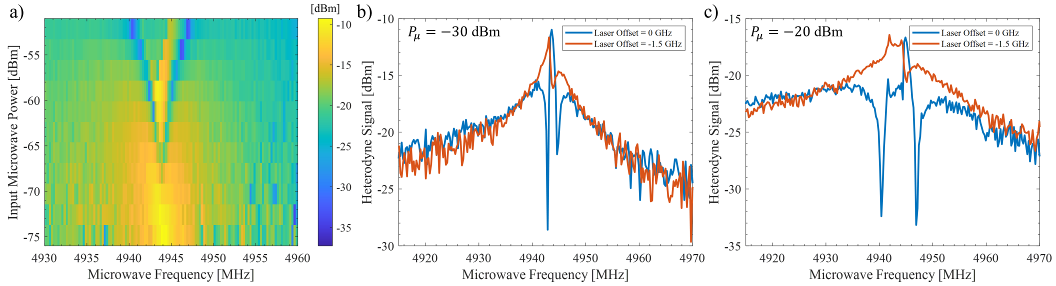

Figure C.2: a) CW transduction vs optical power. Microwave frequency dependence of the transduction signal for b) P_μ=–30 dBm and c) P_μ=–20 dBm.